

Alloy catalysts for fuel cell-based alcohol sensors

By

Mohammadreza Zamanzad Ghavidel

A Thesis Submitted in Partial Fulfillment of the Requirements for the Degree of

Doctor of Philosophy

University of Ontario Institute of Technology
Faculty of Science
Materials Science

May 2016

©Mohammadreza Zamanzad Ghavidel, 2016

Certificate of Approval

Abstract

Direct ethanol fuel cells (DEFCs) are attractive from both economic and environmental standpoints for generating renewable energy and powering vehicles and portable electronic devices. There is a great interest recently in developing DEFC systems. The cost and performance of the DEFCs are mainly controlled by the Pt-base catalysts used at each electrode. In addition to energy conversion, DEFC technology is commonly employed in the fuel-cell based breath alcohol sensors (BrAS). BrAS is a device commonly used to measure blood alcohol concentration (BAC) and enforce drinking and driving laws. The BrAS is non-invasive and has a fast respond time. However, one of the most important drawback of the commercially available BrAS is the very high loading of Pt employed. One well-known and cost effective method to reduce the Pt loading is developing Pt-alloy catalysts. Recent studies have shown that Pt-transition metal alloy catalysts enhanced the electroactivity while decreasing the required loadings of the Pt catalysts.

In this thesis, carbon supported Pt-Mn and Pt-Cu electrocatalysts were synthesized by different methods and the effects of heat treatment and structural modification on the ethanol oxidation reaction (EOR) activity, oxygen reduction reaction (ORR) activity and durability of these samples were thoroughly studied. Finally, the selected Pt-Mn and Pt-Cu samples with the highest EOR activity were examined in a prototype BrAS system and compared to the Pt/C and Pt₃Sn/C commercial electrocatalysts.

Studies on the Pt-Mn catalysts produced with and without additives indicate that adding trisodium citrate (SC) to the impregnation solution improved the particle dispersion, decreased particle sizes and reduced the time required for heat treatment. Further studies show that the optimum weight ratio of SC to the metal loading in the impregnation solution

was 2:1 and optimum results achieved at pH lower than 4. In addition, powder X-ray diffraction (XRD) analyses indicate that the optimum heat treatment temperature was 700 °C where a uniform ordered PtMn intermetallic phase was formed. Although the electrochemical active surface area (ECSA) decreased due to the heat treatment, the EOR activity of Pt-Mn samples was improved. Moreover, it was shown that the heat-treated samples prepared in the presence of SC showed superior the EOR activity compared to the samples made without SC.

The Pt-Cu/C alloys were produced by three different methods: impregnation, impregnation in the presence of sodium citrate and microwave assisted polyol methods. These studies showed that the polyol method was the optimum method to produce the Pt-Cu alloy. The XRD analysis indicates that the heat treatment at 700 °C developed catalysts rich in the PtCu and PtCu₃ ordered phases. The highest EOR activity was measured for the Pt-Cu/C-POL (sample made by the polyol method) and heat treated at 700 °C for 1h. Comparing the EOR activity of the Pt-Cu and Pt-Mn samples also demonstrates that the heat treated Pt-Cu/C-POL sample showed higher EOR activity compared to the Pt-Mn samples. These results indicate that the benefits of thermally treating alloy nanoparticles could outweigh any activity losses that may occur due to the particle size growth and the ECSA loss. Besides, accelerated stress tests (ASTs) illustrate that the heat treatment improved the durability of the Pt-Mn and Pt-Cu samples. The durability and EOR activity of the heat treated Pt-Mn and Pt-Cu samples was similar or better than commercial samples. On the other hand, the ORR activity of Pt-Mn and Pt-Cu after the heat treatment was slightly lower than the commercial samples but the ORR activity loss can be compensated by the economic benefits from using the lower Pt loading.

Finally, studying the alcohol sensing characteristic of different samples shows that the heat treated Pt-Mn and Pt-Cu catalysts could be used for the ethanol sensing. Additionally, among the different commercial samples tested for ethanol sensing, Pt-Sn/C showed the highest sensitivity but with slightly higher standard deviation. Further studies on the Pt-Cu/C and Pt-Mn/C samples indicate that the heat treatment improved the sensitivity of these samples and the highest normalized sensitivity among all the samples belonged to the Pt-Cu/C-POL (sample produced by polyol method) and heat treated at 700 °C. It can be concluded that the heat treated Pt-Mn and Pt-Cu samples could be used as an alternative to replace Pt black in commercial sensors which would dramatically decrease the Pt loading. This could reduce the price and increase the sensitivity of commercial alcohol sensors.

Keywords: Breath alcohol sensor, fuel cell sensor, breathalyzer, proton exchange membrane fuel cell, direct alcohol fuel cell, electrocatalyst, Pt-base alloys, electrochemistry, ethanol oxidation, oxygen reduction reaction, heat treatment, durability

Acknowledgements

Art is I, science is we.

(Claude Bernard)

No words could express depth of my gratitude to my supervisor, Dr. Brad Easton. I highly appreciate his guidance, support and motivation over the last four years. I learned a lot from his passion for the science and chemistry. I am very grateful to him for providing this unique opportunity for me to grow and learn more.

I would also like to extend a sincere thank you to my supervisory committee: Dr. Liliana Trevani, and Dr. Andrew Vreugdenhil for all your valuable comments and advice throughout the course of my PhD studies. My sincere gratitude to Dr. Daniel Guay, my external examiner, and to Dr. Jean-Paul Desaulniers, my internal examiner, for their valuable time and agreeing to be part of the process.

I am also pleased to appreciate the great help that I received from experts, technicians and professors during my thesis research. Specially, I would like to thank Dr. Liliana Trevani and Dr. Franco Gaspari for giving unlimited access to their labs and treating me as their own students. I would like to acknowledge specifically Mike Allison at UOIT who helped with ICP-OES analysis and Dr. Ranganathan Santhanam at UOIT for SEM training and analysis. I acknowledge Dr. Wen He Gong (McMaster University) for the XRD data, Dr. Richard B. Gardiner (University of Western Ontario) and Dr. Yan WANG-DUFFORT (University of Waterloo (WATLab)) for the TEM images and Dr. Mark Biesinger (Surface Science Western, University of Western Ontario) for XPS analysis.

I am very grateful to be part of the Easton research lab and my special thanks go to, both past and present members of this group. I truly appreciate the help that I received from

everyone in the lab. In particular, I would like to thank Dr. Jennie Eastcott, Stephanie Mavilla and Patrick Edge for treating me like their family and supporting me during my first years in Canada. My thanks go out to Dr. Mohammad Rahman and Dr. Jesse Allan for the assistance in building and developing alcohol sensing station and to O'Rian Reid for support in making electrodes.

Finally, I would like to thank my dear parents and my dear brothers and wish them happiness and prosperity. Everything that I have done or achieved was not possible without their valuable love and support. They were and they will be my motivation and courage to pursue my dreams and goals. I would like to dedicate this work to my beloved mother and father.

Table of content

Certificate of Approval.....	i
Abstract.....	ii
Acknowledgements	v
Table of content.....	vii
List of Tables	xiii
List of Figures.....	xv
List of Abbreviations and Symbols	xxiv
Chapter 1: Introduction	1
1.1 Fuel Cell.....	2
1.1.1 Proton Exchange Membrane Fuel Cells	2
1.1.2 Direct alcohol fuel cells	4
1.1.3 Catalysts used in direct alcohol fuel cells.....	7
1.1.3.1 Pt alloy catalysts.....	8
1.1.3.2 Fabrication of Pt alloy catalysts	11
1.1.3.3 Post heat treatment of Pt alloy catalysts.....	13
1.1.4 Oxygen reduction reaction on Pt-based catalysts	15
1.2 Breath alcohol sensors	17
1.3 Electrochemical Evaluation of Catalysts and DAFC Electrodes	20
1.4 Cyclic Voltammetry.....	21
1.4.1 Electrochemical Impedance Spectroscopy	22
1.5 Thesis Objectives	27
1.6 References.....	29
Chapter 2: Chemicals and Instrumentation	36
2.1 Material Preparation.....	37

2.1.1	Catalyst Synthesis.....	37
2.1.1.1	Pt and Pt-Mn catalysts.....	37
2.1.1.2	Pt-Cu catalysts.....	39
2.1.2	Post heat treatment.....	40
2.2	Inductively-Coupled Plasma Optical Emission Spectroscopy.....	41
2.2.1	Before electrochemical tests.....	41
2.2.2	After electrochemical tests	41
2.3	Thermogravimetric Analysis	42
2.4	Powder X-ray Diffraction (XRD)	42
2.5	Transmission Electron Microscopy	43
2.6	X-ray Photo Spectrometry	43
2.7	Electrochemical Testing.....	44
2.7.1	Electrode preparation.....	44
2.7.1.1	Electrochemical studies in half-cell	44
2.7.1.2	Gas diffusion electrode.....	46
2.7.2	Cyclic and Linear Sweep voltammetry.....	47
2.7.3	Electrochemical Impedance Spectroscopy	48
2.7.4	Half-Cell durability tests.....	49
2.7.4.1	Accelerated stress tests (ASTs).....	49
2.7.5	Oxygen Reduction Reaction.....	50
2.7.6	Fuel Cell and Sensor Electrochemical Measurements.....	50
2.7.6.1	Calibration curves and 7-day sensing tests	51
2.7.6.2	Sensing tests at constant concentration	52
2.8	References.....	55
	Chapter 3: Production and Thermally Induced Changes in the Structure and Electrochemical Activity of Pt-Mn/C Alloys	56

3.1	Introduction.....	57
3.2	Experimental	59
3.2.1	Catalyst synthesis.....	59
3.2.2	Materials characterization.....	60
3.2.3	Electrochemical characterization.....	61
3.3	Results and Discussion	62
3.3.1	Materials characterization.....	62
3.3.2	Electrochemical characterization.....	81
3.4	Conclusion	87
3.5	References.....	88
Chapter 4: Improving the Ethanol Oxidation Activity of Pt-Mn Alloys through the Use of Additives During Deposition		91
4.1	Introduction.....	92
4.2	Experimental Section	94
4.2.1	Catalyst Synthesis.....	94
4.2.2	Materials Characterization.....	95
4.2.3	Electrochemical Characterization.....	96
4.3	Results and Discussion	97
4.3.1	Preliminary studies and pH effects	97
4.3.2	Material Characterization	98
4.3.3	Electrochemical Characterization.....	112
4.4	Conclusions.....	119
4.5	Reference	119
Chapter 5: The Influence of Synthetic Methods on the Structure and Ethanol Oxidation Activity of Pt-Cu/C Alloys.....		122
5.1	Introduction.....	123

5.2	Experimental	125
5.2.1	Catalyst synthesis.....	125
5.2.2	Materials characterization.....	126
5.2.3	Electrochemical characterization.....	127
5.3	Result and discussion	128
5.3.1	Materials characterization.....	128
5.3.1.1	ICP-OES and TGA analyses	128
5.3.1.2	XRD analysis.....	130
5.3.1.3	TEM analysis.....	136
5.3.2	Electrochemical characterization.....	139
5.3.2.1	ECSA measurements.....	139
5.3.2.2	EOR measurements	145
5.4	Conclusion	151
5.5	References	152
Chapter 6: Durability of the Pt-Mn and Pt-Cu Alloys		155
6.1	Introduction.....	156
6.2	Experimental	158
6.2.1	Catalyst synthesis.....	158
6.2.2	Materials characterization.....	160
6.2.3	Electrochemical characterization and accelerated stress test (AST) ..	160
6.2.3.1	Electrode preparation	160
6.2.3.2	AST	161
6.3	Result and discussion	163
6.3.1	Ex-situ ICP analysis of different samples.....	163
6.3.2	Ex-situ XRD analysis of different samples	164

6.3.3 AST and ECSA.....	174
6.3.3.1 AST of commercial samples (Pt/C and Pt ₃ Sn/C).....	174
6.3.3.2 AST of Pt-Mn/C-SC and Pt-Mn/C-SC-700 °C	179
6.3.3.3 AST of Pt-Cu/C-POL and Pt-Cu/C-POL-700 °C.....	186
6.3.4 AST and EOR activity.....	192
6.4 Conclusion	201
6.5 References.....	202
Chapter 7: Oxygen Reduction Properties of Pt-Mn/C and Pt-Cu/C Alloys in Comparison with Commercial Samples.....	206
7.1 Introduction.....	207
7.2 Experimental	210
7.2.1 Catalyst synthesis.....	210
7.2.2 Electrochemical characterization.....	211
7.3 Result and discussion	212
7.3.1 Materials characterization.....	213
7.3.2 Electrochemical characterization.....	214
7.3.2.1 ECSA measurements.....	214
7.3.2.2 ORR measurements.....	215
7.4 Conclusion	225
7.5 References.....	227
Chapter 8: Sensor Performance of the Pt-Mn and Pt-Cu Samples and Durability of Sensors	231
8.1 Introduction.....	232
8.2 Experimental	234
8.2.1 Catalyst synthesis.....	234
8.2.2 Electrodes and MEAs Fabrication.....	234

8.2.3	Fuel cell and Sensing Measurements.....	235
8.2.3.1	Calibration curves and 7-day sensing tests	236
8.2.3.2	Sensing tests at constant concentration	237
8.3	Result and discussion.....	237
8.3.1	CVs and EIS responses of MEA.....	237
8.3.2	Sensing properties of the selected samples.....	248
8.3.3	Sensing behaviour in single concentration	261
8.4	Conclusion	267
8.5	References.....	269
Chapter 9: Summary and Future Directions.....		272
9.1	Summary	273
9.2	Future Directions	278
9.3	References.....	280
Chapter 10: Appendices.....		281

List of Tables

Table 2.1. Summary of precursors and additives were used to produce 250 mg of the Pt-Mn/C catalysts.....	38
Table 2.2. Summary of precursors and additives were used to produce 250 mg of the Pt-Cu/C catalysts.....	40
Table 3.1. Composition of the samples and concentration of Pt and Mn in filtrated solution which was measured by ICP.....	63
Table 3.2. Lattice parameters were calculated from Figure 3.3 and 3.4.....	69
Table 3.3. The binding energies, FWHM and species percentage of different Pt species as observed from the Pt (4f) X-ray photoelectron spectra of the heat treated and untreated Pt-Mn alloys.....	77
Table 3.4. Summary of particle size calculated by TEM and electrochemical properties of the catalysts studied in this work.....	84
Table 4.1. Composition of the samples and concentration of Pt and Mn in filtrated solution, which was measured by ICP, along with grain size measured by TEM.....	98
Table 4.2. The metal loading and the Vulcan carbon combustion temperature measured from Figure 4.3.....	103
Table 4.3. Lattice parameters were calculated using Figure 4.4, 4.5 and 4.6.....	107
Table 4.4. Summary of ethanol oxidation reaction (EOR) activity parameters of the Pt-Mn samples. Also listed are the measured electrochemical active surface area (ECSA) values for each sample.....	115
Table 5.1. Composition of the samples, metal loading and carbon black combustion Temperature which were measured by ICP and TGA, respectively.....	128
Table 5.2. Lattice parameters for Pt-Cu alloy catalysts, calculated from the XRD patterns in Figure 5.2.....	133
Table 5.3. Summary of electrochemical properties of the catalysts studied in this work and the mean particle sizes determined by XRD.....	145
Table 6.1. Composition of the samples before (BT) and after (AT) running AST which was measured by ICP and TGA, respectively.....	164
Table 7.1. The on-set potential (V_{on-set}) and limiting current density (j_L) calculated from Figure 7.2, 3 and 4 and the slop of Koutecky–Levich plot measured using Figure 7.5.....	220

Table 8.1. Summary of ECSA and sensitivity data determined for Pt/C and Pt ₃ Sn/C.....	253
Table 8.2. Summary of ECSA and sensitivity data determined for Pt-Mn/C-SC and Pt-Mn/C-SC-700 °C	258
Table 8.3. Summary of ECSA and sensitivity data determined for (a) Pt-Cu/C-POL and (b) Pt-Cu/C-POL-700 °C	263

List of Figures

Figure 1.1. Schematic of a Proton Exchange Membrane Fuel Cell (PEMFC)	3
Figure 1.2. Different products formed from ethanol electrooxidation (EOR) in acidic medium [12, 13].....	6
Figure 1.3. Schematic diagram of direct ethanol fuel cell (DEFC) [26].....	7
Figure 1.4. Phase diagram of Pt-Mn (Reprinted from, Ji, C-X and et al, An investigation of phase transformation behavior in sputter deposited PtMn thin films, JOM 2006, 58, 50-54.) [84] and Pt-Cu (Reprinted from, Abe, Taich, Thermodynamic assessment of the Cu–Pt system, Journal of phase equilibria 2006, 27, 5-13) [87], Copyright 2006, with permission from Springer.	16
Figure 1.5. Simplified sketch map of oxygen reduction reaction pathway [37].....	17
Figure 1.6. (a) A schematic diagram of an electrochemical fuel-cell type breath alcohol sensor (BrAS) (b) image of commercial fuel cell for alcohol sensor with Dräger Wafer [26].....	20
Figure 1.7. Cyclic voltammogram (CV) of the carbon-supported Pt catalyst. The shaded region is used to calculate ECSA. (Oxide formation (Q_O) and reduction (Q_R), hydrogen adsorption (H_A) and desorption (H_D), quinone (C_O) and hydroquinone (C_R)).	22
Figure 1.8. Transmission Line Model for impedance spectroscopy of catalyst layer.	25
Figure 1.9. Example of (a) Nyquist (b) capacitance and (c) normalized capacitance plots for a carbon-supported Pt catalyst layer prepared in the presence of Nafion. Measurements obtained at room temperature with a N_2 -purged WE and H_2 -purged CE.	26
Figure 2.1. (a) Half-cell electrochemical set-up used for evaluating powder catalysts and image of the fuel cell (b), (c) cathode and (d) and (e) and anode side used for the breath alcohol sensor tests.	45
Figure 2.2. The sensor test station and schematic diagram of all the connections.	53
Figure 2.3. (a) An example of the sensing data collected for MEA produced with the Pt-Mn/C sample and (b) the corresponding calibration curve was plotted from same data.	54
Figure 3.1. (a) The weight loss and (b) derivative weight loss (c) heat flow and (d) derivative heat flow versus temperature for Pt, Mn and Pt-Mn alloys deposited on a Vulcan carbon support and pure Vulcan carbon. Measurements were made at a heating rate of 5 °C/min under flowing argon.	65

Figure 3.2. The cyclic weight loss, derivative weight loss and derivative heat flow versus temperature in argon atmosphere for Pt-Mn alloys deposited on a Vulcan carbon support. Measurements were made at a heating rate of 20 °C/min under flowing argon.	66
.....	
Figure 3.3. XRD analysis of the Pt-Mn alloys before and after heat treatment in nitrogen atmosphere for constant period (1hour) at different temperatures.....	68
Figure 3.4. XRD analysis of the Pt-Mn alloys before and after heat treatment for different periods at (a) 500 °C and (b) 700 °C in nitrogen atmosphere.....	72
Figure 3.5. XRD analysis of the Pt-Mn alloy which is heat treated at 700 °C in nitrogen atmosphere for 1hour before and after exposing to 0.5 M H ₂ SO ₄ solution (These XRD spectra are acquired by Rigaku Ultima IV multipurpose X-ray diffraction (XRD) system with graphite monochrometer and Cu K α 1 radiation)	73
Figure 3.6. XPS spectra of Pt 4f for the Pt _{0.25} Mn _{0.75} alloy deposited on Vulcan carbon (a)As-produced and heat treated at (b) 700 °C and (c) 875 °C for 1h in nitrogen atmosphere.	74
.....	
Figure 3.7. XPS spectra of Mn 2p for the Pt _{0.25} Mn _{0.75} alloy deposited on Vulcan carbon (a)As-produced and heat treated at (b) 700 °C and (c) 875 °C for 1h in nitrogen atmosphere	76
Figure 3.8. TEM images of the Pt-Mn alloys before and after heat treatment in nitrogen atmosphere for constant period (1hour) at different temperatures (a) untreated (b) 500, (c) 700 (d) 875 and (e) 950 °C.....	79
Figure 3.9. The variation of average catalyst Pt-Mn particle size as a function of (a) temperature and (b) heat treatment time.	80
Figure 3.10. CVs obtained for (a) Pt/C and (b) Pt-Mn/C catalysts before and after heat treatment for 1 hour at different temperature. (c) CVs obtained for Pt-Mn/C catalysts heat treated for different time periods. Measurements were made in N ₂ -purged 0.5 M H ₂ SO ₄ at a scan rate of 20 mV/s.	83
Figure 3.11. LSVs obtained for pure Pt catalysts deposited on Vulcan carbon before and after heat treatment. The data is presented with the current normalized on the basis of (a) Pt content and (b) geometric area. Measurements were made in 0.5 M H ₂ SO ₄ containing 0.1 M ethanol at a scan rate of 20 mV/s.....	85
Figure 3.12. LSVs obtained for Pt-Mn alloys deposited on Vulcan carbon before and after heat treatment at (a,b) different temperatures for 1 h and (c,d) different temperatures for 2 – 6 h. The data is presented with the current normalized on the basis of (a,c) Pt content and (b,d) geometric area. Measurements were made in 0.5 M H ₂ SO ₄ containing 0.1 M ethanol at a scan rate of 20 mV/s.....	86

Figure 4.1. (a) TG in air and (b) LSV in the 0.5 M H ₂ SO ₄ + 0.1 M ethanol solution at a scan rate of 20 mV/s for Pt-Mn alloys which were synthesized on Vulcan carbon support in the presence of sodium citrate at different pHs.	99
Figure 4.2. (a) TG, (b) DTG, (c) DSC and (d) derivative weight-corrected DSC for Pt-Mn alloys, which were synthesized on Vulcan carbon support in the presence and absence of sodium citrate (The solid line is the Pt _{0.75} Mn _{0.25} sample prepared without SC and the dash line is the sample prepared in the presence of SC).	102
Figure 4.3. The effect of sodium citrate concentration on the weight loss of Pt-Mn alloys, which were synthesized on Vulcan carbon support.	103
Figure 4.4. XRD analysis of the samples, which were prepared in the presence and absence of sodium citrate.	105
Figure 4.5. The XRD patterns of the sample prepared in the presence 2X SC and after heat treatment at different temperatures.	106
Figure 4.6. The XRD patterns of the sample prepared in the presence of 2X sodium citrate (SC) and after heat treatment at 700 °C for different periods.	108
Figure 4.7. TEM image of Pt _{0.75} Mn _{0.25} samples prepared in the presence of different contents of sodium citrate: (a) no additive; (b) 1X; (c) 2X; and (d) 3X.	110
Figure 4.8. TEM image of Pt _{0.75} Mn _{0.25} samples prepared in the presence 2X of sodium citrate and after heat treatment at different temperatures: (a) 500 °C; (b) 700 °C; (c) 875 °C; and (d) 950 °C.	111
Figure 4.9. TEM images of Pt _{0.75} Mn _{0.25} samples prepared (a) without additive and (b) in the presence 2X of sodium citrate and heat treated at 700 °C for 1 h.	112
Figure 4.10. Cyclic voltammetry (CV) in the 0.5 M H ₂ SO ₄ solution at a scan rate of 20 mV/s for samples prepared (a) with different sodium citrate contents and then heat treated (b) at different temperatures for 1 h and (c) at 500 and 700 °C for different periods.	114
Figure 4.11. ECSA changes at different SC concentrations and after heat treatment at different temperatures, measured from Figure 4.10, and the ethanol oxidation peak current, measured from Figure 11.	115
Figure 4.12. Linear sweep voltammetry (LSV) in the 0.5 M H ₂ SO ₄ + 0.1 M ethanol solution at a scan rate of 20 mV/s for: (a) the samples prepared with different sodium citrate contents; (c) the sample produced with 2X sodium citrate content and heat treated at different temperatures. (b) The same as (d), normalized for platinum content of (a) and (d), respectively.	117

Figure 4.13. LSV of the samples prepared in the presence of sodium citrate and heat treated at 500 and 700 °C for different periods, in the 0.5 M H ₂ SO ₄ + 0.1 M ethanol solution at a scan rate of 20 mV/s.....	118
Figure 5.1. The effect of different deposition methods on the weight loss of the Pt-Cu alloys, which were synthesized on Vulcan carbon support.....	129
Figure 5.2. The XRD analysis of the Pt-Cu alloys before and after the heat treatment in nitrogen atmosphere for the constant period (1hour) (unless it is specified) at different temperatures for the samples prepared by the (a) impregnation (b) impregnation + SC and (c) polyol methods.....	131
Figure 5.3. The expanded XRD patterns from Figure 5.2 for the Pt-Cu samples prepared by the (a) (d) impregnation (b) (e) impregnation + SC and (c)(f) polyol methods.....	132
Figure 5.4. TEM images of the Pt-Cu alloys before and after heat treatment in nitrogen atmosphere for constant period (1hour) (a) Pt-Cu alloys prepared by the impregnation method and (b) heat treated at 700 °C, (c) Pt-Cu alloy prepared in presence of SC and (d) heat treated at 700 °C and (e) Pt-Cu alloys prepared by the polyol method and (f) heat treated at 700 °C.....	138
Figure 5.5. The first three CVs recorded before reaching stabilized CVs which were reported in Fig.7 for the as-produced Pt-Cu samples prepared by the (a) impregnation (b) impregnation + SC and (c) polyol methods. Measurements were made in the N ₂ -purged 0.5 M H ₂ SO ₄ solution at a scan rate of 100 mV/s.....	140
Figure 5.6. The first three CVs recorded before reaching stabilized CVs which were reported in Fig.7 for the Pt-Cu samples prepared by the (a) impregnation (b) impregnation + SC and (c) polyol methods and later heat treated at 700 °C for 1h. Measurements were made in the N ₂ -purged 0.5 M H ₂ SO ₄ solution at a scan rate of 100 mV/s.....	142
Figure 5.7. CVs obtained for the Pt-Cu/C catalysts made by the (a) impregnation (b) impregnation + SC and (c) polyol methods, before and after heat treatment at different temperature. Measurements were made in the N2-purged 0.5 M H ₂ SO ₄ solution at a scan rate of 20 mV/s.	144
Figure 5.8. CVs obtained for Pt-Cu alloys deposited on Vulcan carbon by the (a) impregnation (b) impregnation + SC and (c) polyol methods, before and after heat treatment at different temperatures.	148
Figure 5.9. LSVs normalized with the current normalized on the basis of the Pt loading for the Pt-Cu/C catalysts made by the (a) impregnation (b) impregnation + SC and (c) polyol methods, before and after heat treatment at different temperature. Measurements were made in the N ₂ -purged 0.5 M H ₂ SO ₄ containing 0.1 M ethanol at a scan rate of 20 mV/s.....	149

Figure 5.10. The IF/IB ratio for different samples are compared after heat treating at 700 °C.....	150
Figure 6.1. The Mn and Pt concentration in the testing electrolyte at the specific cycles of AST (a) (b) for Pt-Mn/C-SC and (c) (d) for Pt-Mn/C-SC-700 °C which were determined by ICP.....	165
Figure 6.2. The Cu and Pt concentration in the testing electrolyte at the specific cycles of AST (a) (b) for Pt-Cu/C-POL and (c) (d) for Pt-Cu/C-POL-700 °C which were determined by ICP.....	166
Figure 6.3. The XRD patterns for Pt ₃ Sn/C at the specific cycles of AST.....	168
Figure 6.4. The XRD patterns for Pt-Mn/C-SC at the specific cycles of AST.....	169
Figure 6.5. The XRD patterns for Pt-Mn/C-SC-700 °C at the specific cycles of AST	170
Figure 6.6. The XRD patterns for Pt-Cu/C-POL at the specific cycles of AST.....	172
Figure 6.7. The XRD patterns for Pt-Cu/C-POL-700 °C at the specific cycles of AST.	173
Figure 6.8. CVs obtained for the commercial samples (a) Pt/C and (b) Pt ₃ Sn/C at the specific cycles of AST. Measurements were made in the N ₂ -purged 0.5 M H ₂ SO ₄ solution at a scan rate of 20 mV/s.....	175
Figure 6.9. (a) (b) and (c) The EIS responses obtained at a DC bias potential of 0.360 V vs. NHE for the commercial sample (Pt/C) at the specific cycles of AST. (d), (e) and (f) Expansion of the high frequency region. Measurements were made in the N ₂ -purged 0.5 M H ₂ SO ₄ solution.	177
Figure 6.10. (a) (b) and (c) The EIS responses obtained at a DC bias potential of 0.360 V vs. NHE for the commercial sample (Pt ₃ Sn/C) at the specific cycles of AST. (d), (e) and (f) Expansion of the high frequency region. Measurements were made in the N ₂ -purged 0.5 M H ₂ SO ₄ solution.	178
Figure 6.11. CVs obtained for (a) Pt-Mn/C-SC and (b) Pt-Mn/C-SC-700 °C at the specific cycles of AST. Measurements were made in the N ₂ -purged 0.5 M H ₂ SO ₄ solution at a scan rate of 20 mV/s.	181
Figure 6.12. The EIS responses obtained at a DC bias potential of 0.360 V vs. NHE for Pt-Mn/C-SC at the specific cycles of AST. Measurements were made in the N ₂ -purged 0.5 M H ₂ SO ₄ solution.	184
Figure 6.13. The EIS responses obtained at a DC bias potential of 0.360 V vs. NHE for Pt-Mn/C-SC-700 °C at the specific cycles of AST. Measurements were made in the N ₂ -purged 0.5 M H ₂ SO ₄ solution.	185

Figure 6.14. CVs obtained for the pure Pt/C sample made in-house at the specific cycles of AST. Measurements were made in the N ₂ -purged 0.5 M H ₂ SO ₄ solution at a scan rate of 20 mV/s.....	186
Figure 6.15. The EIS responses obtained at a DC bias potential of 0.360 V vs. NHE for the pure Pt/C sample made in-house at the specific cycles of AST. Measurements were made in the N ₂ -purged 0.5 M H ₂ SO ₄ solution.	188
Figure 6.16. CVs obtained for (a) Pt-Cu/C-POL and (b) Pt-Cu/C-POL-700 °C at the specific cycles of AST. Measurements were made in the N ₂ -purged 0.5 M H ₂ SO ₄ solution at a scan rate of 20 mV/s.	189
Figure 6.17. The EIS responses obtained at a DC bias potential of 0.360 V vs. NHE for Pt-Cu/C-POL at the specific cycles of AST. Measurements were made in the N ₂ -purged 0.5 M H ₂ SO ₄ solution.	191
Figure 6.18. The EIS responses obtained at a DC bias potential of 0.360 V vs. NHE for Pt-Cu/C-POL-700 °C at the specific cycles of AST. Measurements were made in the N ₂ -purged 0.5 M H ₂ SO ₄ solution.	192
Figure 6.19. The ECSA changes for different samples which were determined from Figure 6.8, 11 and 16 at the specific cycles of AST.	194
Figure 6.20. CVs obtained for the commercial samples (a) Pt/C and (b) Pt ₃ Sn/C at the specific cycles of AST. Measurements were made in the N ₂ -purged 0.5 M H ₂ SO ₄ containing 0.1 M ethanol at a scan rate of 20 mV/s.....	196
Figure 6.21. CVs obtained for (a) Pt-Mn/C-SC and (b) Pt-Mn/C-SC-700 °C at the specific cycles of AST. Measurements were made in the N ₂ -purged 0.5 M H ₂ SO ₄ containing 0.1 M ethanol at a scan rate of 20 mV/s.	197
Figure 6.22. CVs obtained for (a) Pt-Cu/C-POL and (b) Pt-Cu/C-POL-700 °C at the specific cycles of AST. Measurements were made in the N ₂ -purged 0.5 M H ₂ SO ₄ containing 0.1 M ethanol at a scan rate of 20 mV/s.	198
Figure 6.23. The intensity of the peak current measured by (a) the forward scan (I _F), (b) backward scan (I _B) and (c) the ratio of I _F /I _B for different samples which were determined from Figure 6.20, 6.21 and 6.22 at the specific cycles of AST.	199
Figure 6.24. The intensity of the peak current measured by the forward scan (I _F) and normalized for Pt loading for different samples which were determined from Figure 6.20, 6.21 and 6.22 at the specific cycles of AST.	200
Figure 7.1. (a) The weight loss and (b) derivative weight loss versus temperature for Pt-Cu/C-POL and Pt-Cu/C-POL-700 °C. Measurements were made at a heating rate of 20 °C/min under flowing argon.	214

Figure 7.2. RRDE measurements of (a) Pt/C (b) Pt ₃ Sn/C to study the ORR activity of the samples. Measurements were carried out in O ₂ -saturated 0.5 M H ₂ SO ₄ using different rotation rates by a scan rate of 10 mV/s.....	217
Figure 7.3. RRDE measurements of (a) Pt-Mn/C-SC (b) Pt-Mn/C-SC-700 °C to study the ORR activity of the samples. Measurements were carried out in O ₂ -saturated 0.5 M H ₂ SO ₄ using different rotation rates by a scan rate of 10 mV/s.....	218
Figure 7.4. RRDE measurements of (a) Pt-Cu/C-POL and (b) Pt-Cu/C-POL-700 °C to study the ORR activity of the samples. Measurements were carried out in O ₂ -saturated 0.5 M H ₂ SO ₄ using different rotation rates by a scan rate of 10 mV/s.....	219
Figure 7.5. Koutecky-Levich plot for different samples (a) Pt/C and Pt ₃ Sn/C (b) Pt-Mn/C-SC and Pt-Mn/C-SC-700 °C (C) Pt-Cu/C-POL and Pt-Mn/C-POL-700 °C which were determined using Figure 7.2, 7.3 and 7.4.....	221
Figure 7.6. The cracks and delamination of the catalyst layer deposited on the GC electrode for Pt-Cu samples (a) before and (b) after heat treatment.	223
Figure 7.7. Comparison of the ORR activities of different samples. Measurements were carried out in O ₂ -saturated 0.5 M H ₂ SO ₄ at a scan rate of 10 mV/s using an electrode rotation rate of (a) 1600 RPM and (b) 900 RPM.	225
Figure 8.1. CVs obtained for the anode electrodes produced by commercial samples (a) Pt/C and (b) Pt ₃ Sn/C before the beginning of every day sensing test. Measurements were made in the full cell configuration at a scan rate of 20 mV/s. In both case the cathode electrode made by Pt/C and humidify-H ₂ gas was used at the cathode electrode and the humidify-N ₂ gas was used at the anode.	239
Figure 8.2. (a), (b) and (c) The EIS responses obtained at a DC bias potential of 0.360 V vs. NHE for Pt/C before the beginning of every day sensing test. The cathode electrode made by Pt/C and the humidify-H ₂ gas was used at the cathode electrode and the humidify-N ₂ gas was used at the anode.	240
Figure 8.3. (a), (b) and (c) The EIS responses obtained at a DC bias potential of 0.360 V vs. NHE for Pt ₃ Sn/C before the beginning of every day sensing test. The cathode electrode made by Pt/C and the humidify-H ₂ gas was used at the cathode electrode and the humidify-N ₂ gas was used at the anode.	243
Figure 8.4. CVs obtained for the anode electrodes produced by (a) Pt-Mn/C-SC and (b) Pt-Mn/C-SC-700 °C before the beginning of every day sensing test. Measurements were made in the full cell configuration at a scan rate of 20 mV/s. In both case the cathode electrode made by Pt/C and humidify-H ₂ gas was used at the cathode electrode and the humidify-N ₂ gas was used at the anode.	244
Figure 8.5. (a), (b) and (c) The EIS responses obtained at a DC bias potential of 0.360 V vs. NHE for Pt-Mn/C-SC before the beginning of every day sensing test. The cathode	

electrode made by Pt/C and the humidify-H ₂ gas was used at the cathode electrode and the humidify-N ₂ gas was used at the anode.	245
Figure 8.6. (a), (b) and (c) The EIS responses obtained at a DC bias potential of 0.360 V vs. NHE for Pt-Mn/C-SC-700 °C before the beginning of every day sensing test. The cathode electrode made by Pt/C and the humidify-H ₂ gas was used at the cathode electrode and the humidify-N ₂ gas was used at anode side.	246
Figure 8.7. CVs obtained for the anode electrodes produced by (a) Pt-Cu/C-POL and (b) Pt-Cu/C-POL-700 °C before the beginning of every day sensing test. Measurements were made in the full cell configuration at a scan rate of 20 mV/s. In both case the cathode electrode made by Pt/C and humidify-H ₂ gas was used at the cathode electrode and the humidify-N ₂ gas was used at the anode.	247
Figure 8.8. (a), (b) and (c) The EIS responses obtained at a DC bias potential of 0.360 V vs. NHE for Pt-Cu/C-POL before the beginning of every day sensing test. The cathode electrode made by Pt/C and the humidify-H ₂ gas was used at the cathode electrode and the humidify-N ₂ gas was used at the anode.	249
Figure 8.9. (a), (b) and (c) The EIS responses obtained at a DC bias potential of 0.360 V vs. NHE for Pt-Cu/C-POL-700 °C before the beginning of every day sensing test. The cathode electrode made by Pt/C and the humidify-H ₂ gas was used at the cathode electrode and the humidify-N ₂ gas was used at the anode.	250
Figure 8.10. Calibration curve obtained at different days for commercial samples (a) Pt/C and (b) Pt ₃ Sn/C as the anode electrode on the carbon paper. Measurements were made in the full cell. The humidify-N ₂ gas was used as the carrier gas at the anode. The cathode electrode was exposed to air.	252
Figure 8.11. Sensitivity of the commercial samples (a) Pt/C and (b) Pt ₃ Sn/C calculated using Figure 8.10.	253
Figure 8.12. Sensing responses for (a) Pt/C and (b) Pt ₃ Sn/C at 0.06 g/dL for the first day.	254
Figure 8.13. Calibration curve obtained at different days for (a) Pt-Mn/C-SC and (b) Pt-Mn/C-SC-700 °C as the anode electrode. Measurements were made in the full cell. The humidify-N ₂ gas was used as the carrier gas at the anode. The cathode electrode was exposed to air.	256
Figure 8.14. Sensitivity of the commercial samples (a) Pt-Mn/C-SC and (b) Pt-Mn/C-SC-700 °C calculated using Figure 8.13.	259
Figure 8.15. Sensing responses for (a) Pt-Mn/C-SC and (b) Pt-Mn/C-SC-700 °C at 0.06 g/dL for the first day.	260
Figure 8.16. Calibration curve obtained at different days for (a) Pt-Cu/C-POL and (b) Pt-Cu/C-POL-700 °C as the anode electrode. Measurements were made in the full cell.	

The humidify-N ₂ gas was used as the carrier gas at the anode. The cathode electrode was and exposed to air.....	261
Figure 8.17. Sensitivity of the commercial samples (a) Pt-Cu/C-POL and (b) Pt-Cu/C-POL-700 °C calculated using Figure 8.16.....	262
Figure 8.18. Sensing responses for (a) Pt-Cu/C-POL and (b) Pt-Cu/C-POL-700 °C at 0.06 g/dL for the first day.....	264
Figure 8.19. The mean sensitivity and normalized sensitivity of different samples in the course of 7-day measurements.....	265
Figure 8.20. The results of readings at the single concentration of 0.06 g/dL for commercial sample (a) Pt/C and (b) Pt ₃ Sn/C.....	266
Figure 8.21. The results of readings at the single concentration of 0.06 g/dL for (a) Pt-Mn/C-SC-700 °C and (b) Pt-Cu/C-POL-700 °C.....	267

List of Abbreviations and Symbols

AC	Alternating Current
AST	Accelerated Stress Test
BAC	Blood Alcohol Concentration
BrAC	Breath Alcohol Concentration
BrAS	Fuel-Cell Based Breath Alcohol Sensors
CO	Carbon Monoxide
CO ₂	Carbon Dioxide
CTA	Cyclic Thermal Analysis
CV	Cyclic Voltammetry
DAFC	Direct Alcohol Fuel Cell
DC	Direct Current
DEFC	Direct Ethanol Fuel Cell
DMFC	Direct Methanol Fuel Cell
DSC	Differential Scanning Calorimetry
DTG	Derivative Thermogravimetry
ECSA	Electrochemical Active Surface Area
EG	Ethylene Glycol
EIS	Electrochemical Impedance Spectroscopy
EOR	Ethanol Oxidation Reaction
GC	Glassy Carbon
GDE	Gas Diffusion Electrode
GDL	Gas Diffusion Layer
ICP-OES	Inductively Coupled Plasma Optical Emission Spectroscopy
IPA	Isopropanol Alcohol
LC	Limiting Capacitance
LSV	Linear Scanning Voltammetry
MEA	Membrane Electrode Assembly
MOR	Methanol Oxidation Reaction
NC	Normalized Capacitance
ORR	Oxygen Reduction Reaction
PEM	Proton Exchange Membrane
PEMFC	Proton Exchange Membrane Fuel Cell
PFSA	Perfluorosulfonic Acid
Pt	Platinum Black
Pt/C	Platinum Supported on Carbon
PTFE	Polytetrafluoroethylene
PVC	Polyvinyl Chloride
<i>R</i> _{elect}	Electronic Transport Resistance
<i>R</i> _{ionic}	Ion Transport Resistance
RRDE	Rotating Ring Disk Electrode
SC	Trisodium Citrate

TEM	Transmission Electron Microscopy
TG	Thermogravimetry
TGA	Thermogravimetric Analysis
XPS	X-ray Photoelectron Spectroscopy
XRD	Powder X-ray Diffraction
Z'	Real Impedance

Chapter 1: Introduction

1.1 Fuel Cell

Worldwide industrial and technological development requires new and renewable sources of energy due to the increase in pollution levels and lack of fossil fuel in the near future [1-5]. William Grove in 1839 discovered that it is possible to directly produce electricity by reacting hydrogen and oxygen [6, 7]. Since then, different fuel cells have been invented and developed using a variety of reactants and component materials to produce electricity for different applications. Fuel cells have the potential to be a great source of green electrical energy and the side products are theoretically water and carbon dioxide (CO_2) [7, 8].

1.1.1 Proton Exchange Membrane Fuel Cells

The proton exchange membrane fuel cell (PEMFC) was initially developed toward the end of 1950s. In 1963, general electric developed PEMFC and it was used in Gemini spacecraft. However, major improvement in PEMFCs did not occur until the late 1980s [8, 9].

The catalysts used in PEMFC are commonly Pt-based catalysts and hydrogen gas is usually used as a fuel [1, 2, 4, 8]. Hydrogen gas is oxidized by the catalyst to protons and electrons at the anode (negative electrode) compartment of the cell [7-9]. Electrons travel through an external circuit to the cathode (positive electrode) where they then participate in the oxygen reduction reaction (ORR) at the catalyst surface. The protons migrate through the proton exchange membrane (PEM) and react with oxygen ions and produce water in the cathode side to complete the circuit [7-9]. The catalysts used in PEMFC are commonly Pt-based catalysts [1, 2, 4, 8]. A schematic of PEMFC is shown in Figure 1.1.

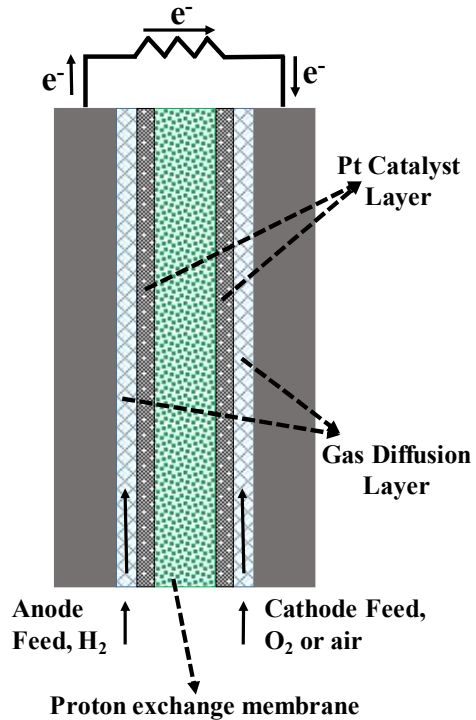
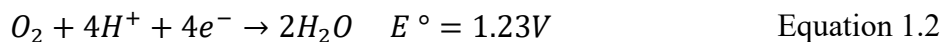


Figure 1.1. Schematic of a Proton Exchange Membrane Fuel Cell (PEMFC)

The two main reactions which are happening in PEMFC are shown in Equation 1.1 and Equation 1.2 [6, 7]:



The total theoretical cell voltage for PEMFC should be 1.23 V, though practical cell potentials are often lower than 1 V [6, 7].

The main part of PEMFC is the membrane electrode assembly (MEA). The MEA consists of PEM sandwiched between the anode and cathode. These electrodes are prepared using the carbon supported catalysts [6, 8]. The membrane is normally made from a perfluorosulfonic acid (PFSA) polymer. Nafion is one of the commonly used membranes which based on the application is available with different thicknesses. An ideal membrane should be electronically resistive but allow protons to transfer from the anode to cathode

electrode. Anode and cathode electrodes are usually fabricated by depositing electrochemically active catalyst layer on a gas diffusion layer (GDL). GDL should be an electronically conductive and porous substrate through which hydrogen and oxygen can permit to reach to the catalyst layer. Carbon fiber paper or carbon cloth materials are typically utilized as GDL for PEMFCs [7, 8, 10]. The catalyst layer typically consists of either platinum black (Pt) or platinum supported on carbon (Pt/C). In order to bind the catalysts powder to GDL and improve ionic conductivity, a polymer binder such as Teflon (Polytetrafluoroethylene, PTFE) or Nafion is employed [10].

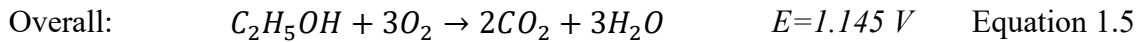
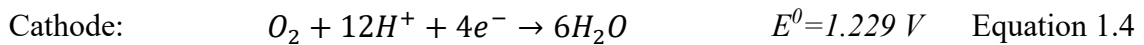
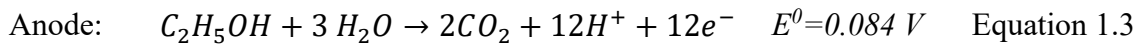
1.1.2 Direct alcohol fuel cells

One major issue affecting commercialization of PEMFC technology is the lack of cost effective hydrogen storage technologies and the absence of hydrogen transportation and distribution systems [6, 7, 10]. Using liquid fuels such as ethanol and methanol in fuel cells is one potential solution, as these fuels could be delivered through the existing gasoline infrastructure. Furthermore, methanol and ethanol are renewable fuels which can be produced from biomass sources which could help reduce the global production of CO₂ [6, 7, 10]. As a result, it is beneficial to develop direct alcohol fuel cells (DAFCs) as a subgroup of PEMFCs where alcohol (methanol, ethanol, etc.) is used as the anode fuel instead of hydrogen. The direct methanol fuel cell (DMFC) and the direct ethanol fuel cell (DEFC) are the two most well-known DAFCs.

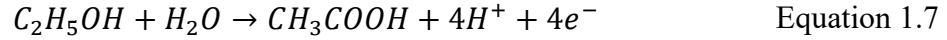
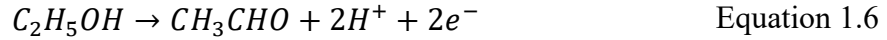
The DMFC has been studied more because methanol is a simpler alcohol with only one carbon atom, so its oxidization process is much simpler. However, the higher toxicity of methanol is a drawback. The excessive inhalation of methanol can lead to permanent

blindness [7, 11]. On the other hand, ethanol is less toxic and a very promising substitute from an ecological perspective. It can be easily produced by oxidation of all organic fuels and fermentation of various agricultural biomasses. The theoretical mass energy of ethanol is higher than methanol, 8.0 vs. 6.1 kWh/kg, respectively [7, 11]. Therefore, DEFCs are attractive fuel cells from both an economic and environmental viewpoint and there is a great interest recently in developing DEFC systems.

The half reaction for the DEFC are shown by Equation 1.3 and 1.4 while the overall equation is shown in Equation 1.5.



Complete electrooxidation of ethanol produces water (H_2O) and carbon dioxide (CO_2) with 12 electrons [6, 7, 10]. However, the mechanism of ethanol oxidation is much more complex inside the fuel cell and on Pt-based catalysts, leading to a distribution of products and it is summarized in Figure 1.2. The major challenge of the ethanol oxidation reaction (EOR) is due to C-C bond breaking [12, 13]. As a result, instead of a 12 electron process, other reactions also take place which produce only 2 or 4 electrons. The main by-product of the ethanol oxidation is acetaldehyde (CH_3CHO) and acetic acid (CH_3COOH). The main intermediate is carbon monoxide (CO) which may adsorb on the surface of Pt and poison the Pt catalysts. The formation of acetaldehyde and acetic acid are displayed in Equation 1.6 and 1.7 [6, 7].



The formation of these by-products and intermediates on the electrocatalysts (instead of CO₂ and H₂O) could reduce the efficiency and poison the catalysts.

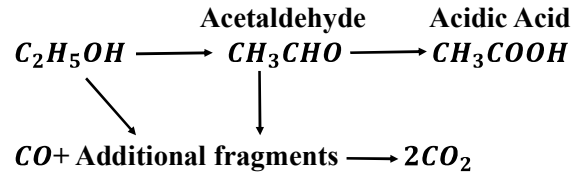


Figure 1.2. Different products formed from ethanol electrooxidation (EOR) in acidic medium [12, 13].

The structure of DEFC is presented in Figure 1.3. The structure is very similar to PEMFCs, except that aqueous ethanol is supplied to the anode. However, the oxidation of ethanol is much more complex, leading to slower oxidation kinetics and significant activation loss compared to hydrogen [7, 14]. Therefore, there are significant number of studies on developing new catalysts in order to enhance the EOR activity [4, 15-25]. The next section will discuss Pt and Pt-alloy catalysts which are used in developing modern fuel cells.

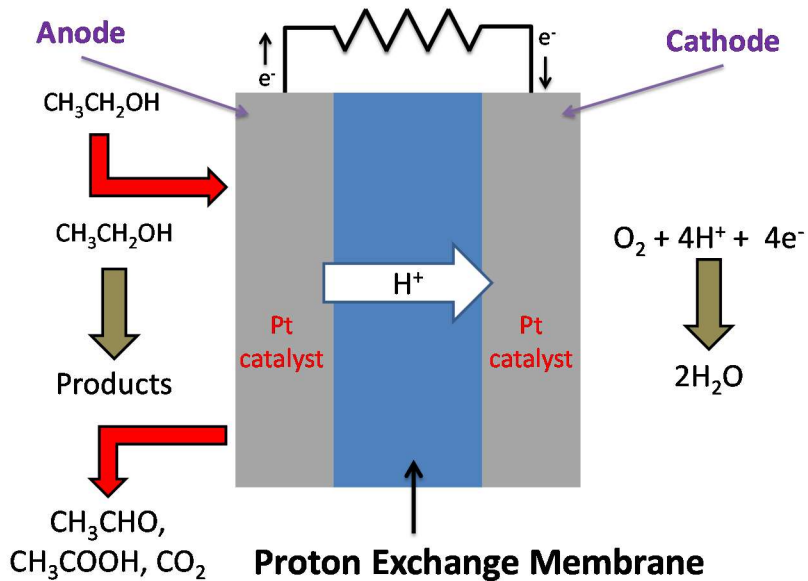


Figure 1.3. Schematic diagram of direct ethanol fuel cell (DEFC) [26].

1.1.3 Catalysts used in direct alcohol fuel cells

Pt is the most commonly used electrocatalyst, which is an expensive metal with limited abundance [27, 28]. In order to decrease the cost of DAFCs, it is essential to lower the required loading of Pt and increase the EOR activity. The U.S. Department of Energy targets the mass activity of $0.44 \text{ A/mg}_{\text{pt}}$ for MEAs¹ of the hydrogen PEMFCs in year 2020 and the target lifetime is over 5000 h for the cycling systems (automotive) and over 60,000 h for the stationary systems [30]. Achieving these targets requires improvement in the activity of the Pt catalysts.

There are three proven ways to improve the activity of Pt-base catalysts and/or prevent poisoning: first, by developing Pt-alloy catalysts by adding co-catalysts such as Ru, Sn, Mo, Mn, Cu or Ni [15-21]; second, by increasing the accessible surface area of the Pt

¹ Details on the fabricating of MEA have explained in this paper [29] H.A. Gasteiger, S.S. Kocha, B. Sompalli, F.T. Wagner, Applied Catalysis B: Environmental, 56 (2005) 9-35.

particles typically by reducing particle size and improving particle dispersion [4, 16, 22, 23]; third, by modifying the structure of the Pt or Pt-alloy particles, for instance, by producing Pt shell/alloy-core or Pt shell/alloy multi-core or developing intermetallic Pt-alloys particles [4, 21, 22, 24, 25]. Commonly, one or more of these techniques are used to produce Pt-base catalysts. As a result, identifying and choosing the right techniques for the desired application is critical and it is also crucial to optimize the effect of their combinations.

1.1.3.1 Pt alloy catalysts

The Pt electrodes are susceptible to poisoning by strongly adsorbed species such as CO which are formed during the alcohol oxidation process, resulting in severe activity and efficiency losses [4, 22, 31]. To overcome this problem and improve the electroactivity of Pt catalysts, several approaches have been studied in the past decades. One of the most common and reliable ways to eliminate the poisoning and enhanced the mass activity is to develop Pt-alloys with transition metals [15, 21, 24, 32, 33]. There have been numerous studies of Pt-transition alloys for anodic fuel cell reactions, including Pt-Cu, Pt-Mo, Pt-Ni, Pt-Fe, Pt-Co, Pt-Sn and Pt-Ru [4, 15-20, 31, 34]. It has been shown that Pt-Ru has the highest activity towards the methanol oxidation reaction (MOR) [5, 16, 33, 35-37]. Conversely, Pt-Sn has been shown to be more active than Pt-Ru towards EOR, with the most active phase believed to be Pt_3Sn [5, 33, 36, 38, 39].

There are very limited studies on Pt-Mn system for fuel cell applications [15, 40-42]. Previous study in alkaline solution has shown that the electrodeposited Pt-Mn catalyst that contains only trace amounts of Mn (≤ 0.1 atomic% Mn) exhibited enhanced activity toward

methanol but the EOR activity has been improved less significantly [41]. Jeon et al studied Pt-Ru-M ternary alloys ($M = \text{Mn, Mo, W}$) in acidic media and observed that Mn addition to Pt-Ru structure increased the MOR activity more than EOR, though it was less effective compared to W [42]. In addition, it has been illustrated that Mn-oxide layers on the surface of the Pt-Mn alloys are not stable in acid solution, which can increase the dissolution of Mn during electrochemical experiments [40]. Pt-Mn alloy has been shown to have enhanced activity towards the formic acid oxidation reaction, and was also shown to be more active than Pt-Cu alloys [15]. However, in all these studies the Mn content of the alloys was less than than 25 at%.

Our group has recently reported Pt-Mn alloys with high EOR activity [20, 31, 34] . Furthermore, the most active alloys contained less than 25 at% Pt, which is beneficial from a cost standpoint. Alloy formation was confirmed with XRD analysis. Those results showed that the presence of Mn affects both the particle size and the intrinsic activity of the catalysts. Further studies of ternary and quaternary Pt-Mn alloys, with a variety of alloying elements (Fe, Co, Ni, Cu, Mo and Sn), showed that adding copper and molybdenum to the Pt-Mn alloys further improved the catalytic properties [20, 34]. Nevertheless, in all binary, ternary and quaternary alloys two major issues were detectible, which are an agglomeration of particles and the presence of oxide phases [20, 31, 34]. These problems affect the performance of the catalysts and should be solved before these catalysts can be used in commercial fuel cells or sensors.

There have been many more studies of Pt-Cu alloys [27, 43-50] compared to Pt-Mn alloys [15, 31, 40]. Those studies have shown that adding Cu to the Pt structure, either as an alloying element or by producing a Pt-Cu core-shell structure, was very effective in improving the electrochemical activity of the Pt-base catalysts toward MOR [27, 43-46]

and EOR [47-50]. However, there is still debate about how the addition of Cu improves the activity of Pt-base catalysts. A few factors have been proposed, including an favorable change in the d-band energies of Pt due to the presence of the alloying element (a so called electronic effect), the creation of surface defects and/or changes in Pt–Pt interatomic distance [43-45]. The crystalline structure modification during post treatment processes or the dealloying process during electrochemical studies, which can alter all these three factors, makes it difficult to identify the main reason for the enhanced EOR and MOR activities.

Ammam and Easton studied the Pt-Cu/C binary alloy and Pt(Cu)/C core-shell system for their ethanol electro-oxidation properties. They showed that both of the Pt-Cu alloys and the core-shell structures have enhanced activity towards EOR compared to the pure Pt catalysts and reduced the Pt content to 37 at% Pt. The Pt-Cu/C alloyed sample showed the highest stability and activity [32]. Further studies have also illustrated that the presence of Cu as a ternary alloying element have enhanced the activity of the Pt-Mn alloys toward EOR [20]. However, the synthetic method employed (impregnation method) created a mixture of weakly alloyed samples with a high degree of agglomeration, which makes it difficult to reach a general conclusion on the reason of the EOR enhancement activity of samples [20, 23, 32]. Consequently, to improve EOR activity and investigate Pt-Cu samples, it is essential to prevent agglomeration and increase the alloying degree of Pt and Cu.

1.1.3.2 Fabrication of Pt alloy catalysts

Catalyst particle size and their dispersion on the carbon support are very important factors which control the electrochemical activity and performance of catalysts. It has been shown that decreasing the Pt and Pt alloy particle sizes and improving particle dispersion can further increase performance [4, 16, 51, 52], although there is some debate about the effects of particle size on catalytic activity [22, 53]. The particle sizes and dispersion is highly related to the synthesis methodology of the supported Pt and Pt alloy.

There are generally three methods to synthesize the nanomaterial particles: impregnation, colloidal method or polyol method and microemulsion or water-in-oil method. The impregnation method is the most widely used of the three methods [4, 54, 55]. It is a simple and straightforward chemical technique for catalyst preparation. This method consists of two steps: first, preparing aqueous solutions of metal salts (impregnation step); second, the reduction step which is done in the presence of reduction agents such as $\text{Na}_2\text{S}_2\text{O}_3$, $\text{Na}_4\text{S}_2\text{O}_5$, NaBH_4 and N_2H_4 [4, 55]. During the impregnation step, precursors are mixed with high-surface-area supported materials such as carbon black in the aqueous solution to form a homogeneous mixture. As a result, the supporting material plays an important role in forming nano particles [54]. Reaction time, and the kinetics and mass-transfer of the reducing agent, will also affect the nucleation and growth of the nanoparticles [55]. The major drawback of the impregnation method is the difficulty in controlling nanoparticle size and distribution.

Functionalizing different carbon supports [56, 57] and using surfactants [58, 59] are two significant strategies to improve particle distribution and dispersion for the impregnation method. It has been shown that oxygenated surface groups on the carbon support can enhance the dispersion and the stability of Pt/C catalysts [60]. Studies have

shown that nitrogen functionalization on carbon can improve cathode performance [60-63]. Meanwhile, adding a surfactant to the impregnation method is a simpler process compared to the functionalizing method. Several studies [58, 59, 64, 65] have shown that adding surfactants reduces the particle sizes of Pt and Pt alloys nanoparticles and also improves their dispersion on the support [29]. Sodium citrate (SC) is a common surfactant used in both aqueous and organic solutions by numerous researchers to produce Pt [59], Pt-Au [66], PtRuIr [67] and Pt-Co [68] nano-particles that were small (2–6 nm) with a narrow size distribution.

The colloidal method is another widely explored route for preparing pure and alloyed catalysts [4, 54, 69, 70]. This method is generally conducted in three steps: (1) preparation of precursor containing colloids; (2) deposition of the colloids onto the carbon support; (3) chemical reduction of the mixture. Typically, in the colloidal method a protective agent, such as surfactant molecules, is used to stabilize the metal nanoparticles. [69, 70]. This method could produce catalysts with better dispersion and a higher specific surface area in comparison with the conventional impregnation method [4, 54]. One of the most well-known solutions for the colloidal method is ethylene glycol, which also serves as the reducing agent and stabilizer. This methods has been successfully used to produce different noble metals and alloyed nanoparticles such as Pt, Pt-Ru and Pt-Cu [4, 44, 71-74]. The presence of the protecting agent (stabilizer) at the end of the synthesis is the major disadvantage of the colloidal method which may hinder the catalytic function of the nanoparticles [4, 54].

The microemulsion method has been used to prepare different catalysts such as: Au [75], Pt [76], Pt-Ru [77], Pt-Co and Pt-Fe [78]. In this method, the first step is to prepare a water-in-oil microemulsion of precursors by utilizing mixture of proper organic media with

water, precursors, surfactant and sometimes cosurfactant. The next step is to add a reduction agent which can be directly added into the microemulsion system or in the form of reducing agent-containing microemulsion [79-81].

The microemulsion is composed of nanoscaled aqueous liquid droplets containing precursors. The water droplets are surrounded by surfactant molecules (reverse micelles) and uniformly dispersed in an immiscible continuous organic phase. These droplets work as nanoscaled reactors which control the size and dispersion of the particles [79, 81]. However, the microemulsion method is an expensive process because of costly surfactant molecules and a substantial number of separation and washing steps [79].

1.1.3.3 Post heat treatment of Pt alloy catalysts

Heat treatment has also been recognized as an important and sometimes necessary step for catalytic activity improvement [8, 60, 67]. Heat treatment often leads to the removal of undesirable impurities present in the initial preparation (such as oxide phases and surfactants). Furthermore, it can also lead to the formation of more uniform alloy particles with increased stability. This can often lead to an enhancement of catalytic performance, but not always. For example, heat treatment of Pt supported catalysts, even at low temperatures, leads to Pt particle growth via sintering. Sintering occurs via the migration and coalescence of the platinum particles or by evaporation and condensation of the atoms from small crystallites [60]. Therefore, the use of a heat treatment process can be detrimental, particularly for high purity single-element nanoparticle catalysts. However, the benefits of thermally treating alloy nanoparticles often outweigh any activity losses that may occur due to particle size growth. Optimization of the synthesis and heat treatment

process is often complex, and careful study is required in order to fully understand the reason for enhanced activity [8, 15, 60].

As with pure platinum particles, the grain sizes of the alloy particles can become enlarged at higher heat treatment temperatures. However, alloy catalysts often exhibit a better resistance to sintering than pure catalysts [60]. During heat treatment, the Pt lattice parameter and degree of alloying can be altered, and intermetallic and ordered phases can be formed depending upon the alloying element and the heat treating temperature [15, 60, 82]. Increasing the degree of alloying can lead to enhanced electrocatalytic activity because of electronic changes brought about by the presence of the alloying elements and changes in the inter-atomic Pt-Pt distance [37, 60]. Furthermore, the heat treatment of alloy catalysts can potentially weaken [83] or improve [18] their durability and stability.

The phase diagram of Pt-Mn and Pt-Cu binary alloys are shown in Figure 1.4 . Studying these phase diagrams shows that heat treatment at different temperatures could result in structural changes. The Pt-Mn phase diagram shows that three major ordered intermetallic phases with different Mn at% could be formed at the room temperature: Pt_3Mn , PtMn and PtMn_3 [84, 85]. The ordered intermetallic phases will be formed at slow quenching rates which gives enough time to the Mn and Pt atoms to rearrange [84, 85]. Otherwise, disordered and mixed structures will be observed. The phases diagram of Pt-Cu is more simple compared to Pt-Mn. The formation of Cu and Pt solid solution is possible in all atomic percentages (Figure 1.4b) [86, 87]. However, the Pt-Cu phase diagram shows that at room temperature ordered phases would be generated with slow quenching rate similar to the Pt-Mn system. There are two well-known ordered phases for the Pt-Cu system: PtCu and PtCu_3 [86, 87].

1.1.4 Oxygen reduction reaction on Pt-based catalysts

The oxygen reduction reaction (ORR) at the cathode is a major reaction which happens parallel to the alcohol oxidation at the anode in DAFCs [29, 60]. A recently published [37] ORR pathway (Figure 4) showed that the rate-determining step to be initial adsorption by molecular oxygen with or without a charge-transfer step. The desirable product of ORR is H_2O , but H_2O_2 could also be generated. H_2O_2 is believed to be a threatening factor for fuel cell lifetime and membrane degradation [37, 60, 88]. The rates of both ORR and EOR are slow and comparable; as result, to have a better efficiency in DAFCs both of the reactions should be accelerated [60].

Previous studies have shown that the alloying of Pt with transition metals (Cr, Mn, Fe, Co or Ni) also improves ORR activity [29, 37, 60]. The alloying elements decrease the desorption free energy (G_{ads}) of oxide species on Pt, particularly OH. This fact can be majorly associated with the following effects: (i) electronic factors (higher Pt 5d band vacancy for the alloys in the oxidized state); (ii) geometric effects (shorter Pt–Pt bond distance, coordination number, crystal structures and metal particle size effects). To be brief, the transition metals eliminate the OH adsorption poisoning and display superior characteristics toward ORR. On the other hand, the alloying process can affect the size, shape, dispersion and surface composition of electrocatalysts which alter the ORR rate [29, 37, 60]. Therefore, adding transition metals, especially Mn and Cu, to the Pt structure is an interesting topic and worth investigating.

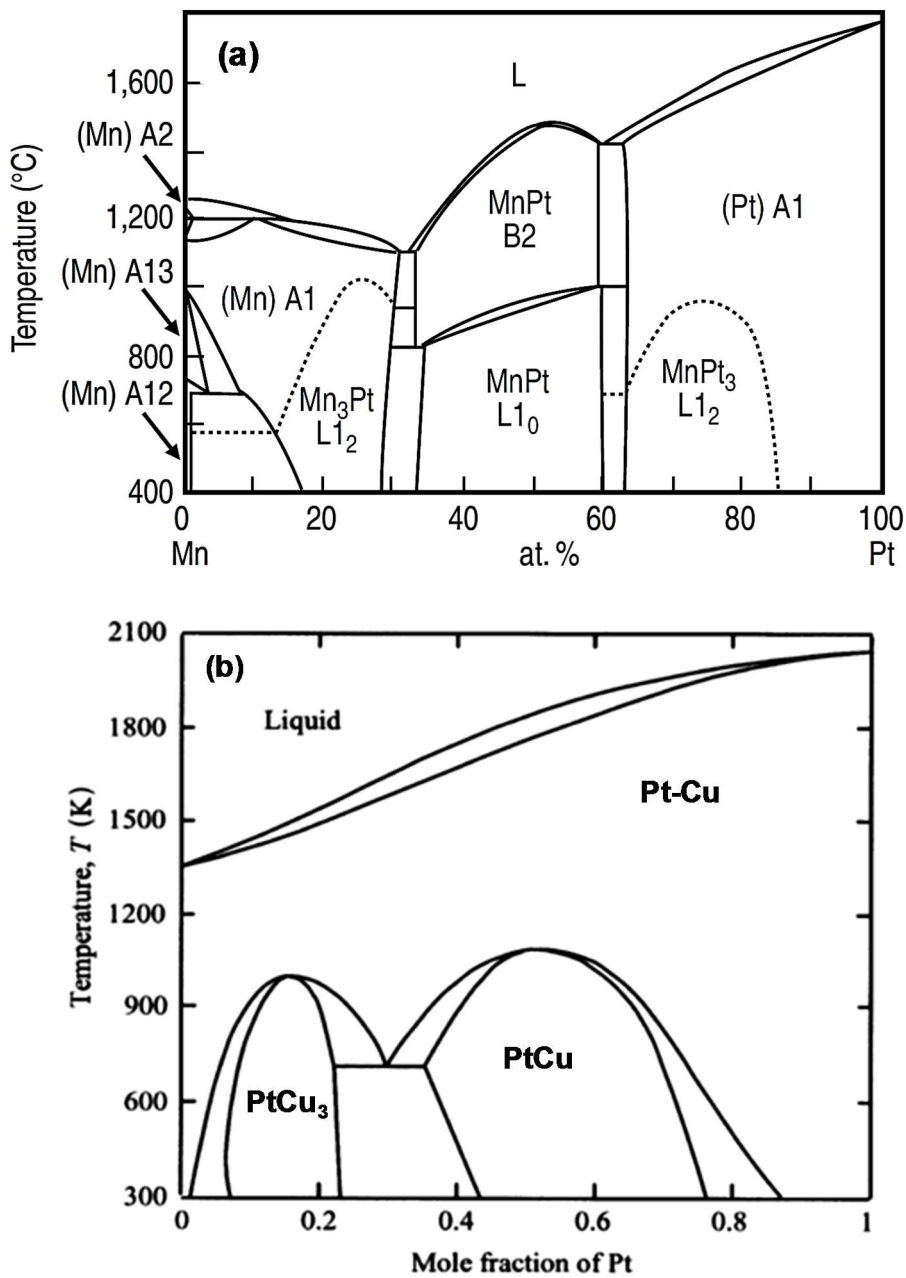


Figure 1.4. Phase diagram of Pt-Mn (Reprinted from, Ji, C-X and et al, An investigation of phase transformation behavior in sputter deposited PtMn thin films, JOM 2006, 58, 50-54.) [84] and Pt-Cu (Reprinted from, Abe, Taich, Thermodynamic assessment of the Cu–Pt system, Journal of phase equilibria 2006, 27, 5-13) [87], Copyright 2006, with permission from Springer.

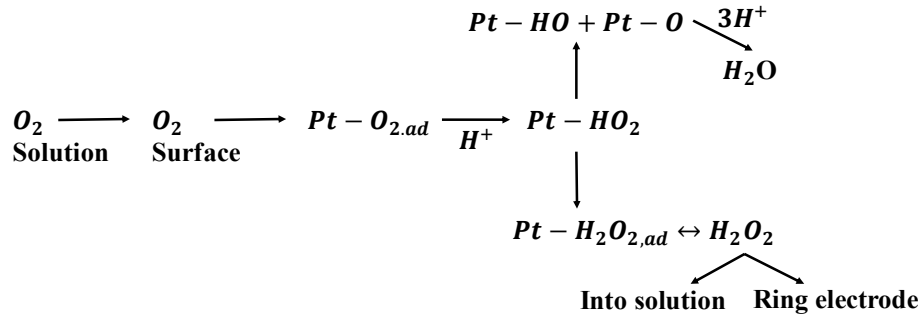


Figure 1.5. Simplified sketch map of oxygen reduction reaction pathway [37].

Recent studies have revealed that Pt-Cu are also very good candidate for ORR [24, 45, 71, 72, 89-92]. Pt-Cu nanoparticles with Pt rich surface showed that the presence of Cu modified the electronic properties of Pt atoms on the surface and enhanced the ORR activity [91]. Different Pt-M (M=Au, Pd, or Cu) nanorods have also been studied, with Pt-Cu nanorods displaying the highest ORR activity [92]. Tseng et al.[72] used both the impregnation and polyol methods to produce Pt-Cu alloys and studied the effect of heat treatment on the ORR activity of the Pt-Cu particles. Their findings have illustrated that the polyol method and the heat treatment at 300 °C in a hydrogen atmosphere caused the ORR activity enhancement. In addition, it has been shown that the heat treatment and formation of the ordered Pt-Cu alloys could improve the stability and the ORR activity due to better retention of the copper inside the ordered structure [24].

1.2 Breath alcohol sensors

In addition to energy conversion, DEFC technology is commonly employed in the fuel-cell based breath alcohol sensors (BrAS). This next section will give an overview of BrAS and its structure.

The legal limit for ethanol concentration in a driver's blood was added to the Criminal Code of Canada (Section 235) in December 1969. Since then it has been illegal in Canada to operate a motor vehicle with a blood alcohol concentration (BAC) greater than 0.08 g/dL, which is equivalent to 80 mg of ethanol per 100 mL of blood [26]. Despite these laws, impaired driving continues to be problem in many jurisdictions. During the 5-year period, there were 793 incidents of impaired driving that caused deaths in Canada [93]. Therefore, continuous screening for impaired drivers on roads is very important for police force to prevent same accidents in Canada.

There are different direct and indirect methods to measure BAC. These include an electrochemical sensor [26, 94-97], solid-state sensor [95], infrared spectrometry [95, 98], biosensors [95, 99], gas chromatography [95, 100], multi-sensor array (semiconductors and infrared devices) [101] and colorimetry [102]. The methods such as infrared spectrometry and gas chromatography are very complicated and expensive. In addition, it is very difficult and hazardous, especially in the case of gas chromatography, to build portable devices due to the presence of compressed flammable gases and open flames [103]. Furthermore, it has been shown that interference of organic species and non-linearity in response to alcohol vapour and oxygen concentration can cause inaccuracy in the sensors produced using semiconductors [95, 103]. As a result, the police force of Canada widely uses BrAS as a screening device (alcohol screener) [103]. A BrAS determined the BAC in an indirect method by first determining the concentration of alcohol vapor in human breath. It is well proven that there are volatile compounds in human breath which makes it possible to detect chemical compounds present in the body [104]. Breath sampling is a very appealing method because it is non-invasive and it can be done in a very short time. Studies have shown that

the breath alcohol concentration (BrAC) is proportional to the BAC , with the ratio of 1:2100 [94].

The structure of BrAS is very simple and shown in Figure 1.6a. It consists of a mouth piece and blow tube which are connected to a mini fuel cell. The structure and working principle of mini fuel cell is exactly same as a DEFC. In order to measure BrAC, small portion of breath is injected into the fuel cell by means of a mini pump. The alcohol present in the breath sample is oxidized at the anode while oxygen (from air) is reduced at the cathode. This produces a current which is measured. The measured current (or charge) is proportional to the concentration or amount of ethanol introduced into the fuel cell. Thus, after calibration, the sensor can determine the ethanol concentration in unknown samples, including BrAC levels in humans.

In commercial BrAS devices (Figure 1.6b), the MEA is composed of a porous polyvinyl chloride (PVC) membrane that is filled with H_2SO_4 (aq) and two electrodes that contain large amounts of Pt black catalyst ($7 - 14 \text{ mg/cm}^2$) held together with a Teflon binder [26, 105]. Studies in our group have indicated that the Pt utilization was very low in the commercial sensors [26, 106].

The most commonly used electrocatalyst in the modern power generating fuel cell is Pt nanoparticles supported on carbon. Innovation in the fuel cell industry has resulted in the manufacture fuel cells with substantially lower Pt loadings [3, 4, 8, 15, 89]. These developments have not been utilized in the production of commercial BrASs, nor has the applicability of these advances been validated for alcohol sensing. The sensitivity and performance of the BrAS are related directly to the electrocatalyst which was used to build the mini DEFC [107-111]. In this thesis project, for the first time the possibility of using the Pt alloy catalysts in BrAS was evaluated.

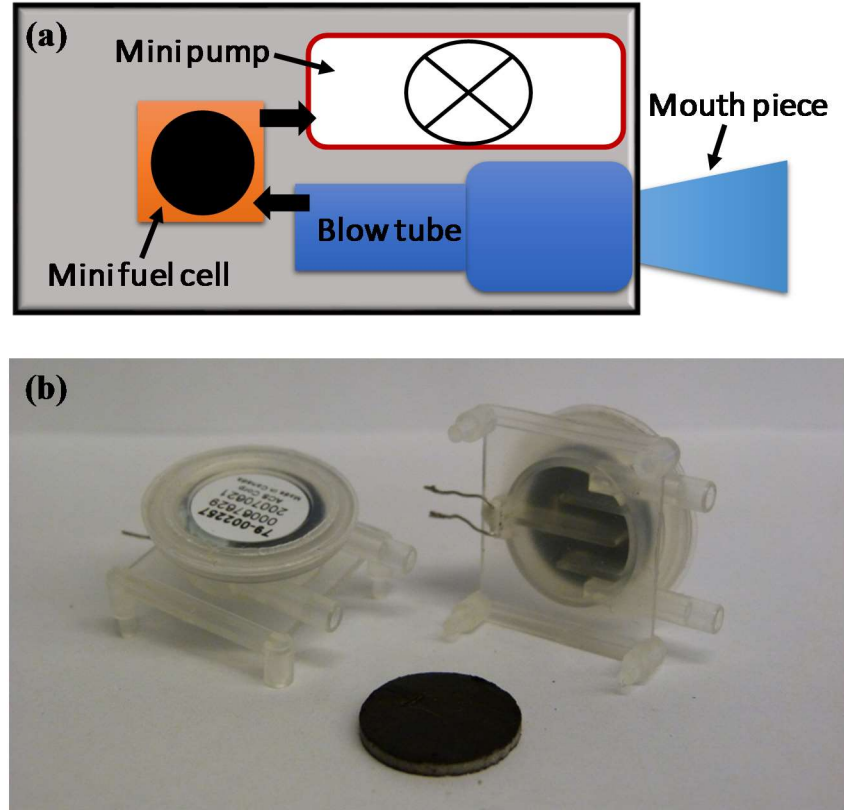


Figure 1.6. (a) A schematic diagram of an electrochemical fuel-cell type breath alcohol sensor (BrAS) (b) image of commercial fuel cell for alcohol sensor with Dräger Wafer [26].

1.3 Electrochemical Evaluation of Catalysts and DAFC Electrodes

Different electrochemical techniques could be used in order to characterize catalysts and DAFCs. Catalysts activity and degradation could be monitored using cyclic voltammetry (CV), linear scanning voltammetry (LSV), chronoamperometry and electrochemical impedance spectroscopy (EIS). In addition, the most important tests utilized to study DAFCs are CVs and EIS along with polarization tests. The following section describes the most important concepts about the CV and EIS analyses and their application in studying catalysts and DAFCs.

1.4 Cyclic Voltammetry

Cyclic voltammetry (CV) is a technique widely used to study electrochemical reactions. This method rapidly acquires information on oxidation, reduction, adsorption and electron transfer processes which occur on the surface of an electrode [6, 112]. CVs are usually the first experiments performed in half cell or fuel cell measurements. In this experiment, the potential is scanned linearly at a constant rate using a triangular potential waveform in both the positive and negative directions. During the potential sweep, current resulting from the applied potential are recorded by a potentiostat and the current–potential plot is referred as a cyclic voltammogram [112]. A three-electrode cell is used to measure CVs for half-cell measurements. The cell consists of a working electrode (sample), a reference electrode (to measure potential), and a counter electrode (to complete the circuit and provide current). In fuel cell measurements, the “cathode electrode” uses as both the counter and reference electrodes and the hydrogen gas are used to saturate the cathode. On the other hand, the anode is saturate by nitrogen gas and uses as working electrode.

A common CV of a carbon-supported Pt catalyst is presented in Figure 1.7. Several processes occur in this CV such as Pt-OH (Q_{O1}) and Pt-O formation (Q_{O2}), Pt-oxide reduction (Q_R), hydrogen adsorption on different Pt crystalline facets ($H_{A1}:Pt(110)$, $H_{A2}:Pt(100)$ steps, and $H_{A3}:Pt(100)$ terraces), hydrogen desorption from Pt different facets ($H_{D1}:Pt(110)$ and $H_{D1}:Pt(100)$) and formation of quinone (C_O) and hydroquinone (C_R) on the surface of carbon [113-116]. The charge in the hydrogen adsorption region is proportional to the electrochemical active surface area (ECSA) of the Pt particles (Figure 1.7). The charge required to adsorb a monolayer of protons on Pt platinum surface is $210 \mu\text{C}/\text{cm}^2$ [113, 117-119]. Therefore, the integrated charge in highlighted region can

be used to calculate ECSA. ECSA is a very important parameter which helps to monitor the performance of catalysts and fuel cells overtime [119-121].

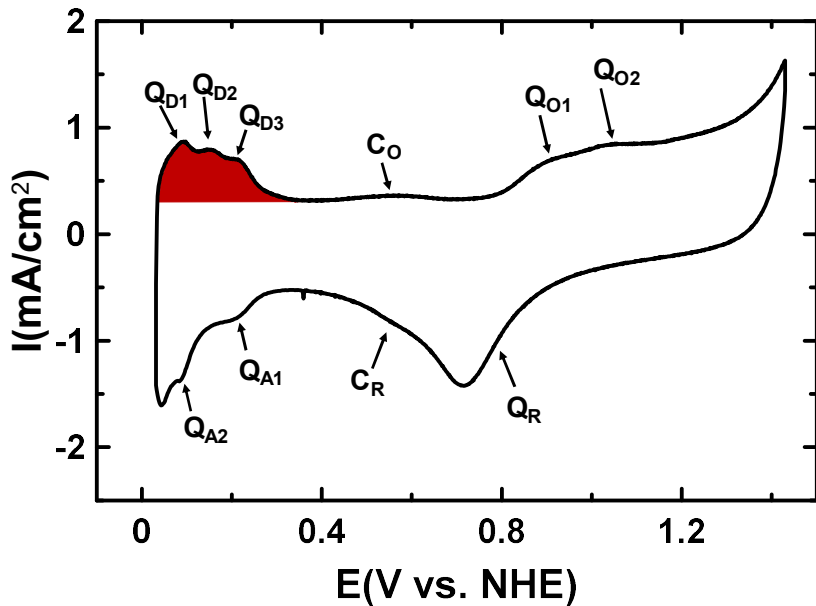


Figure 1.7. Cyclic voltammogram (CV) of the carbon-supported Pt catalyst. The shaded region is used to calculate ECSA. (Oxide formation (Q_O) and reduction (Q_R), hydrogen adsorption (H_A) and desorption (H_D), quinone (C_O) and hydroquinone (C_R)).

1.4.1 Electrochemical Impedance Spectroscopy

Electrochemical impedance spectroscopy (EIS) is non-destructive diagnostic test which is very useful method in order to study the changes in resistance and capacitance of the catalyst layer (CL). EIS measurements are performed by applying a small-amplitude (ca. 5-10 mV) perturbing sinusoidal voltage signal at a frequencies to the electrochemical cell and measuring the current response [112]. A defined frequency range is scanned from high to low values and the changes in the impedance response will be recorded. Using these data, it is possible to evaluate the resistance and capacitance of CL [119, 122-124].

The relation of current, voltage and resistance for direct current (DC) is shown by Ohm's Law (Equation 1.8):

$$V = IR \quad \text{Equation 1.8}$$

where R is resistance, V is voltage, and I is the current [112].

However, for alternating current (AC) conditions are slightly different. The current and voltage are function of time at a specific frequency and are shown by *Equation 1.9* and *1.10* [112]. In this case a new term should be defined instead of resistance which is also function of time and follows *Equation 1.11*:

$$V(t) = V_m \sin(\omega t + \theta) \quad \text{Equation 1.9}$$

$$I(t) = I_m \sin(\omega t + \varphi) \quad \text{Equation 1.10}$$

$$V = IZ_R$$

$$\text{Equation 1.11}$$

where $V(t)$ is the voltage value at the time t , V_m is the signal amplitude, $I(t)$ is the current value at the time t , I_m is the maximum value, ω is the angular frequency (where $\omega = 2\pi f$, where f is frequency in Hz), Z is the impedance, φ and θ are the phase angle and t is time in seconds [112].

For a pure resistor, the difference between phase angles is 0. Therefore, Z_R is equal to R . For pure capacitor, there is difference of $\frac{\pi}{2}$ for the phase angles of current and voltage. As a result, the the impedance of capacitor (Z_c) and capacitance (C) are defined by *Equation 1.12* and *1.13* as [112]:

$$Z_C = \frac{1}{i\omega C} \quad \text{Equation 1.12}$$

$$I_m = \omega C V_m \quad \text{Equation 1.13}$$

where i is the imaginary number ($\sqrt{-1}$).

However, in a real electrochemical system both the resistor and capacitor are present and contribute to the overall impedance of the system. In the system where a resistor and capacitor are connected in parallel, the overall AC impedance defines by *Equation 1.14* [112]:

$$Z_{R/C} = Z_R + Z_C \quad \text{Equation 1.14}$$

Knowing that $Z_R = R$ and using *Equation 1.12*, it is possible to show that the Z_R contains the real component of impedance, while Z_C contains the imaginary component. Therefore, *Equation 1.14* can be rewrite as *Equation 1.15*:

$$Z_{total} = Z' + Z'' \quad \text{Equation 1.15}$$

where Z' is the real impedance and Z'' is the imaginary impedance [112]. The measuring unit of impedance is ohms and it is usually reported as ohms/cm² for fuel cells and electrodes.

It is possible to model all EIS responses by an equivalent circuit. The transmission line model illustrated in *Equation 1.8*, has been studied extensively. This model can be used to evaluate CL and MEA [113, 122, 123].

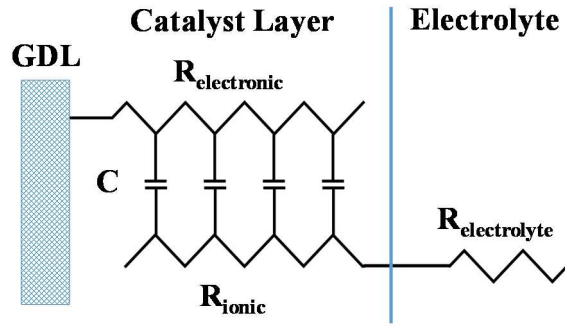


Figure 1.8. Transmission Line Model for impedance spectroscopy of catalyst layer.

In this model, two parallel resistive rails are used to represent the electronic transport resistance (R_{elect}) of the catalyst particles and the ion transport resistance (R_{ionic}) of the catalyst layer (catalyst powder + ionomer). The rails are connected by capacitors (C) in series in order to represent the capacitance of the carbon and platinum within the catalyst layer. As carbon and platinum are excellent conductors of electrons, the resistance contribution from R_{elect} is negligible compared to the ionic R_{ionic} [113, 122, 123].

The data collected from the EIS analysis can be displayed in three forms: Nyquist, capacitance, and normalized capacitance (NC) plots from which valuable information would be determined. An example of EIS profile is shown in Figure 1.9. A 45° Warburg-like region should be observed in the low frequency region of Nyquist plots. The formation of Warburg region is due to unrestricted diffusion to a large planar electrode which is the catalyst layer in this case. The projection of the Warburg length onto the real impedance (Z') axis is proportional to the total catalyst layer resistance ($R_\Sigma/3$), where R_Σ corresponds to the sum of ionic (R_{ionic}) and electronic resistance (R_{elect}) in the catalyst layer. For most fuel cell catalyst layers, the electronic contribution to the impedance is negligible and consequently $R_\Sigma = R_{ion}$ [113, 122, 123]. The variations in ionic resistivity within the

catalyst layer can be better visualized through capacitance and NC plots [125, 126]. In the capacitance plots, the series capacitance ($-1/\omega Z''$) is plotted against the real impedance (Z'). A steeper slope in the high frequency region of the capacitance plot is an indication of higher proton conductivity within the catalyst layer and the limiting capacitance (LC) is proportional to active surface area (Platinum + carbon) [119, 126]. To draw the NC plots, the capacitances were normalized by the maximum capacitance in each graph [119, 126].

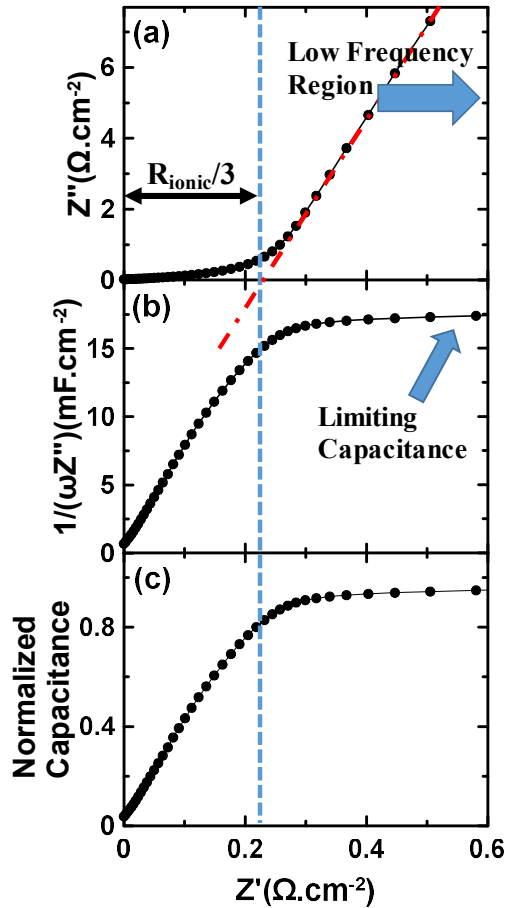


Figure 1.9. Example of (a) Nyquist (b) capacitance and (c) normalized capacitance plots for a carbon-supported Pt catalyst layer prepared in the presence of Nafion. Measurements obtained at room temperature with a N₂-purged WE and H₂-purged CE.

1.5 Thesis Objectives

The main objective of this thesis is to understand how the structure and composition of Pt-Mn and Pt-Cu alloy catalysts influence their activity towards the EOR and ORR. To do this, synthetic parameters and post treatment conditions are optimized to produce alloy catalysts with more uniform structure and a degree of dispersion.

Chapter 3 examines the effects of heat treatment temperature and heating time on the crystalline structure and uniformity of the Pt-Mn alloy system. Additionally, the influence of heat treatment on particle size, catalyst dispersion and electrochemical active surface area (ECSA) are studied. This structural information is correlated with EOR activity to determine the most active phases.

Chapter 4 investigates the effect of trisodium citrate (SC) on particle size, dispersion, structure and EOR activity of Pt-Mn. In addition, the influence of the impregnation solution pH, concentration of SC and the heat treatment on the crystalline structure, the uniformity of alloyed phases and the EOR activity of the catalysts are examined.

In Chapter 5, the effect of three methods: 1) the impregnation, 2) impregnation in the presence of SC and 3) microwave assisted polyol method. on the particle sizes, catalyst dispersion and crystalline structure and consequently on EOR activity of Pt-Cu/C are studied. Moreover, the effects of heat treatment on the crystalline structure and the uniformity of Pt-Cu alloy phases are explored. At the end of this chapter, the structural modification is linked to the EOR activity to determine which structures are more favorable for the higher EOR activities.

In chapter 6, the influence of the crystalline structure and heat treatment on the durability of the Pt-Mn and Pt-Cu samples are investigated. The samples are selected based on the EOR activities which were recorded in chapter 3, 4 and 5. Different methods such

as EIS, *ex situ* ICP and *ex situ* XRD analyses are utilized to determine the main parameters affecting the degradation of these catalysts.

Chapter 7 explores the ORR activity of the selected Pt-Mn and Pt-Cu samples. The ORR activity of these alloys is compared to different commercially available samples (Pt/C and Pt-Sn/C). Additionally, the effects of the heat treatment and crystalline structure modification on ORR activity for both the Pt-Cu and Pt-Mn systems are examined.

Finally, the sensing properties of the Pt-Mn and Pt-Cu samples with the best EOR activity are studied in chapter 8. These catalysts are evaluated in a BrAS sensor cell and their sensing performance are compared to that of obtained with commercial samples. The variations in sensing response and the accuracy of measurements are monitored over time using different electrochemical methods. Lastly, the effects of heat treatment on the sensing properties of the Pt-Mn and Pt-Cu alloys are investigated.

Together, all of the experiments conducted on the Pt-Mn and Pt-Cu alloys will provide a detailed understanding of the important parameters which are effecting EOR activity of these alloys along with the best methods to improve the accuracy and sensitivity of electrocatalysts used in the breath alcohol sensors.

1.6 References

- [1] Y. Xu, B. Zhang, Chemical Society Reviews, 43 (2014) 2439-2450.
- [2] Y.-W. Lee, S. Cha, K.-W. Park, J.I. Sohn, J.M. Kim, Journal of Nanomaterials, 2015 (2015) 1-20.
- [3] E. Antolini, Materials Chemistry and Physics, 78 (2003) 563-573.
- [4] H. Liu, C. Song, L. Zhang, J. Zhang, H. Wang, D.P. Wilkinson, Journal of Power Sources, 155 (2006) 95-110.
- [5] L. Li, L. Hu, J. Li, Z. Wei, Nano Res., 8 (2015) 418-440.
- [6] H. Wang, H. Li, X.-Z. Yuan, PEM fuel cell failure mode analysis, CRC Press, 2011.
- [7] V.S. Bagotsky, Fuel cells: problems and solutions, John Wiley & Sons, 2012.
- [8] W. Vielstich, A. Lamm, H.A. Gasteiger, Handbook of Fuel Cells: Fundamental, Technology, and Applications, Wiley, 2003.
- [9] J. Larminie, A. Dicks, M.S. McDonald, Fuel cell systems explained, Wiley New York, 2003.
- [10] V. Mehta, J.S. Cooper, Journal of Power Sources, 114 (2003) 32-53.
- [11] S.P.S. Badwal, S. Giddey, A. Kulkarni, J. Goel, S. Basu, Applied Energy, 145 (2015) 80-103.
- [12] J. Souza-Garcia, E. Herrero, J.M. Feliu, ChemPhysChem, 11 (2010) 1391-1394.
- [13] F. Colmati, G. Tremiliosi-Filho, E.R. Gonzalez, A. Berná, E. Herrero, J.M. Feliu, Faraday discussions, 140 (2009) 379-397.
- [14] C. Lamy, Direct Alcohol Fuel Cells (DAFCs), in: G. Kreysa, K.-i. Ota, R.F. Savinell (Eds.) Encyclopedia of Applied Electrochemistry, Springer New York, New York, NY, 2014, pp. 321-330.
- [15] T. Ghosh, B.M. Leonard, Q. Zhou, F.J. DiSalvo, Chemistry of Materials, 22 (2010) 2190-2202.
- [16] T. Sato, K. Okaya, K. Kunimatsu, H. Yano, M. Watanabe, H. Uchida, ACS Catalysis, 2 (2012) 450-455.
- [17] E. Antolini, J.R.C. Salgado, E.R. Gonzalez, Applied Catalysis B: Environmental, 63 (2006) 137-149.
- [18] W. Roh, J. Cho, H. Kim, J Appl Electrochem, 26 (1996) 623-630.

- [19] T.J. Schmidt, H.A. Gasteiger, R.J. Behm, *Electrochemistry Communications*, 1 (1999) 1-4.
- [20] M. Ammam, E.B. Easton, *Journal of The Electrochemical Society*, 159 (2012) B635-B640.
- [21] M.R. Zamanzad Ghavidel, E.B. Easton, *Applied Catalysis B: Environmental*, 176–177 (2015) 150-159.
- [22] F. Vigier, S. Rousseau, C. Coutanceau, J.-M. Leger, C. Lamy, *Top Catal*, 40 (2006) 111-121.
- [23] M. Ghavidel, E. Easton, *Catalysts*, 5 (2015) 1016.
- [24] N. Hodnik, C. Jeyabharathi, J.C. Meier, A. Kostka, K.L. Phani, A. Recnik, M. Bele, S. Hocevar, M. Gaberscek, K.J.J. Mayrhofer, *Physical Chemistry Chemical Physics*, 16 (2014) 13610-13615.
- [25] M. Oezaslan, M. Heggen, P. Strasser, *Journal of the American Chemical Society*, 134 (2012) 514-524.
- [26] M.R. Rahman, J.T.S. Allan, M. Zamanzad Ghavidel, L.E. Prest, F.S. Saleh, E.B. Easton, *Sensors and Actuators B: Chemical*, 228 (2016) 448-457.
- [27] T. Page, R. Johnson, J. Hormes, S. Noding, B. Rambabu, *Journal of Electroanalytical Chemistry*, 485 (2000) 34-41.
- [28] C. Sealy, *Materials Today*, 11 (2008) 65-68.
- [29] H.A. Gasteiger, S.S. Kocha, B. Sompalli, F.T. Wagner, *Applied Catalysis B: Environmental*, 56 (2005) 9-35.
- [30] in, 2014, pp. 1-49.
- [31] M. Ammam, L.E. Prest, A.D. Pauric, E.B. Easton, *Journal of The Electrochemical Society*, 159 (2011) B195-B200.
- [32] M. Ammam, E.B. Easton, *Journal of Power Sources*, 222 (2013) 79-87.
- [33] E. Antolini, F. Colmati, E.R. Gonzalez, *Electrochemistry Communications*, 9 (2007) 398-404.
- [34] M. Ammam, E.B. Easton, *Journal of Power Sources*, 215 (2012) 188-198.
- [35] F. Vigier, C. Coutanceau, A. Perrard, E. Belgsir, C. Lamy, *J Appl Electrochem*, 34 (2004) 439-446.
- [36] T. Almeida, L. Palma, C. Morais, K. Kokoh, A. De Andrade, *Journal of The Electrochemical Society*, 160 (2013) F965-F971.

- [37] Q. He, S. Mukerjee, *Electrochimica Acta*, 55 (2010) 1709-1719.
- [38] C. Lamy, S. Rousseau, E. Belgsir, C. Coutanceau, J.-M. Léger, *Electrochimica Acta*, 49 (2004) 3901-3908.
- [39] E. Antolini, E.R. Gonzalez, *Catalysis Today*, 160 (2011) 28-38.
- [40] J.E. Harlow, D.A. Stevens, R.J. Sanderson, G.C.-K. Liu, L.B. Lohstroter, G.D. Vernstrom, R.T. Atanasoski, M.K. Debe, J.R. Dahn, *Journal of The Electrochemical Society*, 159 (2012) B670-B676.
- [41] C. Xu, Y. Su, L. Tan, Z. Liu, J. Zhang, S. Chen, S.P. Jiang, *Electrochimica Acta*, 54 (2009) 6322-6326.
- [42] M.K. Jeon, K.R. Lee, S.I. Woo, *Korean journal of chemical engineering*, 26 (2009) 1028-1033.
- [43] J. Georgieva, E. Valova, I. Mintsova, S. Sotirovopoulos, S. Armanov, A. Kakaroglou, A. Hubin, O. Steenhaut, J. Dille, *J Appl Electrochem*, 44 (2014) 215-224.
- [44] M. Huang, L. Guan, *International Journal of Hydrogen Energy*, 40 (2015) 6546-6551.
- [45] J. Sun, J. Shi, J. Xu, X. Chen, Z. Zhang, Z. Peng, *Journal of Power Sources*, 279 (2015) 334-344.
- [46] Y.-X. Wang, H.-J. Zhou, P.-C. Sun, T.-H. Chen, *Journal of Power Sources*, 245 (2014) 663-670.
- [47] F. Saleem, Z. Zhang, B. Xu, X. Xu, P. He, X. Wang, *Journal of the American Chemical Society*, 135 (2013) 18304-18307.
- [48] X. Zhang, D. Li, D. Dong, H. Wang, P.A. Webley, *Materials Letters*, 64 (2010) 1169-1172.
- [49] X. Zhang, W. Lu, J. Da, H. Wang, D. Zhao, P.A. Webley, *Chemical Communications*, (2009) 195-197.
- [50] M. Huang, Y. Jiang, C. Jin, J. Ren, Z. Zhou, L. Guan, *Electrochimica Acta*, 125 (2014) 29-37.
- [51] R.J. Isaifan, S. Ntais, E.A. Baranova, *Applied Catalysis A: General*, 464 (2013) 87-94.
- [52] K. Matsutani, K. Hayakawa, T. Tada, *Platinum Metals Review*, 54 (2010) 223-232.
- [53] O. Cherstiouk, A. Gavrilov, L. Plyasova, I.Y. Molina, G. Tsirlina, E. Savinova, *Journal of Solid State Electrochemistry*, 12 (2008) 497-509.

- [54] K.-Y. Chan, J. Ding, J. Ren, S. Cheng, K.Y. Tsang, *Journal of Materials Chemistry*, 14 (2004) 505-516.
- [55] C. Coutanceau, S. Brimaud, C. Lamy, J.-M. Léger, L. Dubau, S. Rousseau, F. Vigier, *Electrochimica Acta*, 53 (2008) 6865-6880.
- [56] K. Lee, J. Zhang, H. Wang, D.P. Wilkinson, *J Appl Electrochem*, 36 (2006) 507-522.
- [57] P. Antonucci, V. Alderucci, N. Giordano, D. Cocke, H. Kim, *J Appl Electrochem*, 24 (1994) 58-65.
- [58] C. Hui, X. Li, I.-M. Hsing, *Electrochimica acta*, 51 (2005) 711-719.
- [59] R.B. Moghaddam, P.G. Pickup, *Electrochimica Acta*, 65 (2012) 210-215.
- [60] C.W. Bezerra, L. Zhang, H. Liu, K. Lee, A.L. Marques, E.P. Marques, H. Wang, J. Zhang, *Journal of Power Sources*, 173 (2007) 891-908.
- [61] V. Di Noto, E. Negro, *Fuel Cells*, 10 (2010) 234-244.
- [62] V. Di Noto, E. Negro, *Electrochimica Acta*, 55 (2010) 7564-7574.
- [63] J. Tian, F. Wang, Z.Q. Shan, R. Wang, J. Zhang, *J Appl Electrochem*, 34 (2004) 461-467.
- [64] X. Wang, I.-M. Hsing, *Electrochimica acta*, 47 (2002) 2981-2987.
- [65] J. Yang, J.Y. Lee, H.-P. Too, *Analytica chimica acta*, 571 (2006) 206-210.
- [66] J. Zeng, J. Yang, J.Y. Lee, W. Zhou, *The Journal of Physical Chemistry B*, 110 (2006) 24606-24611.
- [67] S. Liao, K.-A. Holmes, H. Tsaprailis, V.I. Birss, *Journal of the American Chemical Society*, 128 (2006) 3504-3505.
- [68] J. Zeng, J.Y. Lee, *Journal of power Sources*, 140 (2005) 268-273.
- [69] H. Bönnemann, R.M. Richards, *European Journal of Inorganic Chemistry*, 2001 (2001) 2455-2480.
- [70] M. Boutonnet, J. Kizling, P. Stenius, G. Maire, *Colloids and Surfaces*, 5 (1982) 209-225.
- [71] H. El-Deeb, M. Bron, *Electrochimica Acta*, 164 (2015) 315-322.
- [72] C.-J. Tseng, S.-T. Lo, S.-C. Lo, P.P. Chu, *Materials Chemistry and Physics*, 100 (2006) 385-390.
- [73] Z. Liu, J.Y. Lee, W. Chen, M. Han, L.M. Gan, *Langmuir*, 20 (2004) 181-187.

- [74] F. Bonet, C. Guery, D. Guyomard, R.H. Urbina, K. Tekaia-Elhsissen, J.-M. Tarascon, International journal of inorganic materials, 1 (1999) 47-51.
- [75] A. Pal, S. Shah, S. Devi, Colloids and Surfaces A: Physicochemical and Engineering Aspects, 302 (2007) 483-487.
- [76] S. Rojas, F.J. García-García, S. Järas, M.V. Martínez-Huerta, J.L.G. Fierro, M. Boutonnet, Applied Catalysis A: General, 285 (2005) 24-35.
- [77] L. Xiong, A. Manthiram, Solid State Ionics, 176 (2005) 385-392.
- [78] L. Xiong, A. Manthiram, Electrochimica acta, 50 (2005) 2323-2329.
- [79] S. Eriksson, U. Nylén, S. Rojas, M. Boutonnet, Applied Catalysis A: General, 265 (2004) 207-219.
- [80] I. Capek, Advances in colloid and interface science, 110 (2004) 49-74.
- [81] A. Zielińska-Jurek, J. Reszczyńska, E. Grabowska, A. Zaleska, Microemulsions—An Introduction to Properties and Applications (InTech, Poland, 2012), (2012) 235.
- [82] J.A. Wittkopf, J. Zheng, Y. Yan, Acs Catalysis, 4 (2014) 3145-3151.
- [83] B.C. Beard, P.N. Ross, Journal of the Electrochemical Society, 137 (1990) 3368-3374.
- [84] C.-X. Ji, P.F. Ladwig, R.D. Ott, Y. Yang, J.J. Yang, Y.A. Chang, E.S. Linville, J. Gao, B.B. Pant, JOM, 58 (2006) 50-54.
- [85] P.F. Ladwig, Y.A. Chang, E.S. Linville, A. Morrone, J. Gao, B.B. Pant, A.E. Schlutz, S. Mao, Journal of Applied Physics, 94 (2003) 979-987.
- [86] B. Predel, Cu-Pt (Copper-Platinum), in: O. Madelung (Ed.) Cr-Cs – Cu-Zr, Springer Berlin Heidelberg, 1994, pp. 1-6.
- [87] T. Abe, B. Sundman, H. Onodera, Journal of phase equilibria and diffusion, 27 (2006) 5-13.
- [88] F. Jaouen, J.-P. Dodelet, The Journal of Physical Chemistry C, 113 (2009) 15422-15432.
- [89] A. Rabis, P. Rodriguez, T.J. Schmidt, ACS Catalysis, 2 (2012) 864-890.
- [90] L. Xiong, A. Manthiram, Journal of The Electrochemical Society, 152 (2005) A697-A703.
- [91] Z. Xu, H. Zhang, S. Liu, B. Zhang, H. Zhong, D.S. Su, International Journal of Hydrogen Energy, 37 (2012) 17978-17983.

- [92] T.-H. Yeh, C.-W. Liu, H.-S. Chen, K.-W. Wang, *Electrochemistry Communications*, 31 (2013) 125-128.
- [93] S. Perreault, in, Canadian Centre for Justice Statistics, Component of Statistics Canada catalogue no. 85-002-X Juristat, 2013 pp. 1-29.
- [94] P. Millet, A. Michas, R. Durand, *J Appl Electrochem*, 26 (1996) 933-937.
- [95] M. Mason, K.M. Dubowski, *Journal of forensic sciences*, 21 (1976) 9-41.
- [96] R.G. Gullberg, *Forensic science international*, 131 (2003) 30-35.
- [97] K. Dubowski, M. Mason, *Journal of Forensic Science*, 21 (1976) 9-41.
- [98] B. Goldberger, Y. Caplan, *Journal of forensic sciences*, 31 (1986) 16-19.
- [99] J.-K. Park, H.-J. Yee, K.S. Lee, W.-Y. Lee, M.-C. Shin, T.-H. Kim, S.-R. Kim, *Analytica chimica acta*, 390 (1999) 83-91.
- [100] T. Kamei, T. Tsuda, Y. Mibu, S. Kitagawa, H. Wada, K. Naitoh, K. Nakashima, *Analytica chimica acta*, 365 (1998) 259-266.
- [101] N.J. Paulsson, F. Winquist, *Forensic science international*, 105 (1999) 95-114.
- [102] M.B. Williams, H.D. Reese, *Analytical chemistry*, 22 (1950) 1556-1561.
- [103] J. Wigmore, R. Langille, *Canadian Society of Forensic Science Journal*, 42 (2009) 276-283.
- [104] B. Krotoszynski, G. Gabriel, H. O'Neill, M. Claudio, *Journal of chromatographic science*, 15 (1977) 239-244.
- [105] J.T. Allan, L.E. Prest, E.B. Easton, *Journal of Membrane Science*, 489 (2015) 175-182.
- [106] L. Prest, in, UOIT, UOIT, 2011.
- [107] K. Artyushkova, P. Atanassov, M. Dutta, S. Wessel, V. Colbow, *Journal of Power Sources*, 284 (2015) 631-641.
- [108] F. De Bruijn, V. Dam, G. Janssen, *Fuel cells*, 8 (2008) 3.
- [109] C. He, S. Desai, G. Brown, S. Bollepalli, *Interface-Electrochemical Society*, 14 (2005) 41-46.
- [110] A. Mehmood, M.A. Scibioh, J. Prabhuram, M.-G. An, H.Y. Ha, *Journal of Power Sources*, 297 (2015) 224-241.
- [111] X. Yu, S. Ye, *Journal of Power Sources*, 172 (2007) 145-154.

- [112] J. Wang, Analytical electrochemistry, John Wiley & Sons, 2006.
- [113] O.R. O'Rian, F.S. Saleh, E.B. Easton, ECS Transactions, 61 (2014) 25-32.
- [114] T. Frelink, W. Visscher, J. Van Veen, *Electrochimica acta*, 40 (1995) 545-549.
- [115] F.G. Will, *Journal of The Electrochemical Society*, 112 (1965) 451-455.
- [116] E. Bertin, S. Garbarino, D. Guay, *Electrochimica Acta*, 134 (2014) 486-495.
- [117] M. Oezaslan, F. Hasché, P. Strasser, *Journal of The Electrochemical Society*, 159 (2012) B444-B454.
- [118] F.S. Saleh, E.B. Easton, *Electrochimica Acta*, 114 (2013) 278-284.
- [119] F.S. Saleh, E.B. Easton, *Journal of The Electrochemical Society*, 159 (2012) B546-B553.
- [120] J. Wu, X.Z. Yuan, J.J. Martin, H. Wang, J. Zhang, J. Shen, S. Wu, W. Merida, *Journal of Power Sources*, 184 (2008) 104-119.
- [121] S. Zhang, X.-Z. Yuan, J.N.C. Hin, H. Wang, K.A. Friedrich, M. Schulze, *Journal of Power Sources*, 194 (2009) 588-600.
- [122] J.I. Eastcott, E.B. Easton, *Journal of The Electrochemical Society*, 162 (2015) F764-F771.
- [123] E.B. Easton, P.G. Pickup, *Electrochimica Acta*, 50 (2005) 2469-2474.
- [124] Z.-M. Zhou, Z.-G. Shao, X.-P. Qin, X.-G. Chen, Z.-D. Wei, B.-L. Yi, *International Journal of Hydrogen Energy*, 35 (2010) 1719-1726.
- [125] N. Jia, R.B. Martin, Z. Qi, M.C. Lefebvre, P.G. Pickup, *Electrochimica acta*, 46 (2001) 2863-2869.
- [126] F.S. Saleh, E.B. Easton, *Journal of Power Sources*, 246 (2014) 392-401.

Chapter 2: Chemicals and Instrumentation

Unless otherwise stated, all commercial chemicals and solvents were used as received without further purification or work-up.

2.1 Material Preparation

Two types of catalysts were used in this thesis: commercial catalysts which was used as-received and catalysts made in-house. Carbon supported Pt/C (Premetek Co.) and Pt-Sn/C (Pt₃Sn/C) (Premetek Co.) commercial samples both with 20 wt% metal loading were studied and compared to the samples made in-house.

2.1.1 Catalyst Synthesis

In order to facilitate and increase the consistency of the synthesizing process, a stock solution for each metal precursor with a define concentration were prepared and summarized in Table 2.1 and 2.2. Afterward, the specified volume of the stock solutions was used to synthesize catalysts with the desired metal loading.

2.1.1.1 Pt and Pt-Mn catalysts

Pt-Mn/C catalysts with a composition of Pt_{0.25}Mn_{0.75} were synthesized by an impregnation method similar to our group previous report [1]. Metal precursors were H₂PtCl₆.H₂O (Aldrich) and MnCl₂.4H₂O (Aldrich). Based on Table 2.1, the specific volume of the Pt and Mn solutions were mixed with deionized water, in order to reach to the anticipated composition. To this mixture, sufficient mass of Vulcan XC72R carbon black (Cabot Corp.) was added so that the final product had a total metal content of 20 wt%.

The ratio of $\frac{25}{8} \frac{mg}{mL}$ was kept constant for the mass of catalyst powder (targeted mass) to the volume of deionized water. This mixture was sonicated for 20 min. The pH of the solution was controlled and adjusted to 3 using HCl (15 v/v %) and/or 1 M NaOH solution, after

which NaBH₄ was added in solid form to the mixture in a weight ratio of 3:1 (molar ratio ~ 20:1) to the metal content. The final mixture was left overnight under constant stirring at room temperature. The powder was collected by suction filtration, washed with isopropanol alcohol (IPA), acetone, and deionized water until a neutral pH was measured for the filtered residual. Finally, the collected powder was dried in an oven at 80 °C overnight.

In order to study the effect of surfactant on the particle dispersion and particle size, trisodium citrate (SC) (Fisher Scientific) was used for producing another set of the Pt-Mn samples. These samples prepared with the same impregnation method, just with SC added to the impregnation solution. The SC was added in a weight ratio of 1:1, 2:1 and 3:1 to the metal ratios, which are denoted as 1X, 2X and 3X, respectively. An example of the specifications used to produce the Pt-Mn catalysts in the presence of SC are shown in Table 2.1. The SC presence caused the pH of solution to increase around ~4.5, therefore it is necessary to monitor and adjust pH before and after sonication to achieve intended pH.

In addition, a control sample of 20 wt% Pt on Vulcan XC72R carbon black was prepared via the same impregnation synthetic procedure without adding SC, which is hereafter referred to as Pt/C_{in-house}.

Table 2.1. Summary of precursors and additives were used to produce 250 mg of the Pt-Mn/C catalysts.

Sample	Method	Additive	Pt concentration (0.02 M) (8.6 g/L)	Mn concentration (0.1 M) (19.8 g/L)	Vulcan carbon loading (mg)
Pt-Mn/C	Impregnation	-	7.01 mL	4.09 mL	200
Pt-Mn/C	Impregnation + SC	SC: 50 mg (1X) 100 mg (2X) 150 (3X)	7.01 mL	4.09 mL	200

2.1.1.2 Pt-Cu catalysts

The carbon supported Pt_{0.25}Cu_{0.75} alloys were prepared using three different methods: impregnation, impregnation in the presence of SC additive and microwave assisted polyol method, which are hereafter referred to as (Pt-Cu/C-IMP), (Pt-Cu/C-SC) and (Pt-Cu/C-POL), respectively. Metal precursors were H₂PtCl₆.H₂O (Aldrich) and CuCl₂.2H₂O (Aldrich). The carbon support and metal loading (~20 wt%) was kept similar to previous samples. The specifications of solutions and metal precursors were used to produce different Pt-Cu catalysts are shown in Table 2.2. In this case, the pH of the solution was also adjusted using a HCl solution (15 v/v %) and/or a 1 M NaOH solution. In all the methods, the resulting powder was filtered and washed with isopropanol alcohol (IPA), acetone, and deionized water, and finally dried in an oven at 80 °C overnight.

The impregnation method was done exactly with the same procedure which was explained in section 2.1.1.1. However, for the Pt-Cu samples made in the presence of SC, a single weight ratio of 2:1 was used. The pH of impregnation solution was adjusted to pH 3.

For the polyol method, the metal precursors and Vulcan carbon were mixed with ethylene glycol (EG) (Aldrich) using a mechanical stirrer. The ratio of $\sim \frac{100}{50} \frac{mg}{mL}$ was kept constant for the mass of catalyst powder (targeted mass) to the volume of EG. The solution pH was adjusted to pH 9 using a HCl solution (15 v/v %) and/or a 1 M NaOH solution, after which it was sonicated for 45 min to achieve a uniform suspension. The suspension was placed into the household microwave oven (SANYO - 2450 MHz) and heated for 8 min and then left to cool down under mechanical stirring.

Table 2.2. Summary of precursors and additives were used to produce 250 mg of the Pt-Cu/C catalysts.

Sample	Method	Additive	Pt concentration (0.02 M) (8.6 g/L)	Cu concentration (0.1 M) (17.04 g/L)	Vulcan carbon loading (mg)
Pt-Cu/C	Impregnation	-	6.05 mL	3.9 mL	200
Pt-Cu/C	Impregnation + SC	SC: 100 mg (2X)	6.05 mL	3.9 mL	200
			Pt concentration (0.2 M) 85.6 g/L	Cu concentration (1 M) 170.5 g/L	
Pt-Cu/C	Polyol	-	648 µL	389 µL	200

2.1.2 Post heat treatment

A Barnstead Thermolyne tube furnace with a quartz tube was used for heat treating the samples. Heat treatment was performed in a nitrogen atmosphere at 500, 700, 875 and 950 °C for the Pt-Mn/C samples, 500, 700 or 875 °C for all the Pt-Cu/C samples and at 500 °C and 900 °C for the Pt/C_{in-house} samples. The period of heat treatment was kept constant (1 hour) for most of the samples and temperatures. In some cases, the time of the heat treatment has increased to 2 and 4 hours which are specified in the body of thesis. After the heat treatment, the samples were cooled down under a constant flow of nitrogen gas and were preserved inside the furnace until room temperature was reached. The flow of nitrogen during and after the heat treatment was kept at 40 ml/min.

2.2 Inductively-Coupled Plasma Optical Emission Spectroscopy

2.2.1 Before electrochemical tests

The Pt/Mn and Pt/Cu molar ratios of in-house samples were determined using a Varian Vista-MPX Inductively Coupled Plasma Optical Emission Spectroscopy (ICP-OES) system. Approximately, 10 mg of the catalyst was dispersed in an Aqua Regia solution and left to dissolve for at least two days. Afterwards, the residue was filtered and the mother liquor was diluted and used for ICP-OES analysis. Four standard solutions of Pt, Mn and Cu with a concentration of 1, 5, 10 and 20 ppm were used for calibration.

2.2.2 After electrochemical tests

The chemical composition of the different samples and the solution inside the electrochemical cell along or after electrochemical tests was also examined by ICP-OES. For the tests performed on the electrodes, after the electrochemical tests an Aqua Regia solution was used to dissolve the metal powders on the electrodes and the diluted solutions were consumed for ICP-OES analysis. For the rest of the experiments, the solution extracted from the electrochemical cell was used. The starting volume of solution in the electrochemical cell was 30 mL and for each analyses 4 mL of solution was used, which it was later replaced with fresh solution (for further details please see section 2.7.4). For these experiments, the ICP-OES instrument was calibrated by four standard solutions of Pt, Mn, Cu and Sn with a concentration of 1, 5, 10 and 20 ppm.

2.3 Thermogravimetric Analysis

Thermogravimetric analysis (TGA) and differential scanning calorimetry (DSC) were utilized to study phase transition versus temperature for the catalyst powder and to determine carbon/metal weight ratio. In addition, to study the effect of the heat treatment time on the phase transformations, cyclic thermal analysis (CTA) was utilized. The CTA provides the opportunity to analyze the same sample several times by defined cycles and to study fast (instantaneous) and slow phase transformations. Thermal analysis was performed using a TA Instruments Q600 SDT system. Measurements were made in both argon and air atmospheres, using a heating ramp of 5 °C/min and 20 °C/min, respectively.

2.4 Powder X-ray Diffraction (XRD)

Powder X-ray diffraction (XRD) patterns were obtained for each catalyst. Measurements were made using either a Bruker D8 Advance powder X-ray diffractometer (Bruker, East Milton, Canada) equipped with a germanium monochromator (provided by Bruker) or a Rigaku Ultima IV X-ray diffractometer (Rigaku, Toronto, Canada) equipped with a graphite monochromator (provided by Rigaku). Both instruments employ a Cu K_{α1} X-ray source. The XRD analysis by the Bruker D8 Advance powder X-ray diffractometer was performed by the lab specialist at McMaster University but the Rigaku Ultima IV X-ray diffractometer was located at UOIT. The XRD analysis was performed on the as-produced and heat treated powder samples and also it was applied as an *ex situ* method to study the degradation of catalysts on the carbon paper (for more details please see section 2.7.4).

2.5 Transmission Electron Microscopy

Two different transmission electron microscopy (TEM) were used to analyze the morphology and microstructure of the samples. A Philips CM 10 instrument equipped with an AMT digital camera system at the University of Western Ontario and A Zeiss Libra 200MC TEM system operating at 200 kV at the University of Waterloo (WATLab). In both cases, the TEM images were obtained by the lab specialist. Samples for TEM analysis were dispersed in a mixture of water and isopropanol and applied to nickel 400 mesh reinforced grids coated by carbon and allowed to dry under air before being introduced into the chamber. The mean particle sizes were determined by measuring the diameter of 100–200 metal particles using the ImageJ software.

2.6 X-ray Photo Spectrometry

X-ray photoelectron spectroscopy (XPS) was conducted using a Kratos Axis Ultra spectrometer equipped with a monochromatic Al K α source (15 mA, 14 kV). The instrument work function was calibrated to give a binding energy (BE) of 83.96 eV for the Au 4f_{7/2} line of metallic gold and the spectrometer dispersion was adjusted so that the position of the Cu 2p_{3/2} line for metallic copper was 932.62 eV. The Kratos charge neutralizer system was used on all specimens. Spectra were charge corrected so that the main line for the carbon 1s spectrum (adventitious carbon) set to 284.8 eV. Spectra were analysed using CasaXPS software (version 2.3.14). The XPS tests were performed and results were analyzed by the lab specialist at the University of Western Ontario (Surface Science Western lab).

2.7 Electrochemical Testing

The half-cell electrochemical experiments were performed in a three-compartment cell constructed with a Pt wire counter electrode and an double junction Ag/AgCl reference electrode. Different solutions were used based on the electrochemical analysis was conducted. The structure of three-compartment cell is shown in Figure 2.1a.

The fuel cell and sensor tests were conducted using the cell shown in Figure 2.1. This cell design was based on the design of a similar commercially available fuel cell (H-Tec Company). The in-house cell was fabricated by DPM Solutions (Hebbville, NS, Canada) from poly ether ether ketone (PEEK) and contains stainless steel mesh current collectors and leads. The anode is closed with a serpentine flow field which has a dead space volume of only 0.5 mL. The cathode uses a parallel style flow field, but also has an optional port that allows for air introduction.

2.7.1 Electrode preparation

2.7.1.1 Electrochemical studies in half-cell

To study the electrochemical activity of the samples, an electrode ink for each catalyst was prepared and used to deposit catalyst layers on glassy carbon (GC) electrodes. Two different types of electrodes were used in this study. The catalyst inks were produced by mixing 10 mg of the catalyst with 100 μ L Nafion solution (5% in alcohols, Dupont) and a 400 μ L 50:50 mixture of isopropyl alcohol (IPA) and water. A uniform suspension was achieved after sonicating for 45 minutes.

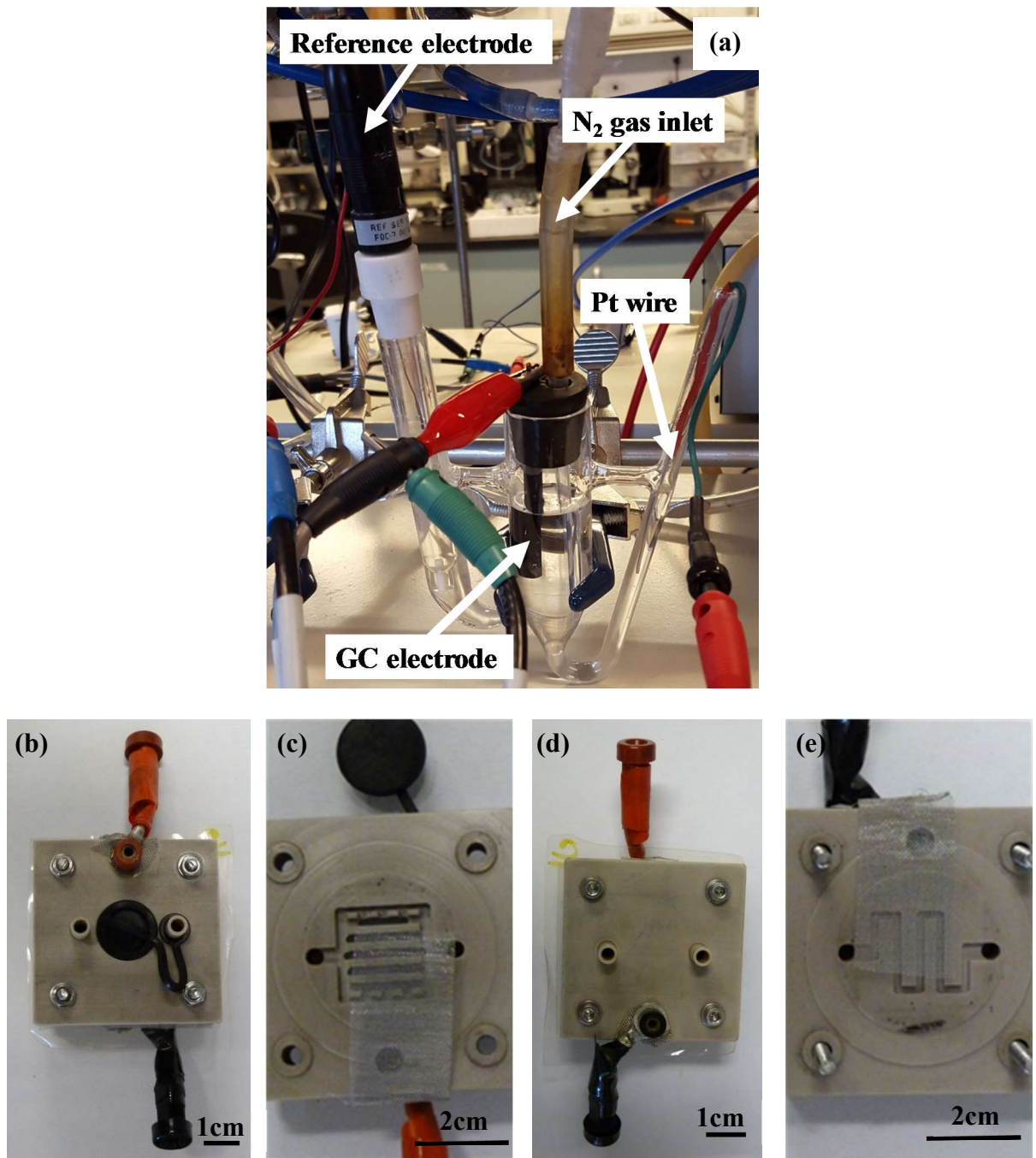


Figure 2.1. (a) Half-cell electrochemical set-up used for evaluating powder catalysts and image of the fuel cell (b), (c) cathode and (d) and (e) and anode side used for the breath alcohol sensor tests.

In order to study the general electrochemical properties of the catalysts, a 2 μL droplet of the well-dispersed catalyst ink was deposited onto a clean and polished GC electrode (diam = 3 mm, CH instruments) and dried in the air at room temperature prior to electrochemical tests. The total metal loading of the catalyst layer was $\sim 0.11 \text{ mg/cm}^2$. These electrodes were used to perform the electrochemical impedance spectroscopy (EIS) analysis and measure the changes in the electrochemical active surface area (ECSA) and the ethanol oxidation reaction (EOR).

For studying oxygen reduction reaction (ORR) a rotating ring disk electrode (RRDE) with a 5 mm glassy carbon disk and a platinum ring with a 7.5 mm inner diameter and 8.5 mm outer diameter from Pine research instrumentation was used and a 5 μL droplet of the ink was deposited onto the GC disk. In this case, the total metal loading of the catalyst layer was $\sim 0.12 \text{ mg/cm}^2$.

2.7.1.2 Gas diffusion electrode

For fuel cell studies and characterize chemical and structural changes of catalysts, larger surface area of the electrode was necessary. Therefore, gas diffusion electrodes (GDEs) were fabricated from similar mixture of the catalysts, water, IPA and the Nafion solution with some modification. The amount of water and IPA was scaled up to fit the new condition. For 250 mg of catalysts powder, a 60 mL 50:50 IPA and water was used and the corresponding volume of the Nafion solution was calculated in a way to produce electrodes with a Nafion loading of 30 wt%. The ratio of powder and total solution volume was kept constant for all the samples. The mixture was sonicated for 45 min, stirred over-night and sonicated for 45 min before spray deposition onto a gas diffusion layer (GDL) (Toray

TPGH-090, 10 % wet-proofing) using an airbrush [2]. The electrodes were dried for 30 min at room temperature and then at 80°C for over-night. The targeted total metal loading of the catalyst layer was around 0.4 mg/cm². Afterward, 4 cm² of coated samples were cut and exposed to the test solution or used for fuel cell and sensor tests. The total metal loadings of electrodes after fabrication were as follows: (a) Pt-Mn/C-SC with 0.33 mg/cm² (b) Pt-Mn/C-SC-700 °C with (c) Pt-Cu/C-POL with 0.4 mg/cm² (d) Pt-Cu/C-POL-700°C with 0.31 mg/cm², (e) Pt₃Sn/C with 0.33 mg/cm² and (f) Pt/C with 0.43 mg/cm² metal loading.

This set of electrodes was utilized to examine the chemical composition and crystalline structure variations by ICP-OES and XRD during degradation test and also used to build membrane electrode assembly (MEA) for the sensor and fuel cell tests. Later, MEAs were prepared by hot-pressing (150 kg cm⁻² 120 s at 130 °C) two 4-cm² electrodes across a Nafion 115 membrane (Ion Power). The cathode electrode was made using the commercial Pt/C powder and kept same for all MEAs. The electrode that was employed as the anode was prepared by different samples and named after the sample powder which was used for making the ink.

2.7.2 Cyclic and Linear Sweep voltammetry

All electrochemical tests, such as cyclic voltammetry (CV) and linear sweep voltammetry (LSV), were conducted using a Solartron 1470 potentiostat multichannel potentiostat controlled using Multistat software (Scribner Associates). The half-cell measurements were made in N₂-purged 0.5 M H₂SO₄ (aq) electrolyte to determine the electrochemical active surface area (ESCA). EOR activity was assessed in a N₂-purged aqueous solution containing both 0.5 M H₂SO₄ + 0.1 M ethanol. For fuel cell and sensor

measurements, humidified N₂ was flowed at the anode with humidified H₂ flowed at the cathode, serving as both the reference and counter electrode. In the half-cell and fuel cell measurements, two scan rates were used: 100 mV/s for cleaning and hydrating of the samples and subsequently, the scan rate of 20 mV/s which are reported in this thesis and were used to calculate ECSA. A minimum of 20 cycles were performed before collecting the final CVs.

2.7.3 Electrochemical Impedance Spectroscopy

Electrochemical Impedance Spectroscopy (EIS) was conducted using a Solatron 1260 frequency response analyzer controlled using Multistat software (Scribner Associates). EIS measurements were performed to evaluate the degradation and resistance of electrode materials in both half-cell and fuel cell. The frequency range was scanned between 100 kHz to 0.1 Hz at a DC bias potential of 0.360 V (vs. NHE) (double layer region in CVs). EIS profiles were analyzed using the finite transmission line model [3, 4] which was discussed in Chapter 1, in order to estimate the ionic conductivity and capacitance of the catalyst layer. The half-cell measurements were made in N₂-purged 0.5 M H₂SO₄ (aq) electrolyte. For fuel cell and sensor measurements, humidified N₂ was flowed at the anode with humidified H₂ flowed at the cathode, serving as both the reference and counter electrode.

2.7.4 Half-Cell durability tests

2.7.4.1 Accelerated stress tests (ASTs)

A three compartment cell equipped with a Pt wire counter and a double-junction Ag/AgCl reference electrode was used to perform AST on GC and carbon paper electrodes (see section 2.7.1). CVs and EIS were performed the same way as explained in section 2.7.2 and 2.7.3. The durability of samples in the 0.5 M H₂SO₄ and 0.5 M H₂SO₄ + 0.1M ethanol solutions were examined by repeated CV cycles with the appropriate lower and upper potential limits [4-6]. The AST protocols to study the electrochemical and structural degradation of samples were as follows:

- 1) Accelerated ageing applied for the samples deposited on the GC electrodes by potential cycling between 0.03 and 1.43 V (vs NHE) in the N₂-purged 0.5 M H₂SO₄ solution for specific number of cycles with the scan rate of 50 mV/s. However, after the specific number of cycles (1, 50, 100, 200, 400, 1000, 2000, 3000, and 4000) 2 cycles recorded at 20 mV/s and the last one were plotted for comparison and used to calculate ECSA. In addition, immediately after recording the cycles at 20 mV/s, the EIS analysis were conducted at 0.360 V (double layer region in CVs).
- 2) Same aging protocol used for 0.5 M H₂SO₄ + 0.1M ethanol solution to study degradation of the samples deposited on the GC electrodes at a shorter potential range from 0.23 to 1.03V
- 3) Slightly different protocol applied for the samples deposited on carbon papers. Aging cycles were done from 0.03 and 1.43 V (vs NHE) at the higher scan rate of 100 mV/s. The cycling process was paused after the specific number of cycles (1, 50, 150, 400, 1000, 2000 and 3000) and samples were analyzed by ex-situ XRD. At the same time, 4 ml

of the 0.5 M H₂SO₄ solution was removed for ex-situ ICP analyses and replaced by fresh solution. In order to perform the XRD analyses, the samples were washed by deionized water and dried with flowing air.

2.7.5 Oxygen Reduction Reaction

The oxygen reduction reaction (ORR) activity of samples studied using RRDE (for details on the electrode preparation please see section 2.7.1.1). A Pine bipotentiostat/galvanostat WaveDriver 10 controlled with AfterMath software was used for ORR measurements. Linear sweep voltammograms (LSVs) were obtained for each set of samples without any rotation in a N₂-purged 0.5M H₂SO₄ solution to determine the background due to the Vulcan carbon particles. Following the background test, LSVs were recorded to evaluate ORR in a 0.5M H₂SO₄ solution saturated with pure O₂ gas for 15 min. LSV was repeated at five different rotation rates: 200 rpm, 400 rpm, 900 rpm, 1600 rpm, and 2500 rpm, starting from the highest rpm. The limiting current and onset potentials were determined and compared at a rotation rate of 1600 rpm unless otherwise specified. The limiting current is determined from the point at which the measurements plateau (0.332 mV vs NHE) and the onset potential is defined as the potential at 5% of the limiting current. The RRDE collection experiments were utilized to study the hydrogen peroxide production (H₂O₂). The ring potential was held at 1.2 V to oxidize any evolved H₂O₂.

2.7.6 Fuel Cell and Sensor Electrochemical Measurements

The breath simulator and the sensor test station along with the schematic diagram of all the connections are shown in Figure 2.2. This setup has been previously optimized and

validated for Pt/C based MEAs [7]. The structure of the fuel cell was utilized for sensing measurement is displayed in Figure 2.1. The same cell with electrode surface area of 4 cm² was used for all the measurements. A 3-necked round bottom flask was employed as a breath simulator. A heater and a thermocouple connected to temperature controller were maintained temperature of an aqueous alcohol solution. The temperature of alcohol solution was kept constant at 34 °C to simulate typical human expired breath [7, 8]. In order to obtain calibration curves for different samples, the concentration of ethanol was varied between 0 and 0.18 g/dL using proper amount of ethanol solution (95%). An example of the sensing data collected and the corresponding calibration curve are presented in Figure 2.3. A DC rotary pump (Parker CTS Diaphragm Pump, Model Number E155-11-050) was used for the alcohol vapor injection to the cell which was connected to the breath simulator. The pump was connected to a 5 V DC power supply to keep the flow rate constant for all readings (145 mL/min). The injections were controlled with electronic timers (Omega TRFP240AC). Nitrogen gas with high purity (99.9999%) with the pressure of 10 PSI was used as a carrier gas to eliminate any contribution from oxygen or other contaminations to the sensor readings.

Two different testing protocol was used to investigate sensing properties of the samples, which explained as follows:

2.7.6.1 Calibration curves and 7-day sensing tests

In this set of tests, the pump was triggered to work for 10 s via the electronic timer to simulate a breath injection and the current transient was recorded. A minimum of four breath injections were made at each concentration (0, 0.03, 0.06, 0.08, 0.12, 0.15 and 0.18

g/dL). The resting time between injections was 10 min. From every set of 4 injections, last three used to determine the charge under the peaks and to calculate standard deviation. This test was repeated for 7 days and the cell was kept in sealed bag for the next day to prevent the MEA drying. A recovery protocol was applied to the cell every day before performing the sensing test. Our studies showed that the recovery is necessary to achieve more reproducible sensing results [7]. In this recovery protocol, the cell was exposed to humidified nitrogen gas in the anode side and humidified hydrogen gas in the cathode side while CV was recorded at scan rate of 100 mV/s. This continued until a clean and reproducible CVs (~10 to 20 cycles) were observed. CVs at scan rate of 20 mV/s was also recorded to determine ESCA. In addition, immediately after recording the cycles at 20 mV/s, EIS analysis were conducted at 0.360 V vs. NHE in order to study the performance of the electrodes and estimate the degradation of samples during the 7-day tests.

2.7.6.2 Sensing tests at constant concentration

In this set of tests, almost same protocol as section 2.7.6.1 was used with some modifications. The injection and resting time was kept same but the alcohol concentration was not changed during these tests. A single alcohol concentration of 0.06 g/dL was used for all samples. The testing time was ~8 hours and repeated for 7 days. The alcohol solution was replaced every ~4 hours to prevent alcohol depletion and the first four reading of alcohol sensing for fresh solution was used to study the behaviour of sensors over time in the single concentration. This test aimed to study the fluctuation and errors that would occur in a signal reading for the sensors over time such as effects of alcohol poisoning, or other

parameters such as dryness of MEA. The similar recovery protocol was used at the beginning of every day as section 2.7.6.1 for this set of data.

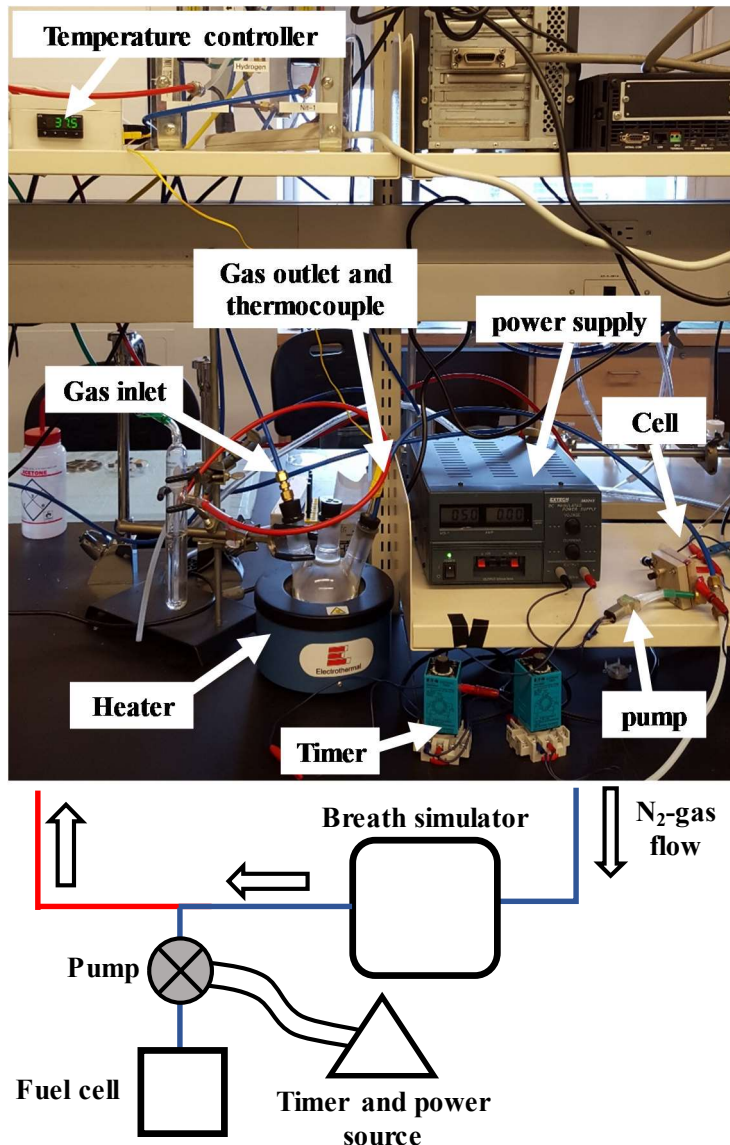


Figure 2.2. The sensor test station and schematic diagram of all the connections.

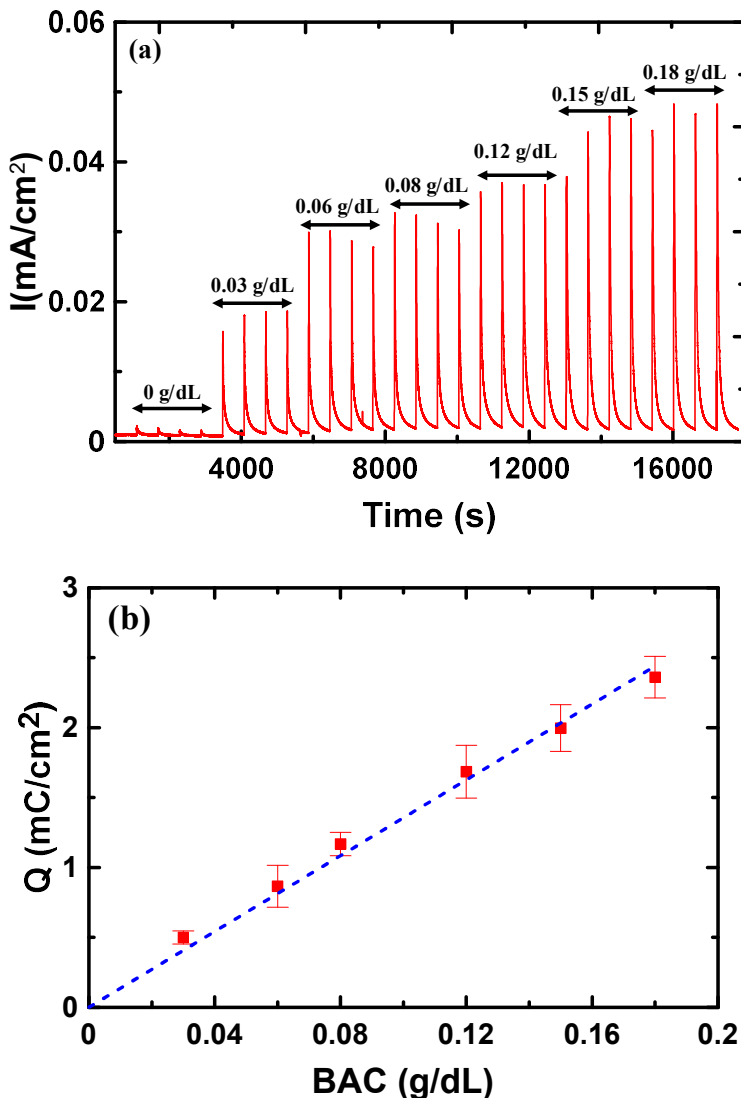


Figure 2.3. (a) An example of the sensing data collected for MEA produced with the Pt-Mn/C sample and (b) the corresponding calibration curve was plotted from same data.

2.8 References

- [1] M. Ammam, E.B. Easton, Journal of The Electrochemical Society, 159 (2012) B635-B640.
- [2] J.I. Eastcott, K.M. Yarrow, A.W. Pedersen, E.B. Easton, Journal of Power Sources, 197 (2012) 102-106.
- [3] E.B. Easton, P.G. Pickup, *Electrochimica Acta*, 50 (2005) 2469-2474.
- [4] O.R. O'Rian, F.S. Saleh, E.B. Easton, *ECS Transactions*, 61 (2014) 25-32.
- [5] F.S. Saleh, E.B. Easton, *Journal of Power Sources*, 246 (2014) 392-401.
- [6] F.S. Saleh, E.B. Easton, *Journal of The Electrochemical Society*, 159 (2012) B546-B553.
- [7] M.R. Rahman, J.T.S. Allan, M. Zamanzad Ghavidel, L.E. Prest, F.S. Saleh, E.B. Easton, *Sensors and Actuators B: Chemical*, 228 (2016) 448-457.
- [8] P. Millet, A. Michas, R. Durand, *J Appl Electrochem*, 26 (1996) 933-937.

Chapter 3: Production and Thermally Induced Changes in the Structure and Electrochemical Activity of Pt-Mn/C Alloys

Part of the work described in this chapter has been published as:

M.R. Zamanzad Ghavidel, E.B. Easton, *Applied Catalysis B: Environmental*, 176–177 (2015) 150-159.

3.1 Introduction

In the last few decades, significant research efforts have focused on the reduction of the costs associated with direct alcohol fuel cells (DAFCs) [1-5]. The cost and lifetime of the DAFCs are mainly controlled by the catalysts used at each electrode. Pt is the most commonly utilized electrocatalyst. In order to decrease the cost and increase the lifetime of the DAFCs, it is essential to lower the required loading of Pt. In general, there are two methods to enhance the performance of a catalyst; first, by increasing the real surface area in contact with the reactant, which can be achieved by reducing particle size and improving particle dispersion; second, by enhancing the fundamental catalytic activity through the production of new materials or alloys [3, 6].

There have been numerous studies of Pt-transition alloys for anodic fuel cell reactions, including Pt-Cu, Pt-Mo, Pt-Ni, Pt-Fe, Pt-Co, Pt-Sn and Pt-Ru [3, 4, 7-13][3,4,7-12]. It has been shown that Pt-Ru has the highest activity towards the methanol oxidation reaction (MOR) [7, 14-18]. Conversely, Pt-Sn is has been shown to be more active than Pt-Ru towards the ethanol oxidation reaction (EOR), with the most active phase believed to be Pt_3Sn [14, 16, 17, 19, 20].

Our group has recently reported Pt-Mn alloys with high EOR activity [9-11] . Furthermore, the most active alloys contained less than 25 at% Pt, which is beneficial from a cost standpoint. Alloy formation was confirmed with XRD analysis. Those results showed that the presence of Mn affects both particle size and the intrinsic activity of the catalysts. However, the catalysts contained a mixture of weakly alloyed Pt-Mn and in-active oxide phases, which represents a limiting factor for performance.

Heat treatment has been recognized as an important and sometimes necessary step for catalytic activity improvement [5, 21, 22]. Heat treatment often leads to the removal of

undesirable impurities present in the initial preparation (such as oxide phases). Furthermore, it can also lead to the formation of more uniform alloy particles with increased stability. This can often lead to an enhancement of catalytic performance, but not always. For example, heat treatment of Pt supported catalysts, even at low temperatures, leads to Pt particle growth via sintering. Sintering occurs via the migration and coalescence of the platinum particles or by evaporation and condensation of the atoms from small crystallites [22]. Therefore, the use of a heat treatment process can be detrimental, particularly for high purity single-element nanoparticle catalysts. However, the benefits of thermally treating alloy nanoparticles often outweigh any activity losses that may occur due to particle size growth. Optimization of the synthesis and heat treatment process is often complex, and careful study is required in order to fully understand the reason for enhanced activity [4, 5, 22].

As with pure platinum particles, the grain sizes of the alloy particles can become enlarged at higher heat treatment temperatures. However, alloy catalysts often exhibit a better resistance to sintering than pure catalysts [22]. During heat treatment, the Pt lattice parameter and degree of alloying can be altered, and intermetallic and ordered phases can be formed depending upon the alloying element and the heat treating temperature [4, 22, 23]. Increasing the degree of alloying can lead to enhanced electrocatalytic activity because of electronic changes brought about by the presence of the alloying elements and changes in the inter-atomic Pt-Pt distance [18, 22]. Furthermore, the heat treatment of alloy catalysts can potentially weaken [24] or improve [12] their durability and stability.

In this chapter, we have studied the effects of heat treatment temperature and heating time on the crystalline structure and uniformity of Pt-Mn alloy phases. Additionally, the influence of heat treatment on particle size, catalyst dispersion and electrochemical surface

area (ECSA) was examined. This structural information was correlated with EOR activity to determine the most active phases.

3.2 Experimental

3.2.1 Catalyst synthesis

Pt-Mn/C catalysts with a composition of $\text{Pt}_{0.25}\text{Mn}_{0.75}$ were synthesized by an impregnation method similar to our previous reports [9]. One equivalent of $\text{H}_2\text{PtCl}_6 \cdot \text{H}_2\text{O}$ (Aldrich) and three equivalents of $\text{MnCl}_2 \cdot 4\text{H}_2\text{O}$ (Aldrich) were dissolved in deionized water. To this mixture, sufficient mass of Vulcan XC72R carbon black (Cabot Corp.) was added so that the final product had a total metal content of 20 wt%. This mixture was sonicated for 20 min. The pH of the solution was controlled and adjusted to 3 using HCl (15 v/v %), after which NaBH_4 was added in solid form to the mixture in a weight ratio of 3:1 to the metals. The final mixture was left overnight under constant stirring at room temperature. The powder was collected by suction filtration, washed with isopropanol alcohol (IPA), acetone, and deionized water, and finally dried in an oven at 80 °C overnight. For comparison, a control sample of 20 wt% Pt on carbon was prepared via the same synthetic procedure, which is hereafter referred to as Pt/C_{in-house}.

A Barnstead Thermolyne tube furnace with a quartz tube was used for heat treating the samples. Heat treatment was performed in a nitrogen atmosphere at 500, 700, 875 and 950 °C for Pt-Mn/C samples and at 500 °C and 900 °C for the Pt/C_{in-house} samples. The period of heat treatment was kept constant (1 hour) for all samples and temperatures, unless otherwise specified. After the heat treatment, the samples were cooled to room temperature under a constant flow of nitrogen.

3.2.2 Materials characterization

The Pt/Mn molar ratio in each sample was determined using a Varian Vista-MPX Inductively Coupled Plasma Optical Emission Spectroscopy (ICP-OES) system. Approximately, 10 mg of the catalyst was dispersed in an Aqua Regia solution and left to dissolve for at least two days. Afterwards, the residue was filtered and the mother liquor was diluted and used for ICP-OES analysis. Four standard solutions of Pt and Mn with a concentration of 1, 5, 10 and 20 ppm were used for calibration.

X-ray photoelectron spectroscopy (XPS) was conducted using a Kratos Axis Ultra spectrometer equipped with a monochromatic Al K α source (15 mA, 14 kV). The instrument work function was calibrated to give a binding energy (BE) of 83.96 eV for the Au 4f_{7/2} line of metallic gold and the spectrometer dispersion was adjusted so that the position of the Cu 2p_{3/2} line for metallic copper was 932.62 eV. The Kratos charge neutralizer system was used on all specimens. Spectra were charge corrected so that the main line for the carbon 1s spectrum (adventitious carbon) set to 284.8 eV. Spectra were analysed using CasaXPS software (version 2.3.14). The XPS tests were performed and results were analyzed by the lab specialist at the University of Western Ontario (Surface Science Western lab).

Powder X-ray diffraction (XRD) patterns were obtained using a Bruker D8 Advance powder X-ray diffractometer, with germanium monochromator and Cu K α_1 radiation. The XRD analysis was performed by the lab specialist at McMaster University. Thermogravimetric Analysis (TGA) and differential scanning calorimetry (DSC) were

utilized to study phase transition versus temperature for the catalyst powder and to determine carbon/metal weight ratio. In addition, to study the effect of the heat treatment time on the phase transformations, cyclic thermal analysis (CTA) was utilized. The CTA provides the opportunity to analyze the same sample several times by defined cycles and to study fast (instantaneous) and slow phase transformations. Thermal analysis was performed using a TA Instruments Q600 SDT system. Measurements were made in both argon and air atmospheres, using a heating ramp of 5 °C/min and 20 °C/min, respectively.

Transmission Electron Microscopy (TEM) images were acquired using a Philips CM 10 instrument equipped with an AMT digital camera system. Samples for TEM analysis were dispersed in a mixture of water and isopropanol (IPA) and applied to nickel 400 mesh reinforced grids coated with carbon and allowed to dry under air before being introduced into the chamber. The TEM images were obtained by the lab specialist at the University of Western Ontario.

3.2.3 Electrochemical characterization

To study the electrochemical activity of the samples, an electrode ink for each catalyst was prepared and used to deposit catalyst layers on glassy carbon (GC) electrodes. The inks were produced by mixing ca. 10 mg of catalyst with 100 µL of Nafion solution (5% in alcohols, DuPont) and 400 µL of a 50:50 mixture of isopropanol alcohol (IPA) and water. The mixture was sonicated for 45 min to achieve a uniform suspension. A 2 µL droplet of the well-dispersed catalyst ink was deposited onto a clean and polished glassy carbon electrode (diam = 3 mm, CH instruments), using a micro syringe, such that it covered the entire surface of the glassy carbon. The ink droplet was allowed to air dry at room

temperature prior to electrochemical tests. The resultant catalyst layer had a total metal loading of 0.11 mg/cm². All electrochemical tests, such as cyclic voltammetry (CV) and linear sweep voltammetry (LSV), were conducted using a Solartron 1470 potentiostat. Measurements were made in N₂-purged 0.5 M H₂SO₄ (aq) electrolyte to determine the electrochemical active surface area (ESCA). EOR activity was assessed in a N₂-purged aqueous solution containing both 0.5 M H₂SO₄ + 0.1 M ethanol.

3.3 Results and Discussion

3.3.1 Materials characterization

The chemical composition of the samples and the residual solutions after chemical reduction were determined by ICP-OES and presented in Table 3.1. The ICP-OES tests showed that the Pt-Mn alloys were produced with a composition of 22 at% Pt and 78 at% Mn, quite close to the expected composition values (Pt_{0.25}Mn_{0.75}). The amount of Pt and Mn ions in the filtrate was also zero, indicating that nearly all of the metal ions were successfully reduced. TGA analysis performed under air indicated that the metal loading for all Pt/C and Pt-Mn/C samples were close to the expected 20 wt% metal. The metal loading was ca. 16 wt% for pure Mn sample (Table 3.1).

Table 3.1. Composition of the samples and concentration of Pt and Mn in filtrated solution which was measured by ICP.

Samples	Alloy molar ratios measured by ICP		Ions concentration in filtered solution by ICP		Metal Loading wt%
	Pt (%)	Mn (%)	Pt (ppm)	Mn(ppm)	
Pt/C _{in-house}	100	0	-	-	25.27
Pt _{0.25} Mn _{0.75}	22.18	77.82	nil	nil	22.75
Mn/C _{in-house}	0	100	-	-	16.19

Figure 3.1a and b shows the thermogravimetry (TG) and derivative thermogravimetry (DTG) curves obtained for the carbon supported pure Pt, pure Mn and Pt-Mn alloy catalysts and Vulcan carbon. Five distinctive mass loss regions were observed. The mass loss occurring between 100 °C and 250 °C was attributed to the thermal decomposition of functional groups on carbon and the evaporation of any residual water in the samples [25, 26]. A second major mass loss was observed around 300 °C, which was attributed to the oxidation of the carbon support by oxygen or the air trapped within the powdered samples [26]. The mass loss observed around 700 °C was attributed to loss of functional groups on carbon and its graphitization [25]. The mass losses observed at ca. 500 and 900 °C were attributed to Mn oxide phase modifications. Stobbe et al. have shown that pure MnO₂ is reduced to Mn₂O₃ at 500 °C, and further reduced to Mn₃O₄ at 900 °C [27]. However, at room temperature, a mixture of these oxides is most likely present. Mn oxide transitions occurred at lower temperatures for the Pt-Mn/C alloy sample compared to the Mn/C samples, which indicates that Pt may help facilitate these transformations.

The DSC curves obtained for the pure and alloyed samples are illustrated in Figure 3.1c and d. Most of the observed transitions were endothermic except those related to carbon combustion between 300 to 400 °C. The measured heat flow between 700 and 1000 °C for the Pt-Mn alloy (20.21W/g) was higher than that measured for the pure Mn (12.04 W/g) and Pt (16.99 W/g) samples. This indicates that the alloy phase transformation began around 700 °C and completed at higher temperatures.

The cyclic weight loss, cyclic derivative weight loss and cyclic heat flows versus temperature are shown for the Pt-Mn alloy in Figure 3.2. All phase transformations that occur below 700 °C were completed during the first cycle as there was no major mass loss in the second cycle in the same range (Figure 3.2b). However, mass changes were observed at temperatures above 700 °C during the second cycle. The endothermic processes that occurred during the second cycle were most likely related to the alloying process and oxide removal at the higher temperature, indicating that these processes were somewhat slow (Figure 3.2c). Therefore, the influence of heat treatment time on the structure and EOR activity of the samples was investigated in more detail. Based on the DSC results, heat treatment temperatures of 500, 700, 875 and 950 °C were selected for the Pt-Mn alloys catalysts, and at 500 and 900 °C for the pure Pt samples. In addition, the hold time at these heat treatment temperatures was also examined.

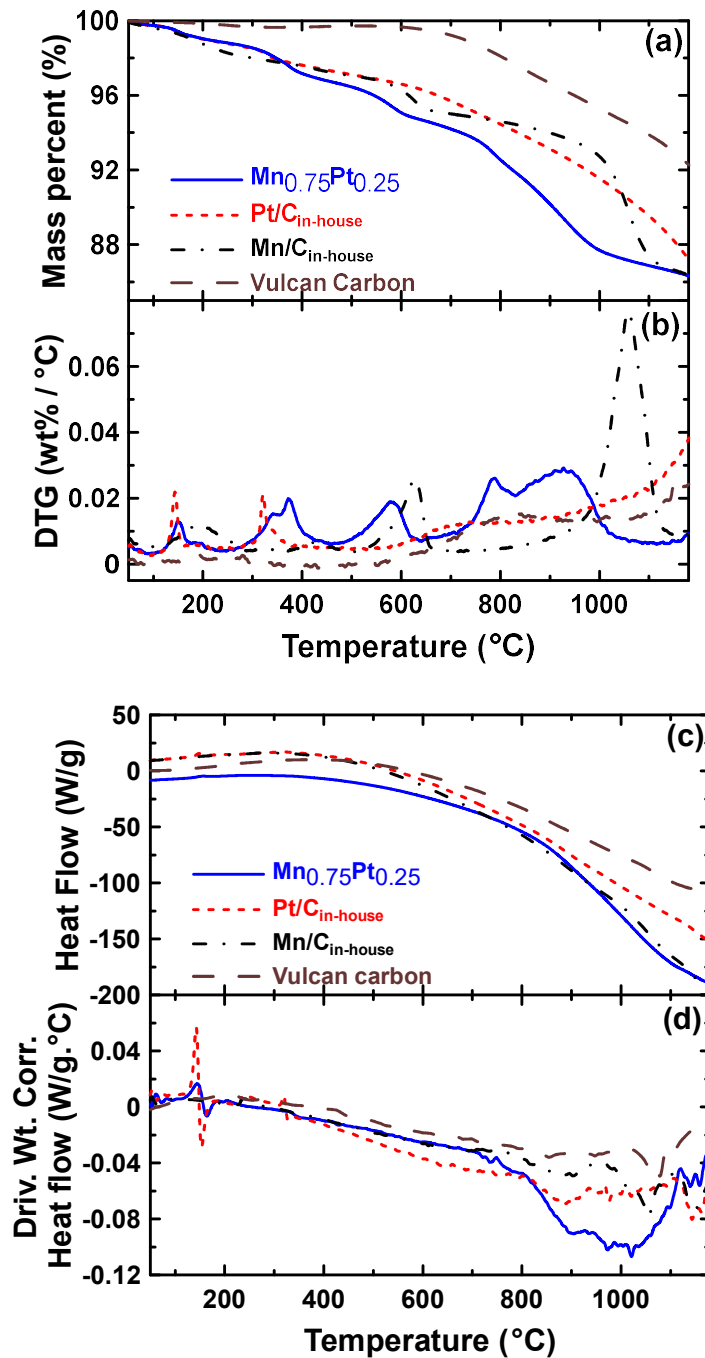


Figure 3.1. (a) The weight loss and (b) derivative weight loss (c) heat flow and (d) derivative heat flow versus temperature for Pt, Mn and Pt-Mn alloys deposited on a Vulcan carbon support and pure Vulcan carbon. Measurements were made at a heating rate of 5 °C/min under flowing argon.

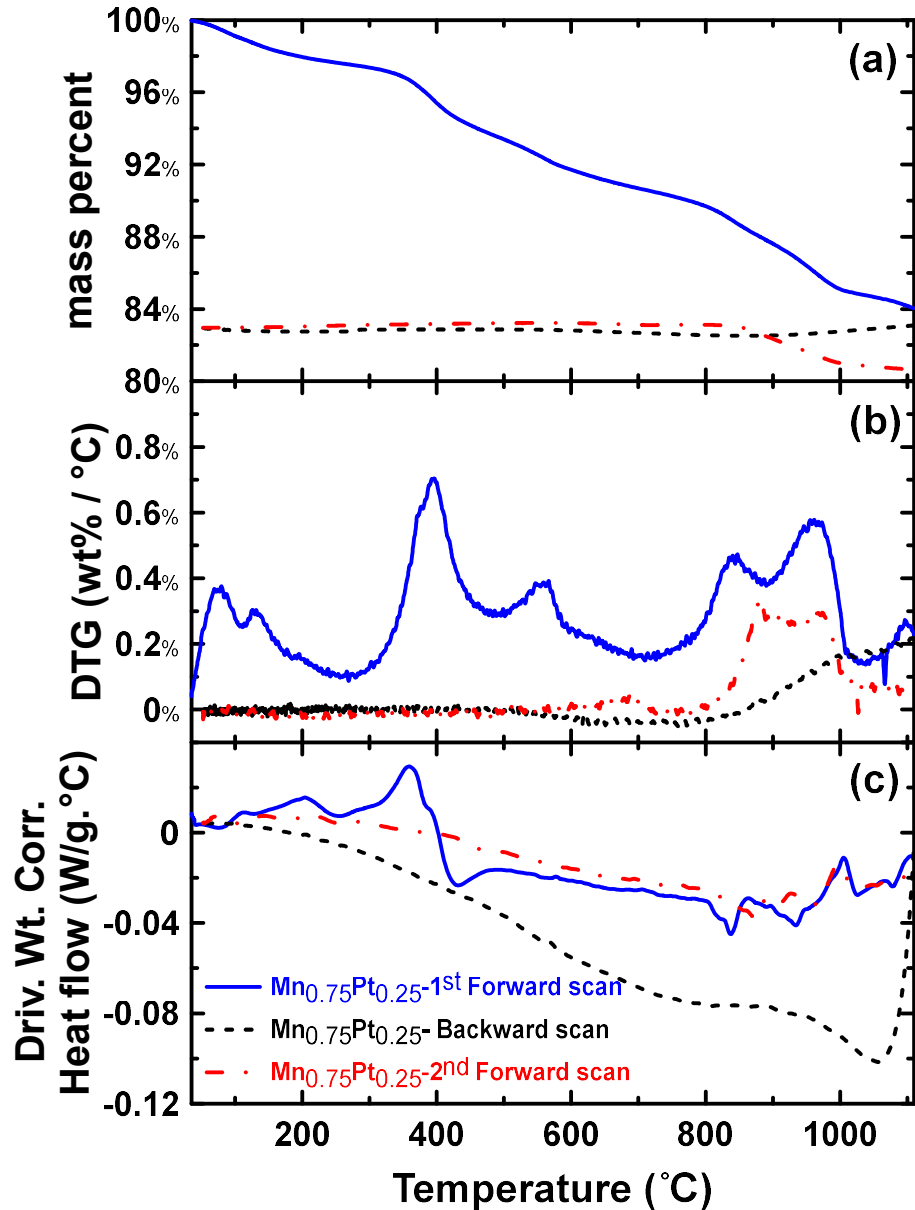


Figure 3.2. The cyclic weight loss, derivative weight loss and derivative heat flow versus temperature in argon atmosphere for Pt-Mn alloys deposited on a Vulcan carbon support. Measurements were made at a heating rate of 20 °C/min under flowing argon.

The XRD patterns obtained for samples heat treated at different temperatures for 1h are shown in Figure 3.3. The lattice parameters for each phase were also calculated from the XRD patterns and are listed in Table 3.2. Broad peaks were obtained for the untreated samples, indicating that the catalysts were produced with small grain sizes. The broadening of the peaks could also be due to the presence of oxide phases and non-uniform alloy. The diffractogram displayed the characteristics pattern expected for the face centered cubic (fcc) structure of Pt. The peak positions were shifted to higher angles and the lattice parameter decreased to 3.885 Å compared to pure Pt (3.923 Å), indicating the incorporation of Mn in the fcc Pt structure. Additionally, there was a peak observed at 36.2° which was likely related to Mn rich phases. Because of the extremely broad peaks, it was very difficult to precisely identify which alloy phases were formed during the chemical reduction. However, we can reasonably infer that the as-deposited catalysts contained a mixture of Pt-Mn alloys and other non-alloyed phases.

Heat treatment was employed to induce structural changes in the catalyst. Upon heat treatment at 500 °C, the reflections associated with the Mn rich phases in the XRD pattern disappeared. Furthermore, the intensity of the remaining peaks increased, indicating that crystallization and some structural changes were initiated at this temperature, although the predominant structure was still the Pt fcc structure. At this temperature, there were two kinds of distinctive phases: one rich in Mn and the other rich in Pt.

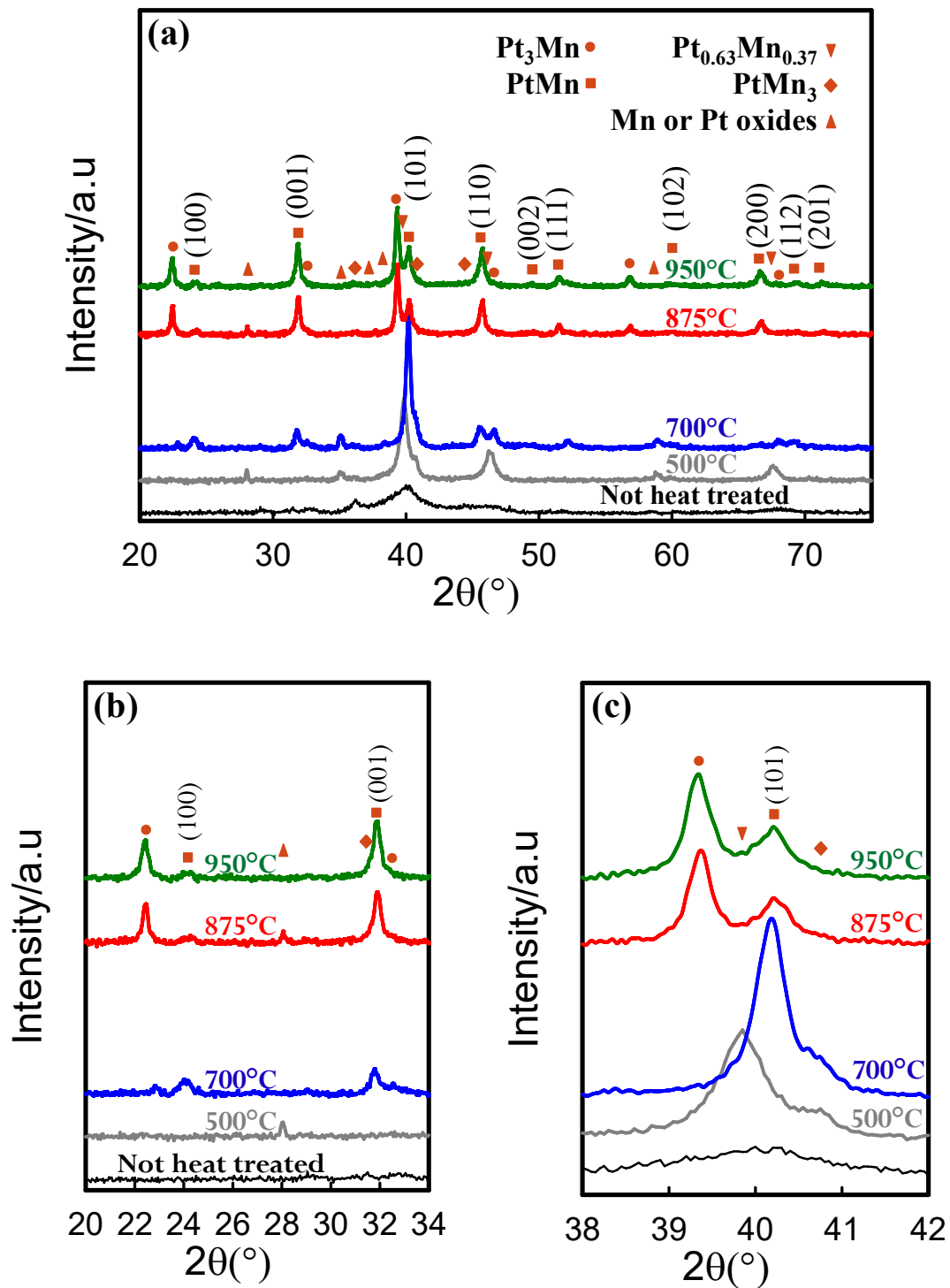


Figure 3.3. XRD analysis of the Pt-Mn alloys before and after heat treatment in nitrogen atmosphere for constant period (1hour) at different temperatures.

Table 3.2. Lattice parameters were calculated from Figure 3.3 and 3.4.

Crystalline phases	Lattice structure	Space group	Lattice parameters (Å)	
			a	c
Pt_{0.25}Mn_{0.75}	-	fcc	Fm $\bar{3}$ m	3.885
Pt_{0.25}Mn_{0.75}-500°C-1h	-	fcc	Fm $\bar{3}$ m	3.915
Pt_{0.25}Mn_{0.75}-500°C-2h	-	fcc	Fm $\bar{3}$ m	3.906
Pt_{0.25}Mn_{0.75}-500°C-4h	-	fcc	Fm $\bar{3}$ m	3.908
Pt_{0.25}Mn_{0.75}-500°C-6h	-	fcc	Fm $\bar{3}$ m	3.901
Pt_{0.25}Mn_{0.75}-700°C-1h	PtMn	Tetragonal	P4/mmm	2.817
Pt_{0.25}Mn_{0.75}-700°C-2h	PtMn	Tetragonal	P4/mmm	2.821
Pt_{0.25}Mn_{0.75}-700°C-4h	PtMn	Tetragonal	P4/mmm	2.823
Pt_{0.25}Mn_{0.75}-875°C-1h	Pt ₃ Mn	Cubic	Pm $\bar{3}$ m	3.961
Pt_{0.25}Mn_{0.75}-950°C-1h	Pt ₃ Mn	Cubic	Pm $\bar{3}$ m	3.965

When the heat treatment temperature was raised to 700 °C, substantial changes in the intensity and position of several peaks were observed, particularly the (101) and (110) reflections. Moreover, new peaks appeared at lower diffraction angles (22° – 40°). All of these observations indicate that an ordered intermetallic phase was formed at 700 °C, which we have assigned to an intermetallic PtMn phase (ICDD card no. 01-071-9672). The important peaks are shown in expanded scales in Figure 3.3b and c. The PtMn intermetallic phase has a tetragonal structure [4]; therefore, the new (100) and (001) peaks were observed at the lower diffraction angles of ~24.1° and ~31.7°, respectively. In addition, upon raising the heat treatment temperature, the peak observed at 39.8° for the sample heat treated at 500 °C shifted to 40.2° when the sample was heat treated at 700 °C, which was a result of further Pt and Mn alloying and intermetallic phase formation. In other words, at 700 °C a uniform alloy with a high alloying degree was generated, with PtMn as the predominant phase.

Upon further increasing the heat treatment temperature to 875 °C and 950 °C, additional peaks at ~22.4° and ~39.4° were observed, which were attributed to variation in

the crystalline structure of the Pt-Mn intermetallic phases. The new peaks were most likely due to phase separation and the formation of phases with higher Pt content such as Pt₃Mn (see Figure 3.3b). The origins of the phase separation warrants further investigation, but we postulate that particles or phases with a lower Mn content have been combined with the PtMn phase and formed Pt₃Mn like structures. The lattice parameters calculated for the heat treated samples and the ordered phases in Table 3.2 were similar to the lattice parameters reported for the standard samples (reported in ICDD cards for PtMn: $a = 2.827 \text{ \AA}$, $c = 3.669 \text{ \AA}$ and Pt₃Mn: $a = 3.897 \text{ \AA}$), especially for the ordered PtMn phase. The lattice parameter for Pt₃Mn phase was slightly higher than the standard lattice parameter which could be due to the phase separation process.

The XRD patterns obtained for Pt-Mn/C samples heat treated for different time periods are illustrated in Figure 3.4a and b. The results showed that increasing the heat treatment time at 500 °C did not change the phases present. However, the intensification of the XRD peaks indicate that further crystallization has occurred. Only trace amounts of ordered phases were detected after 6 hours of heat treatment at 500 °C. However, increasing the heat treatment time impacted the crystalline structure significantly at 700 °C (Figure 3.4b). After 1 hour of the heat treatment at 700 °C, the peaks for the Pt rich phase were still clearly observable (two closely-spaced peaks near 45°). However, when the sample was heat treated for more than one hour at 700 °C, the peaks associated with the Pt rich phase disappeared (e.g. the peak at 46.6°) and the PtMn ordered phase became prevalent. These results also agree with the TGA/DSC data which showed that the processes occurring at 700 °C requiring more time to complete.

To examine the corrosion stability of PtMn/carbon alloy catalysts, a sample was immersed in 0.5 M H₂SO₄ solution for 24 hours. The XRD spectra before and after

exposing the powder catalysts to the acidic solution are shown in Figure 3.5. The black arrows show the location of peaks associated with Mn-oxide phases, which disappear after immersion in acid. However, the Bragg peaks associated with the intermetallic phases are unchanged, indicating their corrosion stability.

PtMn/C alloy catalysts were analyzed by XPS before and after heat treatment in order to study any changes in their surface composition. The Pt 4f XPS spectra obtained for heat treated and untreated samples are shown in Figure 3.6. The spectrum of Pt for treated and untreated samples were deconvoluted into two components, with asymmetric peak shapes. These signals are labeled as Pt0 and Pt1, which arise from zero-valent Pt and PtO, respectively [28-32]. The calculated relative percentages of each species, along with peak position and full width at half-maximum (FWHM) of Pt0 component are listed in Table 3.3.

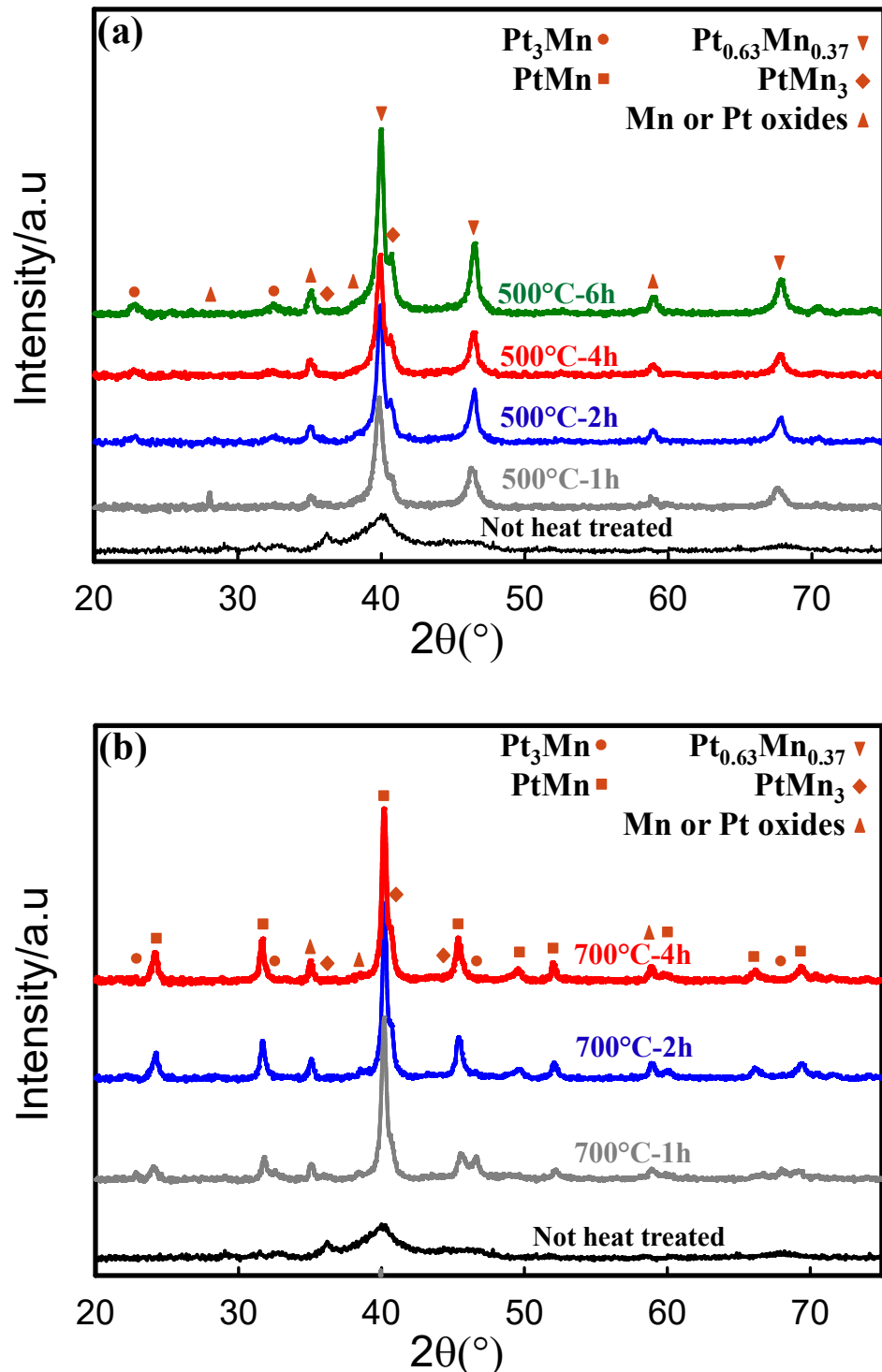


Figure 3.4. XRD analysis of the Pt-Mn alloys before and after heat treatment for different periods at (a) 500 °C and (b) 700 °C in nitrogen atmosphere.

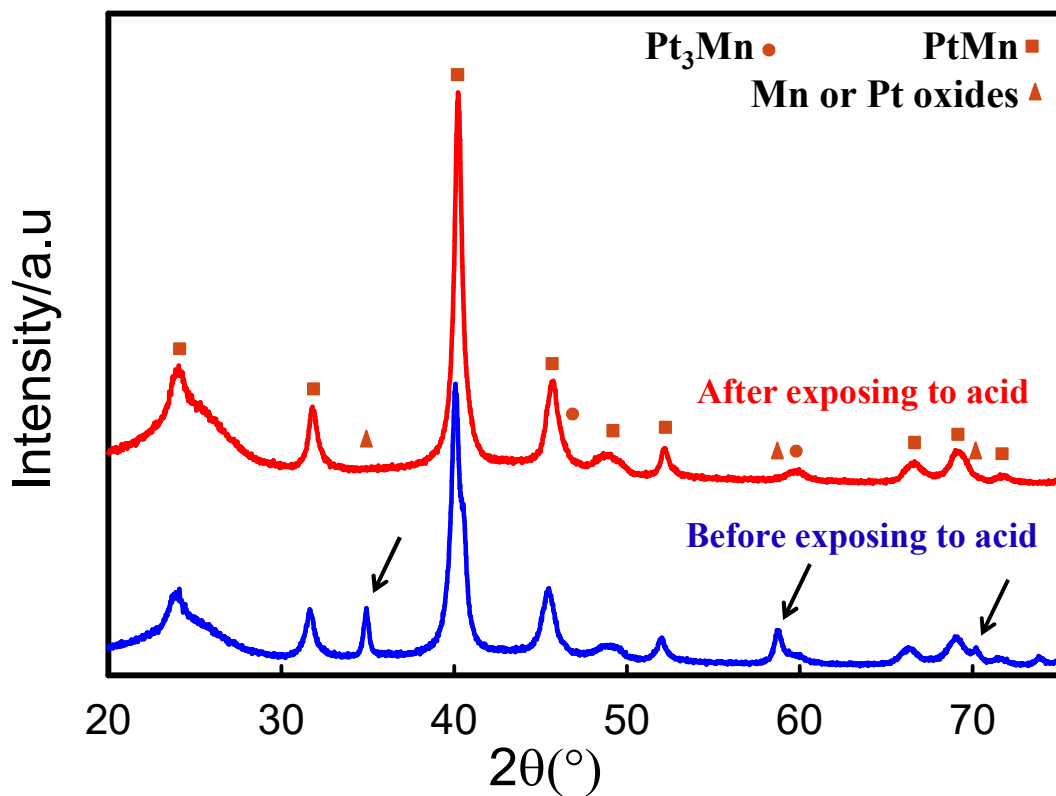


Figure 3.5. XRD analysis of the Pt-Mn alloy which is heat treated at 700 °C in nitrogen atmosphere for 1hour before and after exposing to 0.5 M H₂SO₄ solution (These XRD spectra are acquired by Rigaku Ultima IV multipurpose X-ray diffraction (XRD) system with graphite monochrometer and Cu K α 1 radiation).

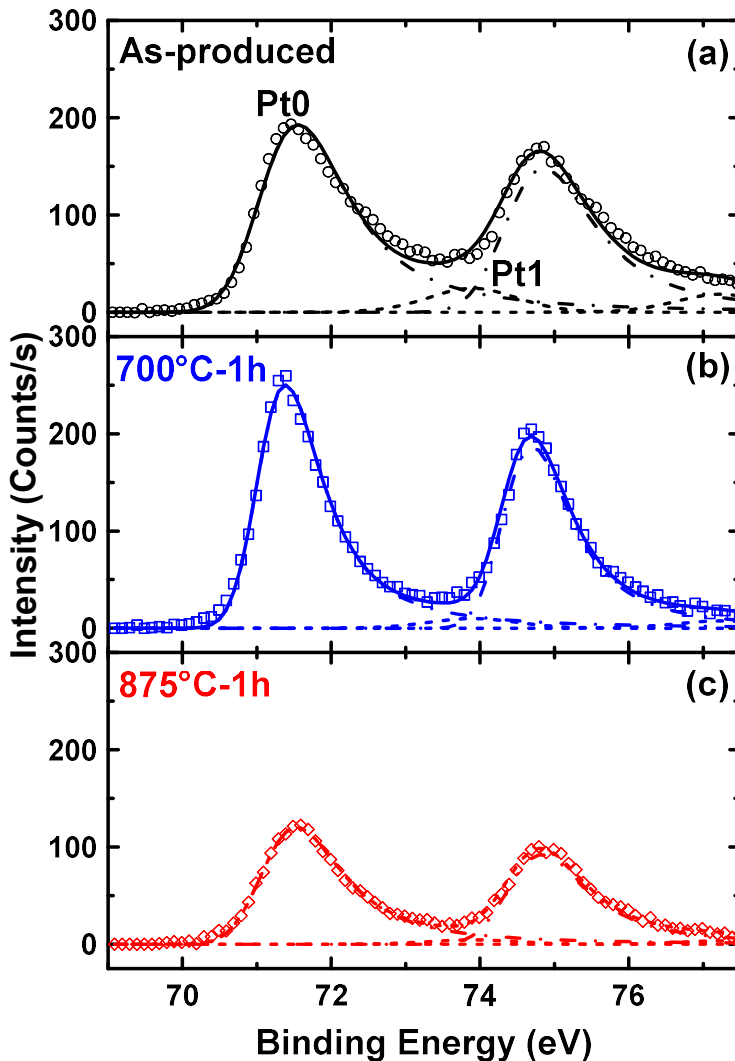


Figure 3.6. XPS spectra of Pt 4f for the $\text{Pt}_{0.25}\text{Mn}_{0.75}$ alloy deposited on Vulcan carbon
 (a) As-produced and heat treated at (b) $700\text{ }^{\circ}\text{C}$ and (c) $875\text{ }^{\circ}\text{C}$ for 1h in nitrogen atmosphere.

The Mn 2p XPS spectra obtained for treated and untreated Pt-Mn/C samples are presented in Figure 3.7. A broad spectrum was observed for Mn $2p_{3/2}$ emission, which indicates that Mn on the surface of the alloyed particles was oxidised and no Mn in metallic state was observable on the surfaces. The Mn oxide formation was also confirmed by the TGA analysis (Figure 3.1a). Deconvolution of the Mn 2p spectrum revealed a complex

mixture of several oxide compounds in multiple oxidation states [33-37]. Since these oxides are inactive towards EOR [11, 38] and unstable in acidic solution [39], detailed study of these phases by XPS was not performed. However, the core Pt-Mn alloy phases formed and Mn within these alloys structures were indeed stable, as confirmed by prior electrochemical durability measurements [11, 38]. The XRD pattern obtained for a Pt-M alloy catalyst heat treated at 700 °C before and after immersion in 0.5 M H₂SO₄ for 24 hours (Figure 3.5) showed that the reflections associated with the alloy phase remain unchanged while the peaks associated with the oxide phases disappeared. This measurement confirms that the oxide layer was removed, revealing the alloy phases at the surface for electrocatalysis. Similar behavior has been reported for Pt-Co alloy catalysts [40] where oxide phases and Co atoms on the surface of the nanoparticles dissolve resulting in a Pt skin surface which protects the alloyed particles from further corrosion and reduces the dissolution rate of the alloying element. We believe similar process has occurred for the Pt-Mn samples. Studies of the electrochemical durability the Pt-Mn alloys will be reported in the near future.

The binding energy for Pt0 and Pt1 (Figure 3.6) in our samples are in good agreement with the literature for Pt/C catalysts [28]. The Pt0 peak position was shifted to higher binding energies compares to bulk Pt metal (71.2 eV vs 70.8 eV), which is attributed to metal-support interaction and/or small cluster-size effects commonly observed in fuel cell catalysts [41]. The amount of Pt oxide content decreased with increasing heat treatment temperature. The atomic ratio of Mn on the surface was ~4 to ~9 at% higher than the bulk composition (Table 3.1). This indicates that some of the Mn migrated to the surface of the particles and formed a Mn oxide, leaving behind a more Pt-rich alloy core. Increasing the

heat treatment temperature to 700 °C has marginally increased the Pt content on the surface which decreased again after the heat treatment at 875 °C.

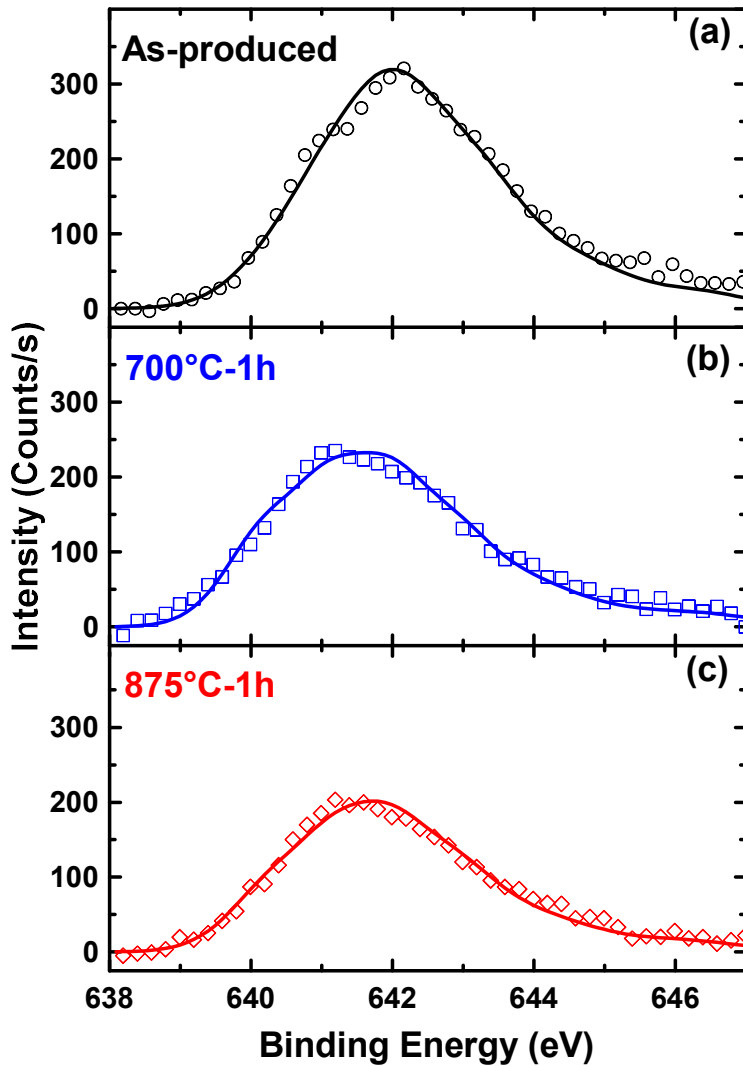


Figure 3.7. XPS spectra of Mn 2p for the $\text{Pt}_{0.25}\text{Mn}_{0.75}$ alloy deposited on Vulcan carbon (a) As-produced and heat treated at (b) 700 °C and (c) 875 °C for 1h in nitrogen atmosphere.

Table 3.3. The binding energies, FWHM and species percentage of different Pt species as observed from the Pt (4f) X-ray photoelectron spectra of the heat treated and untreated Pt-Mn alloys.

Samples	Species relative intensity (%)		Pt 4f _{7/2} Peak position (eV)	Pt 4f _{7/2} Peak FWHM (eV)	Surface Atomic ratios of Mn vs. Pt (%)
	Pt0	Pt1			
Pt_{0.25}Mn_{0.75}	90.6	9.4	71.2	1.20	84.98
Pt_{0.25}Mn_{0.75}-700°C-1h	95.7	4.3	71.1	0.88	82.44
Pt_{0.25}Mn_{0.75}-875°C-1h	96.7	3.3	71.2	1.08	86.76

After heat treatment at 700 °C, the Pt0 (Pt 4f_{7/2}) peak shifted to slightly more negative binding energies (~0.1 eV), and also became sharper (FWHM reduced by ~0.32 eV). These effects can be attributed to the particle size growth (reverse of small cluster-size effects) [42, 43], which is inevitable during the heat treatment process. The negative shift could also be related to polarization of the Pt–Mn bond or an electron withdrawing effect from the neighboring Mn atoms [28, 43, 44]. Further increasing the heat treatment temperature to 875 °C lead to phase separation had some effects on the electronic structure of nano particles. The Pt0 peak shifted to higher binding energies and also became slightly broader. Given the continuous particle size growth that occurred during heat treatment, the only reason for the positive shift is phase separation and the formation of a Pt rich phase (Pt₃Mn), which is in agreement with the XRD results.

TEM images of the as-synthesized samples and those heat treated at different temperatures are shown in Figure 3.8. TEM images show that nano-sized catalyst particles were successfully produced. Furthermore, heat treatment resulted to an increase in particle sizes, including some very large particles with a diameter of more than 20 nm. Comparison of the TEM images acquired for untreated and treated samples revealed that particle

agglomeration greatly contributed to the growth of very large particles during the heat treatment. Overall, the mean particle size was not substantially increased by heat treatment. Even at a heat treatment temperature of 950 °C, the average particle size was enlarged by only 5 nm. This shows that the alloyed particles are resistant to particle growth which has also been observed by others [45]. The particle sizes calculated from the TEM images are summarized in Table 3.4. Figure 3.9a and b show how the average particle size changed as a function of heat treatment temperature and heat treatment time at 500 and 700 °C. These results demonstrate that, although the chance of particle growth is greater at higher temperatures, the alloyed particles showed increased resistance to growth, even with a longer heat treatment period.

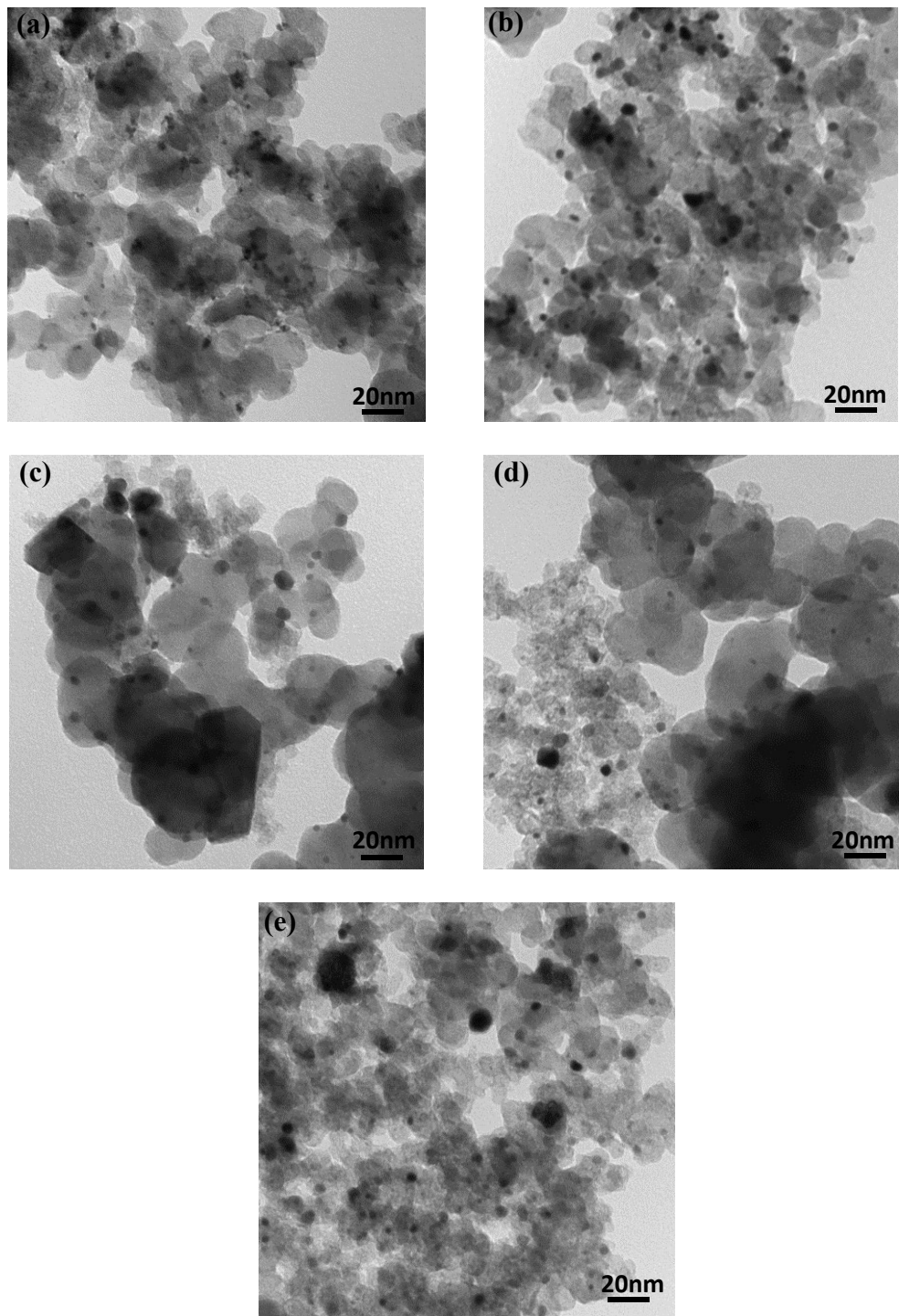


Figure 3.8. TEM images of the Pt-Mn alloys before and after heat treatment in nitrogen atmosphere for constant period (1hour) at different temperatures (a) untreated (b) 500, (c) 700 (d) 875 and (e) 950 °C.

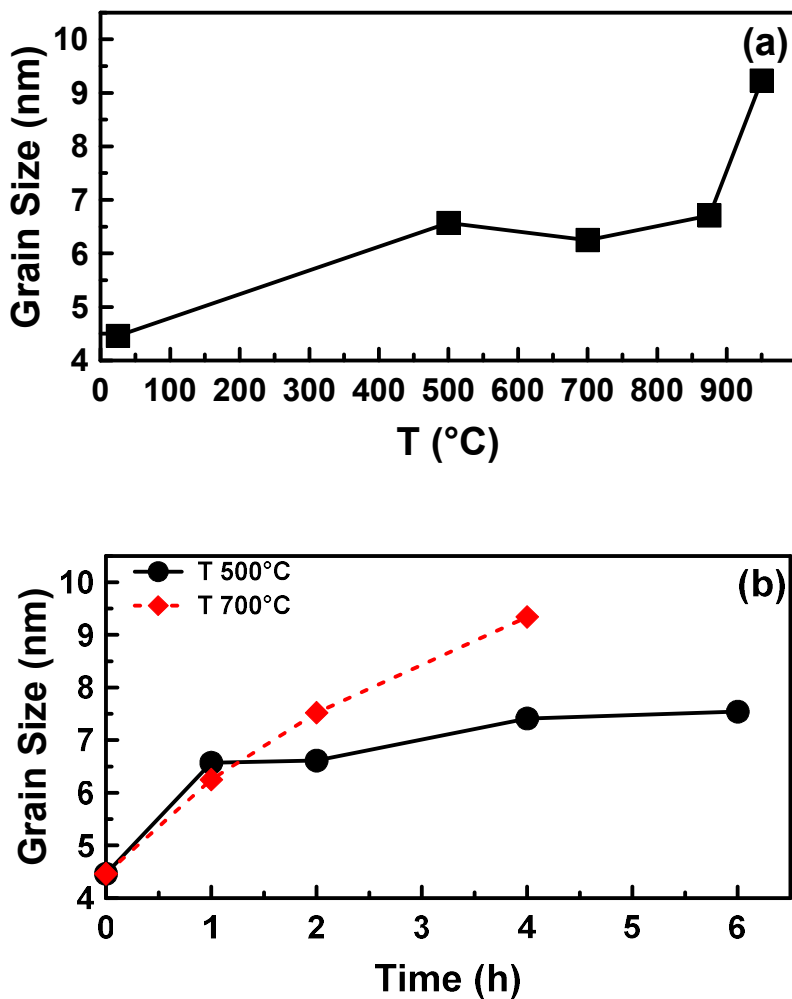


Figure 3.9. The variation of average catalyst Pt-Mn particle size as a function of (a) temperature and (b) heat treatment time.

Based on the materials characterization data, the thermal evolution of the structure of the Pt-Mn alloy particles can be summarized as follow:

- The as-deposited catalysts contained a mixture of oxide phases and Pt-Mn alloy phases.

- b) Heat treatment at 500 °C intensified crystallization, but the Pt fcc structure was still predominant. The heat treatment period had almost no effect on the crystalline phase distribution at this temperature.
- c) At 700 °C, the Pt-Mn alloy phases were modified significantly. The ordered PtMn intermetallic phase was formed at this temperature. However, since the phase transformation was slow, the most predominant PtMn intermetallic alloy structure required longer heat treatment periods (4 h) to form.
- d) By increasing the temperature to 875 °C, phase separation has occurred, which created a mixture of the Pt₃Mn and PtMn intermetallic phases.
- e) All alloy particles had a layer of Mn-oxides present on the surface, which dissolved in acidic media to reveal the underlying Pt-Mn alloy core.

With a clear understanding of the alloy particle composition and morphology for each catalyst, a clear relationship between their structure and electrochemical properties can be more readily made.

3.3.2 Electrochemical characterization

Electrochemical studies in a deaerated 0.5 M H₂SO₄ solution were conducted on the samples before and after heat treatment and the results are presented in Figure 3.10. All samples showed the common Pt CV shape. The presence of clearly resolved hydrogen adsorption/desorption peaks at low potential indicates that any surface manganese oxide layer was removed, revealing the Pt-alloy surface. The ECSA values were calculated by integrating the charge under the hydrogen adsorption peaks and are compiled in Table 3.4. The results show that the ECSA values for pure Pt/C dramatically and

continuously decreased from 15.5 to 7.7 m²/g_{Pt} by treating samples at 500 and 900 °C. However, ECSA values of Pt-Mn/C samples behaved quite differently. After heat treatment at 500 °C, the ECSA values for Pt-Mn samples were reduced by ca. 50%, but the ECSA for the alloyed samples improved after increasing the heat treatment temperature above 700 °C. A similar trend was also observed by increasing the heat treatment time. Particle size growth is one of the main reasons for the drop in ECSA for all heat treated catalysts, both alloy and pure metal. However, the optimal heat treatment process for the Pt-Mn alloy led to an ECSA that was only 20% lower than that of the untreated sample. This resistance to ECSA loss is most likely due to a roughening of the alloy particle surface upon dissolution of the surface oxide layer [39, 40, 46, 47].

The EOR activity of the pure Pt samples, before and after heat treatment, is displayed in Figure 3.11. Comparing the peak current density of the heat treated samples with the as-produced sample showed that the electrochemical activity continuously decreased by increasing the treatment temperature (Table 3.4). This loss in activity can be attributed to the substantial growth in Pt particle size upon heat treatment.

The EOR activity of the Pt-Mn/C catalysts, before and after heat treatment, is shown in Figure 3.12 a and b. Heat treatment at 500 °C led to a decrease in catalytic activity. This was not surprising since at 500 °C no new phases were formed and the particle size increased. Upon increasing the heat treatment temperature, EOR activity began to improve and at 875 °C EOR activity surpassed that of the untreated sample pure Pt sample. Upon raising the heat treatment temperature to 950 °C, EOR activity decreased slightly, though it was still higher than that achieved with the untreated sample.

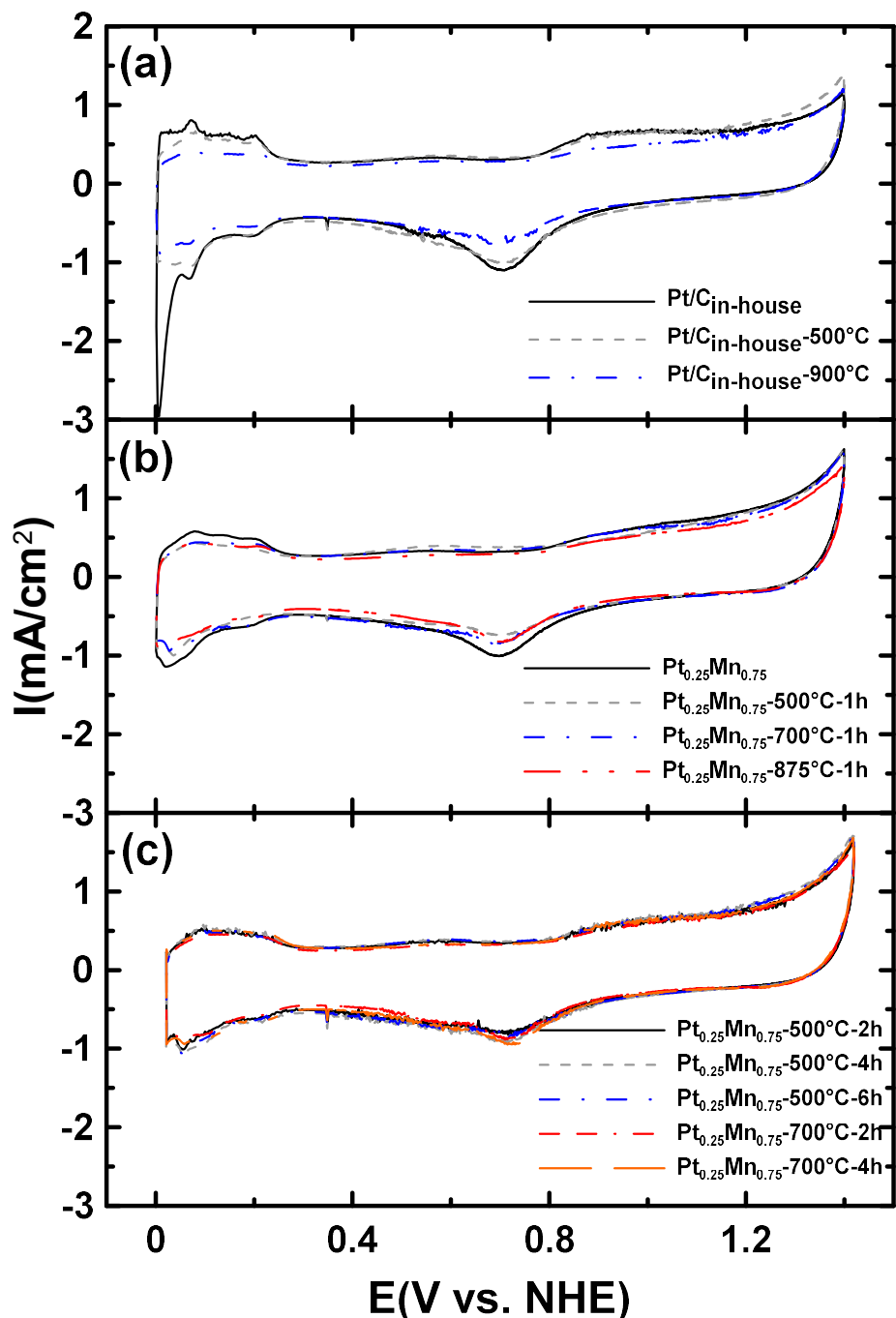


Figure 3.10. CVs obtained for (a) Pt/C and (b) Pt-Mn/C catalysts before and after heat treatment for 1 hour at different temperature. (c) CVs obtained for Pt-Mn/C catalysts heat treated for different time periods. Measurements were made in N_2 -purged 0.5 M H_2SO_4 at a scan rate of 20 mV/s.

Table 3.4. Summary of particle size calculated by TEM and electrochemical properties of the catalysts studied in this work.

	Half-wave potential (mV)	Peak potential (mV)	Peak current (mA.cm⁻²)	ECSA (m²/g_{Pt})	Mean particle size measured by TEM (nm)
Pt/C_{in-house}	745	912	5.34	15.5	-
Pt/C_{in-house} -500°C -1h	718	854	2.22	11.2	-
Pt/C_{in-house} -900°C -1h	734	887	2.04	7.7	-
Pt_{0.25}Mn_{0.75}	697	865	2.49	10.5	4.46
Pt_{0.25}Mn_{0.75}-500°C-1h	720	850	2.02	5.1	6.57
Pt_{0.25}Mn_{0.75}-500°C-2h	742	886	3.26	7.6	6.61
Pt_{0.25}Mn_{0.75}-500°C-4h	738	894	3.00	8.1	7.41
Pt_{0.25}Mn_{0.75}-500°C-6h	748	899	3.17	7.0	7.54
Pt_{0.25}Mn_{0.75}-700°C-1h	744	882	2.60	6.6	6.25
Pt_{0.25}Mn_{0.75}-700°C-2h	745	912	5.34	8.1	7.52
Pt_{0.25}Mn_{0.75}-700°C-4h	737	899	6.49	8.7	9.34
Pt_{0.25}Mn_{0.75}-875°C-1h	673	897	3.58	7.9	6.71
Pt_{0.25}Mn_{0.75}-950°C-1h	675	915	2.88	8.4	9.23

To compare the data based on the Pt content, the EOR activity is plotted using Pt-mass specific current in Figure 3.12a. These plots show that the sample heat treated at 875 °C had about double the mass-activity (measured by peak current) of the pure Pt catalysts. In addition, the most active alloys showed a lower half-wave potential for EOR. This, coupled with the lower ECSA compared to the untreated catalyst, indicates that there is an electronic effect associated with the increased EOR activity of the annealed Pt-Mn/C catalysts, which we have attributed to the presence of the intermetallic alloy phase.

The impact of heat treatment time at 500 °C and 700 °C are shown in Figure 3.12d. Increasing the heat treatment time beyond 2 h at 500 °C had no impact on EOR activity. This is in agreement with our XRD and TGA data that indicated only minimal structural changes at this temperature. However, increasing the treatment period at 700 °C up to 4 h improved the activity continuously, leading to a two-fold increase in peak EOR current and a decrease in the half-wave potential for the EOR. This increased activity parallels the phase

transformations that occurred at 700°C as a function of heat treatment time. Longer heat treatment times at 700 °C produces more of the PtMn intermetallic alloy, which is responsible for the improved EOR activity.

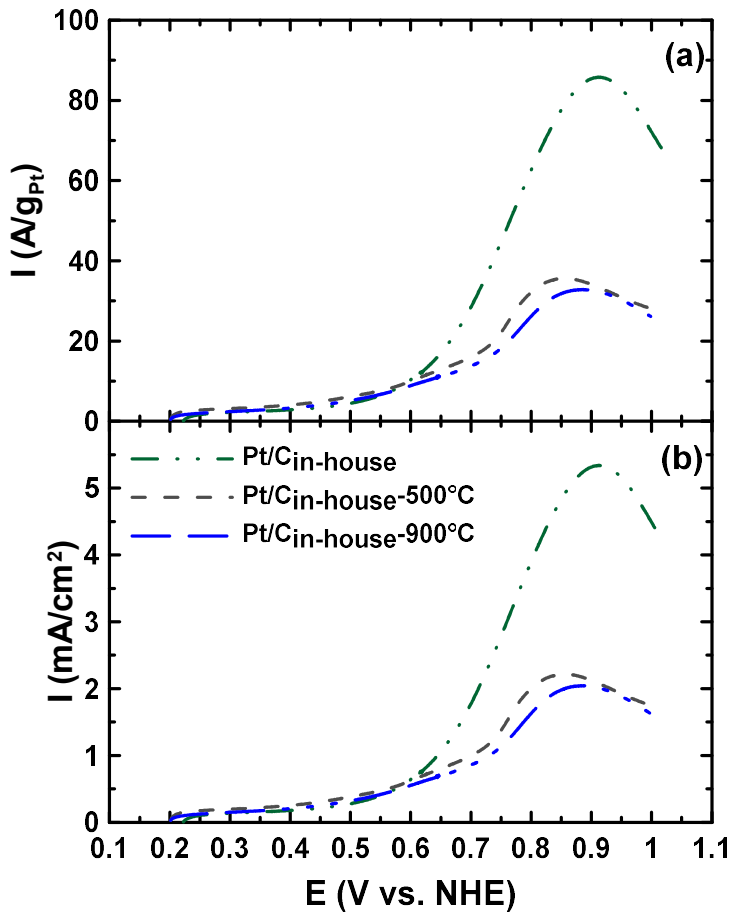


Figure 3.11. LSVs obtained for pure Pt catalysts deposited on Vulcan carbon before and after heat treatment. The data is presented with the current normalized on the basis of (a) Pt content and (b) geometric area. Measurements were made in 0.5 M H₂SO₄ containing 0.1 M ethanol at a scan rate of 20 mV/s.

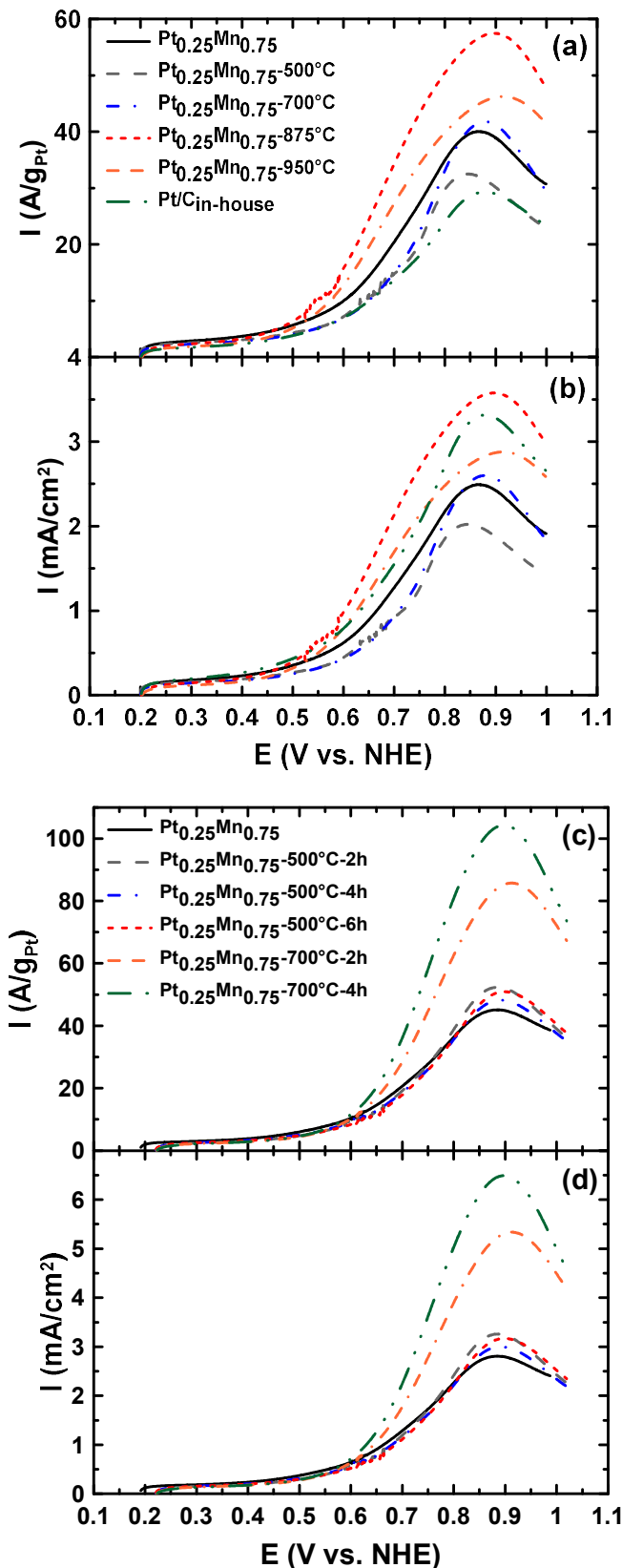


Figure 3.12. LSVs obtained for Pt-Mn alloys deposited on Vulcan carbon before and after heat treatment at (a,b) different temperatures for 1 h and (c,d) different temperatures for 2 – 6 h. The data is presented with the current normalized on the basis of (a,c) Pt content and (b,d) geometric area. Measurements were made in 0.5 M H_2SO_4 containing 0.1 M ethanol at a scan rate of 20 mV/s.

Finally, electrochemical and material characterization confirm that, although different metal deposition rates lead to inhomogeneous alloys during chemical deposition, optimized heat treatment conditions have improved homogeneity and the EOR activity of the catalysts. Furthermore, a specific heat treatment cycle can result in the most active crystalline structures, which enhance the EOR activity.

3.4 Conclusion

In this chapter, Pt and Pt-Mn alloys were synthesized and the effect of both heat treatment temperature and time on the structure and electrochemical properties of Pt-Mn/C alloy catalysts were investigated. The as-deposited Pt-Mn/C catalysts contained a mixture of alloy and oxide. DSC measurements showed that several phase transitions occurred between 500 °C and 900 °C and most of these transitions are endothermic. XRD analysis indicated that the PtMn intermetallic was formed at 700 °C, and that this phase transitions required about 4 hours at that temperature to completely form. Heat treatment at 875 °C resulted in the formation of a mixture of PtMn and Pt₃Mn intermetallic phases. TEM analysis indicated that alloyed particles showed resistance to particle growth. By examining EOR activity for catalysts prepared at different heat treatment temperatures, we have determined that the most active phase for EOR is the PtMn intermetallic phase. Maximum EOR activity occurred when the samples were heat treated at 700 °C for 4 h, which corresponded to the highest concentration of this PtMn intermetallic phase with a relatively small loss in ECSA compared to the as-produced samples.

3.5 References

- [1] E. Antolini, Materials Chemistry and Physics, 78 (2003) 563-573.
- [2] A. Rabis, P. Rodriguez, T.J. Schmidt, ACS Catalysis, 2 (2012) 864-890.
- [3] H. Liu, C. Song, L. Zhang, J. Zhang, H. Wang, D.P. Wilkinson, Journal of Power Sources, 155 (2006) 95-110.
- [4] T. Ghosh, B.M. Leonard, Q. Zhou, F.J. DiSalvo, Chemistry of Materials, 22 (2010) 2190-2202.
- [5] W. Vielstich, A. Lamm, H.A. Gasteiger, Handbook of Fuel Cells: Fundamental, Technology, and Applications, Wiley, 2003.
- [6] F. Vigier, S. Rousseau, C. Coutanceau, J.-M. Leger, C. Lamy, Top Catal, 40 (2006) 111-121.
- [7] T. Sato, K. Okaya, K. Kunimatsu, H. Yano, M. Watanabe, H. Uchida, ACS Catalysis, 2 (2012) 450-455.
- [8] E. Antolini, J.R.C. Salgado, E.R. Gonzalez, Applied Catalysis B: Environmental, 63 (2006) 137-149.
- [9] M. Ammam, E.B. Easton, Journal of The Electrochemical Society, 159 (2012) B635-B640.
- [10] M. Ammam, E.B. Easton, Journal of Power Sources, 215 (2012) 188-198.
- [11] M. Ammam, L.E. Prest, A.D. Pauric, E.B. Easton, Journal of The Electrochemical Society, 159 (2011) B195-B200.
- [12] W. Roh, J. Cho, H. Kim, J Appl Electrochem, 26 (1996) 623-630.
- [13] T.J. Schmidt, H.A. Gasteiger, R.J. Behm, Electrochemistry Communications, 1 (1999) 1-4.
- [14] L. Li, L. Hu, J. Li, Z. Wei, Nano Res., 8 (2015) 418-440.
- [15] F. Vigier, C. Coutanceau, A. Perrard, E. Belgsir, C. Lamy, J Appl Electrochem, 34 (2004) 439-446.
- [16] T. Almeida, L. Palma, C. Morais, K. Kokoh, A. De Andrade, Journal of The Electrochemical Society, 160 (2013) F965-F971.
- [17] E. Antolini, F. Colmati, E.R. Gonzalez, Electrochemistry Communications, 9 (2007) 398-404.
- [18] Q. He, S. Mukerjee, Electrochimica Acta, 55 (2010) 1709-1719.

- [19] C. Lamy, S. Rousseau, E. Belgsir, C. Coutanceau, J.-M. Léger, *Electrochimica Acta*, 49 (2004) 3901-3908.
- [20] E. Antolini, E.R. Gonzalez, *Catalysis Today*, 160 (2011) 28-38.
- [21] S. Liao, K.-A. Holmes, H. Tsaprailis, V.I. Birss, *Journal of the American Chemical Society*, 128 (2006) 3504-3505.
- [22] C.W. Bezerra, L. Zhang, H. Liu, K. Lee, A.L. Marques, E.P. Marques, H. Wang, J. Zhang, *Journal of Power Sources*, 173 (2007) 891-908.
- [23] J.A. Wittkopf, J. Zheng, Y. Yan, *Acs Catalysis*, 4 (2014) 3145-3151.
- [24] B.C. Beard, P.N. Ross, *Journal of the Electrochemical Society*, 137 (1990) 3368-3374.
- [25] K.H. Kangasniemi, D. Condit, T. Jarvi, *Journal of The Electrochemical Society*, 151 (2004) E125-E132.
- [26] O.A. Baturina, S.R. Aubuchon, K.J. Wynne, *Chemistry of Materials*, 18 (2006) 1498-1504.
- [27] E. Stobbe, B. De Boer, J. Geus, *Catalysis Today*, 47 (1999) 161-167.
- [28] A. Shukla, M. Neergat, P. Bera, V. Jayaram, M. Hegde, *Journal of Electroanalytical Chemistry*, 504 (2001) 111-119.
- [29] A. Arico, A. Shukla, H. Kim, S. Park, M. Min, V. Antonucci, *Applied Surface Science*, 172 (2001) 33-40.
- [30] Y. Ma, H. Wang, S. Ji, V. Linkov, R. Wang, *Journal of Power Sources*, 247 (2014) 142-150.
- [31] J. Zeng, J.Y. Lee, *Journal of power Sources*, 140 (2005) 268-273.
- [32] Z.Q. Tian, S.P. Jiang, Y.M. Liang, P.K. Shen, *The Journal of Physical Chemistry B*, 110 (2006) 5343-5350.
- [33] M.C. Biesinger, B.P. Payne, A.P. Grosvenor, L.W. Lau, A.R. Gerson, R.S.C. Smart, *Applied Surface Science*, 257 (2011) 2717-2730.
- [34] R. Iwanowski, M. Heinonen, W. Paszkowicz, R. Minikaev, T. Story, B. Witkowska, *Applied surface science*, 252 (2006) 3632-3641.
- [35] H. Nesbitt, D. Banerjee, *American Mineralogist*, 83 (1998) 305-315.
- [36] Q.-H. Wu, M. Liu, W. Jaegermann, *Materials Letters*, 59 (2005) 1980-1983.

- [37] A.A. Mirzaei, H.R. Shaterian, M. Kaykhaii, Applied surface science, 239 (2005) 246-254.
- [38] M. Ammam, E.B. Easton, Journal of Power Sources, 222 (2013) 79-87.
- [39] J.E. Harlow, D.A. Stevens, R.J. Sanderson, G.C.-K. Liu, L.B. Lohstroter, G.D. Vernstrom, R.T. Atanasoski, M.K. Debe, J.R. Dahn, Journal of The Electrochemical Society, 159 (2012) B670-B676.
- [40] M. Watanabe, K. Tsurumi, T. Mizukami, T. Nakamura, P. Stonehart, Journal of The Electrochemical Society, 141 (1994) 2659-2668.
- [41] A. Shukla, M. Ravikumar, A. Roy, S. Barman, D. Sarma, A. Arico, V. Antonucci, L. Pino, N. Giordano, Journal of the electrochemical society, 141 (1994) 1517-1522.
- [42] W.P. Zhou, A. Lewera, R. Larsen, R.I. Masel, P.S. Bagus, A. Wieckowski, The Journal of Physical Chemistry B, 110 (2006) 13393-13398.
- [43] R.J. Isaifan, S. Ntais, E.A. Baranova, Applied Catalysis A: General, 464 (2013) 87-94.
- [44] K.-W. Park, J.-H. Choi, Y.-E. Sung, The Journal of Physical Chemistry B, 107 (2003) 5851-5856.
- [45] E. Antolini, Journal of Materials Science, 38 (2003) 2995-3005.
- [46] D.A. Stevens, R. Mehrotra, R.J. Sanderson, G.D. Vernstrom, R.T. Atanasoski, M.K. Debe, J.R. Dahn, Journal of The Electrochemical Society, 158 (2011) B905-B909.
- [47] C. Chen, Y. Kang, Z. Huo, Z. Zhu, W. Huang, H.L. Xin, J.D. Snyder, D. Li, J.A. Herron, M. Mavrikakis, M. Chi, K.L. More, Y. Li, N.M. Markovic, G.A. Somorjai, P. Yang, V.R. Stamenkovic, Science, 343 (2014) 1339-1343.

Chapter 4: Improving the Ethanol Oxidation Activity of Pt-Mn Alloys through the Use of Additives During Deposition

Part of the work described in this chapter has been published as:

M.R. Zamanzad Ghavidel, E.B. Easton, *Catalysts*, 5 (2015) 1016-1033.

In chapter 3, it has been shown that the heat treatment improves the activity of the Pt-Mn samples produced by the impregnation method although the catalysts are suffering undesirable particle size enhancement due to the particle agglomeration. Unfortunately, controlling particle dispersion is one of the major challenges in the impregnation method. Therefore, the main goal of this chapter is to improve particle dispersion and eliminate agglomeration as much as possible to reduce the particle size growth.

4.1 Introduction

Problems associated with the costs and efficiency of fuel cells are a great barrier for industrial and consumer applications [1-4]. Direct alcohol fuel cells (DAFCs) are one of the most promising candidates for portable power applications in electronic devices and vehicles [4]. The cost and performance of the DAFCs are mainly controlled by the catalysts used at each electrode. Pt is the most commonly utilized electrocatalyst, which is quite expensive [3]. Furthermore, strongly adsorbing species such as CO which are formed during the alcohol oxidation process on pure Pt particles, result in severe activity and efficiency losses [4, 5]. The development of Pt alloy catalysts offers the potential of greater tolerance to poisoning and significant cost reduction. Likewise, decreasing Pt alloy particle sizes and improving particle dispersion can further increase performance [3], although there is some debate about the effects of particle size on catalytic activity [6, 7].

The Pt-Mn alloy system has recently been identified by our group as having enhanced activity towards the ethanol oxidation reaction (EOR)[4, 8, 9]^{8,9}. Alloy formation was confirmed with X-ray powder diffraction (XRD) analysis, and the most active alloys contained less than 25 at% Pt, which is beneficial from a cost standpoint. The results

showed that the presence of Mn affects both particle size and the intrinsic activity of the catalysts. Further study by the authors also showed that post-heat treatment had a great impact on the activity of the Pt-Mn alloys, and the main reason for enhancing the EOR activity was the formation of Pt-Mn intermetallic phase [10]. However, particle size growth during heat treatment was an unwanted consequence of heat treatment. Sintering can happen by the migration and coalescence of the catalyst particles or by evaporation and condensation of the atoms from small crystallites[11]. While the benefits of thermally treating alloy nanoparticles out-weighed any activity losses that may occur due to particle size growth, it would be desirable to find a way to produce smaller particles with better dispersion that are resistant to particle growth during heat treatment.

Common strategies used to deposit small and well-dispersed metal nanoparticles on carbon include functionalization of the support [12, 13], using the polyol [14] or microemulsion [15, 16] deposition methods and employing surfactants [17, 18], which are significant strategies to improve particle dispersion and to reduce particle sizes. It has been shown that oxygenated surface groups on the carbon support can enhance the dispersion and the stability of Pt/C catalysts [11]. However, oxygen containing groups can be reduced during the reduction step, which can result in the redistribution of platinum particles and less favorable Pt dispersion [11]. Studies have shown that nitrogen functionalization on carbon can improve cathode performance [11, 19]^{11,19}. While Dinotto and Negro [20, 21] have produced some carbon nitride-based electrocatalysts at lower temperatures, nitrogen groups are more commonly introduced via high temperature processes that can also alter the porosity and microstructure of the support [11]. Unfortunately, the efforts in our group to produce Pt-Mn alloys from polyol and microemulsion methods were not successful

because of very negative reduction potential for Mn ions in these solutions, which prevented Mn co-deposition [22].

Several studies [17, 18, 23, 24] have shown that adding surfactants reduces the particle sizes of Pt and Pt alloys nanoparticles and also improves their dispersion on the support [25]. Sodium citrate (SC) is a common surfactant used in both aqueous and organic solutions by numerous researchers to produce Pt [18]¹⁸, Pt-Au [26], PtRuIr [27] and Pt-Co [28] nano-particles that were small (2–6 nm) with a narrow size distribution. However, to the best of our knowledge, SC has not been used to prepare Pt-Mn alloys .

In this chapter, the effect of sodium citrate on particle size, dispersion, structure and EOR activity of Pt-Mn was investigated. In addition, the influence of solution pH and heat treatment on the crystalline structure, the uniformity of alloyed phases and the activity of the catalysts has been examined.

4.2 Experimental Section

4.2.1 Catalyst Synthesis

The impregnation method was used to prepare Pt-Mn/C catalysts with a composition of Pt_{0.25}Mn_{0.75}, similar to that previously published [4]. The metal precursors were H₂PtCl₆·H₂O (Aldrich, Oakville, Canada) and MnCl₂·4H₂O (Aldrich, Oakville, Canada). Trisodium citrate (SC) (Fisher Scientific, Nepean, Canada) and Vulcan XC72R carbon black (Cabot Corp., Billerica, USA) were used as an additive and metal support, respectively. The total metal loading was kept constant at ~20 wt% for all samples. The SC was added in a weight ratio of 1:1, 2:1 and 3:1 to the metal ratios, which are represented in this chapter by 1X, 2X and 3X, respectively. The pH of the solution was adjusted using a

HCl solution (15 v/v %) and/or a 1 M NaOH solution. NaBH₄ powder was used as the reduction agent. The weight ratio of NaBH₄ to the metal content was 3:1. In addition, a control sample of 20 wt% Pt/C was synthesized with the same method without SC, which was referred to as Pt/C_{in-house}. The powders were collected by suction filtration, washed with isopropanol alcohol (IPA), acetone and deionized water and, finally, dried in an oven at 80 °C overnight.

Heat treatment was performed in a nitrogen atmosphere at either 500, 700, 875 or 950 °C in a Barnstead Thermolyne tube furnace with a quartz tube. The period of heat treatment was kept constant (1 h) for all samples and temperatures, unless otherwise specified. After the heat treatment, the samples were cooled down under a constant flow of nitrogen gas and were preserved inside the furnace until room temperature was reached.

4.2.2 Materials Characterization

The chemical composition of the Pt-Mn samples was examined by inductively-coupled plasma optical emission spectroscopy (ICP-OES, Varian Vista-MPX, Mississauga, Canada). Aqua Regia solution was used to dissolve metal powders, and diluted solutions were consumed for ICP-OES analyses. ICP-OES instrument was calibrated by four standard solutions of Pt and Mn with concentrations of 1, 5, 10 and 20 ppm.

The carbon/metal weight ratio and the temperature of phase changes were determined by thermogravimetric analysis (TGA) and differential scanning calorimetry (DSC). Thermal analysis was performed using a TA Instruments Q600 SDT system (TA Instruments, New Castle, USA). Measurements were made in both argon and air atmospheres, using a heating ramp of 5 °C/min and 20 °C/min, respectively.

Powder X-ray diffraction (XRD) patterns were obtained for each catalyst. Measurements were made using either a Bruker D8 Advance powder X-ray diffractometer (Bruker, East Milton, Canada) equipped with a germanium monochromator (provided by Bruker) or a Rigaku Ultima IV X-ray diffractometer (Rigaku, Toronto, Canada) equipped with a graphite monochromator (provided by Rigaku). Both instruments employ a Cu K_{α1} X-ray source. The XRD analysis by the Bruker D8 Advance powder X-ray diffractometer was performed by the lab specialist at McMaster University but the Rigaku Ultima IV X-ray diffractometer was located at UOIT.

A Philips CM 10 instrument equipped with an AMT digital camera system was used for transmission electron microscopy (TEM) (Philips, Andover, USA) analysis. Samples for TEM analysis were dispersed in a mixture of water and isopropanol and applied to nickel 400 mesh reinforced grids coated by carbon and allowed to dry under air before being introduced into the chamber. The TEM images were obtained by the lab specialist at the University of Western Ontario. The mean particle sizes were determined by measuring the diameter of 100–200 metal particles.

4.2.3 Electrochemical Characterization

The electrochemical activity of the samples was studied after applying a thin layer of catalyst on glassy carbon (GC) electrodes. The ink of samples was produced by mixing 10 mg of catalyst with 100 μL Nafion solution (5% in alcohols, Dupont) and a 400 μL 50:50 mixture of isopropyl alcohol and water. A uniform suspension was achieved after sonicating for 45 min. A 2-μL droplet of the well-dispersed catalyst ink was deposited onto a clean and polished GC electrode (diameter = 3 mm, CH instruments) and dried in air at

room temperature prior to electrochemical tests. The total metal loading of the catalyst layer was 0.11 mg/cm². Cyclic voltammetry (CV) and linear sweep voltammetry (LSV) were performed in a N₂-purged solution. A 0.5 M H₂SO₄ solution was used to determine the electrochemical active surface area (ESCA). A 0.5 M H₂SO₄ + 0.1 M ethanol solution was employed to study the EOR activity of the catalysts. Measurements were made in a 3-electrode cell with a Pt wire counter electrode and a Ag/AgCl reference electrode. The LSV and CV for all samples were collected at a scan rate of 20 mV/s. Besides, the sample surfaces were cleaned prior to recording the final electrochemical test, by scanning at a scan rate of 100 mV/s and then at the scan rate of 20 mV/s, until we got a clean and reproducible CV.

4.3 Results and Discussion

4.3.1 Preliminary studies and pH effects

Citric acid is a polyprotic acid, with pKa values of 3.14, 4.76 and 6.40 for each acid site. As such, the charge on SC will be influenced by solution pH, which can influence both Mn and Pt deposition, as well as the resulting particle sizes. Figure 4.1 shows that increasing the pH of the impregnation solution above three resulted in the metal loading decreasing from 20.1 down to 16.1 wt%. As a consequence, the electrochemical activity of the sample was reduced, and different trends were seen from sample to sample at higher pHs. Moreover, a lower combustion temperature was observed for samples produced at higher pHs, which indicates that the particle sizes were reduced, although the EOR activity was lower. The ethanol oxidation reaction (EOR) activity of the samples showed a behavior similar to pure Pt. We believe that at higher pHs, there is a stronger interaction between the

citrate ions and Mn²⁺ ions in the precursor solution, which hinders their deposition. Therefore, a different behavior was observed for these samples, and as a result, in this chapter, all of the samples have been produced at pH 3.

4.3.2 Material Characterization

Table 4.1 contains the post-chemical reduction composition of the Pt-Mn catalyst samples and the residual solutions, which were determined by inductively-coupled plasma optical emission spectroscopy (ICP-OES). Catalysts were prepared using SC to metal weight ratios of 1:1, 2:1 and 3:1, which are hereafter referred to as 1X, 2X and 3X, respectively. These results showed that the Pt-Mn alloys were produced with a molar ratio close to the calculated values. By adding SC, a small increase in the amount of metal ions in the residual solution was observed, especially the Pt content.

Table 4.1. Composition of the samples and concentration of Pt and Mn in filtrated solution, which was measured by ICP, along with grain size measured by TEM.

Samples	Alloy molar ratios measured by ICP		Ions concentration in filtered solution by ICP		Grain size measured by TEM (nm)
	Pt (%)	Mn (%)	Pt (ppm)	Mn (ppm)	
Pt_{0.25}Mn_{0.75}	22.18	77.82	nil	nil	4.5
Pt_{0.25}Mn_{0.75}-1X	20.30	79.70	0.49	nil	2.6
Pt_{0.25}Mn_{0.75}-2X	20.56	79.44	8.23	nil	2.8
Pt_{0.25}Mn_{0.75}-3X	21.94	78.06	11.70	0.20	2.9
Pt_{0.25}Mn_{0.75}-2X-500-1 h	-	-	-	-	5.7
Pt_{0.25}Mn_{0.75}-2X-700-1 h	-	-	-	-	5.8
Pt_{0.25}Mn_{0.75}-2X-875-1 h	-	-	-	-	6.0
Pt_{0.25}Mn_{0.75}-2X-950-1 h	-	-	-	-	6.6

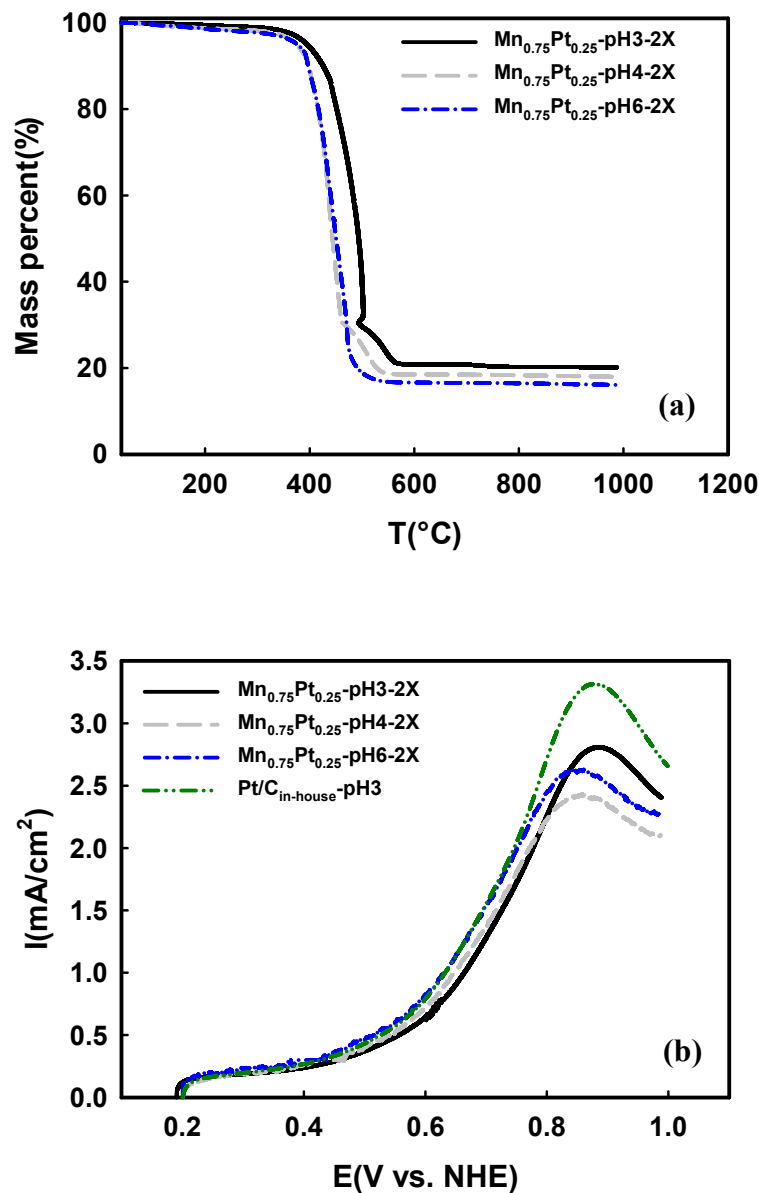


Figure 4.1. (a) TG in air and (b) LSV in the 0.5 M H₂SO₄ + 0.1 M ethanol solution at a scan rate of 20 mV/s for Pt-Mn alloys which were synthesized on Vulcan carbon support in the presence of sodium citrate at different pHs.

The thermogravimetry (TG) and derivative thermogravimetry (DTG) of Pt-Mn alloys, which were synthesized on a Vulcan carbon support in the presence and absence of SC, are shown in Figure 4.2a and b. Five distinctive mass loss regions were observed. The mass loss between 100 °C and 250 °C was attributed to the thermal decomposition of residual, weak carbon functional groups and water evaporation in the powders [7, 29, 30]. A second major mass loss began at 300 °C, which was related to the oxidation of carbon black by the oxygen or the air trapped within the powder particles [30]. The mass loss at 700–800 °C is attributed to the loss of various functionalized groups on the carbon surface and graphitization [29]. The mass loss at 577 and 928 °C, for the sample prepared without additive, and at 460 and 919 °C, for the sample prepared in the presence of SC, was attributed to Mn oxide phase modifications and a reduction in the amount of oxygen [31]. It has been shown that pure MnO₂ is reduced to Mn₂O₃ at 500 °C and further reduced to Mn₃O₄ at 900 °C [30]. The source of mass loss observed at ~1076 °C was not identified. However, from the TG and DTG diagrams of the samples prepared with and without SC, it could be concluded that the temperature required for most of the phase transitions was moved to lower temperatures and facilitated by adding SC.

Figure 4.2b illustrates the DSC curves obtained for Pt-Mn alloys prepared in the presence and absence of SC. Most of the reactions were endothermic, except those related to carbon oxidation at 300–400 °C. The derivative heat flow diagrams from 700–1200 °C showed that the heat flow in the presence of the additive was divided into two separate peaks. The first peak was related to an expected phase transformation from the Pt-Mn phase diagram [32] or Mn oxide phase modifications. The second peak might be attributed to the alloy melting or unknown phase transformation. As catalysts were not prepared at heat treatments above 950 °C, this was not examined in detail. The measured heat follow

between 700 to 1000 °C (3.97 mW/g) for the Pt-Mn alloy prepared without SC was higher than that measured for the sample synthesized by SC (2.89 mW/g). Therefore, adding SC decreased the heat required for the phase transformation and facilitated the alloying process. Based on the DSC results, heat treatment temperatures of 500, 700, 875 and 950 °C were selected to compare the electrochemical and structural changes of Pt-Mn samples prepared with and without SC.

Figure 4.3 shows the TGA curves for the Pt-Mn samples produced in the presence of different SC concentration. The mass lost at around 400 °C was due to carbon combustion. Vulcan carbon ignition occurred around 600 °C. Therefore, the carbon combustion was facilitated in the presence of the metal deposits which have been reported previously [30]. The data calculated from Figure 4.3 are presented in Table 4.2. The results showed that when SC is used, the combustion temperature is reduced by *ca.* 80 °C. This implies that the Pt-alloy particle size was reduced and the particle dispersion was improved. It was previously observed that by increasing Pt loading and available Pt surface area, the combustion temperature of carbon black was decreased because of a higher oxygen and carbon reaction rate [30, 33]. Finally, the residual mass above 600 °C indicated that the metal loading in all samples was close to the expected 20 wt%.

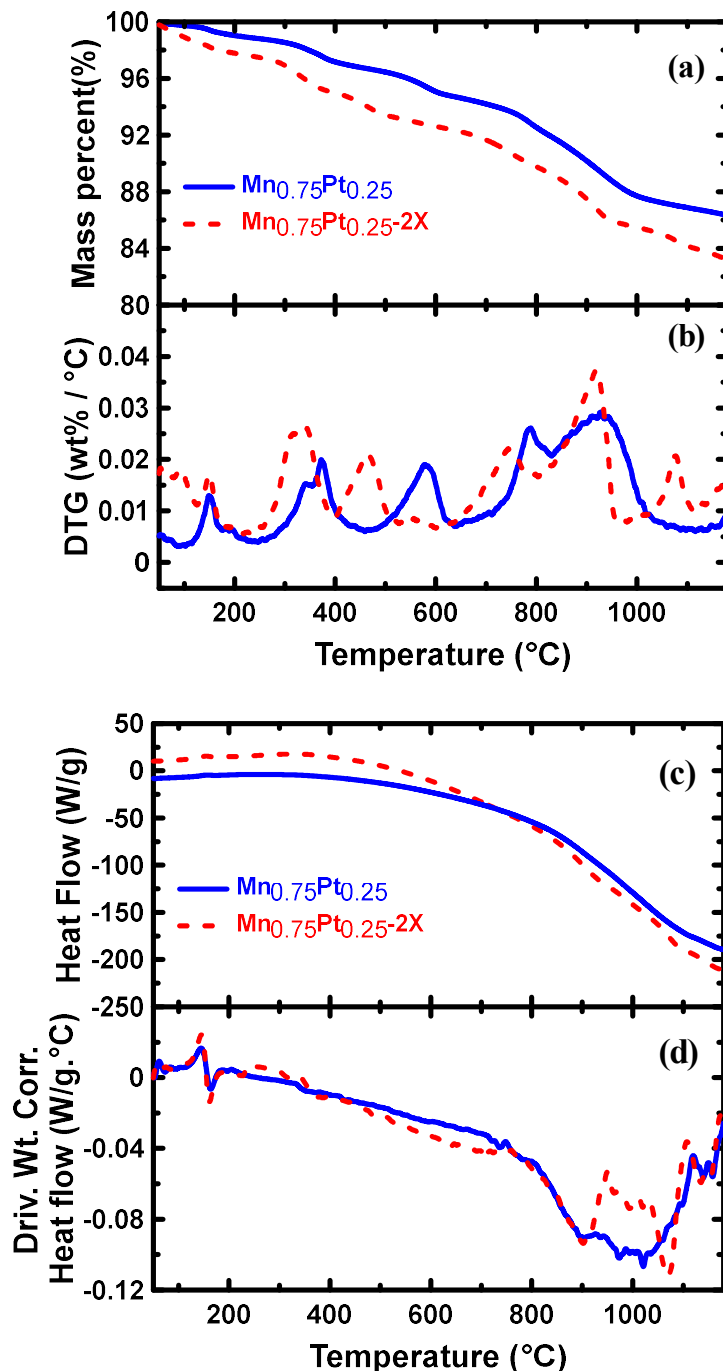


Figure 4.2. (a) TG, (b) DTG, (c) DSC and (d) derivative weight-corrected DSC for Pt-Mn alloys, which were synthesized on Vulcan carbon support in the presence and absence of sodium citrate (The solid line is the $\text{Pt}_{0.75}\text{Mn}_{0.25}$ sample prepared without SC and the dash line is the sample prepared in the presence of SC).

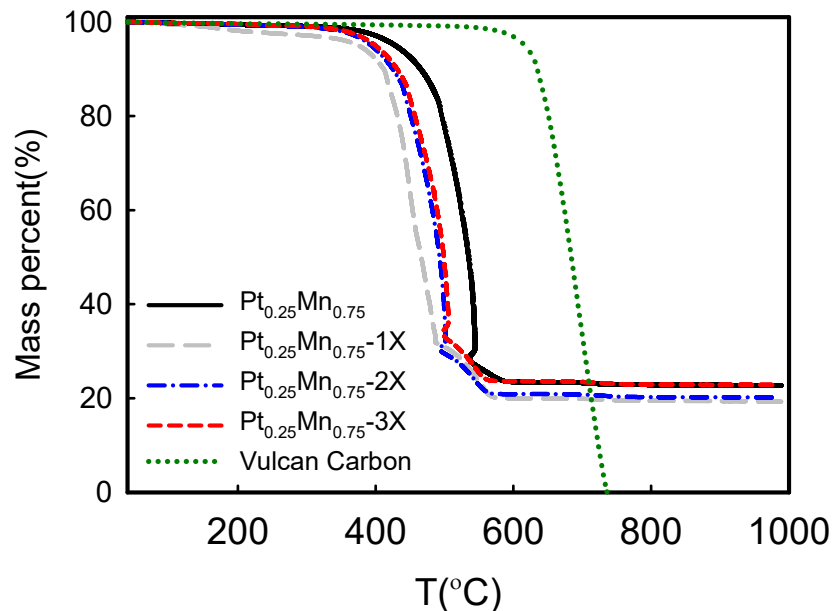


Figure 4.3. The effect of sodium citrate concentration on the weight loss of Pt-Mn alloys, which were synthesized on Vulcan carbon support.

Table 4.2. The metal loading and the Vulcan carbon combustion temperature measured from Figure 4.3.

Samples	Carbon black combustion Temperature (°C)	Metal loading (wt%)
Pt _{0.25} Mn _{0.75}	429.2	22.6
Pt _{0.25} Mn _{0.75} -1X	348.4	19.0
Pt _{0.25} Mn _{0.75} -2X	350.7	20.1
Pt _{0.25} Mn _{0.75} -3X	359.5	22.8
Vulcan carbon	633.4	-

XRD patterns obtained for Pt-Mn alloy catalysts prepared with varying amounts of SC are shown in Figure 4.4. The lattice parameters are listed in Table 4.3. In chapter 3, it has been indicated that as-deposited catalysts contained a mixed structure of Pt-Mn alloys and

non-alloyed phases (the results were published [10]). Broad peaks indicate that alloy particles with small grain sizes were produced. The broadening of the peaks can also be due to the presence of oxide phases and/or non-uniform alloys. The diffractogram displayed the characteristics of the face-centered cubic (fcc) structure of Pt, and the peaks were shifted to higher angles, indicating the incorporation of Mn in the fcc structure. The lattice parameters calculated for the alloyed samples in Table 4.3 indicate that the presence of Mn reduced the lattice parameter of the pure Pt structure (3.923 Å). However, the presence of SC slightly increased the lattice parameter compare to the Pt-Mn samples prepared without SC. Additionally, there is a peak at 36.2°, which is likely related to Mn-rich phases. Moreover, it can be concluded that, by adding SC, the peaks became broader, which was the result of the particle size reduction. Increasing the concentration of sodium citrate up to 2X reduced the amount of oxide phases. However, the oxide phases reappeared after the amount of sodium citrate was increased to 3X. It seems that the optimum amount for the SC concentration is 2X. Therefore, catalysts prepared with a 2X ratio were selected for a more detailed heat-treatment investigation.

The XRD patterns obtained for Pt-Mn catalysts prepared with 2X SC that were heat treated at different temperatures are presented in Figure 4.5. It has been reported in chapter 3, heat treatment has a great impact on the activity and the crystallite structure of the Pt-Mn samples produced without an additive. Here, we have observed similar results for the samples prepared in the presence of SC. The peak at 36.2° associated with the Mn-rich phases in the XRD pattern disappeared after heat treatment at 500 °C for 1h and the intensity of the remaining peaks increased with crystallization. However, the predominant structure was still the Pt face-centered cubic (fcc) structure.

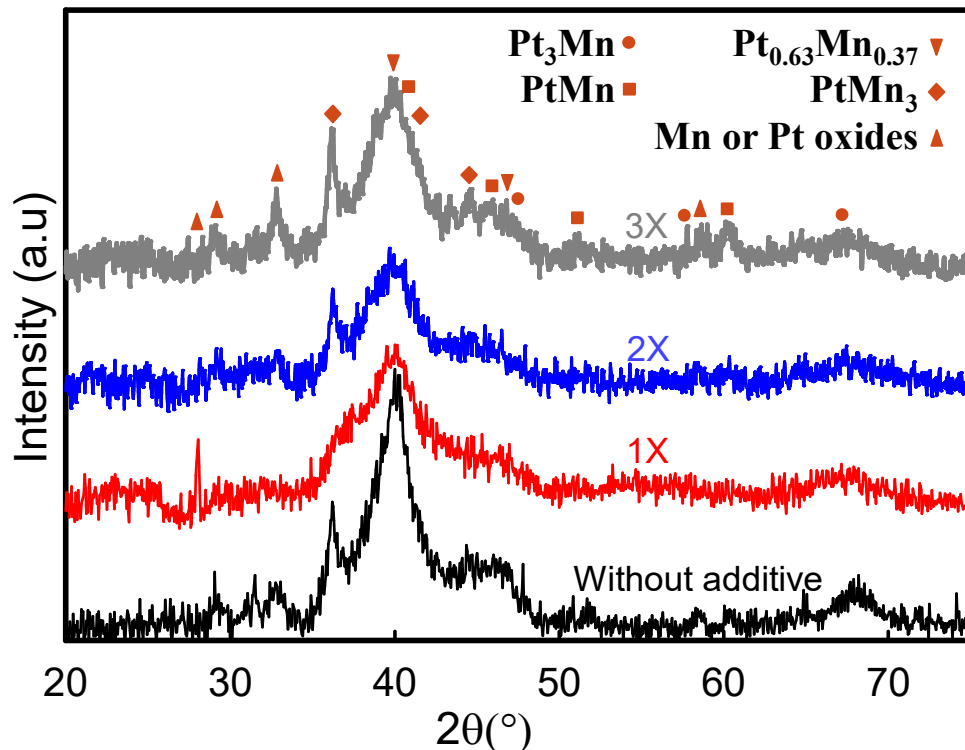


Figure 4.4. XRD analysis of the samples, which were prepared in the presence and absence of sodium citrate.

Upon further increasing the heat treatment temperature to 700 °C, substantial changes were observed. New peaks at lower diffraction angles (22°–40°) indicate that the ordered Pt-Mn intermetallic phase was formed at 700 °C. The Pt-Mn intermetallic phase [10, 34] has a tetragonal structure; therefore, new peaks, (001) and (100), were demonstrated at lower diffraction angles of ~24.1° and ~37.1°, respectively. As a result of Pt and Mn further alloying and intermetallic phase formation, the peak shifts from 39.8° up to 40.2° and 46.5° down to 45.5° were observed when heat treatment temperature increased from 500 up to 700 °C. The shift and the intensity decline of the peaks at 39.8° and 46.5° can be assigned to the completion of phase modifications at 700 °C [10]. In Figure 4.6, the XRD spectra of samples prepared in the presence of SC and heat treated at 700 °C for different periods are

compared. The spectra show that the phase transformation was completed after 1h of heat treatment, and further increasing of the heat treatment time has no effect on the structure of the samples. The optimum heat treatment period for the samples prepared without SC was 4h [10]. Presumably, smaller particle sizes undergo a faster phase transformation, which has also been found by the TGA and DSC analysis. This fast phase transformation is very beneficial, since a shorter treatment time should minimize particle size growth, yielding a higher active surface area and potentially improved electrochemical activity.

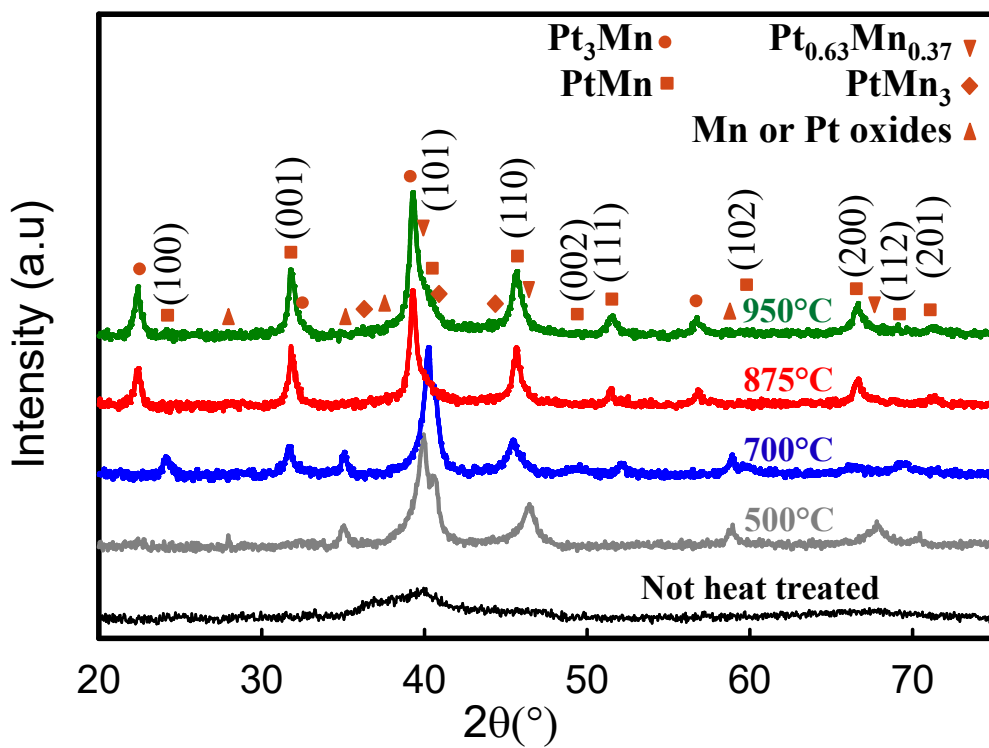


Figure 4.5. The XRD patterns of the sample prepared in the presence 2X SC and after heat treatment at different temperatures.

Table 4.3. Lattice parameters were calculated using Figure 4.4, 4.5 and 4.6.

Crystalline phases	Lattice structure	Space group	Lattice parameters (Å)	
			a	c
Pt _{0.25} Mn _{0.75}	-	fcc	Fm $\bar{3}$ m	3.885
Pt _{0.25} Mn _{0.75} -1X	-	fcc	Fm $\bar{3}$ m	3.904
Pt _{0.25} Mn _{0.75} -2X	-	fcc	Fm $\bar{3}$ m	3.906
Pt _{0.25} Mn _{0.75} -3X	-	fcc	Fm $\bar{3}$ m	3.918
Pt _{0.25} Mn _{0.75} -2X-500-1 h	-	fcc	Fm $\bar{3}$ m	3.905
Pt _{0.25} Mn _{0.75} -2X-700-1 h	PtMn	Tetragonal	P4/mmm	2.831
Pt _{0.25} Mn _{0.75} -2X-875-1 h	Pt ₃ Mn	Cubic	Pm $\bar{3}$ m	3.968
Pt _{0.25} Mn _{0.75} -2X-950-1 h	Pt ₃ Mn	Cubic	Pm $\bar{3}$ m	3.969
Pt _{0.25} Mn _{0.75} -2X-700-2 h	PtMn	Tetragonal	P4/mmm	2.830
Pt _{0.25} Mn _{0.75} -2X-700-4 h	PtMn	Tetragonal	P4/mmm	2.830
				3.700

In Figure 4.5, when the heat treatment temperature increased to 875 °C and 950 °C, additional peaks at 22.4° and 39.4° were observed. This variation in the crystalline structure of the Pt-Mn samples is due to a phase separation and the formation of phases with higher Pt content, such as Pt₃Mn. This phenomenon is also observed for the Pt-Mn samples prepared without SC and reported in chapter 3.

The lattice parameters for the heat treated Pt-Mn alloys were evaluated and recorded in Table 3.2. The results show that the lattice parameters were similar to the standard values reported in ICDD cards (PtMn: a = 2.827 Å, c = 3.669 Å and Pt₃Mn: a = 3.897 Å), especially for the ordered PtMn phase.

TEM images of as-synthesized samples with and without the additive are presented in Figure 4.6. The mean particle sizes measured by using the TEM images are given in Table 4.1. These TEM images showed that the catalysts with nanosized metal particles were synthesized, and adding sodium citrate dramatically decreased the particle sizes and reduced the agglomeration of alloy particles. Correspondingly, the particle dispersion was improved in the presence of sodium citrate. However, increasing the sodium citrate ratio to

3X amplified the agglomeration and deteriorated the particle dispersion. It seems that adding further sodium citrate blocked the particle nucleation sites on the surface of carbon black particles, which directed the metal particle deposition toward the grain boundaries of carbon black particles. Therefore, the metal particle agglomeration was observed in between carbon particles. Furthermore, TEM images once more proved that smaller particle sizes and better particle dispersion in the presence of SC were responsible for facilitating the phase transformation during heat treatment and changing the start temperature of thermally-activated processes, which were observed in the TGA and DSC analyses.

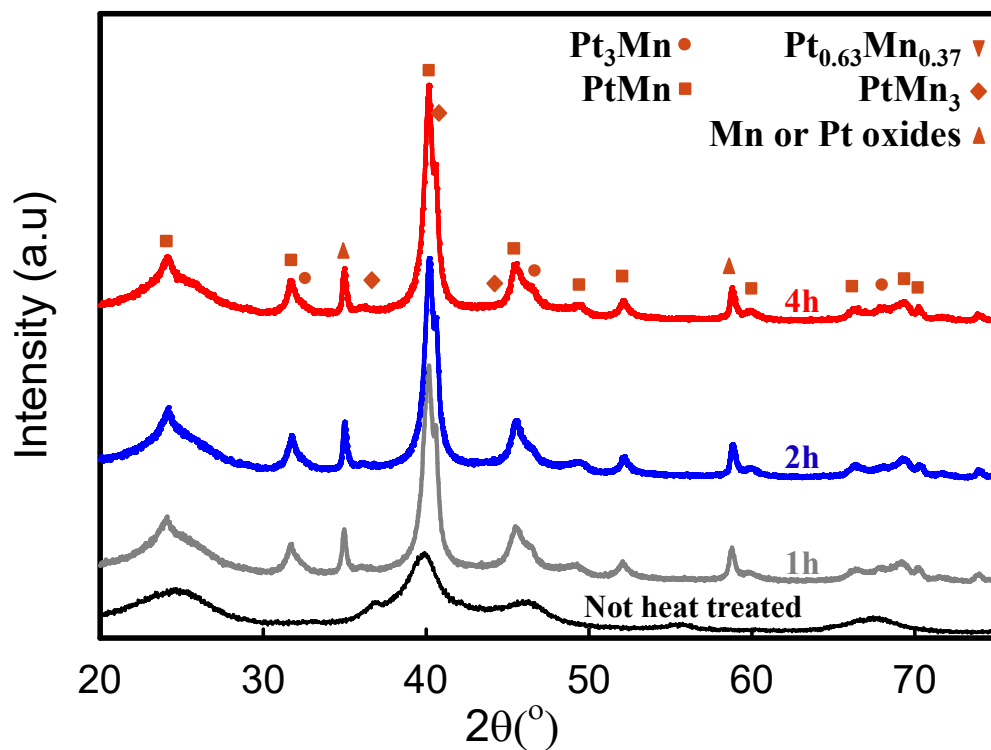


Figure 4.6. The XRD patterns of the sample prepared in the presence of 2X sodium citrate (SC) and after heat treatment at 700 °C for different periods.

Figure 4.8 displays TEM images of samples synthesized in the presence of SC that were heat treated at different temperatures. The particle sizes and details calculated from

the TEM images are summarized in Table 4.1. The heat treatment increased the particle sizes, including some very large particles with a radius of more than 10 nm. However, the average particle size was enlarged by only 3 nm by increasing the heat treatment temperature to 950 °C. This means that Pt-Mn alloys were resistant to particle growth, which has also been observed for other alloys [35] and Pt-Mn samples produced without SC [10]. In Figure 4.9, the TEM images of two samples, which were prepared with and without SC and heat treated for 1h at 700 °C, are compared. It can be concluded that the presence of SC improved the alloy particle dispersion and prevented the particle enlargement to a great extent during heat treatment. Therefore, it is expected that samples prepared with SC should show enhanced activity compared to samples prepared without additives or heat treated for a longer time.

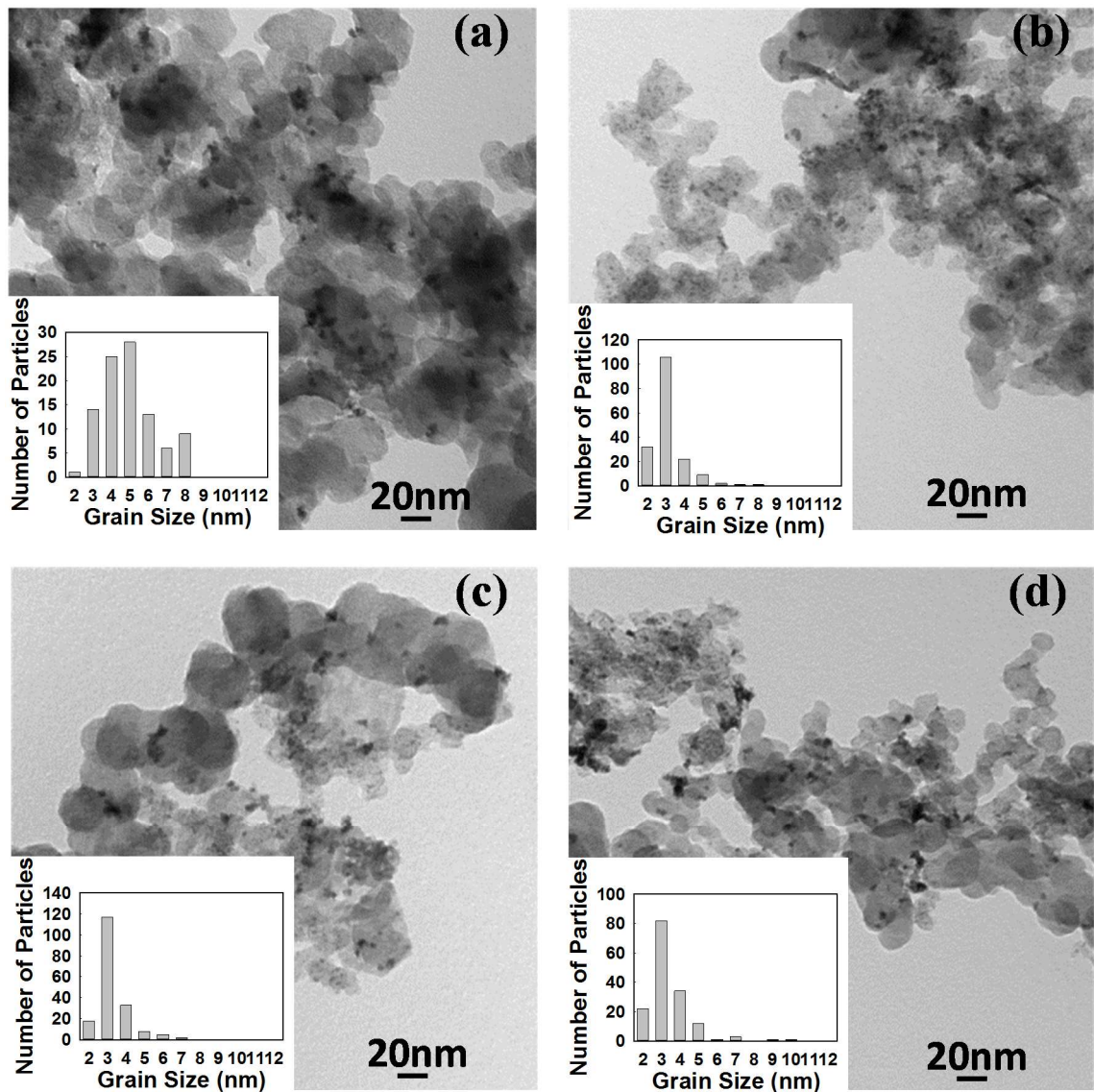


Figure 4.7. TEM image of $\text{Pt}_{0.75}\text{Mn}_{0.25}$ samples prepared in the presence of different contents of sodium citrate: (a) no additive; (b) 1X; (c) 2X; and (d) 3X.

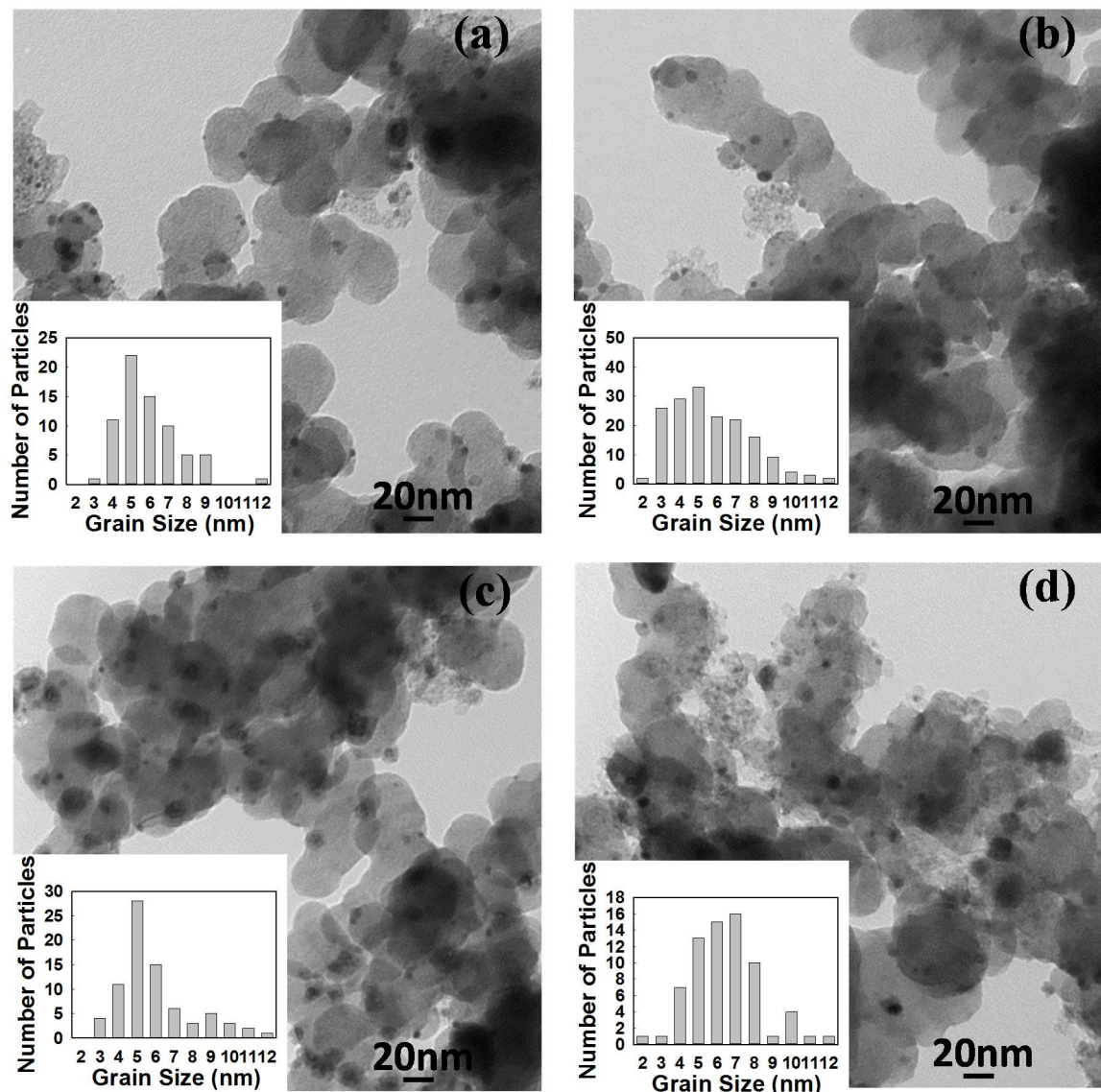


Figure 4.8. TEM image of Pt_{0.75}Mn_{0.25} samples prepared in the presence 2X of sodium citrate and after heat treatment at different temperatures: (a) 500 °C; (b) 700 °C; (c) 875 °C; and (d) 950 °C.

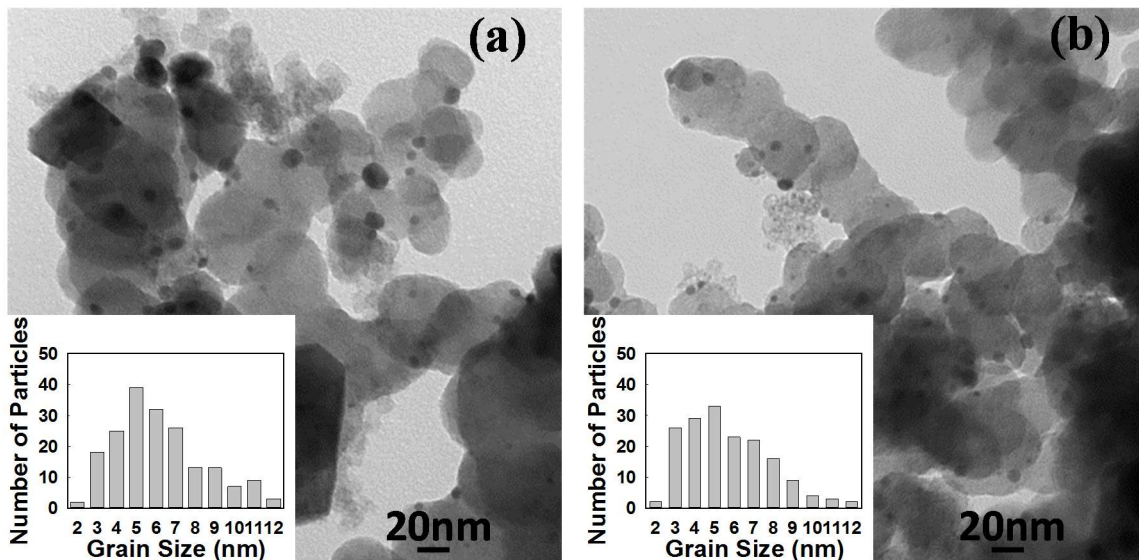


Figure 4.9. TEM images of $\text{Pt}_{0.75}\text{Mn}_{0.25}$ samples prepared (a) without additive and (b) in the presence 2X of sodium citrate and heat treated at 700 °C for 1 h.

4.3.3 Electrochemical Characterization

The results of electrochemical studies for Pt-Mn samples prepared with and without SC are presented in Figure 4.10a. The experiments were conducted in the deaerated 0.5 M H_2SO_4 solution. The common Pt cyclic voltammetry (CV) shape with hydrogen adsorption/desorption peaks at lower potentials was observed for all samples. The electrochemical active surface area (ECSA) was calculated by integrating the charge under the hydrogen adsorption peaks and is compiled in Table 4.4 and Figure 4.11. The results show that the ECSA values were dramatically increased by adding SC from 10.5 - 20.6 $\text{m}^2/\text{g}_{\text{Pt}}$ (Figure 4.11), which is in good agreement with the TEM and XRD results. The ECSA improvement is attributed to the superior particle dispersion and smaller grain sizes in the samples prepared with SC. The maximum ECSA value was achieved with the sample prepared using the 2X SC content. When the amount of SC was increased to 3X, the

measured ECSA was lower than that measured for 2X. Based on the TEM analysis (Figure 5d), this reduced ECSA is the result of uneven particle dispersion on the carbon support.

CV obtained for samples prepared with 2X SC and heat treated at different temperatures is illustrated in Figure 4.10b. Heat treatment at 500 °C reduced the ECSA values for Pt-Mn samples, but the ECSA for the Pt-Mn samples improved after increasing the heat treatment temperature to above 700 °C. The ECSA values never reached the same value as the untreated sample. Particle size growth is the main cause of the drop in ECSA. However, the optimal ECSA was achieved after heat treatment at 700 °C for 1 h and led to an ECSA that was only 7% lower than that of the untreated sample. These results show that Pt-Mn samples prepared with SC are more resistant to particle growth compared to samples prepared without SC. Previously, it has been shown that the formation of the ordered structure and the generation of a higher alloying degree of Pt and Mn by changing the surface composition and structure enhanced the ECSA [10]. This resistance to ECSA loss is most likely due to a roughening of the alloy particle surface upon dissolution of the surface oxide layer and also because of better particle dispersion and smaller grain sizes achieved in the presence of SC [35-39]. Additionally, the CV obtained with samples that were heat treated for different periods is shown in Figure 4.10c. Increasing the time of heat treatment to 4 h at 700 °C reduced the ECSA values (Table 3.1) (not shown in Figure 4.10c). A similar trend was also observed by increasing the heat treatment time at 500 °C.

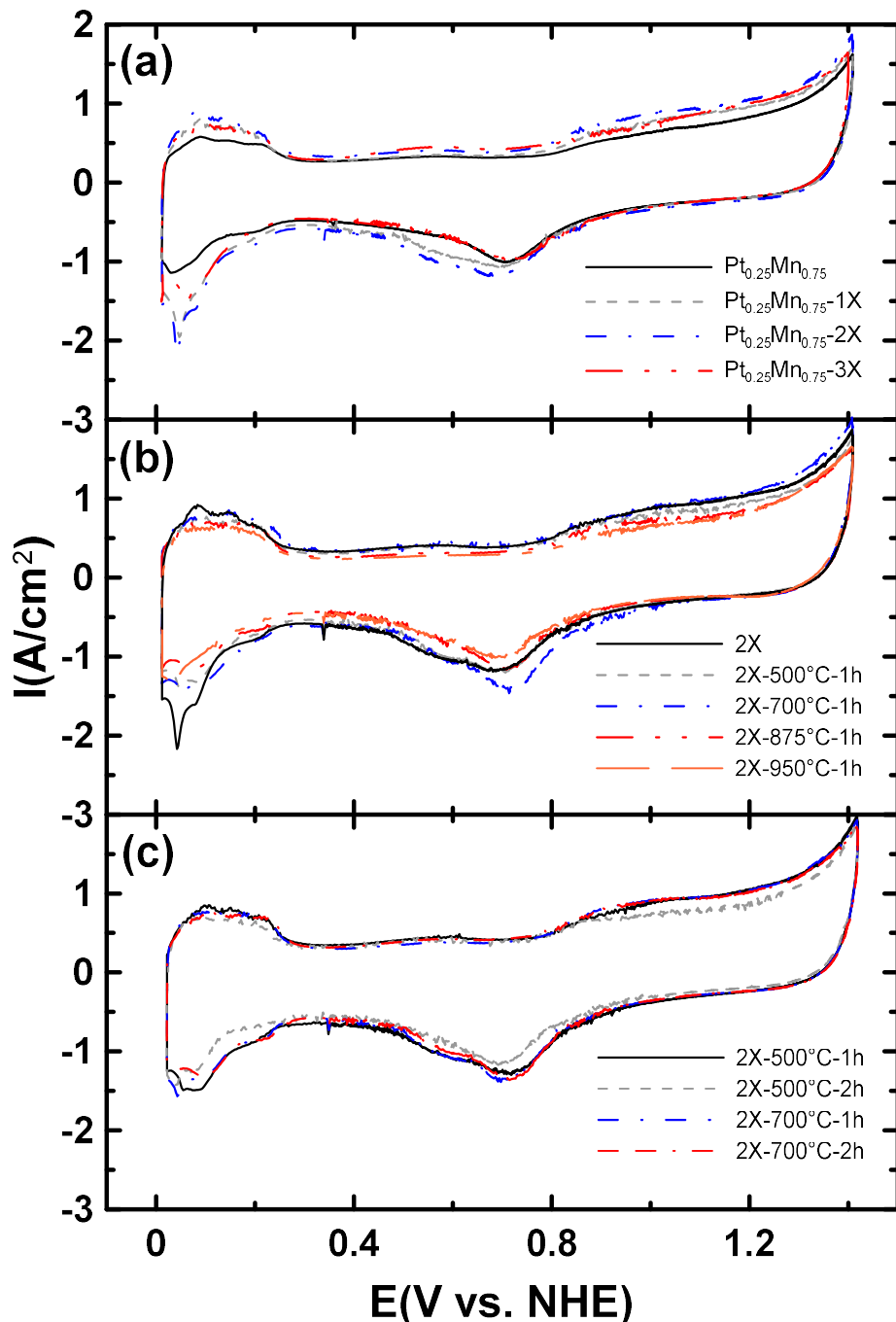


Figure 4.10. Cyclic voltammetry (CV) in the 0.5 M H₂SO₄ solution at a scan rate of 20 mV/s for samples prepared (a) with different sodium citrate contents and then heat treated (b) at different temperatures for 1 h and (c) at 500 and 700 °C for different periods.

Table 4.4. Summary of ethanol oxidation reaction (EOR) activity parameters of the Pt-Mn samples. Also listed are the measured electrochemical active surface area (ECSA) values for each sample.

Samples	Onset potential (mV)	Current (mA.cm ⁻²) at 550 mV	Peak potential (mV)	Peak current (mA.cm ⁻²)	ECSA (m ² /g _{Pt})
Pt _{0.25} Mn _{0.75}	448	0.461	865	2.49	10.5
Pt _{0.25} Mn _{0.75} -1X	447	0.472	878	2.72	16.8
Pt _{0.25} Mn _{0.75} -2X	449	0.489	890	2.81	20.6
Pt _{0.25} Mn _{0.75} -3X	466	0.355	895	2.14	15.7
Pt _{0.25} Mn _{0.75} -2X-500°C-1 h	448	0.880	903	6.49	16.2
Pt _{0.25} Mn _{0.75} -2X-700°C-1 h	440	0.628	910	8.40	19.1
Pt _{0.25} Mn _{0.75} -2X-875°C-1 h	437	0.602	929	4.50	17.1
Pt _{0.25} Mn _{0.75} -2X-950°C-1 h	433	0.638	903	4.76	14.5
Pt _{0.25} Mn _{0.75} -2X-500°C-2 h	445	0.655	862	4.58	13.8
Pt _{0.25} Mn _{0.75} -2X-500°C-4 h	441	0.709	871	3.87	15.4
Pt _{0.25} Mn _{0.75} -2X-700°C-2 h	440	0.588	882	6.30	17.1
Pt _{0.25} Mn _{0.75} -2X-700°C-4 h	441	0.556	898	6.35	15.7

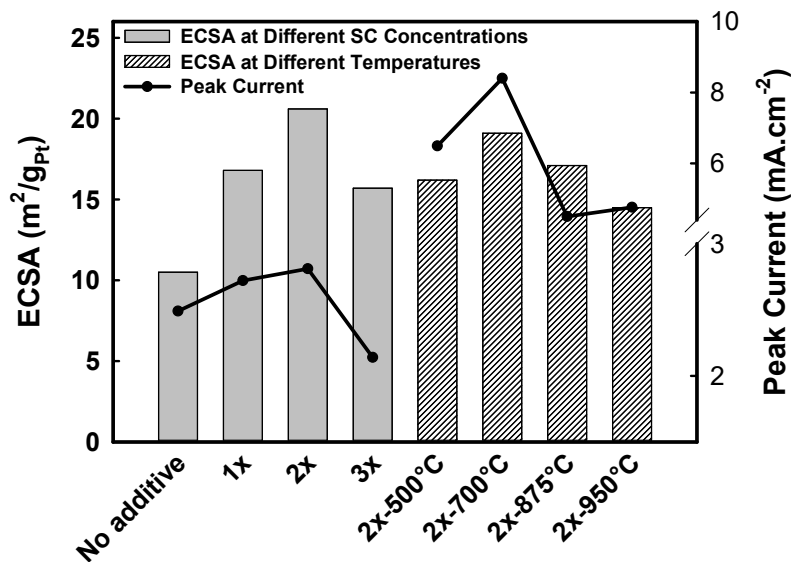


Figure 4.11. ECSA changes at different SC concentrations and after heat treatment at different temperatures, measured from Figure 4.10, and the ethanol oxidation peak current, measured from Figure 11.

The EOR activity of the samples prepared with and without sodium citrate is presented in Figure 4.12a. In addition, Pt/C_{in-house}, which was synthesized without SC, was also tested in ethanol solution. Comparing the electroactivity of the samples (Table 4.4 and Figure 4.11) showed that, by increasing the amount of sodium citrate to the 2X concentration, the activity of the samples was improved. The improvement in activity was a result of the higher ECSA and better particle dispersion, which was concluded from the TEM images and CV analysis in 0.5 M H₂SO₄ solution. However, by increasing the amount of sodium citrate to 3X, the EOR activity was reduced. Based on XRD and TEM results, the lower electrochemical activity of samples prepared with 3X SC was related to the increase in the quantity of the oxide phase and, importantly, to uneven particle dispersion, which resulted in lower ECSA. Furthermore, the linear sweep voltammetry (LSV) in the ethanol solution showed that by adding SC, the onset potential of the samples was almost constant (447–449 mV) up to the optimum ratio (2X), but increased to 466 mV when higher ratios of SC were used.

The EOR activity of the samples after heat treatment is illustrated in Figure 4.12b. After performing the heat treatment at different temperatures, the activity was improved in all samples compared to the as-produced sample. The activity of heat-treated samples is reported in Table 4.4 and compared in Figure 4.11. The most active samples were produced at 700 °C, at which temperature the Pt-Mn ordered phase was formed. Upon increasing the heat treatment temperature to 850 and 950 °C, the EOR activity of the samples was decreased because of particle growth and forming new phases. However, the EOR activity of the heat-treated samples in all temperatures was greater than the untreated sample.

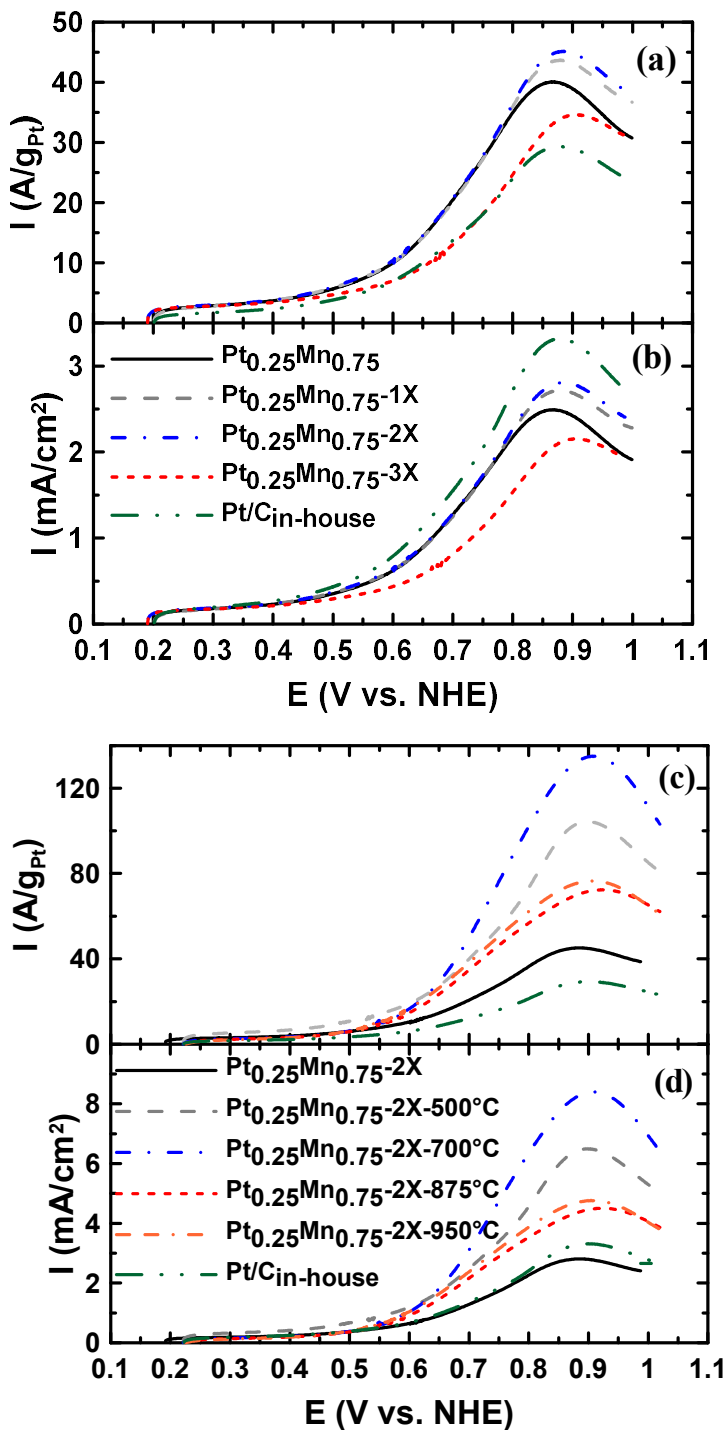


Figure 4.12. Linear sweep voltammetry (LSV) in the 0.5 M H_2SO_4 + 0.1 M ethanol solution at a scan rate of 20 mV/s for: (a) the samples prepared with different sodium citrate contents; (c) the sample produced with 2X sodium citrate content and heat treated at different temperatures. (b) The same as (d), normalized for platinum content of (a) and (d), respectively.

The impact of heat treatment time at 500 °C and 700 °C on the EOR activity is shown in Figure 4.13. At 500 °C and 700 °C, increasing the heat treatment time beyond 1 h had a

negligible impact on the EOR activity, which is in good agreement with the XRD and TGA results. The XRD patterns indicated that phase transformations occurred at 700 °C, and this does not change by increasing the time of heat treatment from 1 h to 4 h (Figure 4.6). Therefore, increasing the time of treatment can only affect the particle sizes, and as shown at 700 °C, the EOR activity slightly reduced by extending the time of the heat treatment.

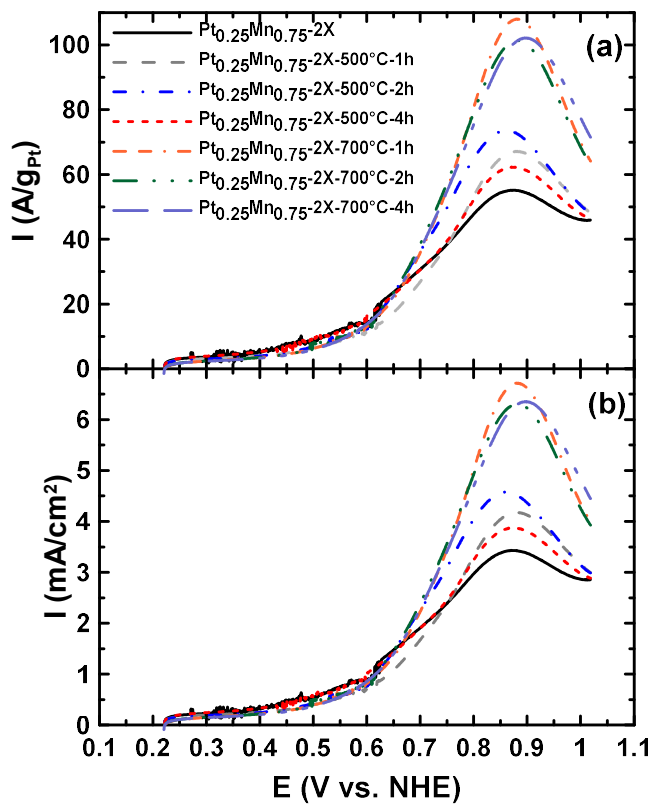


Figure 4.13. LSV of the samples prepared in the presence of sodium citrate and heat treated at 500 and 700 °C for different periods, in the 0.5 M H₂SO₄ + 0.1 M ethanol solution at a scan rate of 20 mV/s.

4.4 Conclusions

In this chapter, it has been shown how the addition of sodium citrate (SC) influences the particle dispersion and grain size of Pt-Mn particles and facilitates the crystalline phase transformation. The results indicated that adding SC to the impregnation solution improved particle dispersion, decreased particle sizes, reduced the heat treatment time from 4 h to 1 h and increased the ECSA. Therefore, the EOR activity of the Pt-Mn alloy catalysts was enhanced. However, the weight ratio of SC to metal loading should be kept lower than 2X, because a higher weight ratio hindered the metal particle dispersion. Furthermore, this investigation proved that the SC had a positive impact on the EOR activity of Pt-Mn alloys when the pH of the impregnation solution was lower than four. Moreover, the heat-treated samples showed superior activity toward ethanol oxidation in comparison with the as-synthesized samples. The EOR activity was the highest for the sample heat treated at 700 °C for 1 h. The XRD analysis illustrated that Pt-Mn intermetallic was formed at the same temperature, and this was the main reason for the superior activity.

4.5 Reference

- [1] E. Antolini, Materials Chemistry and Physics, 78 (2003) 563-573.
- [2] W. Vielstich, A. Lamm, H.A. Gasteiger, Handbook of Fuel Cells: Fundamental, Technology, and Applications, Wiley, 2003.
- [3] H. Liu, C. Song, L. Zhang, J. Zhang, H. Wang, D.P. Wilkinson, Journal of Power Sources, 155 (2006) 95-110.
- [4] M. Ammam, L.E. Prest, A.D. Pauric, E.B. Easton, Journal of The Electrochemical Society, 159 (2011) B195-B200.
- [5] A.M.C. Luna, G.A. Camara, V.A. Paganin, E.A. Ticianelli, E.R. Gonzalez, Electrochemistry communications, 2 (2000) 222-225.

- [6] O. Cherstiouk, A. Gavrilov, L. Plyasova, I.Y. Molina, G. Tsirlina, E. Savinova, Journal of Solid State Electrochemistry, 12 (2008) 497-509.
- [7] F. Vigier, S. Rousseau, C. Coutanceau, J.-M. Leger, C. Lamy, Top Catal, 40 (2006) 111-121.
- [8] M. Ammam, E.B. Easton, Journal of The Electrochemical Society, 159 (2012) B635-B640.
- [9] M. Ammam, E.B. Easton, Journal of Power Sources, 215 (2012) 188-198.
- [10] M.R. Zamanzad Ghavidel, E.B. Easton, Applied Catalysis B: Environmental, 176–177 (2015) 150-159.
- [11] C.W. Bezerra, L. Zhang, H. Liu, K. Lee, A.L. Marques, E.P. Marques, H. Wang, J. Zhang, Journal of Power Sources, 173 (2007) 891-908.
- [12] P. Antonucci, V. Alderucci, N. Giordano, D. Cocke, H. Kim, J Appl Electrochem, 24 (1994) 58-65.
- [13] K. Lee, J. Zhang, H. Wang, D.P. Wilkinson, J Appl Electrochem, 36 (2006) 507-522.
- [14] Z. Liu, J.Y. Lee, W. Chen, M. Han, L.M. Gan, Langmuir, 20 (2004) 181-187.
- [15] H. Bönnemann, R.M. Richards, European Journal of Inorganic Chemistry, 2001 (2001) 2455-2480.
- [16] L. Xiong, A. Manthiram, Journal of The Electrochemical Society, 152 (2005) A697-A703.
- [17] C. Hui, X. Li, I.-M. Hsing, Electrochimica acta, 51 (2005) 711-719.
- [18] R.B. Moghaddam, P.G. Pickup, Electrochimica Acta, 65 (2012) 210-215.
- [19] J. Tian, F. Wang, Z.Q. Shan, R. Wang, J. Zhang, J Appl Electrochem, 34 (2004) 461-467.
- [20] V. Di Noto, E. Negro, Fuel Cells, 10 (2010) 234-244.
- [21] V. Di Noto, E. Negro, Electrochimica Acta, 55 (2010) 7564-7574.
- [22] E.B. Easton, M.R. Zamanzad Ghavidel, O.R. Reid, M. Ammam, L.E. Prest, in: 223rd ECS Meeting, 2013, pp. 1366.
- [23] X. Wang, I.-M. Hsing, Electrochimica acta, 47 (2002) 2981-2987.
- [24] J. Yang, J.Y. Lee, H.-P. Too, Analytica chimica acta, 571 (2006) 206-210.

- [25] H.A. Gasteiger, S.S. Kocha, B. Sompalli, F.T. Wagner, Applied Catalysis B: Environmental, 56 (2005) 9-35.
- [26] J. Zeng, J. Yang, J.Y. Lee, W. Zhou, The Journal of Physical Chemistry B, 110 (2006) 24606-24611.
- [27] S. Liao, K.-A. Holmes, H. Tsaprailis, V.I. Birss, Journal of the American Chemical Society, 128 (2006) 3504-3505.
- [28] J. Zeng, J.Y. Lee, Journal of power Sources, 140 (2005) 268-273.
- [29] K.H. Kangasniemi, D. Condit, T. Jarvi, Journal of The Electrochemical Society, 151 (2004) E125-E132.
- [30] O.A. Baturina, S.R. Aubuchon, K.J. Wynne, Chemistry of Materials, 18 (2006) 1498-1504.
- [31] E. Stobbe, B. De Boer, J. Geus, Catalysis Today, 47 (1999) 161-167.
- [32] C.-X. Ji, P.F. Ladwig, R.D. Ott, Y. Yang, J.J. Yang, Y.A. Chang, E.S. Linville, J. Gao, B.B. Pant, JOM, 58 (2006) 50-54.
- [33] E.B. Easton, R. Yang, A. Bonakdarpour, J. Dahn, Electrochemical and solid-state letters, 10 (2007) B6-B10.
- [34] T. Ghosh, B.M. Leonard, Q. Zhou, F.J. DiSalvo, Chemistry of Materials, 22 (2010) 2190-2202.
- [35] E. Antolini, Journal of Materials Science, 38 (2003) 2995-3005.
- [36] M. Watanabe, K. Tsurumi, T. Mizukami, T. Nakamura, P. Stonehart, Journal of The Electrochemical Society, 141 (1994) 2659-2668.
- [37] J.E. Harlow, D.A. Stevens, R.J. Sanderson, G.C.-K. Liu, L.B. Lohstroter, G.D. Vernstrom, R.T. Atanasoski, M.K. Debe, J.R. Dahn, Journal of The Electrochemical Society, 159 (2012) B670-B676.
- [38] D.A. Stevens, R. Mehrotra, R.J. Sanderson, G.D. Vernstrom, R.T. Atanasoski, M.K. Debe, J.R. Dahn, Journal of The Electrochemical Society, 158 (2011) B905-B909.
- [39] C. Chen, Y. Kang, Z. Huo, Z. Zhu, W. Huang, H.L. Xin, J.D. Snyder, D. Li, J.A. Herron, M. Mavrikakis, M. Chi, K.L. More, Y. Li, N.M. Markovic, G.A. Somorjai, P. Yang, V.R. Stamenkovic, Science, 343 (2014) 1339-1343.

Chapter 5: The Influence of Synthetic Methods on the Structure and Ethanol Oxidation Activity of Pt- Cu/C Alloys

Part of the work described in this chapter has been submitted to the
Journal of Power Sources

5.1 Introduction

The costs and efficiency of direct alcohol fuel cells (DAFCs) are influenced heavily by the catalysts employed to build a membrane electrode assembly (MEA)[1-4]. Pt is the most commonly used electrocatalyst, which is an expensive metal with limited abundance [5, 6]. Moreover, Pt electrodes are susceptible to poisoning by strongly adsorbed species which are formed during the alcohol oxidation process, resulting in severe activity and efficiency losses [4, 7, 8]. There are three proven ways to improve the activity of Pt-base catalysts and/or prevent poisoning: first, by increasing the accessible surface area of the Pt particles typically, by reducing particle size and improving particle dispersion [4, 8-10]; second, by developing Pt-alloy catalysts by adding co-catalysts such as Ru, Sn, Mo, Mn, Cu or Ni [9, 11-16]; third, by modifying the structure of the Pt or Pt-alloy particles, for instance, by producing Pt shell/alloy-core or Pt shell/alloy multi-core or developing intermetallic Pt-alloys particles [4, 8, 16-18]. Commonly, one or the combination of these techniques have been used to produce Pt-base catalysts. As a result, identifying and choosing the right techniques for the desired application is critical and it also is crucial to optimize the effect of their combinations.

There has been strong interest in the Pt-Cu alloy systems [13, 17-28]. However, most of these studies have focused on the oxygen reduction reaction (ORR) of Pt-Cu alloys [17, 24, 25, 28-32]. Studies have shown that different production methods, such as the impregnation and polyol methods, and subsequent heat treatment and dealloying processes have a great impact on the ORR activity of the Pt-Cu alloys. A core-shell or skin type Pt structures with a core rich in Cu has been reported which can be formed due to heat treatment and diffusion of Pt atoms to the surface of particles or can be caused by dissolution of Cu on the surface [17, 23, 24, 30, 32]. The geometrical shape and morphology

of the Pt-Cu particles is also an important factor [31]. Generally, the high ORR activity of Pt-Cu alloys have attributed to the modification of the electronic properties and/or geometric properties of the surface Pt atoms which reduce the formation of stable Pt oxides and facilitate favorable adsorption of O₂ [17, 23, 24, 31]. Additionally, it has shown that ordered Pt-Cu structures have better retention of copper and higher stability [13, 17]. Further studies have also revealed that the Pt-Cu systems have a promising activity toward the methanol and ethanol electro-oxidation [5, 21, 25-27, 33, 34].

There are far more articles that have studied the Pt-Cu alloys for methanol oxidation reaction (MOR) [5, 19-21, 25] compared to those of the ethanol oxidation reaction (EOR) [26, 27, 33, 34]. Studies have shown that adding Cu to the Pt structure as an alloying element or producing a Pt-Cu core-shell structure was a very effective way to improve the electrochemical activity of the Pt-base catalysts toward the methanol and ethanol oxidation [19, 20, 23, 26, 27, 33, 34]. Although there is still debates on how the alloying element of Cu could improve the Pt-base catalyst activities, past studies on Pt-Cu systems have suggested that a few factors are involved. These factors include the electronic effect on the surface Pt atoms, surface defects and/or changes in Pt–Pt interatomic distance [19, 20, 25]. The crystalline structure modification during the heat treatment or the dealloying process in the course of electrochemical studies, which can alter all these three factors, makes it difficult to identify the main reason for the enhanced EOR and MOR activities.

Previous work from our group has studied the Pt-Cu/C binary alloy and Pt(Cu)/C core-shell system for their ethanol electro-oxidation properties. Our study has shown that both of the Pt-Cu/C alloyed and the Pt-Cu core-shell structure enhanced the activity towards EOR compared to the pure Pt catalysts and reduced the Pt content to 37 at% Pt, which is beneficial from a cost standpoint. The Pt-Cu/C alloyed sample has shown the highest

stability and activity among the synthesized samples [35]. Further studies have also illustrated that presence of Cu as a ternary alloying element have enhanced the activity of the Pt-Mn alloys toward EOR [15]. However, the impregnation method created in a mixture of weakly alloyed samples with a high degree of agglomeration, which makes it difficult to reach a general conclusion on the reason of the EOR enhancement activity of samples [10, 15, 35]. Consequently, to improve EOR activity and investigate Pt-Cu samples, it is essential to prevent agglomeration and increase the alloying degree of Pt and Cu.

In this Chapter, the Pt-Cu/C samples have been produced by three methods: 1) the impregnation, 2) impregnation in the presence of additive and 3) microwave assisted polyol method. Afterward, the effect of these three methods on the particle sizes, dispersion and structure and consequently on EOR activity of Pt-Cu/C have been studied. In addition, the effects of heat treatment on the crystalline structure and the uniformity of Pt-Cu alloy phases were investigated. Finally, this structural modification was correlated with the EOR activity to determine which structures were more favorable for the higher EOR activities.

5.2 Experimental

5.2.1 Catalyst synthesis

The carbon supported Pt-Cu alloys were prepared using three different methods: impregnation, impregnation in the presence of sodium citrate additive and microwave assisted polyol method, which are hereafter referred to as (Pt-Cu/C-IMP), (Pt-Cu/C-SC) and (Pt-Cu/C-POL), respectively. The target composition was of $\text{Pt}_{0.25}\text{Cu}_{0.75}$. This composition was chosen based on recent studies [17, 18, 20, 26, 35]. Metal precursors were $\text{H}_2\text{PtCl}_6 \cdot \text{H}_2\text{O}$ (Aldrich) and $\text{CuCl}_2 \cdot 2\text{H}_2\text{O}$ (Aldrich). Vulcan XC72R carbon black (Cabot

Corp.) was used as the carbon support in all cases. The total metal loading was targeted as ~20 wt% for all samples. The pH of the reaction solution was adjusted using a HCl solution (15 v/v %) and/or a 1 M NaOH solution. For the impregnation method with the additive, the Trisodium Citrate (SC) (Aldrich) was added in a weight ratio of 2:1 to the metal ratios. NaBH₄ powder was used as a reduction agent. The weight ratio of NaBH₄ to the metal content was 3:1. The pH of the solution was adjusted to 3 for both impregnation methods. For the polyol method, the metal precursors and Vulcan carbon were mixed with ethylene glycol (EG) (Aldrich) using a mechanical stirrer. The solution pH was adjusted to pH 9, after which it was sonicated for 45 min to achieve a uniform suspension. The suspension was placed into the household microwave oven (SANYO - 2450 MHz) and heated for 8 min and then left to cool down under continues mechanical stirring. In all the methods, the resulting powder was filtered and washed with isopropanol alcohol (IPA), acetone, and deionized water, and finally dried in an oven at 80 °C overnight.

The selected samples were heat treated in a nitrogen atmosphere at either 500, 700 or 875 °C in a Barnstead Thermolyne tube furnace with a quartz tube. The period of heat treatment was kept constant (1 h) for all the samples and temperatures, unless otherwise specified. After the heat treatment, the samples were cooled down under a constant flow of nitrogen gas and were preserved inside the furnace until room temperature was reached.

5.2.2 Materials characterization

The chemical composition of the Pt-Cu samples was examined by Inductively Coupled Plasma Optical Emission Spectroscopy (ICP-OES). An Aqua Regia solution was used to dissolve the metal powders and diluted solutions were prepared for ICP-OES

analysis. The ICP-OES instrument (Varian Vista-MPX) was calibrated by four standard solutions of Pt and Cu with a concentration of 1, 5, 10 and 20 ppm.

Carbon/metal weight ratio was determined by Thermogravimetric Analysis (TGA). Thermal analysis was performed using a TA Instruments Q600 SDT system. Measurements were made under air atmosphere, using a heating ramp of 20 °C/min.

All the samples were characterized by powder X-ray diffraction (XRD) using a Rigaku Ultima IV X-ray diffractometer equipped with a Cu K_{α1} X-ray source and a graphite monochromator. A Zeiss Libra 200MC Transmission Electron Microscopy (TEM) system operating at 200 kV was used to analyze the morphology and microstructure of the samples. The TEM images was obtained by the lab specialist at the University of Waterloo (WATLab).

5.2.3 Electrochemical characterization

The electrochemical activity of the samples was studied after applying a thin layer of the catalyst on glassy carbon (GC) electrodes. The catalyst inks were produced by mixing 10 mg of the catalyst with 100 µL Nafion solution (5% in alcohols, Dupont) and a 400 µL of a 50:50 mixture of isopropyl alcohol and water. A uniform suspension was achieved after sonicating for 45 minutes. A 2 µL droplet of the well-dispersed catalyst ink was deposited onto a clean and polished GC electrode (diam = 3 mm, CH instruments) and dried in the air at room temperature prior to electrochemical tests. The total metal loading of the catalyst layer was ~0.11 mg/cm². Cyclic voltammetry (CV) and linear sweep voltammetry (LSV) were performed in a N₂-purged solution. A solarton 1470E Multichannel Potentiostat controlled using Multistat software (Scribner Associates) was used for the CV

and LSV measurements. A 0.5 M H₂SO₄ solution was used to determine the electrochemical active surface area (ESCA). A 0.5 M H₂SO₄ + 0.1 M ethanol solution was applied to explore the EOR activity of the catalysts.

5.3 Result and discussion

5.3.1 Materials characterization

5.3.1.1 ICP-OES and TGA analyses

ICP-OES was used to determine the chemical composition of the samples which are shown in Table 5.1. The ICP-OES results indicate that the Pt-Cu alloys were produced with some variation in the composition by each method. The Pt concentration was the highest for the Pt-Cu/C-SC sample. The results illustrate that the presence of SC and EG reduced Cu ion deposition.

Table 5.1. Composition of the samples, metal loading and carbon black combustion Temperature which were measured by ICP and TGA, respectively.

Samples	Alloy molar ratios measured by ICP		Metal Loading wt%	Carbon black combustion Temperature (°C)
	Pt (%)	Cu (%)		
Pt/C _{in-house}	100	0	25.3	449.2
Pt-Cu/C-IMP	28.7	71.3	20.3	443.8
Pt-Cu/C-IMP-700 °C	27.4	72.6	-	-
Pt-Cu/C-POL	36.9	63.1	13.0	409.3
Pt-Cu/C-POL-700 °C	37.2	62.8	-	-
Pt-Cu/C-SC	53.5	46.5	19.9	445.9
Vulcan carbon	-	-	-	633.4

The TGA data collected under air confirm that by using the polyol method, the metal loading was altered (Figure 5.1). The Pt-Cu/C-POL sample had the lowest metal loading (13.0 wt%). The metal loading for the other Pt-Cu samples was close to the expected 20 wt% metal loading. Furthermore, the combustion temperature of Vulcan carbon for different samples are presented in Table 5.1. Vulcan carbon ignition occurs around 600 °C in air [36]. The results in Table 5.1 show that the metal particles facilitated the carbon ignition which have been explained by the higher oxygen and carbon reaction rate [36]. The results show that the combustion temperature was reduced to around 450 °C. The lowest combustion temperature was reached by the Pt-Cu/C-POL sample.

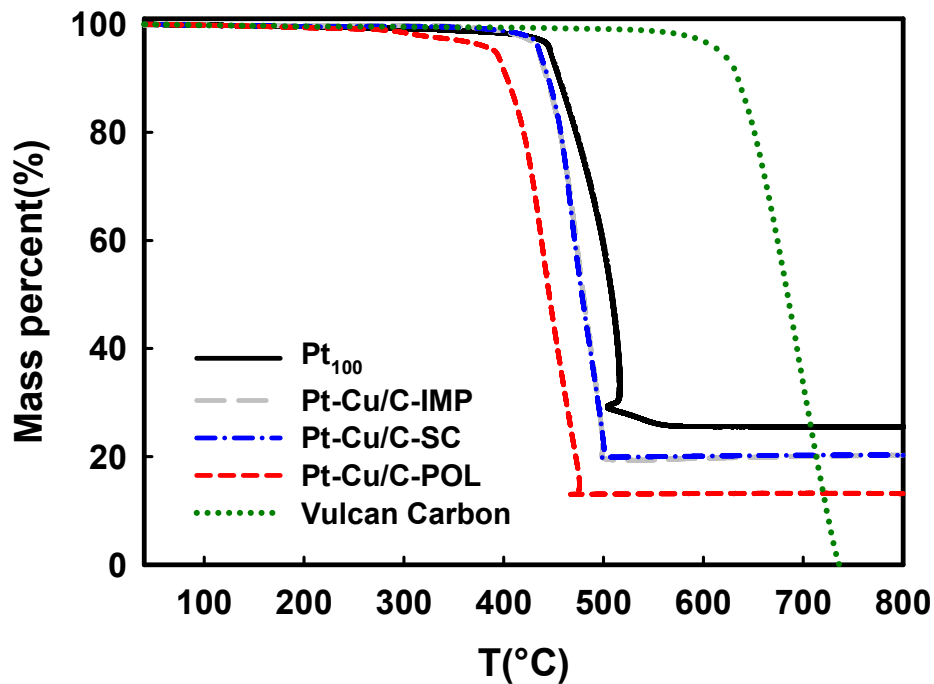


Figure 5.1. The effect of different deposition methods on the weight loss of the Pt-Cu alloys, which were synthesized on Vulcan carbon support.

5.3.1.2 XRD analysis

XRD patterns of the samples prepared by different methods are shown in Figure 5.2 and the expanded XRD patterns at two different ranges are presented in Figure 5.3. The crystalline planes and the alloy phases related to each peak is also assigned in Figure 5.2 and 3. The dash lines in Figure 5.2 show the peak location for the pure Pt with the face centered cubic (fcc) structure. Our previous studies have shown that the as-deposited catalysts likely have a mixture of alloyed and non-alloyed phases [15, 35]. Figure 5.3 shows that the as-produced samples illustrated the fcc structure of Pt and the peaks were shifted to higher angles, indicating the incorporation of Cu in the fcc structure. The highest shift in the peak positions was seen for the Pt-Cu/C-IMP sample which was a sign of the higher Pt-Cu alloying degree. The lattice parameters were determined using the XRD patterns and shown in Table 5.2. The lattice parameter for as-produced alloy samples decreased due to the incorporation of Cu into the Pt fcc lattice and the Pt-Cu/C-IMP sample had the lowest lattice parameter. The broad peaks in Figure 5.2 indicate that the alloy particles with the small grain sizes were produced. The broadening of the peaks can also be due to the presence of oxide phases and/or non-uniform alloys. The presence of peak shoulders and mixed alloy phases for some of the samples makes it difficult to estimate and compare grain sizes accurately based on the XRD results.

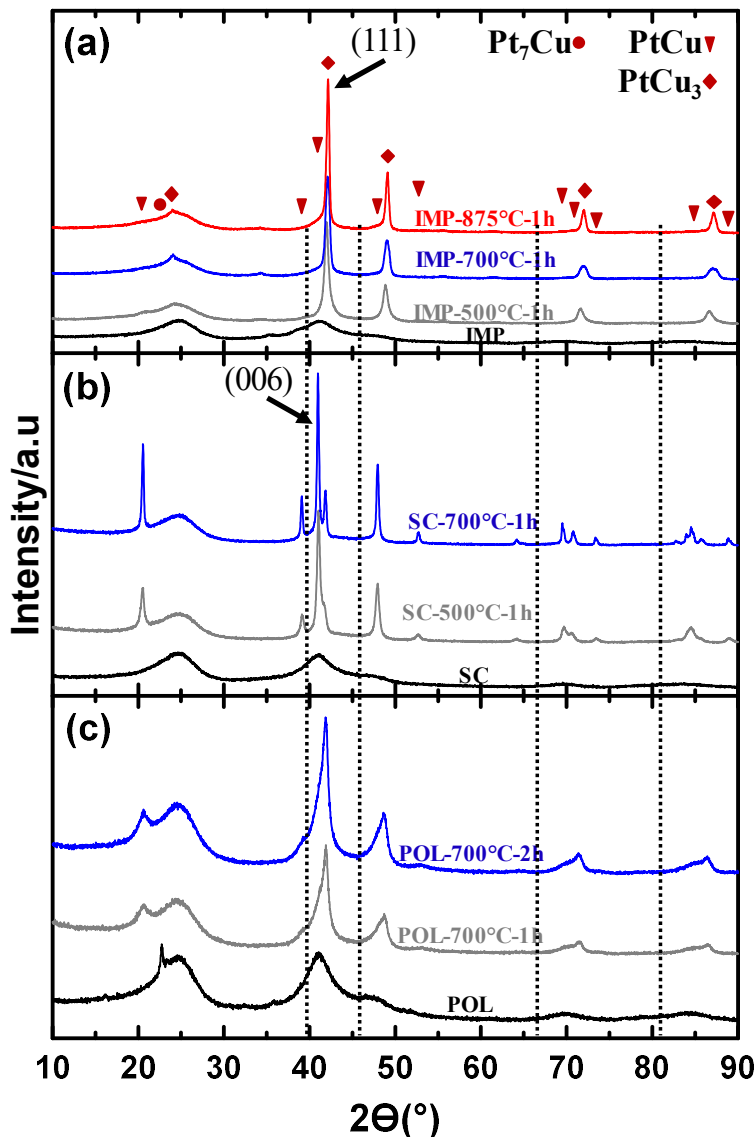


Figure 5.2. The XRD analysis of the Pt-Cu alloys before and after the heat treatment in nitrogen atmosphere for the constant period (1hour) (unless it is specified) at different temperatures for the samples prepared by the (a) impregnation (b) impregnation + SC and (c) polyol methods.

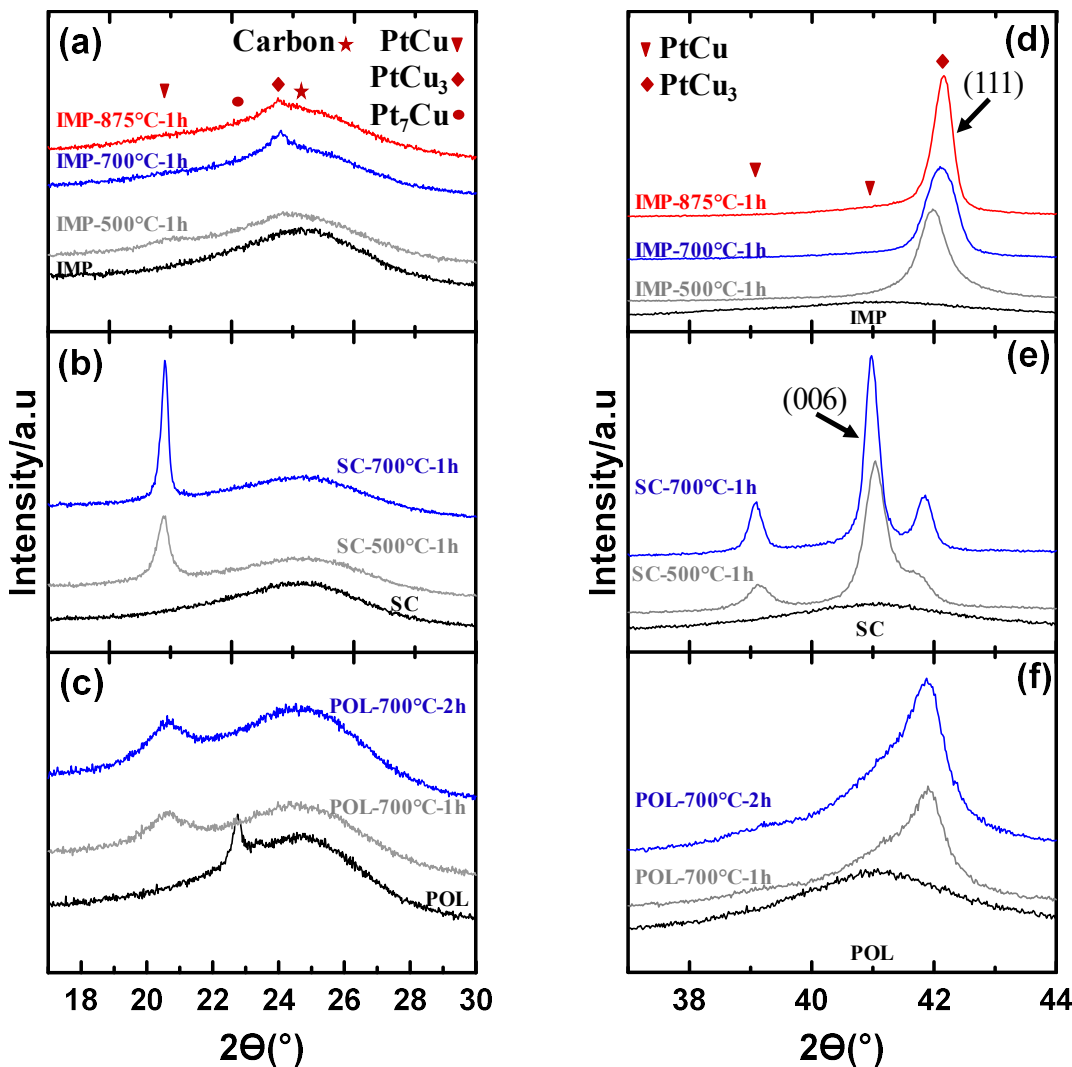


Figure 5.3. The expanded XRD patterns from Figure 5.2 for the Pt-Cu samples prepared by the (a) (d) impregnation (b) (e) impregnation + SC and (c)(f) polyol methods.

Heat treatment at different temperatures changed the crystalline structure of the Pt-Cu alloys. Based on the chemical composition ($Pt_{0.25}Cu_{0.75}$) and the binary phase diagram of the Pt-Cu systems, there is a high probability that PtCu₃ or PtCu ordered phases formed during heat treatment [17, 28]. It is also predictable that each group of samples displays distinctive crystalline structures due to slight changes in the chemical composition,

preparation methods and metal loadings. Figure 5.2 and 5.3 indicate that the heat treatment at different temperatures resulted in sharper peaks with higher intensities. In addition, new peaks were formed at lower diffraction angles. These results confirm that the phase ordering process was occurred by the heat treatment in all three samples. The sharper peaks formed due to crystallization and particle size enhancement. Similar behaviors were also observed in chapter 3 and 4 for the Pt-Mn samples.

Table 5.2. Lattice parameters for Pt-Cu alloy catalysts, calculated from the XRD patterns in Figure 5.2.

	Crystalline phases	Lattice structure	Space group	Lattice parameters (Å)		
				a	b	c
Pt-Cu/C-IMP	-	fcc	Fm $\bar{3}$ m	3.785	-	-
Pt-Cu/C-IMP-500 °C	PtCu ₃	Cubic	Pm $\bar{3}$ m	3.727	-	-
Pt-Cu/C-IMP-700 °C	PtCu ₃	Cubic	Pm $\bar{3}$ m	3.714	-	-
Pt-Cu/C-IMP -875 °C	PtCu ₃	Cubic	Pm $\bar{3}$ m	3.709	-	-
Pt-Cu/C-SC	-	fcc	Fm $\bar{3}$ m	3.814		
Pt-Cu/C-SC-500 °C	PtCu	Trigonal	R $\bar{3}$ m	9.414	9.160	13.194
	PtCu ₃	Cubic	Pm $\bar{3}$ m	3.746	-	-
Pt-Cu/C-SC-700 °C	PtCu	Trigonal	R $\bar{3}$ m	9.446	9.139	13.207
	PtCu ₃	Cubic	Pm $\bar{3}$ m	3.739	-	-
Pt-Cu/C-POL	-	fcc	Fm $\bar{3}$ m	3.806	-	-
Pt-Cu/C-POL-700 °C-1h	PtCu	Trigonal	R $\bar{3}$ m	9.545	9.130	13.098
	PtCu ₃	Cubic	Pm $\bar{3}$ m	3.730	-	-
Pt-Cu/C-POL-700 °C-2h	PtCu	Trigonal	R $\bar{3}$ m	9.552	9.118	13.124
	PtCu ₃	Cubic	Pm $\bar{3}$ m	3.730	-	-

The heat treatment of the Pt-Cu/C-IMP samples at 500 °C for 1h increased the intensity of the peaks and shifted the peaks to higher angles. For instance, the peak at 41.3° shifted to 41.9° (Figure 5.2a). The rise in peak intensity is identified as crystallization and the development of the ordered phases. However, the fcc structure was still predominant for the Pt-Cu/C-IMP sample at 500 °C. Increasing the heat treatment temperature to 700 and 875 °C increased the peak intensities and a new peak was observed at a lower angle

(24.1°) which is an indication of the ordered PtCu₃ formation with a simple cubic structure (Figure 5.3a and d). The peak at 41.9°, which was attributed to the (111) reflection of PtCu₃, was shifted further to 42.1°. Similar shifts were also observed for other peaks associated with PtCu₃. Therefore, by increasing the heat treatment temperature, the alloying process occurred and lead to the formation of the ordered PtCu₃ phase. This process started at 500 °C and completed at 700 °C. The main structure for the Pt-Cu/C-IMP sample after the heat treatment at 700 and 875 °C was PtCu₃.

Increasing the heat treatment temperature for the Pt-Cu/C-SC samples promoted slightly different patterns (Figure 5.2b, 5.3b and 5.3e). New peaks were observed at ~20.5° and ~39.1° after the heat treatment at 500 °C, which indicate that the ordered PtCu trigonal crystalline structure was formed at this temperature [11]. Bragg peaks related to PtCu₃ were also noticeable at this temperature (e. g., the plane (111) at ~41.7°). The ratio of the (006) and (111) plane peak intensities at ~41° and 41.7°, which are correlated to the PtCu and PtCu₃ phases, shows that the PtCu ordered phase was the main component at 500 °C. By increasing the heat treatment temperature to 700 °C, the relative ratios of crystalline phases remained the same.

The as-produced Pt-Cu/C-POL sample contained an additional peak at lower angles (22.7°) (Figure 5.2c, 5.3c and 5.3f). The fcc structure does not have any diffraction peak at this angle. Therefore, this additional peak should belong to one of the ordered Pt-Cu phases or oxide phases. Using the XRD standard patterns, Cu and Pt oxide phases corresponding to this peak were not found. This peak should belong to an ordered phase and the Pt₇Cu type of phase is the closest match in the literature [37, 38]. The Pt₇Cu ordered phase has been shown to form after the heat treatment at temperatures as low as 200 °C [37, 38] which is very close to the boiling temperature of EG (197.3 °C). Consequently, it is

possible that the Pt₇Cu structure formed during the Pt-Cu particles synthesizing process. However, it is very difficult to reach to a solid conclusion because of the peak broadening for as-produced samples. This peak disappeared after heat treatment above 500 °C.

The Pt-Cu/C-POL samples after the heat treatment at 700 °C showed similar but slightly different XRD patterns compared to Pt-Cu/C-IMP samples (Figure 5.2c, 3c and 3f). The intensity of the peaks of the Pt-Cu/C-POL sample at 700 °C were lower and broader than the heat treated Pt-Cu/C-IMP samples. The expanded XRD patterns of peaks from 38°to 45° are shown in Figure 5.3c and f. The XRD patterns analysis indicates that the ordered PtCu phase with the trigonal structure along with the ordered PtCu₃ phase formation was the reason for the broadening of the peaks. The presence of shoulders and mixed alloy phases makes it difficult to estimate grain sizes accurately. However, the lower intensity and broader peak in this sample confirm that particle sizes enlargement were less pronounced. The ratio of PtCu/PtCu₃ phases for the heat treated Pt-Cu/C-POL samples was lower than the heat treated Pt-Cu/C-SC samples. Similarly, the peak intensity of the PtCu₃ phase for the heat treated Pt-Cu/C-POL samples was lower than the heat treated Pt-Cu/C-IMP samples which shows that the quantity of the PtCu₃ phase decreased and more the PtCu phase developed for the heat treated Pt-Cu/C-POL samples. This means that the polyol method and the heat treatment at 700 °C produced samples with a mixed structure consist of the PtCu and PtCu₃ phases. Finally, the XRD patterns show that increasing the time of the heat treatment at 700 °C to 2 h just increased the crystallization and particle sizes but had no effect on the phase structures.

The lattice parameters determined by XRD indicates the formation of the ordered PtCu and PtCu₃ phases. Based on the ICDD cards, the lattice parameters for PtCu phase are as follows: $a = 10.7030 \text{ \AA}$, $b = 10.7030 \text{ \AA}$, $c = 13.1970 \text{ \AA}$ and $\alpha = 90.0^\circ$, $\beta = 90.0^\circ$, $\gamma =$

120.0° and for the PtCu₃ phase are as follows $a = 3.692 \text{ \AA}$ and : $\alpha = \beta = \gamma = 90.0^\circ$. The results in Table 5.2 shows that the calculated lattice parameters were very close to the standard values. However, there were small differences which could be due to the phase separation and variation in the Cu content compared to the standard samples. In addition, increasing time and temperature of the heat treatment reduced the lattice parameters for the PtCu₃ phase which could be due to an increasing in the alloying degree of Cu with Pt.

5.3.1.3 TEM analysis

TEM images of the Pt-Cu/C-IMP, Pt-Cu/C-SC and Pt-Cu/C-POL samples and those heat treated at 700 °C are shown in Figure 5.4. The mean particle sizes were determined using these TEM images and are presented in Table 5.3.

These images illustrate that nano-sized catalyst particles were successfully produced. Comparing the TEM images of Pt-Cu/C-IMP, Pt-Cu/C-SC and Pt-Cu/C-POL reveals that the polyol method was greatly reduced the agglomeration of the Pt-Cu particles. In the presence of SC, the agglomeration was reduced to some extend but still agglomeration of larger particles could be observed and also, there was a variation in the particle distribution from site to site on the carbon particles. In addition, the presence of SC in the impregnation solution promoted the formation of larger particles along with some amorphous deposits which makes it hard to identify and measure particle sizes. The mean particle size measured by the TEM images for the as-produced Pt-Cu/C-IMP, Pt-Cu/C-SC and Pt-Cu/C-POL were 2.5 nm, 3.3 and 2.8 nm, respectively.

Further studies of the TEM images show that the heat treatment resulted in an increase in particle sizes of the Pt-Cu/C-IMP, Pt-Cu/C-SC and Pt-Cu/C-POL samples,

including some very large particles with a diameter of more than 17 nm for the Pt-Cu/C-IMP and Pt-Cu/C-SC samples, and up to 12 nm for the Pt-Cu/C-POL sample. The particle growth was lower for the Pt-Cu/C-POL sample. The highest mean particle size was measured for Pt-Cu/C-SC. It has been shown that agglomeration of particles greatly contributed to the growth of very large particles during heat treatment [16]. The TEM images of the Pt-Cu/C-POL samples before the heat treatment shows that agglomeration has prevented. Therefore, the Pt-Cu particles produced by the polyol method showed higher resistance to the particle enlargement during the heat treatment.

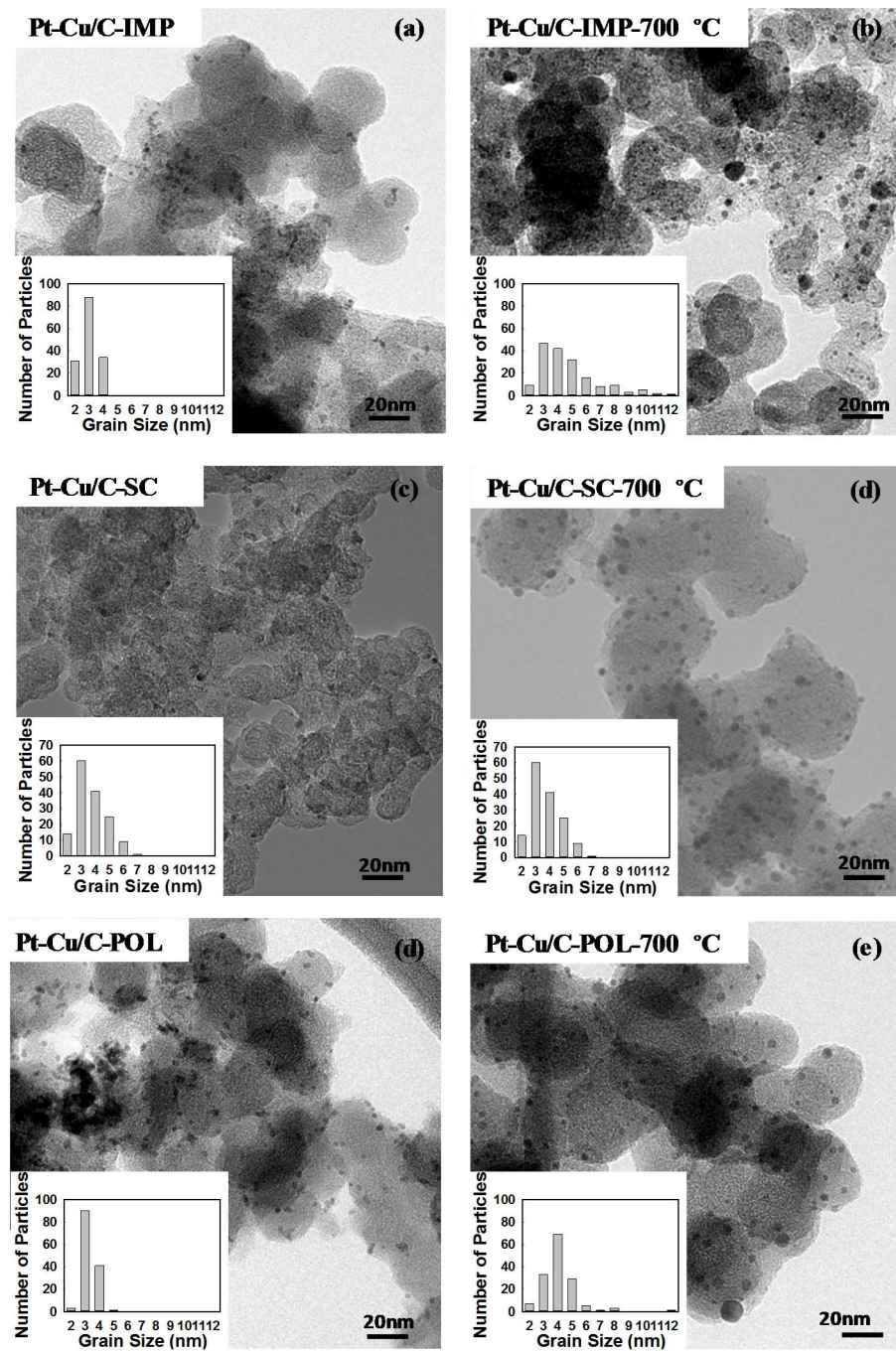


Figure 5.4. TEM images of the Pt-Cu alloys before and after heat treatment in nitrogen atmosphere for constant period (1hour) (a) Pt-Cu alloys prepared by the impregnation method and (b) heat treated at 700 °C, (c) Pt-Cu alloy prepared in presence of SC and (d) heat treated at 700 °C and (e) Pt-Cu alloys prepared by the polyol method and (f) heat treated at 700 °C.

The particle size distribution diagrams (PSD's) of the Pt-Cu samples illustrate that there was a narrow particle distribution for both of the Pt-Cu/C-IMP and Pt-Cu/C-POL samples before the heat treatment (Figure 5.4). PSD's also show that the heat treatment caused to form particles with a broader range of particle sizes. The TEM images indicate that after the heat treatment very small particles can be seen along with the large particles in Pt-Cu/C-IMP and Pt-Cu/C-POL, especially in the Pt-Cu/C-IMP samples and also the large particles have been seen for Pt-Cu/C-SC. It seems that there were some amorphous Pt-Cu deposits on the surface of the carbon black particles which crystalized after the heat treatment and produced these small particles in the Pt-Cu/C-IMP sample and caused formation of large particles for the Pt-Cu/C-SC. There was uneven particle distribution for the Pt-Cu/C-SC samples. In some places, there were more metal deposits even after the heat treatment. As a result, after heat treatment a wide range of the particle sizes was observed for most of the samples but the narrower particle distribution and better particle dispersion was recorded for Pt-Cu/C-POL.

5.3.2 Electrochemical characterization

5.3.2.1 ECSA measurements

Figure 5.5 displays the initial voltammetric responses of different as-produced Pt-Cu samples. Figure 5.5 shows the dissolution of copper in two distinct faradaic current Cu_I and Cu_{II} peaks in the course of the first three cycles. The Cu_{II} presents the dissolution of Pt-coordinated Cu atoms while Cu_I is a result of losing the Cu atoms coordinated to the other Cu atoms [17, 39]. The Cu_I and Cu_{II} peaks became less distinctive by increasing the number of cycles. The Cu_I and Cu_{II} were less visible for the Pt-Cu/C-SC sample compared to the

other two sample. This confirms that the as-produced Pt-Cu/C-SC sample has less tendency to the Cu loss in comparison with Pt-Cu/C-POL and Pt-Cu/C-IMP or the Pt-Cu/C-SC particles may have a more Pt rich surface.

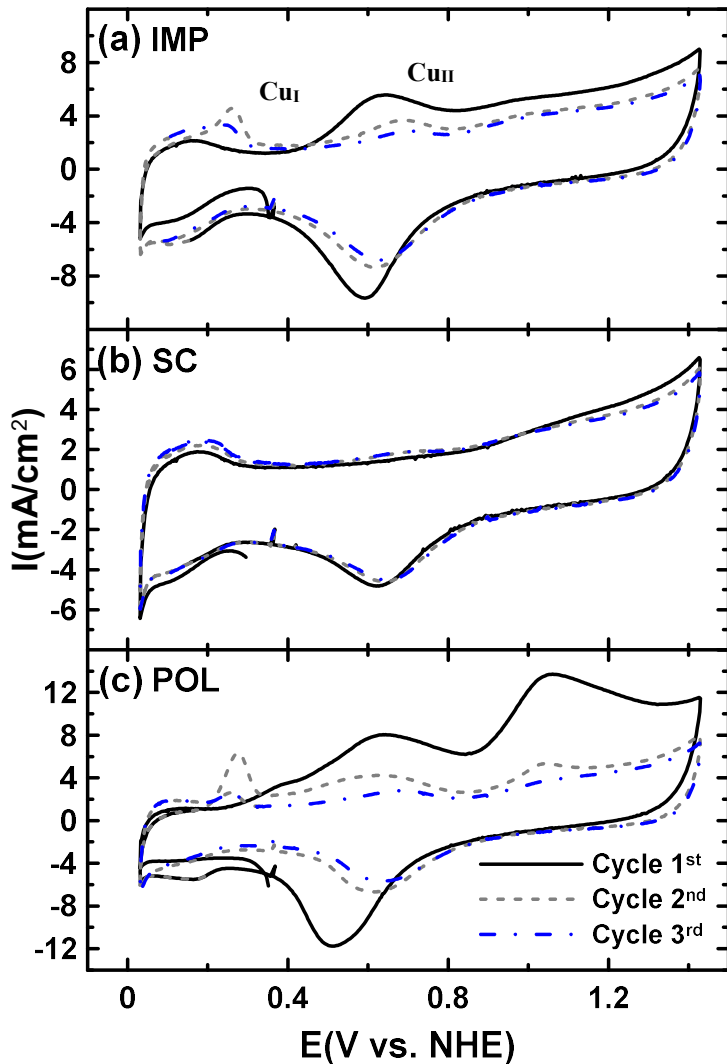


Figure 5.5. The first three CVs recorded before reaching stabilized CVs which were reported in Fig.7 for the as-produced Pt-Cu samples prepared by the (a) impregnation (b) impregnation + SC and (c) polyol methods. Measurements were made in the N₂-purged 0.5 M H₂SO₄ solution at a scan rate of 100 mV/s.

Figure 5.6 illustrate the three initial voltammetric responses of the heat treated Pt-Cu alloys. Comparing Figure 5.6 with Figure 5.5 shows that the voltammetric responses were modified after the heat treatment at 700 °C. Although, it is possible to identify the Cu_I for some samples, the dissolution of Cu was reduced for all samples. The changes were the most dramatic for the Pt-Cu/C-POL sample, when the Cu_I and Cu_{II} peaks were reduced substantially. The most pronounced Cu_I was related to the Pt-Cu/C-IMP samples where a significant amount of Cu was lost.

Steady-state cyclic voltammetry (CV) of the samples, prepared by each method and heat treated at different temperatures, are presented in Figure 5.7. These CVs were recorded after 20 cycles when reproducible steady-state cycles were observed. All samples showed the common Pt voltammograms. The resolved hydrogen adsorption/desorption peaks at low potential indicated that any surface oxide and possibly some atomic layers of Cu were removed, revealing the Pt-alloy surface. The ECSA values were determined by integrating the charge under the hydrogen adsorption peaks and are reported in Table 5.3.

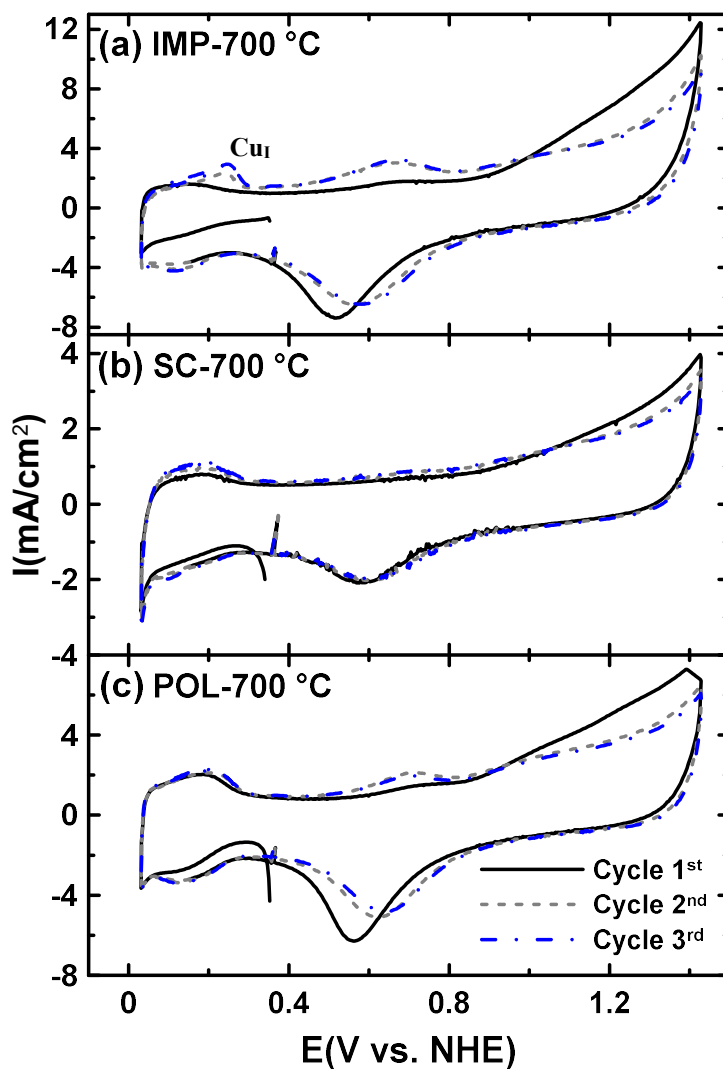


Figure 5.6. The first three CVs recorded before reaching stabilized CVs which were reported in Fig.7 for the Pt-Cu samples prepared by the (a) impregnation (b) impregnation + SC and (c) polyol methods and later heat treated at 700 °C for 1h. Measurements were made in the N_2 -purged 0.5 M H_2SO_4 solution at a scan rate of 100 mV/s.

The ECSA of the as-produced Pt-Cu/C-IMP sample was $14.3 \text{ m}^2/\text{g}_{\text{pt}}$ which was reduced to $13 \text{ m}^2/\text{g}_{\text{pt}}$ after the heat treatment at 500°C for 1h. However, increasing the heat

treatment temperature to 700 °C increased the ECSA to $16.1 \text{ m}^2/\text{g}_{\text{pt}}$ which is 13% larger than the ECSA of the as-produced sample. The ECSA loss is normally attributed to the particle growth during the heat treatment. However, the particle surface roughening due to dissolution of the surface oxides or dealloying would actually increase ECSA [10, 16, 40-42]. Therefore, the Pt-Cu/C-IMP sample resistance to the ECSA loss and gaining the larger ECSA after the heat treatment at 700 °C were most likely due to the surface roughening which caused by losing Cu and oxide phases. This confirms by initial stage CVs (Figure 5.6). As discussed in section 5.3.1.3, this also could be partially because of new particles nucleation during the heat treatment, which was seen in the TEM images (Figure 5.4). On the other hand, the formation of the PtCu_3 intermetallic ordered phase at 700 °C could also increase the concentration of Cu on the particle surface, and as a consequence, increase the Cu dissolution and the surface roughening.

The ECSA values of the Pt-Cu/C-SC samples were the lowest compared to all other samples, despite the fact that the metal loading of this sample was close to Pt-Cu/C-IMP (Table 5.1) and it was expected to see similar ECSA. In addition, the heat treatment had a dramatic effect on the ECSA values. ECSA dropped by ~50% at 700 °C from 9.7 to $5.1 \text{ m}^2/\text{g}_{\text{pt}}$. Therefore, it is safe to conclude that the low ECSA for the as-produced Pt-Cu/C-SC sample was due to the particle agglomeration and larger particles seen from TEM images. This also agrees with the sudden decrease in ECSA and the formation of very sharp peaks in the XRD patterns during the heat treatment at 500 and 700 °C.

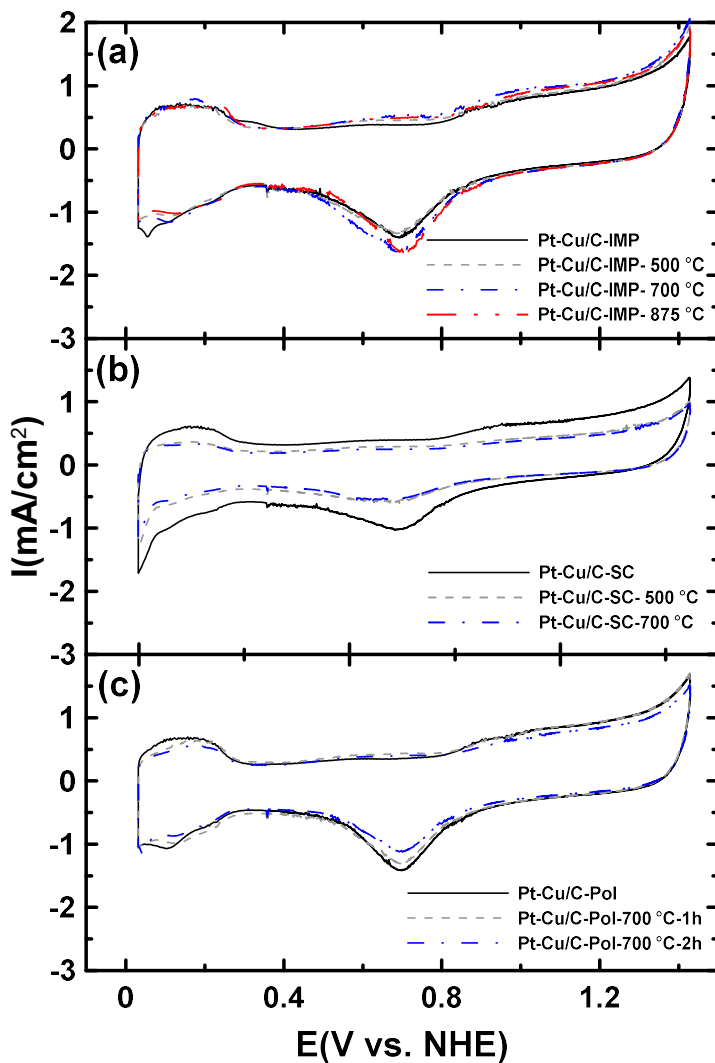


Figure 5.7. CVs obtained for the Pt-Cu/C catalysts made by the (a) impregnation (b) impregnation + SC and (c) polyol methods, before and after heat treatment at different temperature. Measurements were made in the N₂-purged 0.5 M H₂SO₄ solution at a scan rate of 20 mV/s.

The Pt-Cu/C-POL samples had the highest ECSA values among as-produced Pt-Cu samples. ECSA was reduced to $11.9 \text{ m}^2/\text{g}_{\text{pt}}$ after the heat treatment at 700°C for 1h and it continued to decrease by increasing the time of the heat treatment to 2h. The TEM images illustrates that particle growth after the heat treatment at 700 °C was less pronounced for

the Pt-Cu/C-POL samples. Therefore, it was expected to see higher resistance to the ECSA loss for the Pt-Cu/C-POL samples considering small particles, better particle dispersion and surface roughening due to dealloying. However, a 25% ECSA loss was observed after the heat treatment at 700 °C and it was progressive as the time of the heat treatment increased. It can be concluded that the ECSA loss was caused by the gradual merging of Pt-Cu particles and formation of the PtCu ordered phases which reduced the Cu dissolution and particle roughening.

Table 5.3. Summary of electrochemical properties of the catalysts studied in this work and the mean particle sizes determined by XRD.

	Peak potential (mV)	Peak current (mA.cm ⁻²)	Peak ratio (I _F /I _B)	ECSA (m ² /g _{Pt})	Mean particle size measured by TEM (nm)
Pt/C_{in-house}	904	3.61	1.18	15.5	-
Pt-Cu/C-IMP	891	6.14	1.09	14.3	2.5
Pt-Cu/C-IMP-500 °C	885	7.73	1.25	13.0	-
Pt-Cu/C-IMP-700 °C	882	8.56	1.33	16.1	4.4
Pt-Cu/C-IMP -875 °C	876	8.80	1.25	15.2	-
Pt-Cu/C-SC	896	5.19	1.09	9.7	3.3
Pt-Cu/C-SC-500 °C	893	3.34	1.45	5.1	-
Pt-Cu/C-SC-700 °C	912	1.29	1.54	5.3	4.8
Pt-Cu/C-POL	888	7.11	1.12	16.0	2.8
Pt-Cu/C-POL-700 °C-1h	881	10.03	1.32	11.9	3.6
Pt-Cu/C-POL-700 °C-2h	884	9.82	1.27	10.2	-

5.3.2.2 EOR measurements

The EOR activity of each Pt-Cu/C samples, before and after heat treatment, were studied in a deaerated ethanol solution and voltammograms are displayed in Figure 5.8. The summary of key EOR activity parameters are reported in Table 5.3. The results show that the peak current density of all the Pt-Cu samples were higher than Pt/C_{in-house}.

The EOR LSVs which were plotted using a Pt-mass specific current are shown in Figure 5.9. Comparing the Pt-mass specific current of different as-produced samples indicate that the Pt-Cu/C-POL samples had the highest activity using the lowest metal loading. Based on XRD, TEM and ECSA measurements: partly ordered phases, agglomeration reduction and higher ECSA values were the reason for the higher activity of the as-produced Pt-Cu/C-POL sample. The mass activity of Pt-Cu/C-POL was ~40% higher than Pt-Cu/C-IMP.

Heat treatment had a great impact on the EOR activity of the Pt-Cu samples, depending on the method used to produce the Pt-Cu samples (Figure 5.8 and 5.9). The EOR peak current density improved by increasing the heat treatment temperature for the Pt-Cu/C-IMP samples (Figure 5.8a and 5.9a). The highest activity reached at 875 °C for the Pt-Cu/C-IMP samples. The XRD results reveal that the crystallization and ordering process began at 500°C and completed at 700 °C. Table 3.1 shows that the formation of PtCu_3 was associated with ECSA increase and simultaneously, the ordering process changed Pt-Pt distances in the particles which was assigned as an important factor for the EOR activity enhancement. In particular, previous studies showed that the Pt-based ordered structure is stable even after extensive loss of the Cu atom dissolution [13, 17]. It can be concluded that the PtCu_3 intermetallic formation (or Pt-Pt distance changes) and the ECSA improvement due to the surface roughening are the reasons for the higher EOR activity of the heat treated Pt-Cu/C-IMP samples. However, different factors should be considered before defining the best heat treatment temperature for the Pt-Cu/C-IMP samples. The ratio of peak current densities in the forward and backward scans (I_F/I_B) for EOR CVs is an essential parameter to examine. This ratio represents the resistivity of samples against poisoning, the higher the ratio, the higher the resistivity [43, 44]. The I_F/I_B ratio for different samples are presented

in Table 5.3 and compared after heat treating at 700 °C in Figure 5.10. Although the highest activity was achieved at 875 °C, the I_F/I_B ratio after heat treatment at 700 °C was the highest. Therefore, the optimal Pt-Cu/C-IMP sample was produced by the heat treatment at 700 °C.

Heat treatment had a strong negative impact on the the Pt-Cu/C-SC sample (Figure 5.8b and 5.9b) and the EOR activity of this sample decreased dramatically. This sample had the highest Pt content among the Pt-Cu samples. The ECSA and EOR activity of these samples were decreased similar to the pure Pt samples after heat treatment [16]. As a result, any enhanced activity resulting from the formation of ordered phases was not large enough to compensate the effects of particle growth. The intense ECSA loss during the heat treatment along with the lower Cu content for the Pt-Cu/C-SC samples are the reason for the EOR activity reduction.

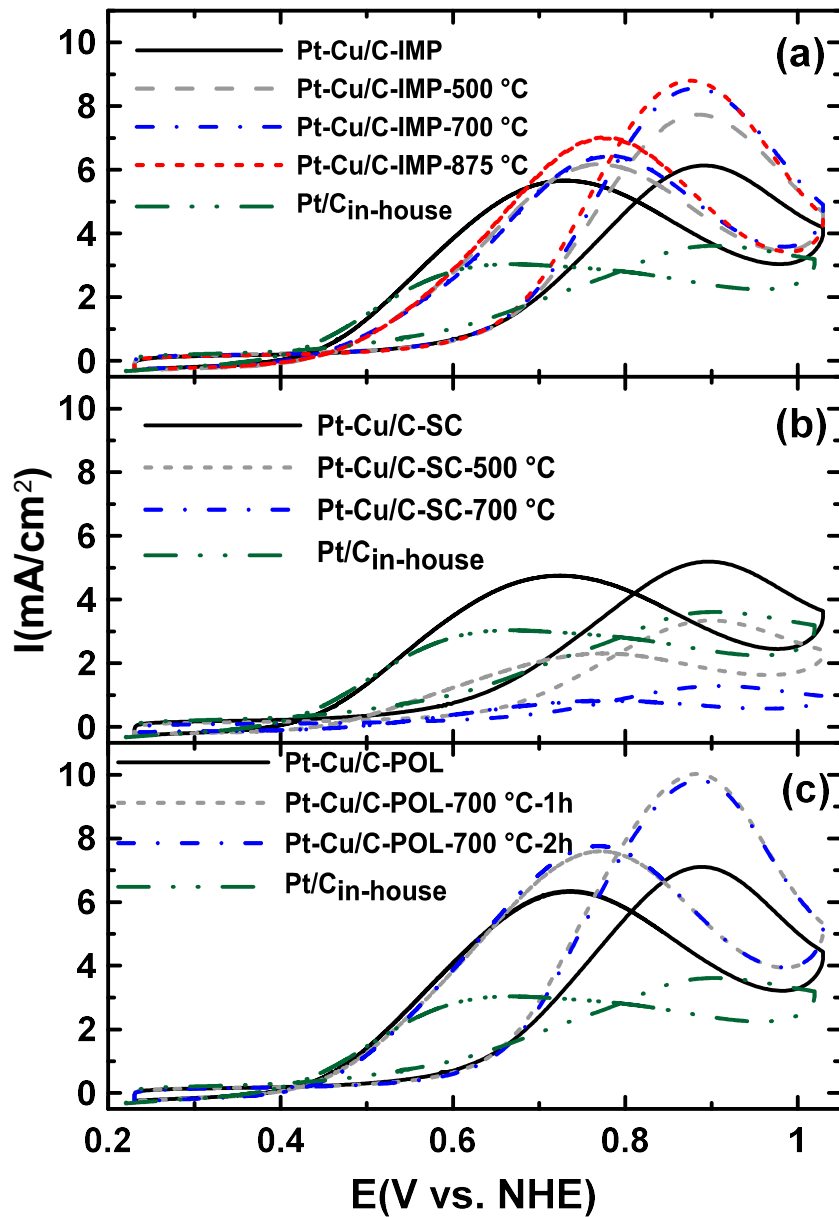


Figure 5.8. CVs obtained for Pt-Cu alloys deposited on Vulcan carbon by the (a) impregnation (b) impregnation + SC and (c) polyol methods, before and after heat treatment at different temperatures.

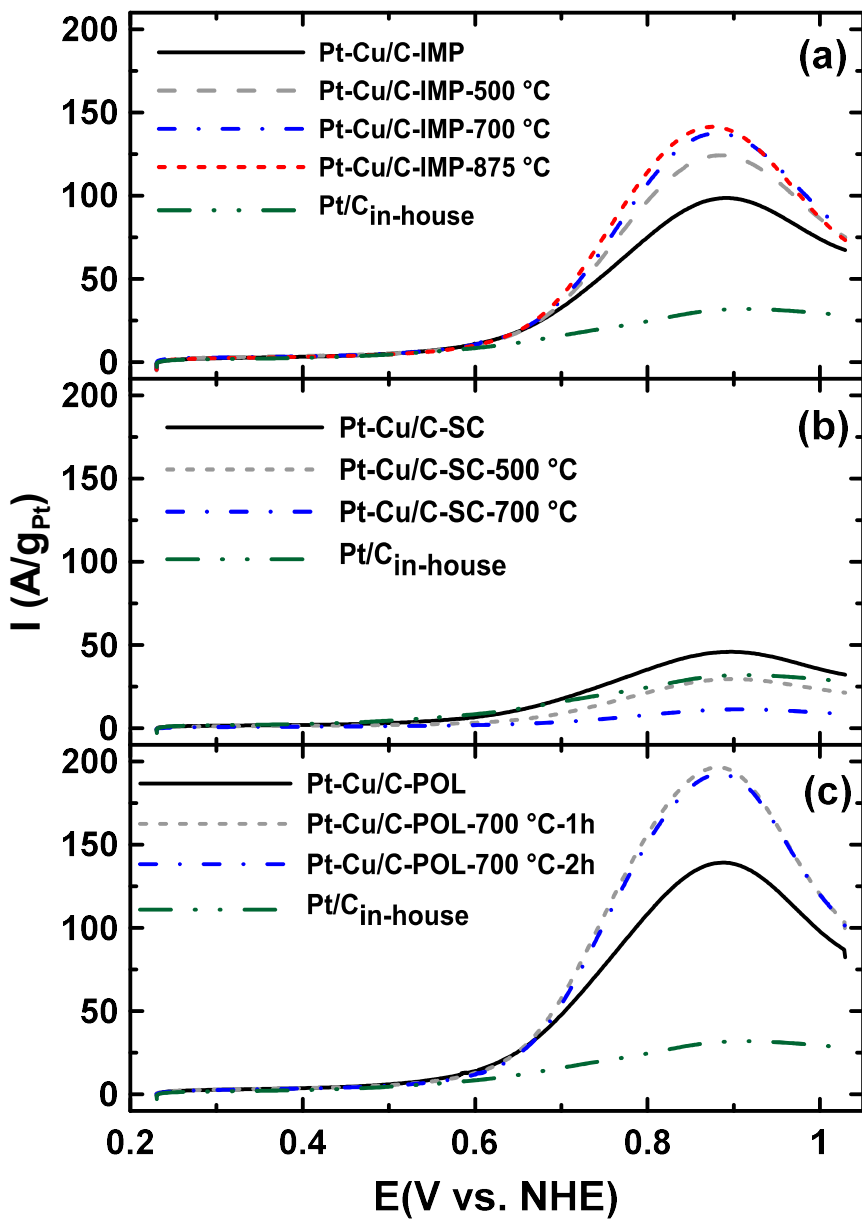


Figure 5.9. LSVs normalized with the current normalized on the basis of the Pt loading for the Pt-Cu/C catalysts made by the (a) impregnation (b) impregnation + SC and (c) polyol methods, before and after heat treatment at different temperature. Measurements were made in the N_2 -purged 0.5 M H_2SO_4 containing 0.1 M ethanol at a scan rate of 20 mV/s.

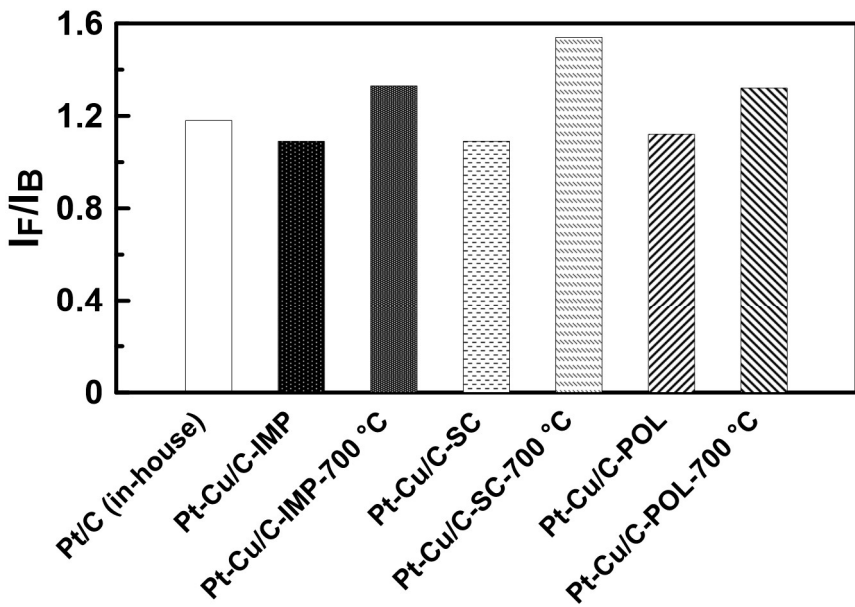


Figure 5.10. The IF/IB ratio for different samples are compared after heat treating at 700 °C.

Heat treatment of the Pt-Cu/C-POL samples had a similar effect as on the Pt-Cu/C-IMP samples (Figure 5.8c and 9c). The heat treatment of the samples at 700 °C increased the electrochemical activity by 40%. It was shown that ECSA of the Pt-Cu/C-POL samples was dropped after the heat treatment. Therefore, surface roughening or ECSA enhancement was not the cause of improved EOR activity for the heat treated Pt-Cu/C-POL samples. It can be concluded that the formation of the ordered PtCu along with the PtCu₃ ordered structure increased the EOR activity of the samples due to better retention of the Cu atoms. Furthermore, the presence of the ordered phases increased the I_F/I_B ratio for the heat treated Pt-Cu/C-POL samples. The increase in the I_F/I_B ratio means that the heat treatment decreased the poisoning for the samples produced by the polyol method. Further studies show that increasing the time of the heat treatment at 700 °C to 2h, just reduced the EOR activity of Pt-Cu samples due to further particle enlargement.

In this section, the electrochemical studies in the ethanol solution and different characterization methods indicate that increasing the available surface area of catalysts, adding an alloying element to build co-catalysts and modifying the crystalline structure of the Pt-alloy catalysts had great effect on increasing the EOR activity of the Pt-Cu catalysts. However, our study shows that the impact of the crystalline structure overawed the other underlying effects. As shown, the Pt-Cu/C-POL samples with the lowest metal loading and the ECSA loss during the heat treatment, generate the highest EOR activity. Regardless of the mechanism affecting EOR activity, it has been confirmed that the ordered crystalline structures could improve the electrochemical activity of the Pt-alloy catalysts. Therefore, the optimized heat treatment conditions and chemical compositions which are resulted in proper crystalline structures are desirable for the high EOR activity.

5.4 Conclusion

In this chapter, the Pt-Cu/C alloys were produced by three different methods and the effects of heat treatment on the structure and the electrochemical properties of the Pt-Cu catalysts were explored. The ICP and TGA results indicate that using different methods altered the chemical composition and the metal loading of samples. The impregnation method without an additive (Pt-Cu/C-IMP) produced the samples with the highest metal loading and the Cu content. The lowest metal loading was related to the samples prepared by the polyol method (Pt-Cu/C-POL). Studies by TEM show that the as-produced samples have the mean particle sizes in a narrow range and the particle dispersion was improved by using the polyol method. The XRD analysis indicate that each group of Pt-Cu samples developed distinctive ordered crystalline structures after the heat treatment at 700 °C. The

Pt-Cu/C-IMP samples developed the ordered PtCu₃ structure and the Pt-Cu/C-POL and Pt-Cu/C-SC samples developed the mixed PtCu and PtCu₃ ordered phases. The highest EOR activity was measured for the Pt-Cu/C-POL samples that heat treated at 700 °C for 1 h which also had the lowest metal loading and low ECSA. It can be concluded that the enhancement of EOR activity was due to the ordered phase formation, especially regarding the PtCu ordered structure. However, the formation of a superior crystalline structure is the consequence of an optimal heat treatment and effective chemical composition.

5.5 References

- [1] Y. Xu, B. Zhang, Chemical Society Reviews, 43 (2014) 2439-2450.
- [2] Y.-W. Lee, S. Cha, K.-W. Park, J.I. Sohn, J.M. Kim, Journal of Nanomaterials, 2015 (2015) 1-20.
- [3] E. Antolini, Materials Chemistry and Physics, 78 (2003) 563-573.
- [4] H. Liu, C. Song, L. Zhang, J. Zhang, H. Wang, D.P. Wilkinson, Journal of Power Sources, 155 (2006) 95-110.
- [5] T. Page, R. Johnson, J. Hormes, S. Noding, B. Rambabu, Journal of Electroanalytical Chemistry, 485 (2000) 34-41.
- [6] C. Sealy, Materials Today, 11 (2008) 65-68.
- [7] M. Ammam, L.E. Prest, A.D. Pauric, E.B. Easton, Journal of The Electrochemical Society, 159 (2011) B195-B200.
- [8] F. Vigier, S. Rousseau, C. Coutanceau, J.-M. Leger, C. Lamy, Top Catal, 40 (2006) 111-121.
- [9] T. Sato, K. Okaya, K. Kunimatsu, H. Yano, M. Watanabe, H. Uchida, ACS Catalysis, 2 (2012) 450-455.
- [10] M. Ghavidel, E. Easton, Catalysts, 5 (2015) 1016.
- [11] T. Ghosh, B.M. Leonard, Q. Zhou, F.J. DiSalvo, Chemistry of Materials, 22 (2010) 2190-2202.

- [12] E. Antolini, J.R.C. Salgado, E.R. Gonzalez, *Applied Catalysis B: Environmental*, 63 (2006) 137-149.
- [13] W. Roh, J. Cho, H. Kim, *J Appl Electrochem*, 26 (1996) 623-630.
- [14] T.J. Schmidt, H.A. Gasteiger, R.J. Behm, *Electrochemistry Communications*, 1 (1999) 1-4.
- [15] M. Ammam, E.B. Easton, *Journal of The Electrochemical Society*, 159 (2012) B635-B640.
- [16] M.R. Zamanzad Ghavidel, E.B. Easton, *Applied Catalysis B: Environmental*, 176–177 (2015) 150-159.
- [17] N. Hodnik, C. Jeyabharathi, J.C. Meier, A. Kostka, K.L. Phani, A. Recnik, M. Bele, S. Hocevar, M. Gaberscek, K.J.J. Mayrhofer, *Physical Chemistry Chemical Physics*, 16 (2014) 13610-13615.
- [18] M. Oezaslan, M. Heggen, P. Strasser, *Journal of the American Chemical Society*, 134 (2012) 514-524.
- [19] J. Georgieva, E. Valova, I. Mintsooli, S. Sotiropoulos, S. Armyanov, A. Kakaroglou, A. Hubin, O. Steenhaut, J. Dille, *J Appl Electrochem*, 44 (2014) 215-224.
- [20] M. Huang, L. Guan, *International Journal of Hydrogen Energy*, 40 (2015) 6546-6551.
- [21] Y.-X. Wang, H.-J. Zhou, P.-C. Sun, T.-H. Chen, *Journal of Power Sources*, 245 (2014) 663-670.
- [22] D. Xu, S. Bliznakov, Z. Liu, J. Fang, N. Dimitrov, *Angewandte Chemie*, 122 (2010) 1304-1307.
- [23] P. Mani, R. Srivastava, P. Strasser, *The Journal of Physical Chemistry C*, 112 (2008) 2770-2778.
- [24] Z. Xu, H. Zhang, S. Liu, B. Zhang, H. Zhong, D.S. Su, *International Journal of Hydrogen Energy*, 37 (2012) 17978-17983.
- [25] J. Sun, J. Shi, J. Xu, X. Chen, Z. Zhang, Z. Peng, *Journal of Power Sources*, 279 (2015) 334-344.
- [26] X. Zhang, D. Li, D. Dong, H. Wang, P.A. Webley, *Materials Letters*, 64 (2010) 1169-1172.
- [27] F. Saleem, Z. Zhang, B. Xu, X. Xu, P. He, X. Wang, *Journal of the American Chemical Society*, 135 (2013) 18304-18307.

- [28] L. Xiong, A. Manthiram, *Journal of The Electrochemical Society*, 152 (2005) A697-A703.
- [29] A. Rabis, P. Rodriguez, T.J. Schmidt, *ACS Catalysis*, 2 (2012) 864-890.
- [30] C.-J. Tseng, S.-T. Lo, S.-C. Lo, P.P. Chu, *Materials Chemistry and Physics*, 100 (2006) 385-390.
- [31] T.-H. Yeh, C.-W. Liu, H.-S. Chen, K.-W. Wang, *Electrochemistry Communications*, 31 (2013) 125-128.
- [32] H. El-Deeb, M. Bron, *Electrochimica Acta*, 164 (2015) 315-322.
- [33] X. Zhang, W. Lu, J. Da, H. Wang, D. Zhao, P.A. Webley, *Chemical Communications*, (2009) 195-197.
- [34] M. Huang, Y. Jiang, C. Jin, J. Ren, Z. Zhou, L. Guan, *Electrochimica Acta*, 125 (2014) 29-37.
- [35] M. Ammam, E.B. Easton, *Journal of Power Sources*, 222 (2013) 79-87.
- [36] O.A. Baturina, S.R. Aubuchon, K.J. Wynne, *Chemistry of Materials*, 18 (2006) 1498-1504.
- [37] M. Carelse, C.I. Lang, *Scripta Materialia*, 54 (2006) 1311-1315.
- [38] C. Mshumi, C. Lang, *Platinum Metals Review*, 51 (2007) 78-82.
- [39] M. Oezaslan, F. Hasché, P. Strasser, *Journal of The Electrochemical Society*, 159 (2012) B444-B454.
- [40] J.E. Harlow, D.A. Stevens, R.J. Sanderson, G.C.-K. Liu, L.B. Lohstroter, G.D. Vernstrom, R.T. Atanasoski, M.K. Debe, J.R. Dahn, *Journal of The Electrochemical Society*, 159 (2012) B670-B676.
- [41] D.A. Stevens, R. Mehrotra, R.J. Sanderson, G.D. Vernstrom, R.T. Atanasoski, M.K. Debe, J.R. Dahn, *Journal of The Electrochemical Society*, 158 (2011) B905-B909.
- [42] M. Watanabe, K. Tsurumi, T. Mizukami, T. Nakamura, P. Stonehart, *Journal of The Electrochemical Society*, 141 (1994) 2659-2668.
- [43] P. Serp, B. Machado, *Nanostructured Carbon Materials for Catalysis*, Royal Society of Chemistry, United Kingdom, 2015.
- [44] H. Gao, S. Liao, J. Zeng, Y. Xie, *Journal of Power Sources*, 196 (2011) 54-61.

Chapter 6: Durability of the Pt-Mn and Pt-Cu Alloys

In previous chapters, the activity, structure and electrochemical properties of the Pt-Mn and Pt-Cu alloys were studied in details. However, the long-term stability and activity of these alloys is always a great concern in order to produce commercial alcohol sensors and DAFCs. Therefore, the durability and long-term activity of the Pt-Mn and Pt-Cu alloys were investigated in this chapter and compared to commercially available samples.

6.1 Introduction

Worldwide industrial and technological development requires new and renewable sources of energy due to the increase in pollution levels and lack of fossil fuel in near future [1-5]. One of the promising candidates which is capable of producing renewable electricity is fuel cells (FCs) [5-8]. Direct alcohol fuel cells (DAFC) could be one of the leading fuel cell technologies in the portable device and automotive industry [9-12]. However, the cost, the stability of power production and lifetime of DAFC are the limiting factors for the industrial applications. Pt is the most commonly used precious electrocatalyst for DAFC, which is a critical factor [13-16]. The U.S. Department of Energy (DOE) targets the mass activity of $0.44 \text{ A/mg}_{\text{pt}}$ for the membrane electrode assembly (MEA) in year 2020 and the target lifetime is over 5000 h for the cycling systems (automotive) and over 60,000 h for the stationary systems[17]. Achieving these targets requires improvement in the activity of the Pt catalysts along with their stability.

The Pt electrodes are susceptible to poisoning by strongly adsorbed species which are formed during the alcohol oxidation process, resulting in severe activity and efficiency losses [4, 9, 18]. To overcome this problem and improve the electroactivity of Pt catalysts, several path has been studied in the past decades. One of the common and reliable ways to eliminate the poisoning and enhanced the mass activity is to develop Pt-alloys with transition metals such as Cu, Mn, Sn , Ru, Ni and Co [10, 19-22]. Unfortunately, the alloying process of the Pt catalysts can make them more venerable to degradation and may reduce the durability of the electrocatalysts. Studies have shown that durability of Pt-alloys can be improved by several methods; for example, functionalization of carbon supports, thermal heat treatment or using new supporting materials [23]. Several studies on the Pt-Cu, Pt-Ni and Pt-Co alloys have illustrated that heat treatment at different temperatures has

increased the alloying element retention and has reduced the sintering probability of the particles during cell performance [23, 24].

The durability studies, especially for Pt-alloy electrocatalysts, are challenging due to the length of measurement and the complexity of the mechanisms. As a result, researchers have designed different accelerated stress tests (ASTs) to reduce the length of the test and achieve reliable results. The catalyst voltage cycling and support corrosion test at fixed potential are two common and reliable methods that have been used [25, 26]. In addition, our lab has developed new AST protocol which combined electrochemical impedance spectroscopy (EIS) with the voltage cycling method. This is a very quick method to screen Pt dissolution/agglomeration, support corrosion and ionomer degradation. This method has been utilized to study the Pt catalysts with different loading and different supporting materials [25-29].

Durability tests are mostly focused on the Pt/C electrodes and there are fewer studies on Pt-alloys catalysts. The previous studies on the Pt systems have suggested that the degradation of Pt/C catalysts is mainly due to loss of Pt active surface area, support corrosion and degradation of the ionomer network [7, 23, 30-34]. Recently, a model for degradation of the Pt, Pt-Cu and Pt-Co systems has been developed in which there are two different degradation stages for the Pt particles and the acid treated Pt-Cu and Pt-Co catalysts. During the first stage, the degradation is caused by reducing electrochemical active surface area (ECSA). In the second stage, the degradation occurred predominantly because of the carbon corrosion and the particle detachment [35]. However, this model can be examined in more detail by using EIS analysis and the protocol developed in our lab. In addition, this model can be verified for other Pt-alloy catalysts.

There are far more articles that have studied the durability of Pt-Cu alloys [11, 19, 21, 35-42] compared to Pt-Mn systems [10, 18, 21]. Studies have shown that using proper heat treatment have drastically improved the electroactivity of these catalysts. Short-term studies have shown that the Pt-Mn and Pt-Cu alloys are stable in acidic media, but their long-term behaviour has not studied systematically [10, 18, 19, 43]. Previous studies on the Pt-Cu, Pt-Co, Pt-Mn and Pt-Ni systems have illustrated that the alloying elements could leach out under potential load [35, 37, 44, 45]. However, the studies on Pt-Mn and Pt-Cu is very restricted and the long-term durability of these alloys are not well understood, especially after being exposed to heat treatment.

In this chapter, the Pt-Mn/C and Pt-Cu/C alloys have been produced by the impregnation, and microwave assisted polyol method, respectively. Next, the effect of crystalline structure and heat treatment on the durability of the Pt-Mn and Pt-Cu samples have been studied and they have been compared to the Pt/C and Pt-Sn/C commercial samples. Different methods such as EIS and ex-situ ICP and ex-situ XRD analyses have been utilized to determine the main parameters affecting the degradation of these catalysts.

6.2 Experimental

6.2.1 Catalyst synthesis

The carbon supported Pt-Mn and Pt-Cu alloys were prepared as explained in section 4.2.1 and 5.2.1. Impregnation in the presence of an additive was used for Pt-Mn/C samples and microwave assisted polyol method used for the Pt-Cu/C samples. In addition, two carbon support commercial samples with 20 wt% metal loading, Pt/C (Premetek Co.) and Pt-Sn/C (Premetek Co.), were studied and compared to the samples made in-house.

These samples are hereafter referred to as Pt-Mn/C-SC, Pt-Cu/C-POL, Pt/C and Pt₃Sn/C, respectively. The target composition was Pt_{0.25}M_{0.75}/C (M=Mn and Cu). This composition was chosen based on the studies in chapter 4 and 5 and recently published articles [11, 22, 37, 46]. Metal precursors were H₂PtCl₆.H₂O (Aldrich), MnCl₂.4H₂O (Aldrich), and CuCl₂.2H₂O (Aldrich). Vulcan XC72R carbon black (Cabot Corp.) was used as the carbon support in all cases. The total metal loading was targeted as ~20 wt% for all samples. The pH of the reaction solution was adjusted using a HCl solution (15 v/v %) and/or a 1M NaOH solution. For the impregnation method with the additive, Trisodium Citrate (SC) (Aldrich) was added in a weight ratio of 2:1 to the metal ratios. NaBH₄ powder was used as a reduction agent. The weight ratio of NaBH₄ to the metal content was 3:1. The pH of the solution was adjusted to 3 for the impregnation method. For the polyol method, the metal precursors and Vulcan carbon were mixed with ethylene glycol (EG) (Aldrich) using a mechanical stirrer. The solution pH was adjusted to pH 9, after which it was sonicated for 45 min to achieve a uniform suspension. The suspension was placed into the household microwave oven (SANYO - 2450 MHz) and heated for 8 min and then left to cool down under continues mechanical stirring. In all the methods, the resulting powder was filtered and washed with isopropanol alcohol (IPA), acetone, and deionized water, and finally dried in an oven at 80 °C overnight.

The selected samples were heat treated in a nitrogen atmosphere at 700 °C in a Barnstead Thermolyne tube furnace with a quartz tube. The period of heat treatment was kept constant (1 h) for all the samples. The heat treatment time and temperature was also chosen base on previous studies by our group [43]. After the heat treatment, the samples were cooled down under a constant flow of nitrogen gas and were preserved inside the furnace until room temperature was reached.

6.2.2 Materials characterization

The chemical composition of the samples and the solution along or after electrochemical tests was examined by Inductively Coupled Plasma Optical Emission Spectroscopy (ICP-OES). An Aqua Regia solution was used to dissolve the metal powders and the diluted solutions were consumed for ICP-OES analysis. The ICP-OES instrument (Varian Vista-MPX) was calibrated by four standard solutions of Pt, Mn, Cu and Sn with a concentration of 1, 5, 10 and 20 ppm.

All the samples were characterized by powder X-ray diffraction (XRD) using a Rigaku Ultima IV X-ray diffractometer equipped with a Cu K_{α1} X-ray source and a graphite monochromator. The XRD analysis used for the characterization of as-produced samples and also utilized to study the crystalline phase changes during the electrochemical tests (ex-situ XRD analyses).

6.2.3 Electrochemical characterization and accelerated stress test (AST)

6.2.3.1 Electrode preparation

Two different types of electrodes were used in this study. First, the catalyst inks were produced by mixing 10 mg of the catalyst with 100 µL Nafion solution (5% in alcohols, Dupont) and a 400 µL 50:50 mixture of isopropyl alcohol (IPA) and water. A uniform suspension was achieved after sonicating for 45 minutes. A 2 µL droplet of the well-dispersed catalyst ink was deposited onto a clean and polished GC electrode (diam = 3 mm, CH instruments) and dried in the air at room temperature prior to electrochemical tests. The total metal loading of the catalyst layer was ~0.11 mg/cm². Second, the electrodes were

also prepared using similar mixture of the catalysts, water, IPA and the Nafion solution with some modification. The mixture was sonicated for 45 min, stirred over-night and sonicated for 45 min before spray deposition onto a gas diffusion layer (Toray TPGH-090, 10 % wet-proofing) using an airbrush [47]. The electrodes were dried for 30 min at room temperature and then at 80°C for over-night. The total metal loading of the catalyst layer (add metal loadings) was ~0.4 mg/cm². Afterward, 4 cm² of coated samples were cut and exposed to the test solution. The electrodes made had a Nafion loading of 30 wt% in each set. The first set of the electrodes were used to run the EIS analysis and measure the changes in the electrochemical active surface area (ECSA) and the ethanol oxidation reaction (EOR) and the second set of electrodes utilized to examine the chemical composition and crystalline structure variations, during AST.

6.2.3.2 AST

A three compartment cell equipped with a Pt wire counter and a double-junction Ag/AgCl reference electrode was used to run AST on both electrodes. Cyclic voltammetry (CV) and electrochemical impedance spectroscopy (EIS) were performed in a N₂-purged solution. A 0.5M H₂SO₄ solution was used to determine ECSA and run the EIS measurements. A 0.5 M H₂SO₄ + 0.1M ethanol solution was applied to explore the EOR activity of the catalysts. A solarton 1470E Multichannel Potentiostat and a Solarton 1260 frequency response analyzer controlled using Multistat software (Scribner Associates) were used for the CV and EIS measurements. The durability of samples in the 0.5 M H₂SO₄ and 0.5 M H₂SO₄ + 0.1M ethanol solutions were examined by repeated CV cycles with the

appropriate lower and upper potential limits [25-27]. The AST protocols to study the electrochemical and structural degradation of samples were as follows:

4) Accelerated ageing applied for the samples deposited on the GC electrodes by potential cycling between 0.03 and 1.43 V (vs NHE) in the N₂-purged 0.5 M H₂SO₄ solution for specific number of cycles with the scan rate of 50 mV/s. However, after the specific number of cycles (1, 50, 100, 200, 400, 1000, 2000, 3000, and 4000) 2 cycles recorded at 20 mV/s and the last one were plotted for comparison and used to calculate ECSA. In addition, immediately after recording the cycles at 20 mV/s, the EIS analysis were conducted at 0.360 V (double layer region in CVs).

5) Same aging protocol used for 0.5 M H₂SO₄ + 0.1M ethanol solution to study degradation of the samples deposited on the GC electrodes at a shorter potential range from 0.23 to 1.03V

6) Slightly different protocol applied for the samples deposited on carbon papers. Aging cycles were done from 0.03 and 1.43 V (vs NHE) at the higher scan rate of 100 mV/s. The cycling process was paused after the specific number of cycles (1, 50, 150, 400, 1000, 2000 and 3000) and samples were analyzed by ex-situ XRD. At the same time, 4 ml of the 0.5 M H₂SO₄ solution was removed for ex-situ ICP analyses and replaced by fresh solution. In order to run the XRD analyses, the samples washed by deionized water and dried with flowing air.

6.3 Result and discussion

6.3.1 Ex-situ ICP analysis of different samples

The chemical composition of different samples deposited on carbon paper, before (BT) and after (AT) accelerated test, was monitored and the results are shown in Table 6.1. Comparing chemical compositions of the samples BT and AT shows that dealloying occurred in all the alloyed samples. However, samples with the higher Pt loading showed the higher resistance to dealloying. The highest loss was recorded for as-produced Pt-Mn (Pt-Mn/C-SC) and the lowest loss was related to Pt₃Sn/C. In addition, the results indicate that the heat treatment at 700 °C reduced the metal loss for the Pt-Mn and Pt-Cu samples. Therefore, the heat treatment could increase the alloying element retention. Similar results have been reported previously for the Pt-Cu alloy [22].

Figure 6.1and 6.2 shows how the concentration of Cu, Mn, and Pt were altered during AST in the testing electrolyte for the Pt-Mn and Pt-Cu samples. The data was corrected for the dilution caused by the solution replacement. These results show that the alloying elements was depleted at a faster rate at the beginning of cycling and then stay almost same for most of the samples which could be due to the presence of the lower alloying element and formation of Pt skin which would protect the inner alloying elements. The content of Cu and Mn in the electrolyte were much more than the Pt content. This shows that the presence of the alloying elements protected and reduced Pt loss. The lowest Pt loss was determined for Pt-Cu/C-POL-700 °C. However, these results and the composition of the electrodes BT and AT (Table 6.1) indicate that there was the Cu and Mn depletion which protect the Pt content during cycling and the heat treatment generally improved the stability of the samples.

Table 6.1. Composition of the samples before (BT) and after (AT) running AST which was measured by ICP and TGA, respectively.

Samples	Alloy molar ratios measured by ICP			
	Pt (%)	Mn (%)	Cu (%)	Sn (%)
Pt-Mn/C-SC-BT	21.30	78.70	-	-
Pt-Mn/C-SC-AT	91.06	8.94	-	-
Pt-Mn/C-SC-700 °C-BT	20.74	79.26	-	-
Pt-Mn/C-SC-700 °C-AT	88.68	11.32	-	-
Pt-Cu/C-POL-BT	41.04	-	58.96	-
Pt-Cu/C-POL-AT	83.67	-	16.33	-
Pt-Cu/C-POL-700 °C-BT	36.36	-	63.64	-
Pt-Cu/C-POL-700 °C-AT	63.28	-	36.72	-
Pt₃Sn/C-BT	67.69	-	-	32.31
Pt₃Sn/C-AT	74.07	-	-	25.93

6.3.2 Ex-situ XRD analysis of different samples

The results of the ex-situ XRD analysis of different samples during AST are shown in Figure 6.3, 4, 5, 6 and 7. The XRD analysis indicates that the crystalline structure of the samples was altered along with their chemical compositions. Unfortunately, it was not possible to monitor all the diffraction patterns of the alloyed samples due to the background caused by the carbon paper and the Vulcan carbon particles. However, the diffraction peak around 40° was strong enough for most of the samples to show how the crystalline structure was affected by cycling and the diffraction due to the carbon paper was very useful to eliminate the diffraction peak displacement. The dash lines in all figures show the peak location for the pure Pt fcc structure.

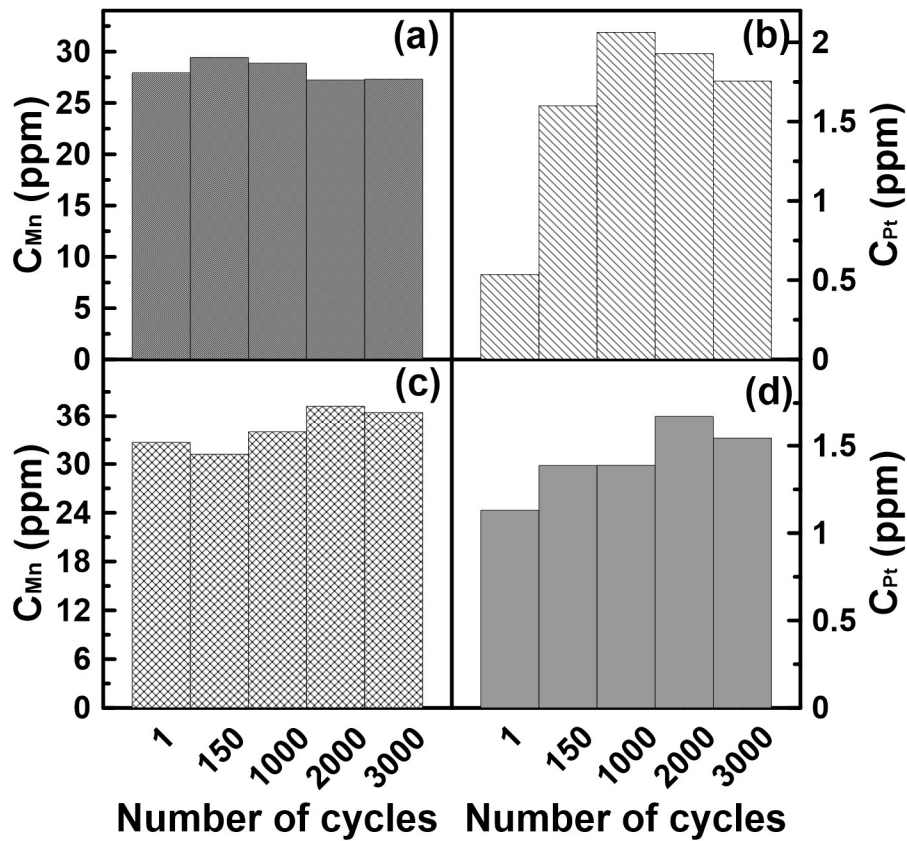


Figure 6.1. The Mn and Pt concentration in the testing electrolyte at the specific cycles of AST (a) (b) for Pt-Mn/C-SC and (c) (d) for Pt-Mn/C-SC-700 °C which were determined by ICP.

In general, the XRD patterns indicate that the intensity of the peak at around 40° and related to the alloyed phases was increased with cycling. In addition, due to cycling and dealloying of the catalysts, these peaks were shifted toward the pure Pt diffraction pattern which are shown by dash lines. In some of the samples, it is also possible to detect another diffraction peak at around 46°. The behaviour of both peaks were similar. Before starting AST, the peak for the Pt-Cu and Pt-Mn samples were detected at the higher angles due to incorporation of the alloying elements (Mn or Cu) in the fcc structure of Pt and also due to the heat treatment. This was more pronounced for Pt-Mn/C-SC-700 °C (Figure 6.5). On the

other hand, the peak for the Pt₃Sn/C sample was located at the lower angles compared to the pure Pt. This is due to deference in the atomic radius of Cu, Mn and Sn and the crystalline structure of the alloys.

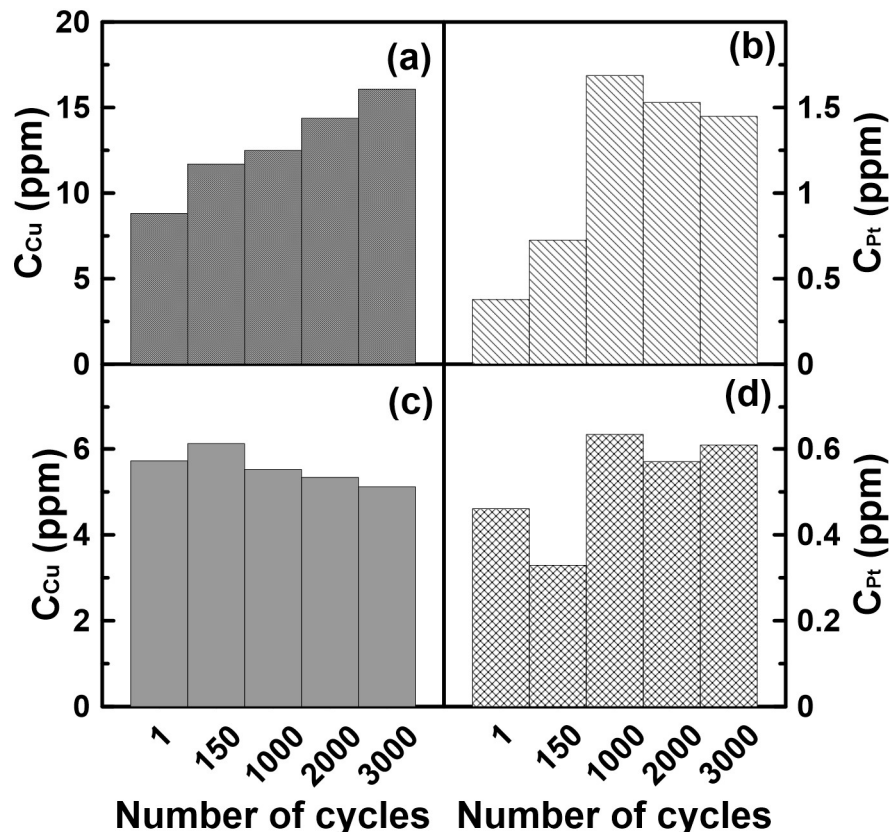


Figure 6.2. The Cu and Pt concentration in the testing electrolyte at the specific cycles of AST (a) (b) for Pt-Cu/C-POL and (c) (d) for Pt-Cu/C-POL-700 °C which were determined by ICP.

The Pt₃Sn/C crystalline structure was altered after the first few cycles (Figure 6.3). The intensity of peak started to grow after first 50 cycles. The peaks were almost stable until 50 cycles, after which the crystalline structure started to change at a higher rate. After

~1000 cycles, the Pt₃Sn/C sample seems to lose most of the alloying element and structure was completely altered to the pure Pt structure.

The behaviour of the crystalline structure for Pt-Mn/C-SC and Pt-Mn/C-SC-700 °C during cycling was different to some extent (Figure 6.4 and 6.5). In chapter 3 and 4, it was shown that the Pt-Mn samples before the heat treatment have fcc structure with very small shift in the peak positions but the heat treatment has a great impact on the crystalline structure and the peak positions of the Pt-Mn alloys and forms the PtMn intermetallic with tetragonal structure [10, 43]. It was difficult to detect any peak before starting AST for the Pt-Mn/C-SC sample (Figure 6.4). As the AST progressed, the peak at ~40° started to grow. The diffraction peak intensity enhancement indicates that the Pt crystals were became more distinctive after 50 cycles. In contrast, the peak related to Pt-Mn/C-SC-700 °C detected even before starting AST (Figure 6.5). The peak positions for Pt-Mn/C-SC-700 °C was shifted to the higher angles due to the formation of the PtMn ordered intermetallic phase and the higher degree of the Pt and Mn alloying. The crystalline structure of Pt-Mn/C-SC-700 °C was almost stable until 400 cycles, but the crystalline changes was enhanced after 400 cycles. The peak at around 40° shifted to the lower angles and the intensity of the peak increased with the potential cycling. The XRD analysis of Pt-Mn/C-SC-700 °C shows that cycling beyond 1000 cycles caused the particles move toward the Pt fcc structure which is due to the depletion of Mn. Comparison of the XRD diffraction in Figure 6.4 and in Figure 6.5 indicates that the Pt-Mn/C-SC particles before the heat treatment were less stable and more susceptible to degradation and the heat treatment was effective to retain Mn in the particle structure and prevented fast decay.

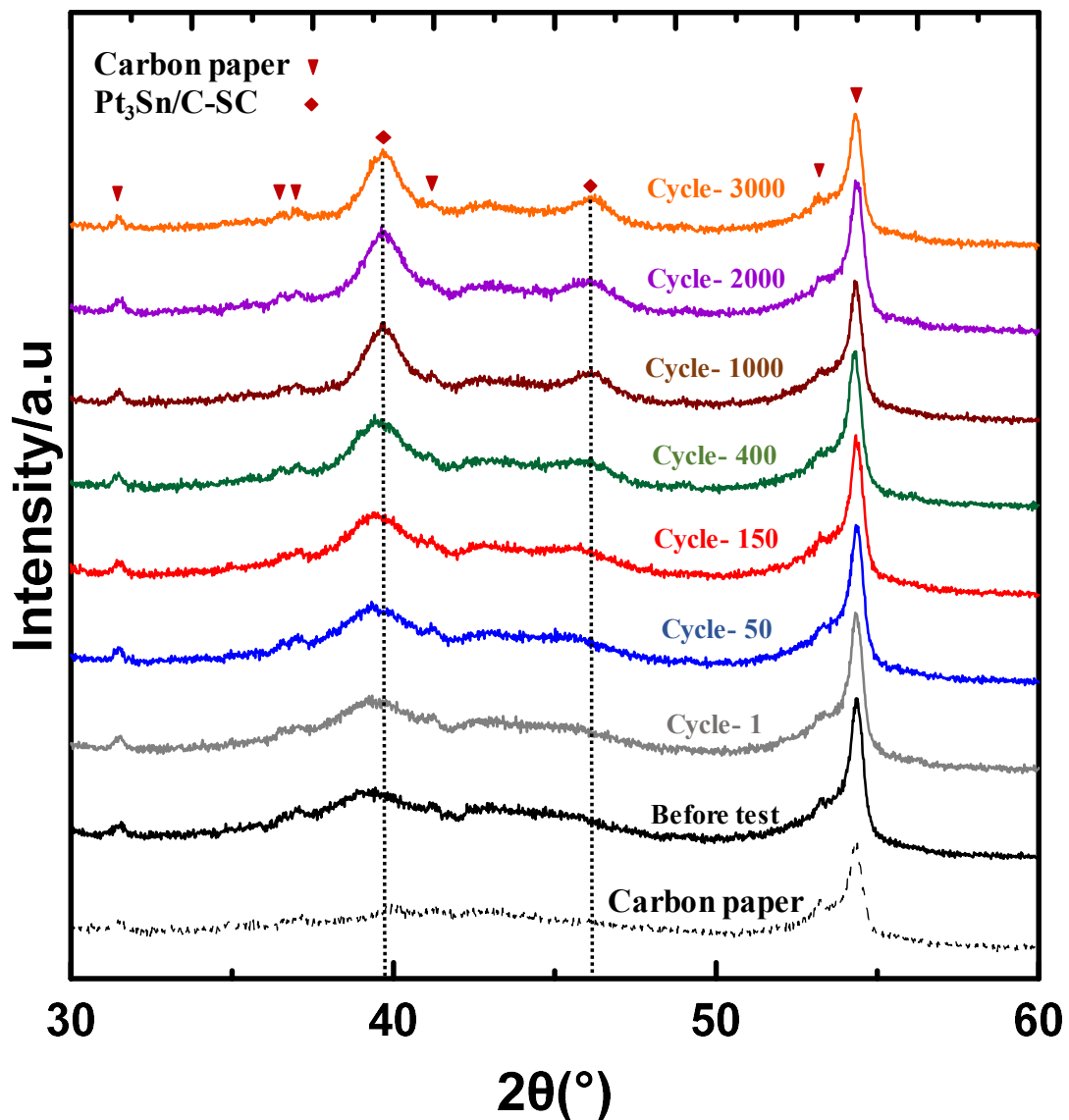


Figure 6.3. The XRD patterns for Pt₃Sn/C at the specific cycles of AST.

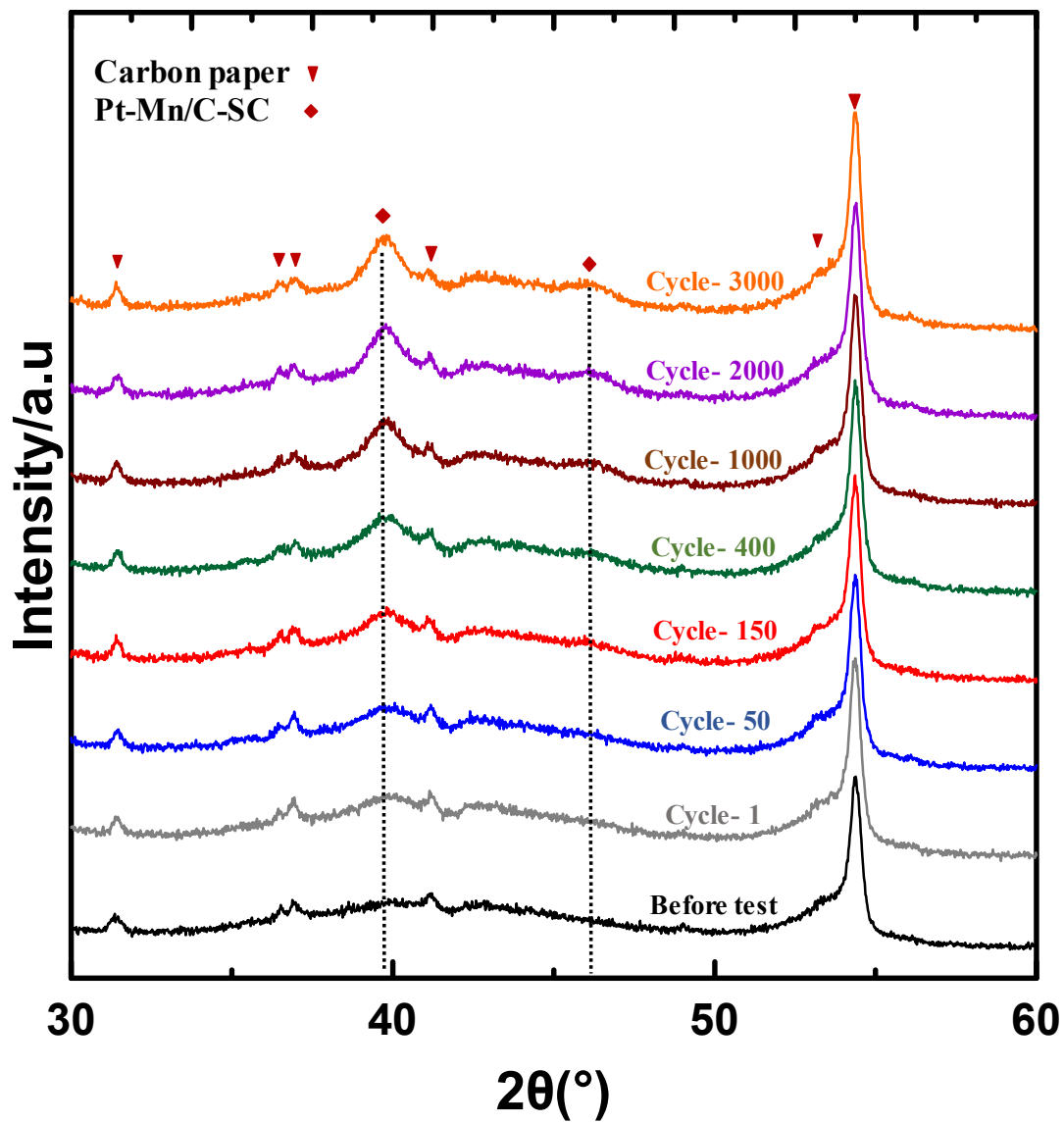


Figure 6.4. The XRD patterns for Pt-Mn/C-SC at the specific cycles of AST.

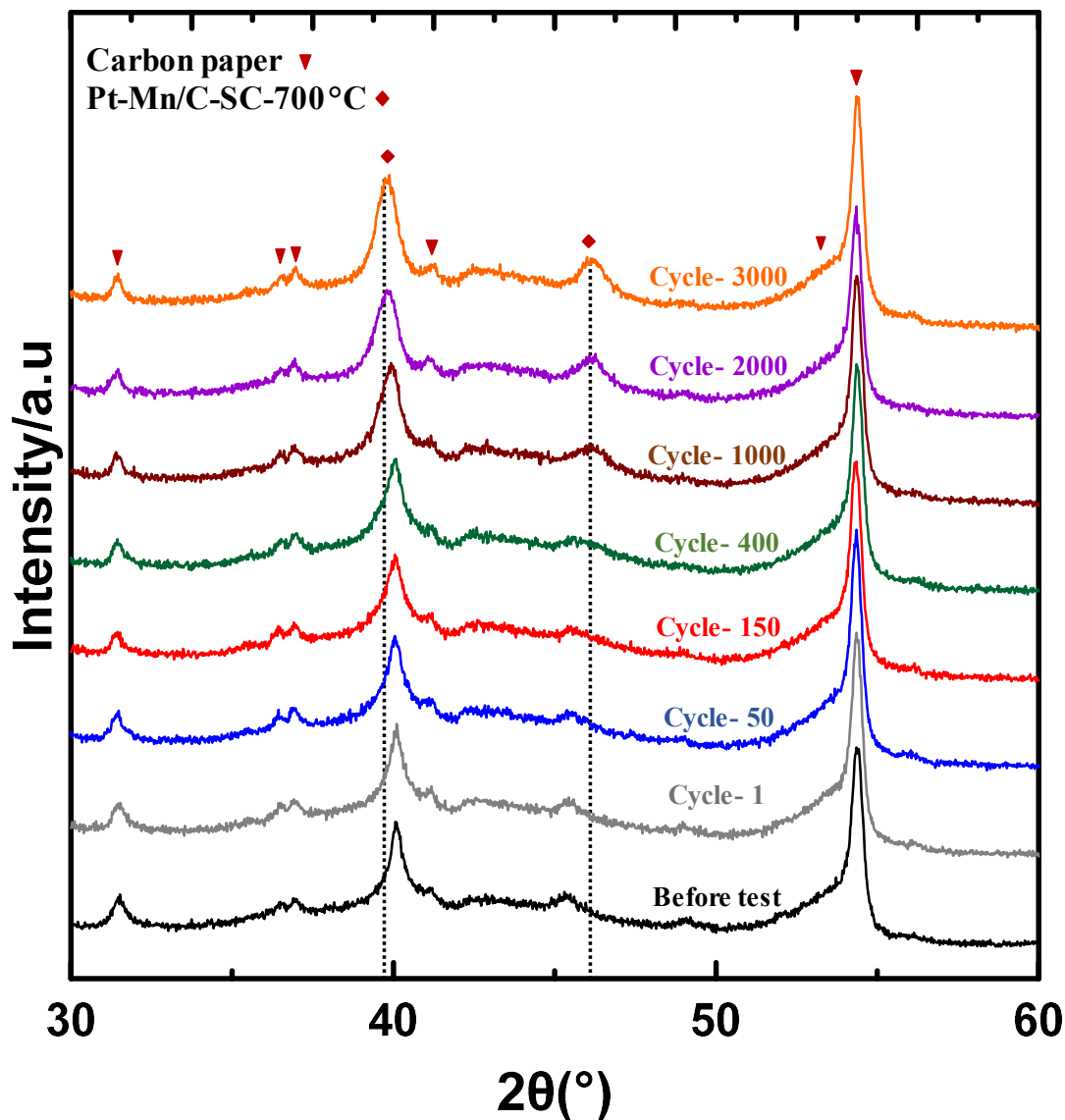


Figure 6.5. The XRD patterns for Pt-Mn/C-SC-700 °C at the specific cycles of AST.

Comparing the Pt-Cu/C-POL and Pt-Cu/C-POL-700 °C crystalline structures during cycling illustrates some differences (Figure 6.6 and 7). For the as-produced Pt-Cu sample, no diffraction peak was detectable before starting AST, but the peak at ~40° started to grow as the cycling continued (Figure 6.6). For the first 400 cycles, the peak detected at the higher angles due to the presence of Cu in the Pt-Cu alloy structure. The rate of Cu depletion

was increased after 400 cycles and the diffraction peak for Pt-Cu/C-POL started to shift toward the pure Pt structure. The results show that this sample lost most of the Cu before reaching to 1000 cycles. Unfortunately, the intensity of the peaks for the heat treated Pt-Cu samples were very low and it was very difficult to detect any peak until 3000 cycles. However, the peak for Pt-Cu/C-POL-700 °C located at the higher angles even after 3000 cycles which indicates that the stability of the sample was improved by the heat treatment and the Cu depletion was reduced. This is in agreement with data presented in Table 6.1 which shows that this sample contain ~37 %at Cu. The ICP data and XRD diffraction results indicate that the alloying element was preserved more strongly in the structure of Pt₃Sn/C at the end of AST but the crystalline structure of Pt₃Sn/C was modified faster compared to the heat treated Pt-Mn and Pt-Cu samples.

By increasing the number of cycles for all the alloyed samples the peak position around 40° shifted to the diffraction peak of the pure Pt due to the alloying element depletion. The intensity of the peaks was increased which could be caused by the new Pt particle nucleation, Pt particle ripening or formation of particles with the Pt rich surface. Previous studies on the Pt-Cu and Pt-Co alloys have shown that dealloying could result in a core-shell structure depending upon the particle sizes (lower than 15 nm) [37, 48]. The particle size for the samples studied here were mostly smaller than 15 nm. The XRD results shows that the intensity of the peak assigned to Pt increased during cycling and ICP results confirms that Pt dissolution was negligible compared to the depletion of the alloying elements. Therefore, the evidence indicates that the core-shell structures may have formed for these samples as well.

Based on XRD analysis and ICP results, it can be concluded that the depletion of the alloying elements and formation of the Pt rich particles are the part of degradation process,

but other mechanisms could be involved. Further studies by the CVs and EIS analyses and measuring ECSA values could be helpful to reach to final conclusion.

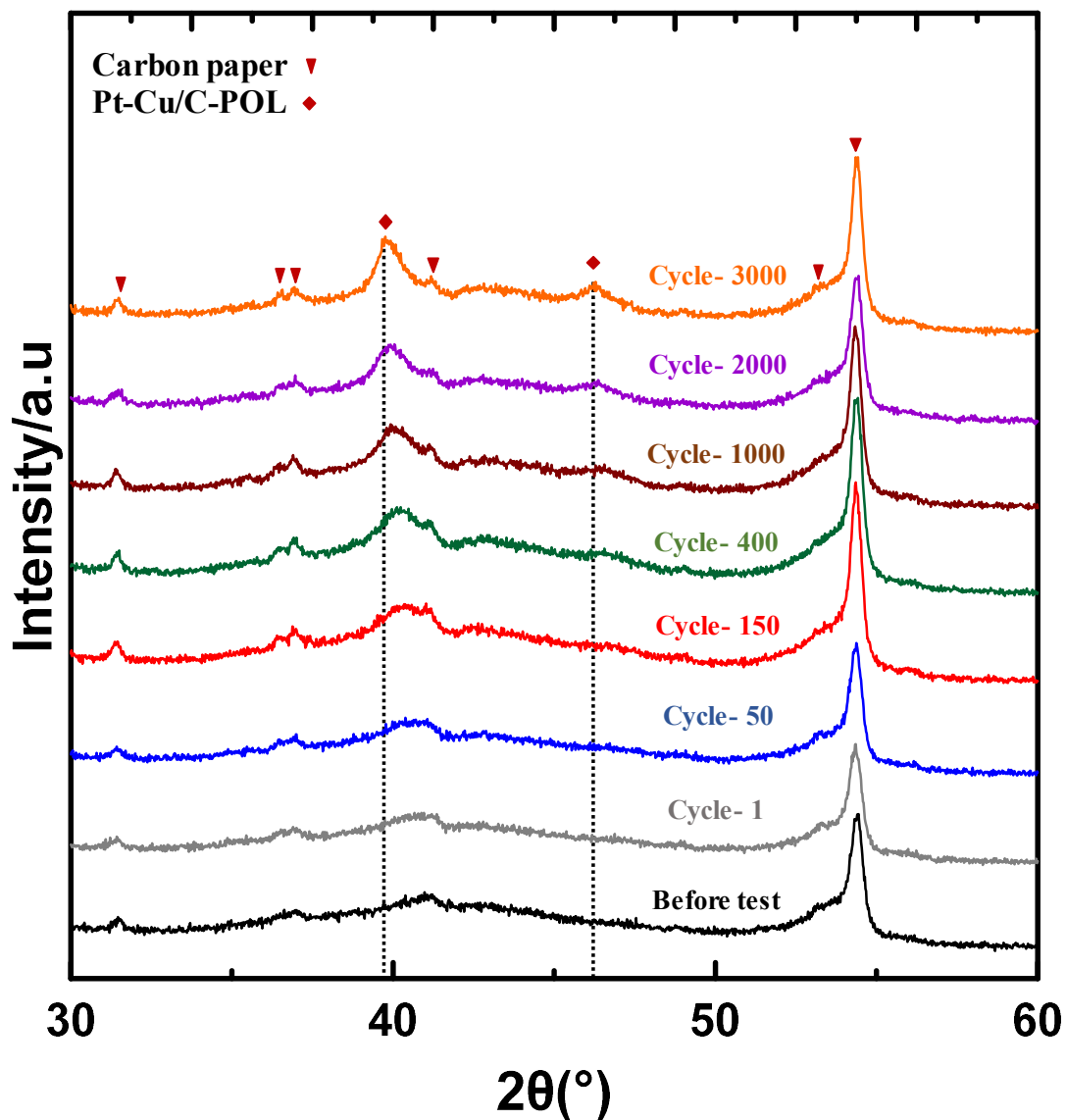


Figure 6.6. The XRD patterns for Pt-Cu/C-POL at the specific cycles of AST.

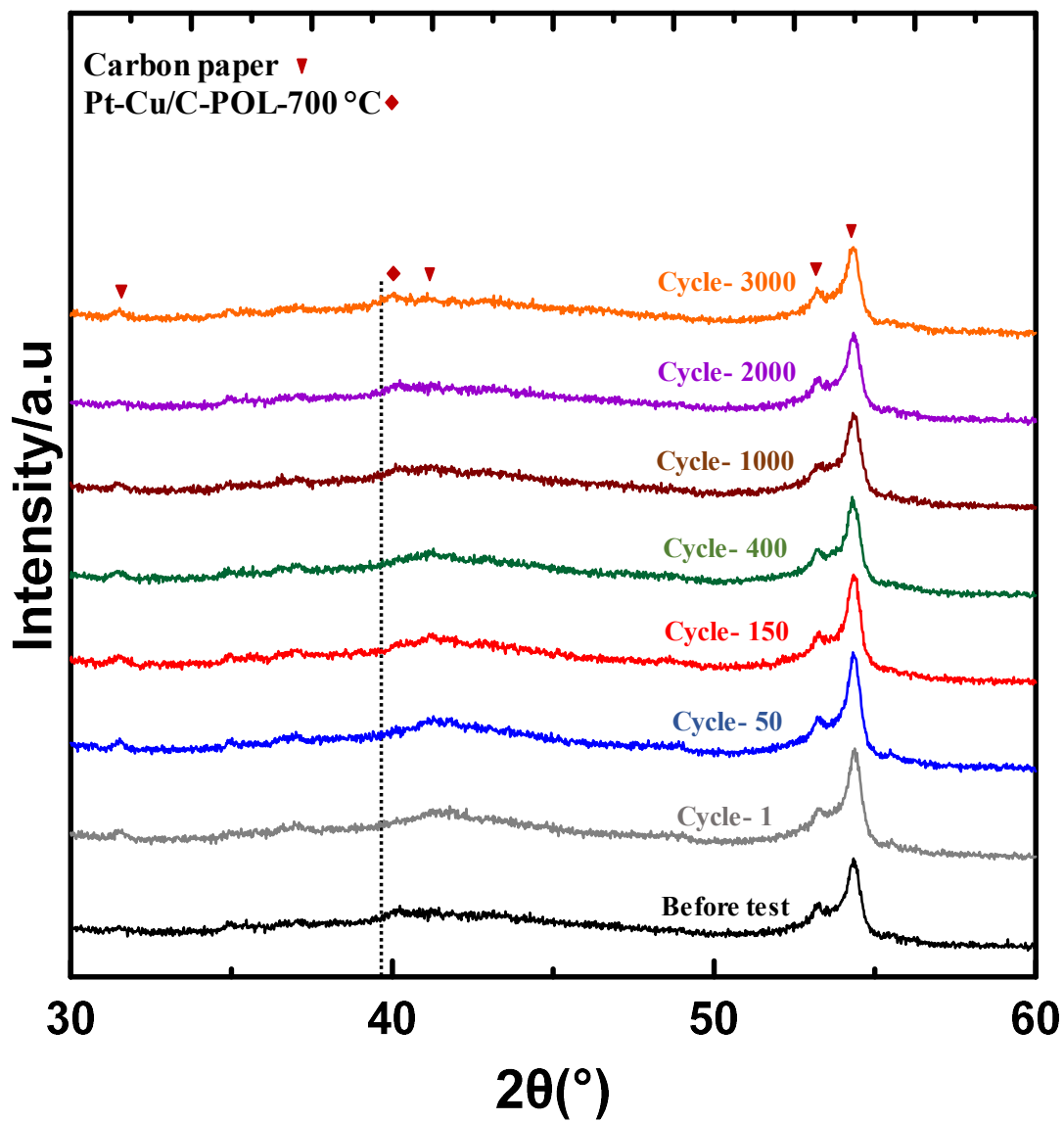


Figure 6.7. The XRD patterns for Pt-Cu/C-POL-700 °C at the specific cycles of AST.

6.3.3 AST and ECSA

6.3.3.1 AST of commercial samples (Pt/C and Pt₃Sn/C)

Figure 6.8 compares CVs obtained for Pt/C and Pt₃Sn/C after the specific number of cycles. The voltammograms in both cases displayed behavior of the common Pt. The resolved hydrogen adsorption/desorption peaks at low potential indicated that any surface oxide and possibly some atomic layers of alloying element of Sn were removed, revealing the Pt surface. However, the presence of Sn reduced the area under the hydrogen adsorption/desorption peaks and as a result reduced the ECSA for the Pt₃Sn/C sample. As the cycling numbers were increased the intensity of peaks related to Pt oxidation and reduction (0.6 to 1 V) and the hydrogen adsorption/desorption peaks (0 to 0.3 V) were gradually reduced. Therefore, the ECSA was also gradually reduced for both commercial samples. The intensity of the hydroquinone/quinone peaks for Pt/C was almost constant. The intensity of the quinone peak for the Pt₃Sn/C sample was increased slightly until 400 cycles and then reduced back to the starting intensity. The changes in the quinone region accompanied by the slight changes in the double layer region. The modification in the double layer region can be studied with more accuracy using the EIS analysis.

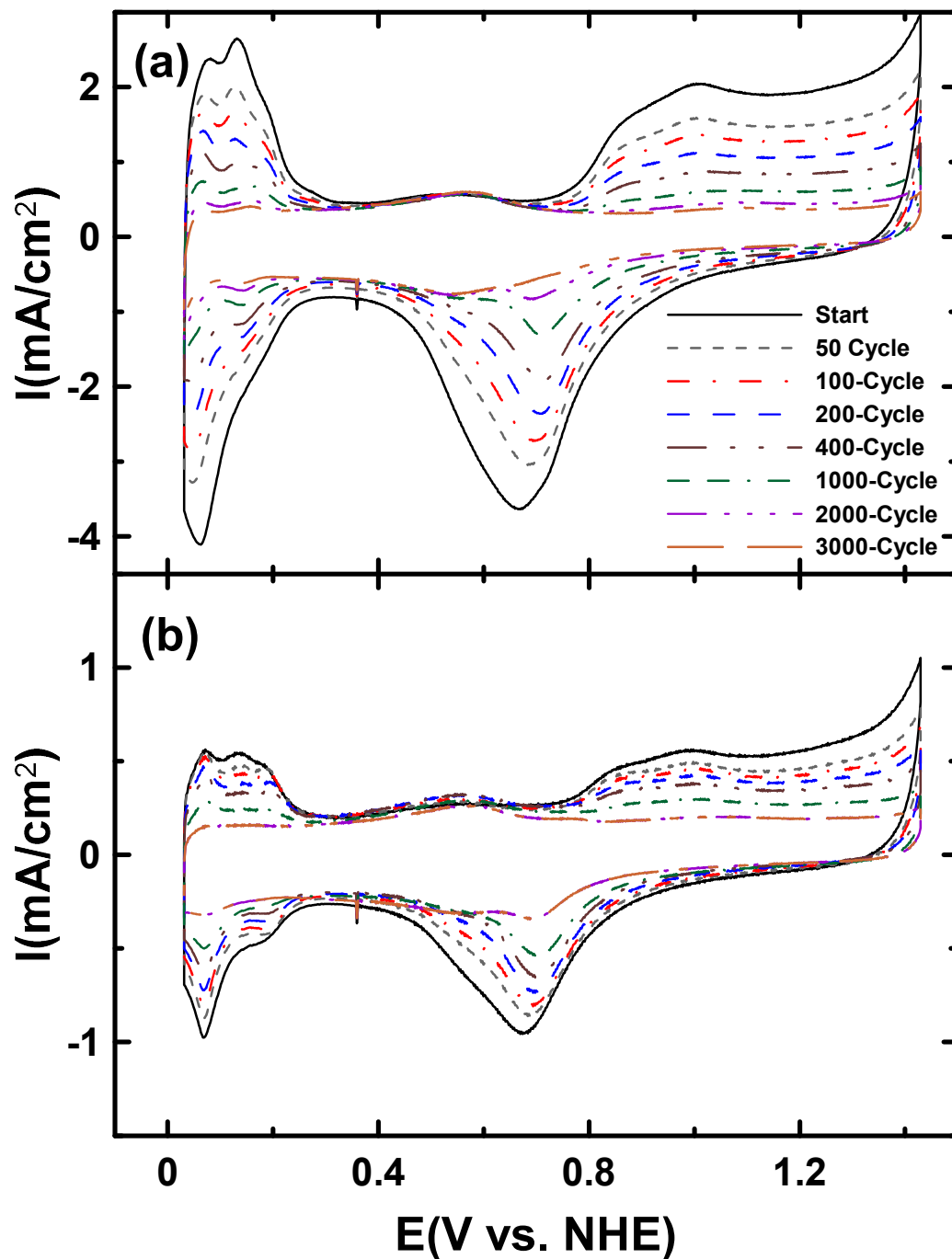


Figure 6.8. CVs obtained for the commercial samples (a) Pt/C and (b) $\text{Pt}_3\text{Sn}/\text{C}$ at the specific cycles of AST. Measurements were made in the N_2 -purged 0.5 M H_2SO_4 solution at a scan rate of 20 mV/s.

The EIS profile of Pt/C and Pt₃Sn/C are shown in Figure 6.9 and 10. This method can provide information such as resistance and capacitance of an electrode. The data collected from the EIS analysis can be displayed in three forms: Nyquist, capacitance, and normalized capacitance (NC) plots from which valuable information would be determined. The projection of the Warburg length with the real impedance (Z') axis is proportional to the total catalyst layer resistance ($R_{\Sigma}/3$), where R_{Σ} corresponds to the sum of ionic (R_{ionic}) and electronic resistance (R_{elect}) in the catalyst layer [49]. The variations in ionic resistivity within the catalyst layer can be better visualized through capacitance and NC plots [25, 50]. In the capacitance plots, the series capacitance ($-1/\omega Z''$) is plotted against the real impedance (Z'). A steeper slope in the high frequency region of the capacitance plot is an indication of higher proton conductivity within the catalyst layer and the limiting capacitance (LC) is proportional to active surface area (Platinum + carbon) [25, 26]. To draw the NC plots, the capacitances were normalized by the maximum capacitance in each graph [25, 26]. For both samples, a 45° Warburg-like region was observed in the high frequency region of Nyquist plots (Figure 6.9a and 10a). Comparing the resistance and capacitance of Pt/C at the different cycles shows that R_{Σ} and LC were almost unchanged and there was only slight decrease in R_{Σ} (Figure 6.9a and b). For Pt/C electrodes that were studied in this paper, the electronic contributions to the impedance are negligible and consequently it is safe to assume $R_{\Sigma} = R_{ionic}$ [49]. This indicates that the cycling process has no effect on the ionomer and carbon degradation and decrease in the initial R_{Σ} should be due to the hydration of ionomer which enhanced the proton conductivity and carbon particle exposure to electrolyte. Similar results have been reported previously for the other commercial Pt/C samples [12].

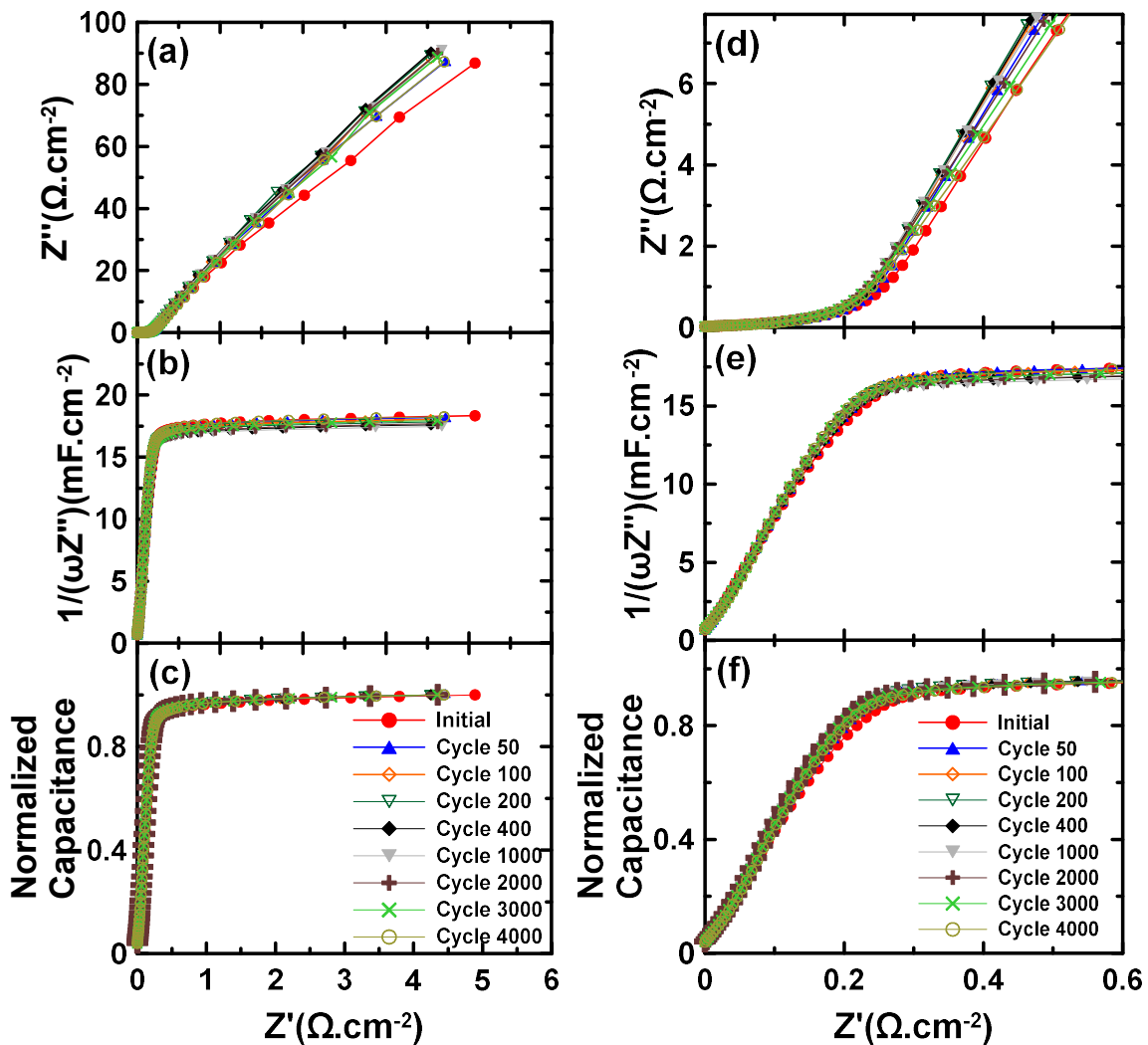


Figure 6.9. (a) (b) and (c) The EIS responses obtained at a DC bias potential of 0.360 V vs. NHE for the commercial sample (Pt/C) at the specific cycles of AST. (d), (e) and (f) Expansion of the high frequency region. Measurements were made in the N_2 -purged 0.5 M H_2SO_4 solution.

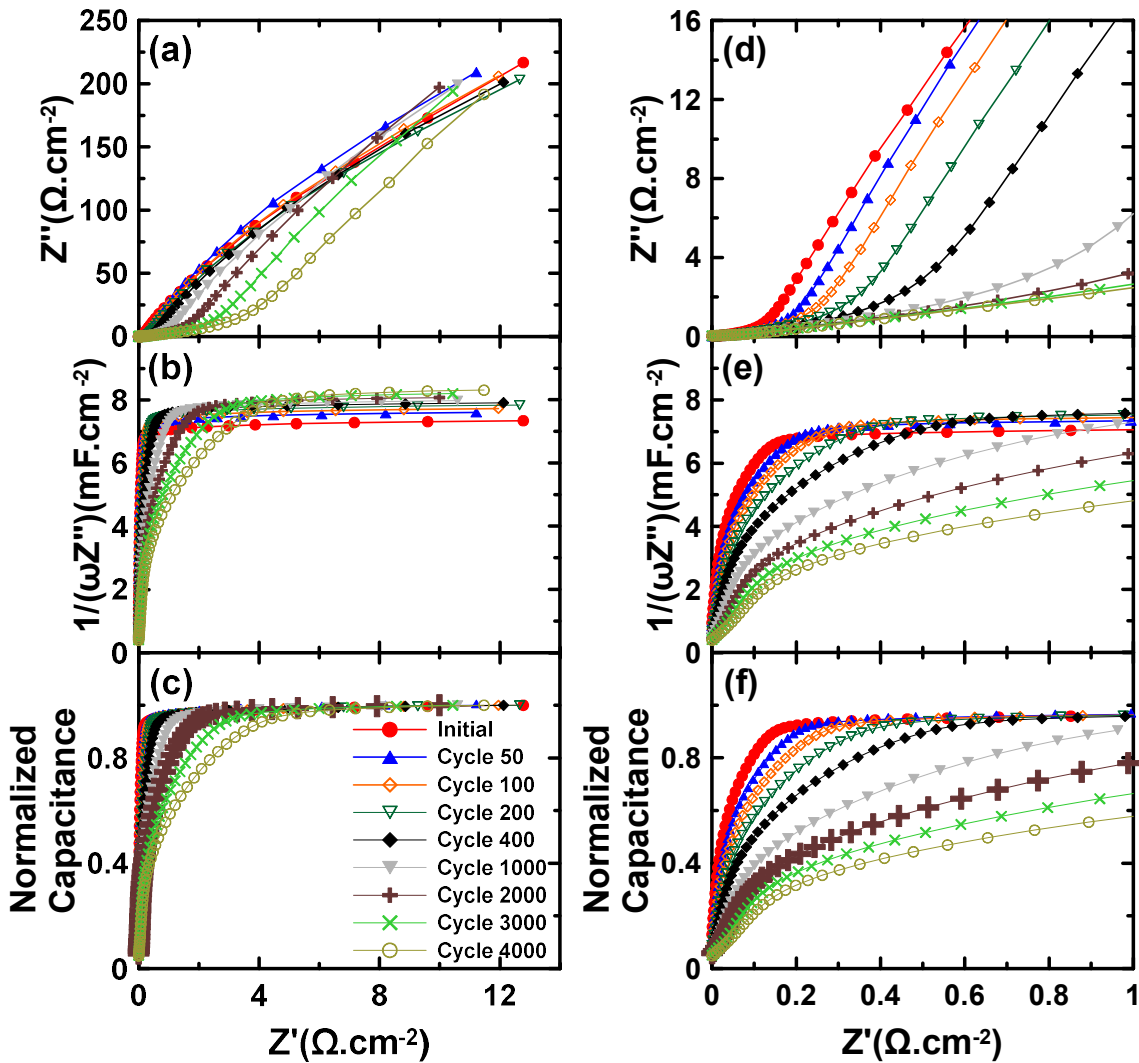


Figure 6.10. (a) (b) and (c) The EIS responses obtained at a DC bias potential of 0.360 V vs. NHE for the commercial sample (Pt₃Sn/C) at the specific cycles of AST. (d), (e) and (f) Expansion of the high frequency region. Measurements were made in the N₂-purged 0.5 M H₂SO₄ solution.

The Pt₃Sn/C sample showed completely different behaviour (Figure 6.10). Both R_{Σ} and LC changed dramatically with increasing the number of cycles. The increase in the impedance of Pt₃Sn/C indicates that either the electronic or ionic resistance was increased during cycling. The procedure and ionomer that were used to produce the Pt/C and Pt₃Sn/C

electrodes were same; therefore, R_{Σ} increased due to the electronic resistance variations or changes within the ionomer. The R_{Σ} changes could better be seen by the NC plots (Figure 6.10c). Furthermore, the increase in LC could be due to hydration and exposing more carbon particles to the solution, the Pt-alloy particles roughening caused by dealloying and removing of Sn-oxides from the particle surface. The ECSA reduction, the quinone peak intensity changes and the R_{Σ} enhancement with cycling indicate that LC and R_{Σ} most probably increased due to dissolution of Sn and interaction of Sn-ions ($\text{Sn}^{2+/4+}$) with the ionomer.

6.3.3.2 AST of Pt-Mn/C-SC and Pt-Mn/C-SC-700 °C

Figure 6.11 shows CVs obtained for the Pt-Mn/C-SC and Pt-Mn/C-SC-700 °C after selected number of cycles. Similar to the commercial samples, the in-house samples also illustrated the typical behaviour of Pt in the acid solution. The hydrogen adsorption/desorption (0.03 to 0.3 V), the hydroquinone/quinone peaks (0.3 to 0.6 V) and the Pt oxidation/reduction (0.6 to 1 V) were all clearly observed. In both samples, increasing the number of cycles dramatically affected the hydrogen adsorption/desorption region and the ECSA loss continued until the end of AST. There were distinctive differences between the Pt-Mn samples before and after the heat treatment. One of the differences was related to the oxidation and reduction peaks of Pt. For Pt-Mn/C-SC-700°C, the Pt oxidation peak moved slightly to the lower potentials and the reduction peak of PtO_x shifted to the higher potentials up to the 100 cycles. It was observed that the shift of PtO_x reduction peak to higher potential has reduced the adsorption strength of the oxygen containing species such as OH_{ads} and has improved the oxygen reduction activity of

catalysts [26]. Afterward, the PtO_x moved toward the lower potentials as observed for the commercial samples. In addition, the intensity of the PtO_x peak was reduced during cycling. The positive shift of the PtO_x peak could be caused by roughening of the particles or by formation of the Pt rich shells during cycling. After 100 cycles, the PtO_x peak shifted toward lower potentials probably caused by the higher ECSA loss which reduced the PtO_x peak intensity.

Comparing the hydrogen region of Figure 6.11a and b illustrates that during first 50 cycles, different Pt crystalline planes become resolved for the as-produced and heat treated Pt-Mn samples. Previous studies have shown that the different surface crystalline planes illustrates distinctive hydrogen adsorption/disruption characteristics [51]. Therefore, the resolved peak in the hydrogen region indicates that by cycling different surface structures became more pronounced. This is due to Mn depletion from the surface during cycling, which left a more Pt rich surface behind which is in agreement with the ICP, XRD and ECSA analyses. The heat treatment promoted (100) facet formation on the surface while the as-produced samples had mostly the (111) plane characteristics. Formation of different facets on the surface of the alloyed particles is related to the formation of the Pt-Mn intermetallic structures upon heat treatment which has reported in chapter 3 and 4.

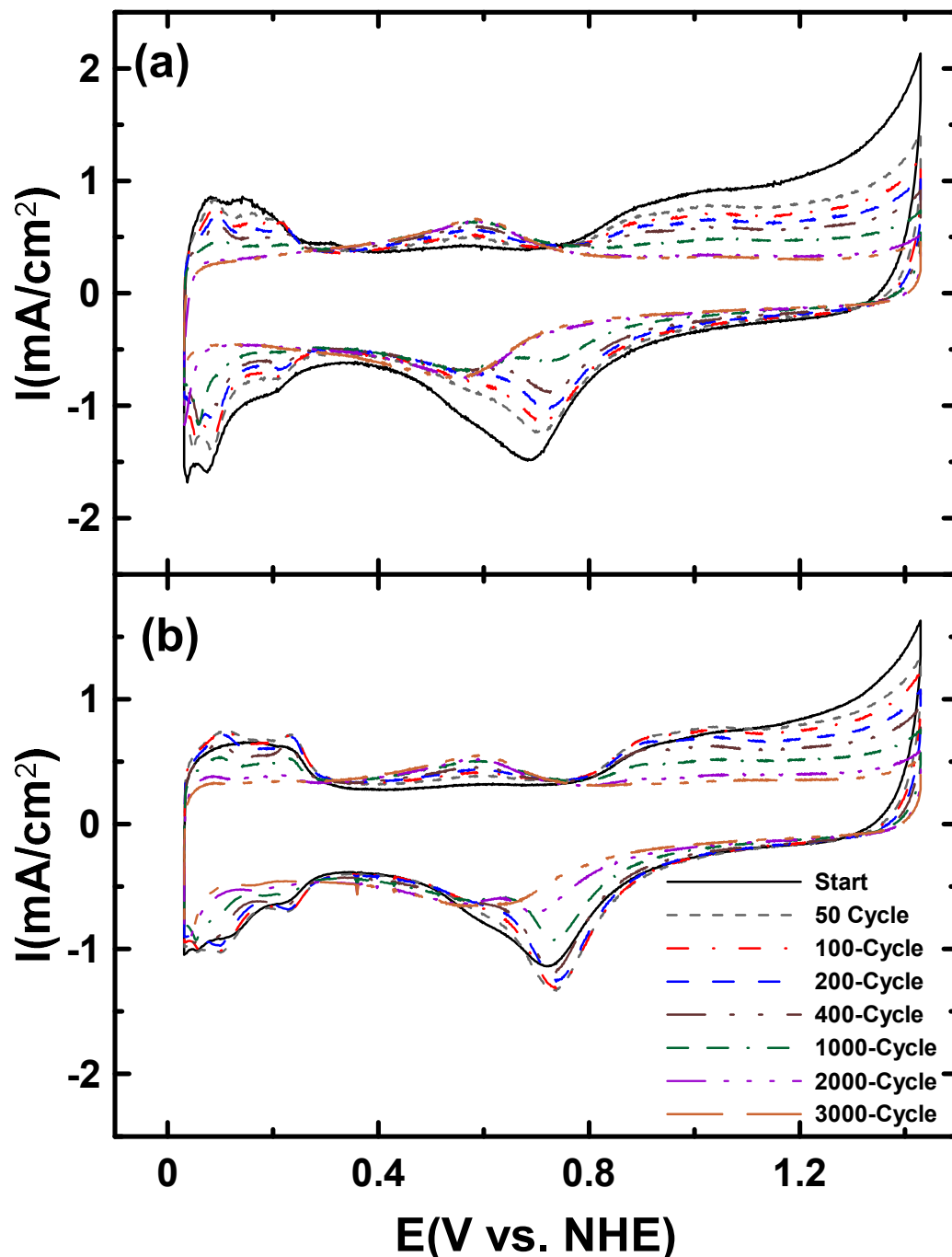


Figure 6.11. CVs obtained for (a) Pt-Mn/C-SC and (b) Pt-Mn/C-SC-700 °C at the specific cycles of AST. Measurements were made in the N_2 -purged 0.5 M H_2SO_4 solution at a scan rate of 20 mV/s.

Additionally, increasing the cycling number increased the intensity of the quinone peak for both samples. This is most likely just partial oxidation of the carbon and it should not be mistaken with carbon corrosion. This could be due to the exposure of the more carbon surface to the acidic solution which could be caused by removal of surface adsorb species or removing of the metal oxides from the surface of the carbon particles. The metal oxides can be formed during the synthesis of the samples or afterward during drying and storing the samples. In order to reach a final conclusion, the EIS tests could be helpful. It has shown that the EIS tests could be useful to identify the mechanism of the catalyst degradation [25, 26].

The EIS responses are shows in Figure 6.12 and 13. The Pt-Mn/C-SC and Pt-Mn/C-SC-700 °C displayed very similar EIS profile. R_{Σ} decreased with cycling and the capacitance was increased for both samples. The R_{Σ} reduction was also shown more distinctively by the NC plots (Figure 6.12c and 13c). The reduction of R_{Σ} can be due to the hydration of the catalyst layer or removal of the oxide phases. The capacitance enhancement during potential cycling could also could be caused dissolving the metal oxide and hydration. Our studies in chapter 3 and 4 by XRD analysis have confirmed the presence of metal oxides for as-produced Pt-Mn samples, but results in Figure 3.5 and the XRD results from chapter 3 have shown that the Mn oxides are not stable in acidic media and should dissolve very fast in contact with acid. This has also been reported by other groups [44]. Therefore, LC should be affected by metal oxide removal. On the other hand, roughening of the alloy particles or nucleation of new particles could be another reason for the higher LC values. Although roughening of the particles was confirmed by CVs and the Mn depletion, the ECSA was continuously decreased with cycling. As a result,

modifications of the particle surface area could not control or increase LC for the Pt-Mn samples. it can be concluded that the LC changes was mostly due to the removal of metal oxide which in the case of Mn had not effected the ionomer resistance.

Although the supporting material was Vulcan carbon for all the commercial and in-house samples, the pure Pt samples was also produced using the same Vulcan carbon that used for Pt-Mn samples. This was done to fully understand the cause of the LC changes for the in-house samples and eliminate any changes could be caused by the presence of the alloying element (Mn). The results are shown in Figure 6.14 and 6.15. The same behaviour as the Pt-Mn samples was observed for pure Pt made in-house. The quinone peaks were intensified, LC was increased and ECSA and R_{Σ} was reduced with the potential cycling. The similar behaviour of LC and R_{Σ} for the pure and alloyed samples indicates that this phenomenon is due to formation of the metal oxide on the surface of carbon particles which was expected due to the production method (impregnation) and lack of further treatment in reducing environment (for example H₂ environment). In addition, these results illustrate that there is no carbon or ionomer degradation and R_{Σ} reduced due to hydration (lower ionic resistance).

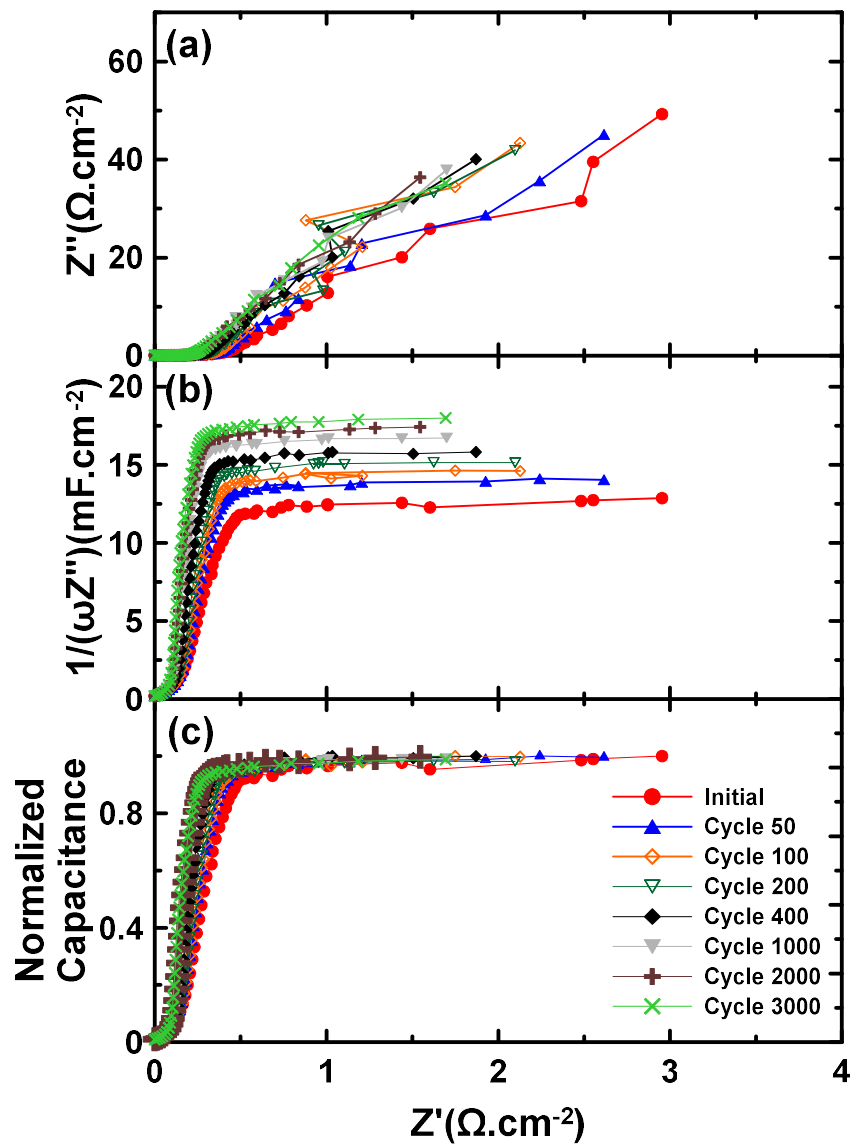


Figure 6.12. The EIS responses obtained at a DC bias potential of 0.360 V vs. NHE for Pt-Mn/C-SC at the specific cycles of AST. Measurements were made in the N_2 -purged 0.5 M H_2SO_4 solution.

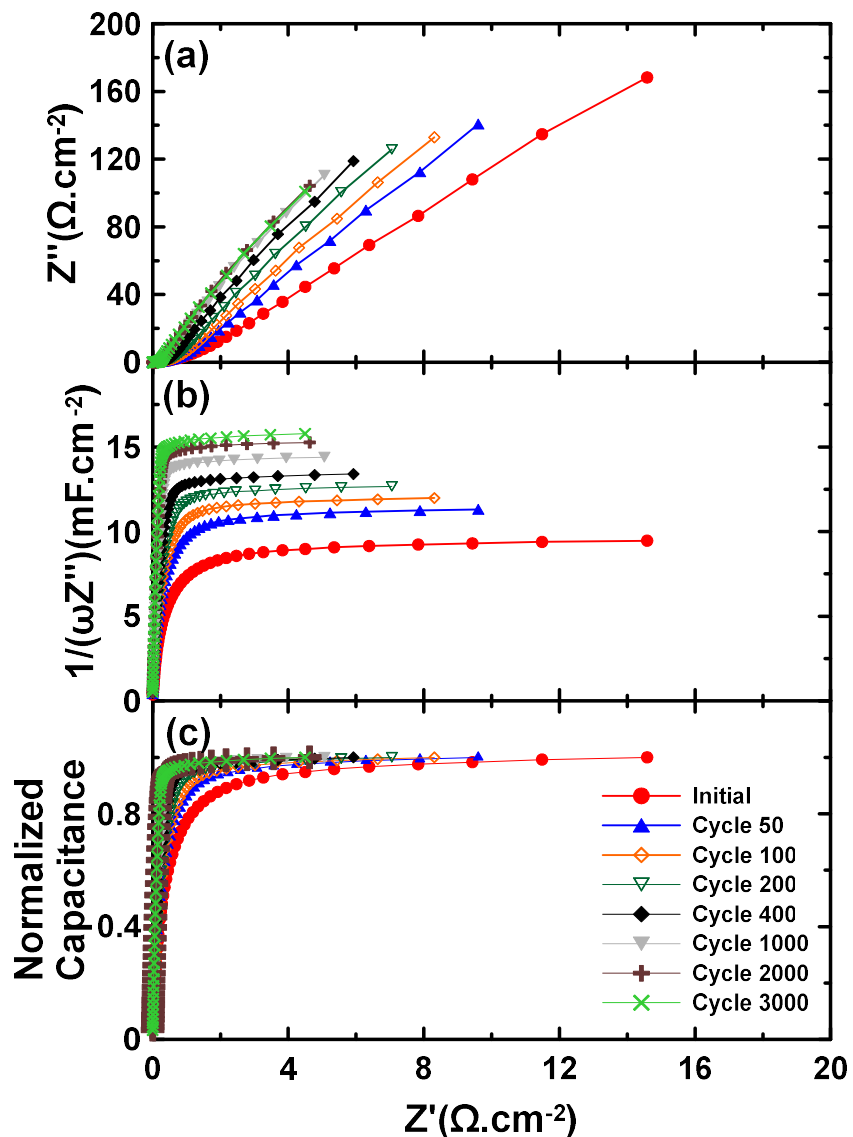


Figure 6.13. The EIS responses obtained at a DC bias potential of 0.360 V vs. NHE for Pt-Mn/C-SC-700 °C at the specific cycles of AST. Measurements were made in the N₂-purged 0.5 M H₂SO₄ solution.

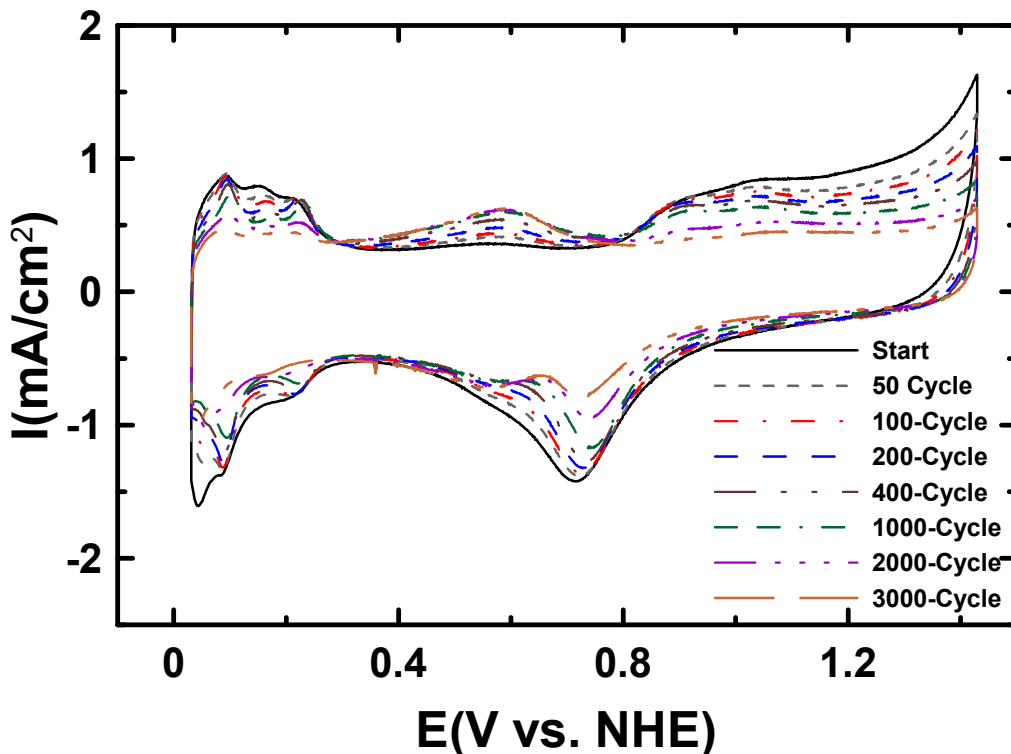


Figure 6.14. CVs obtained for the pure Pt/C sample made in-house at the specific cycles of AST. Measurements were made in the N_2 -purged 0.5 M H_2SO_4 solution at a scan rate of 20 mV/s.

6.3.3.3 AST of Pt-Cu/C-POL and Pt-Cu/C-POL-700 °C

The set of CVs recorded for Pt-Cu/C-POL and Pt-Cu/C-POL-700 °C are displayed in Figure 6.16. These samples showed Pt behaviour as well as the other samples. As it was expected, the ECSA were reduced and the quinone/hydroquinone peaks became more distinctive for the both samples as the cycling continued. Therefore, the LC could be altered as it was seen previously for the Pt-Mn samples. However, there were some differences between as-produced and the heat treated Pt-Cu samples. The hydrogen adsorption/distortion profile was changed by applying the heat treatment. This illustrates

that the crystalline planes on the surface of particles was modified during the heat treatment. The same modification has seen for the Pt-Mn alloy. The hydrogen adsorption/distortion were become more distinctive on specific crystalline planes with cycling up to 400 cycles. Increasing the number of cycles reduced the intensity of these peaks but the adsorption/desorption profiles were almost identical until the end of cycling process. This results confirms that dealloying of Cu was occurred during the cycling and left a Pt rich surface behind. In addition, the adsorption/desorption profiles in Figure 6.16 shows that the heat treatment of the Pt-Cu samples prompted the (100) crystalline facet and the intensity of other adsorption was reduced. It has been reported that the (100) facet adsorption peak should be seen around 0.2 to 0.3 V vs. NHE [52]. This could be due to the formation of the PtCu and PtCu₃ intermetallic phases which has discussed in section 5.3.1.2. These intermetallic phases have the trigonal and simple cubic structures, respectively.

The EIS responds of Pt-Cu/C-POL and Pt-Cu/C-POL-700 °C at selected cycling numbers are shown in Figure 6.17 and 18. The Pt-Cu samples also showed almost similar increase in LC and reduction in R_{Σ} with cycling which were seen for the Pt-Mn and pure Pt samples. The sudden decrease in capacitance at the cycle 3000 for Pt-Cu/C-POL-700 °C (Figure 6.18b) was due to delamination and the cracks occurred in the deposited sample on the GC electrode. The hydration of catalyst layer and removal of metal oxide reduced R_{Σ} and increased LC for the Pt-Cu samples same as the Pt-Mn samples. It can be concluded that neither the synthesis of alloyed samples nor the heat treatment were altered R_{Σ} and LC behaviour for all the samples made in-house. Therefore, it was confirmed that the ECSA loss and the changes in the crystalline structure were the main elements that were

controlling the stability of different sample and these two factors should be studied more carefully.

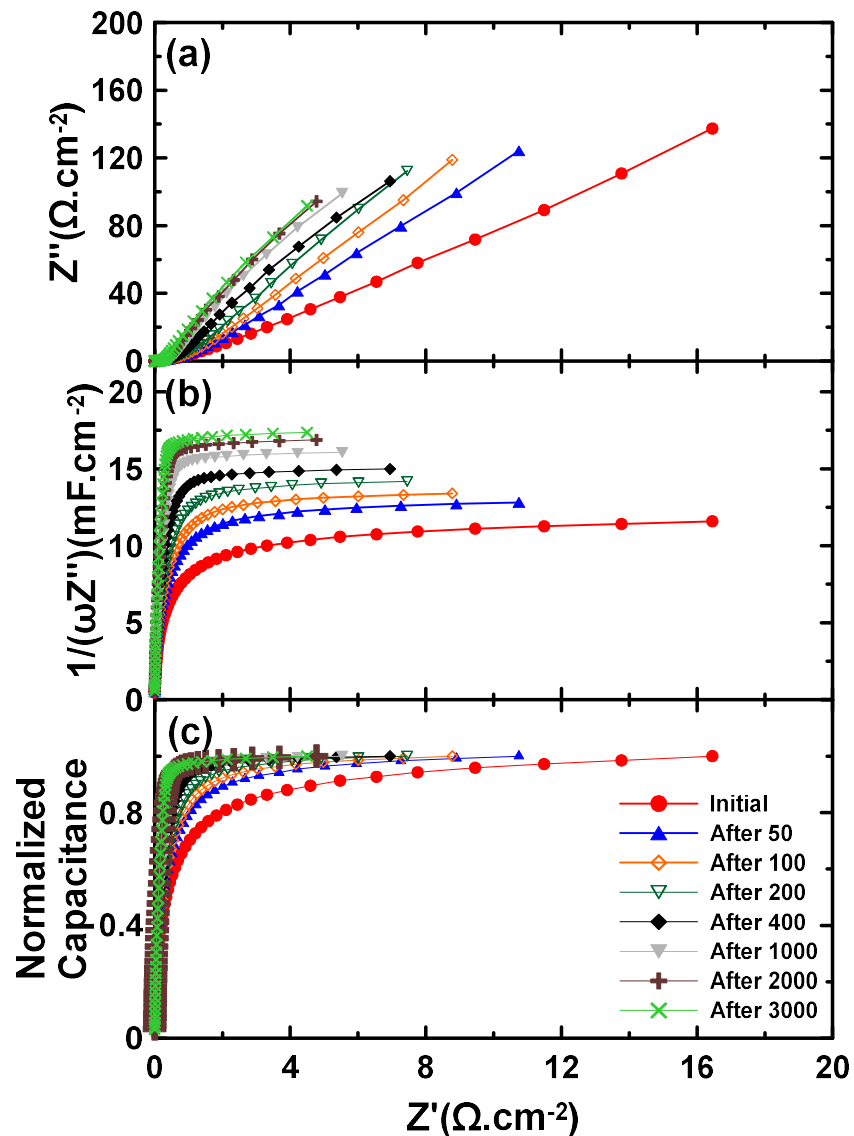


Figure 6.15. The EIS responses obtained at a DC bias potential of 0.360 V vs. NHE for the pure Pt/C sample made in-house at the specific cycles of AST. Measurements were made in the N₂-purged 0.5 M H₂SO₄ solution.

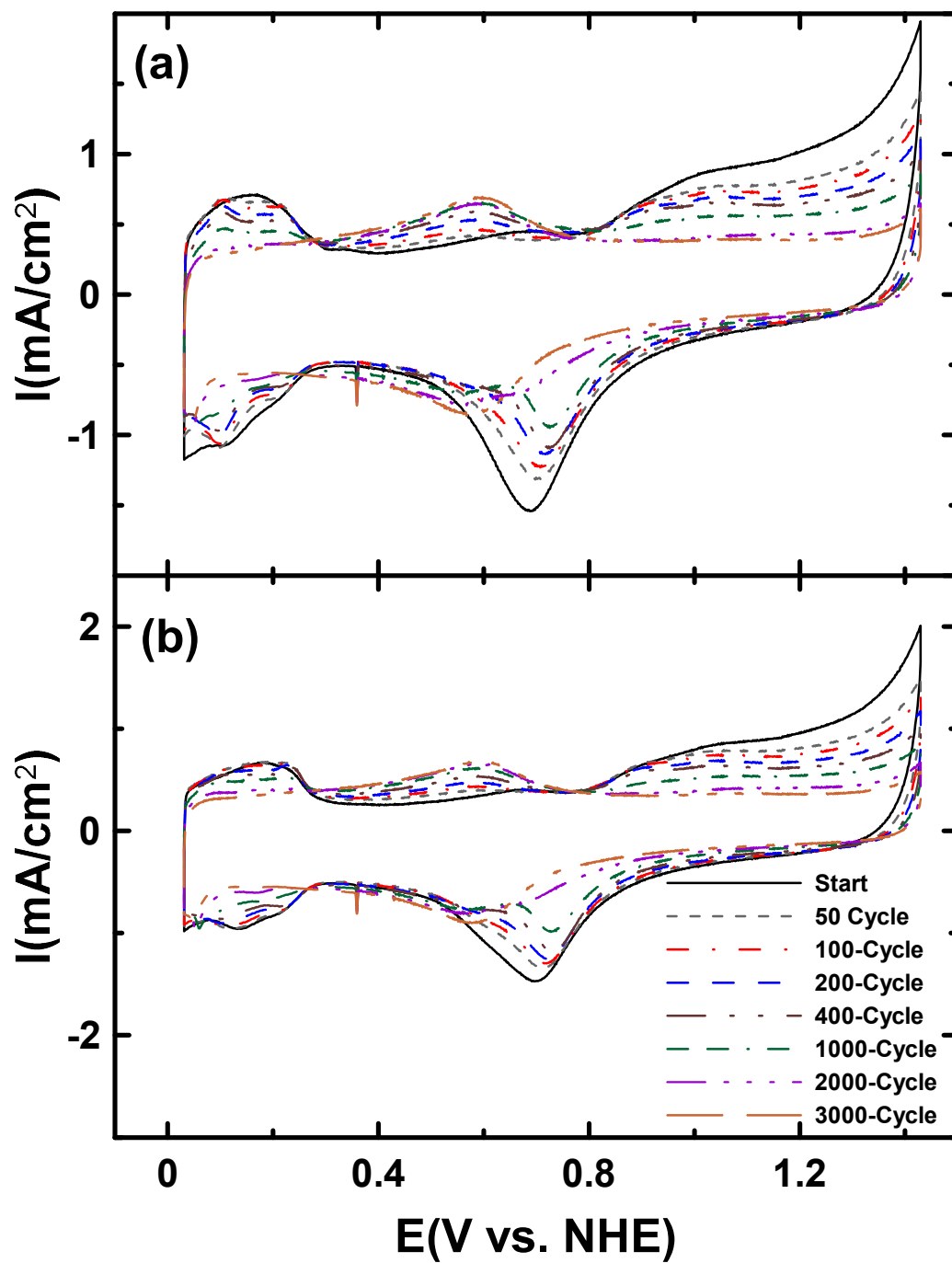


Figure 6.16. CVs obtained for (a) Pt-Cu/C-POL and (b) Pt-Cu/C-POL-700 °C at the specific cycles of AST. Measurements were made in the N_2 -purged 0.5 M H_2SO_4 solution at a scan rate of 20 mV/s.

Figure 6.19 summarizes the ECSA values calculated for all the samples at the selected cycles. The Pt/C samples had the highest ECSA values compared to other samples. The ECSA values at the specific cycles were normalized by the initial ECSA to determine the percentage of ECSA loss for all the samples and presented in Fig. 17b. In addition, the normalized ECSA data are shown in the logarithmic scale in Figure 6.19c to study the beginning of life (BOL) for the samples. The normalized ECSA illustrates that Pt₃Sn/C, Pt-Mn/C-SC-700 °C, Pt-Cu/C-POL, Pt-Cu/C-POL-700 °C showed higher resistance to the ECSA loss compared with the Pt/C and Pt-Mn/C-SC samples. Comparing the heat treated Pt-Mn and Pt-Cu samples to the as-produced ones indicates that the heat treatment in both samples increased the durability of samples. Specially, the stability of the Pt-Mn samples increased significantly by the heat treatment. These results show that heat treatment and polyol method improved the stability of the samples.

Studying BOL for different samples illustrates a unique behaviour for the heat treated samples (Figure 6.19c). Pt-Mn/C-SC-700 °C and Pt-Cu/C-POL-700 °C displayed a great resistance to ECSA loss at the beginning of cycling. This behaviour could be due to dealloying and the surface roughening which resulted in a Pt rich surface for the heat treated samples. It can be concluded that dealloying of the bigger particles and formation of the Pt rich surface protected the rest of alloying element in the core structure from depleting and that was the reason the heat treated samples showed the higher concentration of the alloying element in both Pt-Mn and Pt-Cu samples after test (Table 6.1). Figure 6.19c also shows that, after the first 100 cycles, the slope for the ECSA loss was almost similar for all the plots. This indicates that the mechanism of degradation at BOL was different but it became similar by increasing the number of cycles. Similar results have reported for the

Pt-Co and Pt-Cu systems [35, 37, 48]. It can be concluded that that the initial stage of degradation is controlled by the alloyed particle degradation and after certain number of cycles and formation of the Pt-rich surface for the Pt-Mn and Pt-Cu samples, the degradation mechanisms were become comparable to commercial samples.

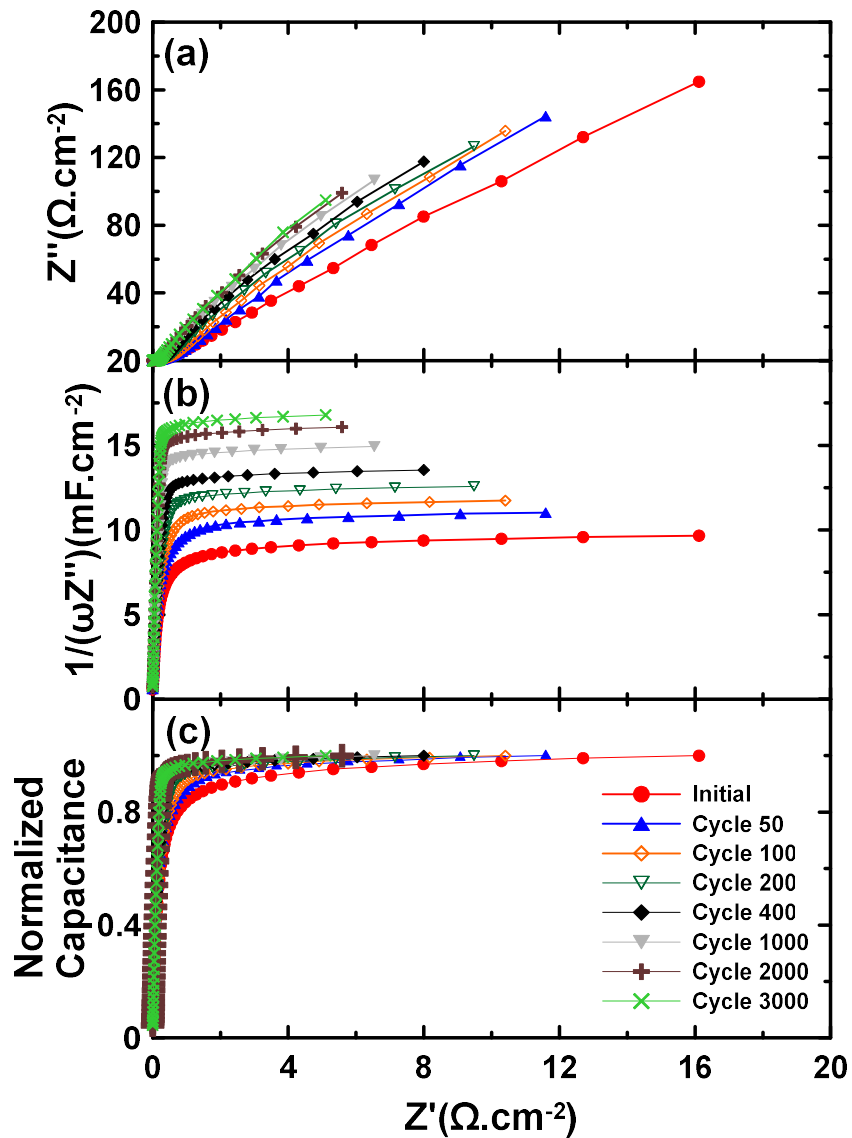


Figure 6.17. The EIS responses obtained at a DC bias potential of 0.360 V vs. NHE for Pt-Cu/C-POL at the specific cycles of AST. Measurements were made in the N_2 -purged 0.5 M H_2SO_4 solution.

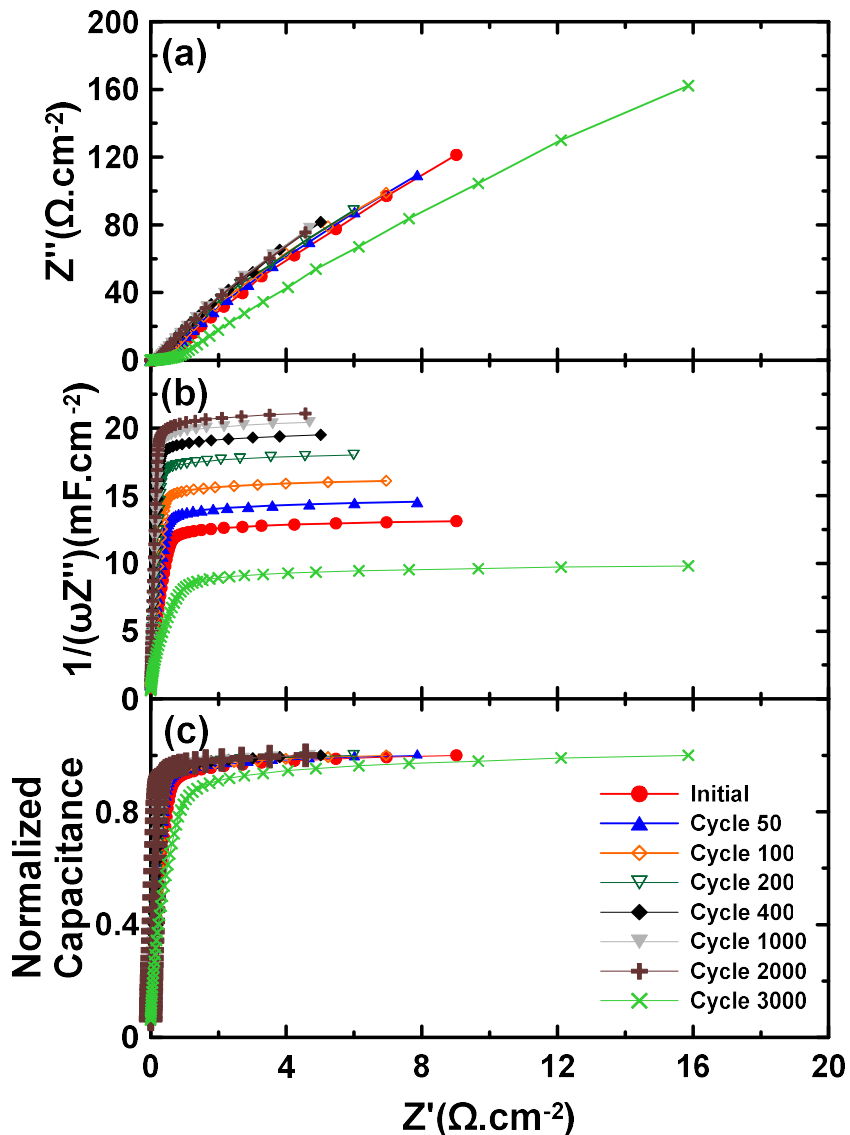


Figure 6.18. The EIS responses obtained at a DC bias potential of 0.360 V vs. NHE for Pt-Cu/C-POL-700 °C at the specific cycles of AST. Measurements were made in the N₂-purged 0.5 M H₂SO₄ solution.

6.3.4 AST and EOR activity

In order to study the effect of ethanol oxidation on the stability of the samples and also to examine the EOR activity changes during AST, all the samples were exposed to the

ethanol solution and CVs were recorded for the specific cycling numbers. The CVs obtained in the ethanol solution for different samples are presented in Figure 6.20, 21 and 22. In general, the EOR activity of the samples were reduced with cycling. This indicates that ECSA loss, the crystalline degradation along with depletion of the alloying element for the alloyed particles reduced the EOR activity of different samples. However, the response of forward and backward scans in CVs were unique for every sample. Therefore, the current density of the peak in the forward (I_F) and backward (I_B) scans were determined for the specific cycles and displayed in Figure 6.23a and b. In addition, the ratio of I_F/I_B are shown in Figure 6.23c. The previous studies have confirmed that the ratio of I_F/I_B can be utilized to evaluate and compare the poisoning resistance of different catalysts. The bigger the ratio, the higher the tolerance [53].

Figure 6.23 shows that although the Pt content was higher for the commercial samples, the EOR activity for the Pt-Mn and Pt-Cu samples after heat treatment was close or better than the commercial samples at BOL. Figure 6.24 shows I_F which was normalized for the Pt content. Figure 6.24 shows that Pt was utilized the best by the Pt-Mn/C-SC-700 °C sample and the Pt-Mn/C-SC-700 °C sample was also better in utilizing Pt compared to the commercial samples. It is important to consider that the degradation of some alloyed samples after 2000 cycles were faster and this caused sudden changes in the activity of the samples during cycling in the ethanol solution; therefore, the results reported here were compared mostly until 2000 cycles.

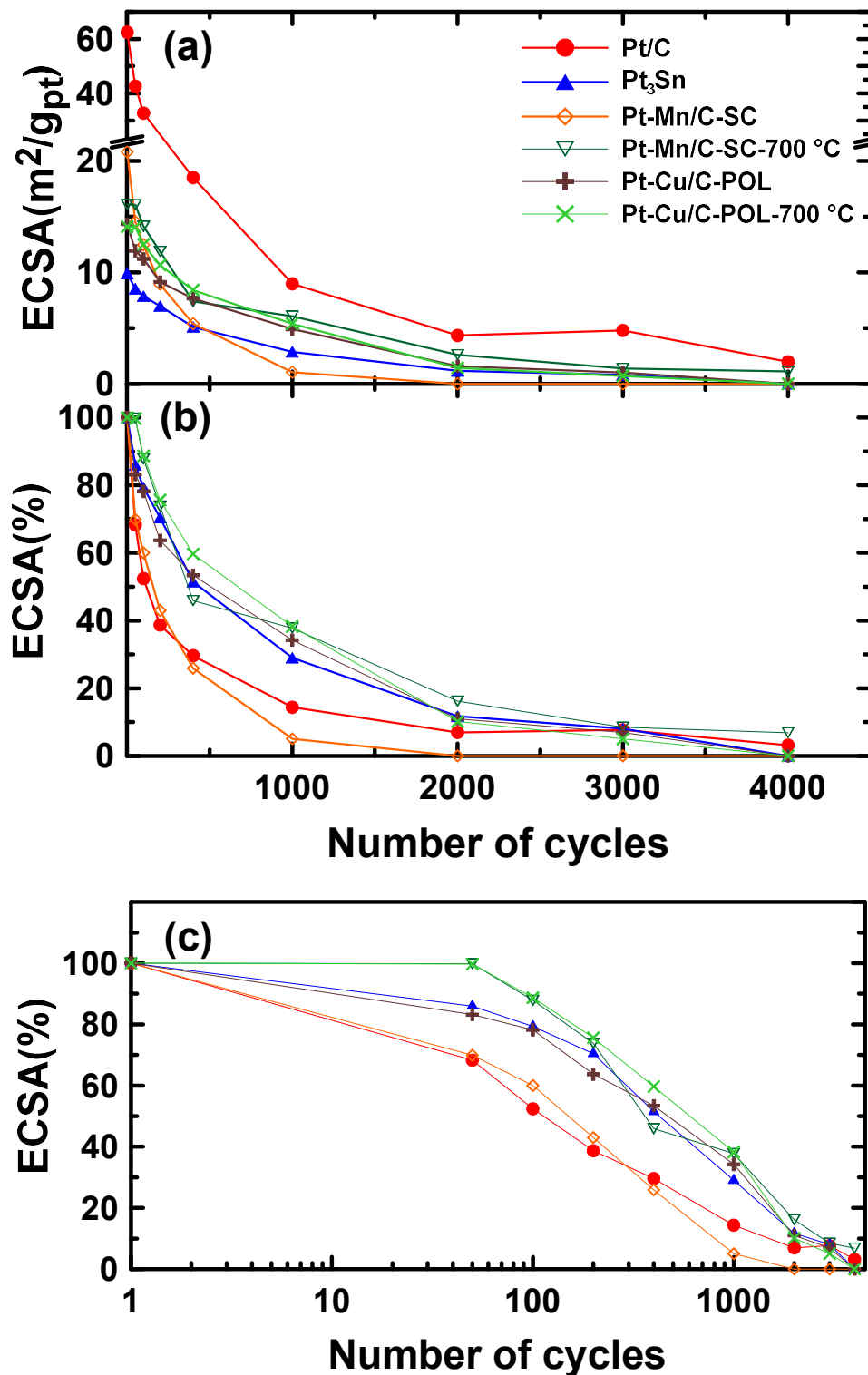


Figure 6.19. The ECSA changes for different samples which were determined from Figure 6.8, 11 and 16 at the specific cycles of AST.

Comparing the activity of the commercial samples (Pt/C and Pt₃Sn/C) illustrates that the intensity of I_F was higher for Pt/C until 2000 cycles afterward the activity for both samples were similar. The intensity of I_B for Pt/C was lower than Pt₃Sn/C at BL but after the first 50 cycle, it was increased and was the highest compared to all the other samples until 2000 cycles. The ratio of I_f/I_B shows that Pt/C has higher resistance to poisoning compared to Pt₃Sn/C. It has been reported previously that Sn is one of the best alloying elements to reduce poisoning and increase the EOR activity of the Pt alloys [20]. However, the commercial samples we used in our lab responded differently. This may be related to the fast degradation in the crystalline structure and depletion of Sn which were shown by the ex-situ ICP and XRD analyses in section 6.3.1 and 6.3.2. Figure 6.24 illustrates that the utilization of Pt in both Pt/C and Pt₃Sn/C were very similar which can be important from cost point of view, but the Pt-Sn sample tested in the lab was not advisable for the fuel cell or sensing application based on the activity, poisoning tolerance and durability responds.

The heat treatment of the as-produced Pt-Mn sample increased I_F more than I_B; therefore, the ratio of I_F/I_B for this sample enhanced for a great extend after the heat treatment. This indicates that the poisoning of Pt-Mn/C-SC-700 °C was much lower than both commercial samples in all cycles except the few first cycles. Former studies have shown that the crystalline planes have a great impact on the ethanol oxidation. For examples, the (100) plane is more favorable to oxidize ethanol compared to the (111) plane [54, 55]. Our studies were shown that due to the heat treatment different crystalline planes were promoted during the cycling; therefore, these modified Pt-Mn particles with different surface crystalline structures could be the reason for the higher poisoning resistivity and the higher EOR activity. Besides, based on Figure 6.24, the Pt utilization was improved after the heat treatment dramatically (almost 4 time). The differences in the activity of Pt-

Mn/C-SC and Pt-Mn/C-SC-700 °C was higher at BOL but it was decreased slightly during cycling.

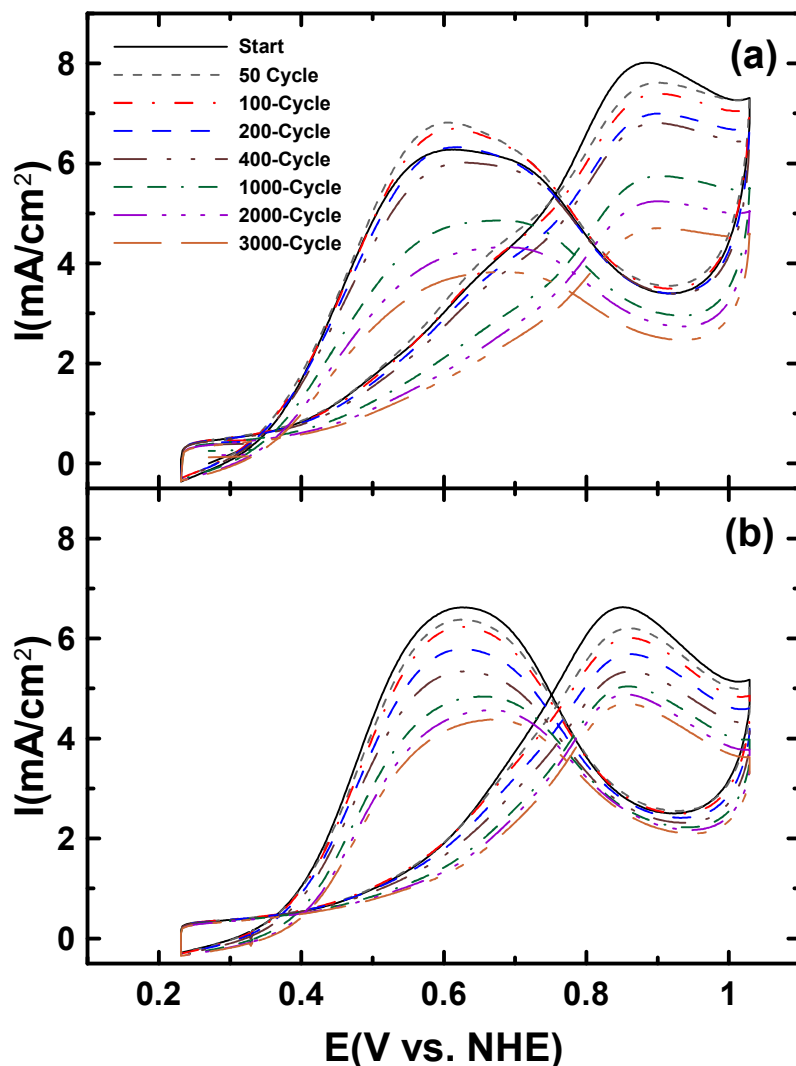


Figure 6.20. CVs obtained for the commercial samples (a) Pt/C and (b) $\text{Pt}_3\text{Sn}/\text{C}$ at the specific cycles of AST. Measurements were made in the N_2 -purged 0.5 M H_2SO_4 containing 0.1 M ethanol at a scan rate of 20 mV/s.

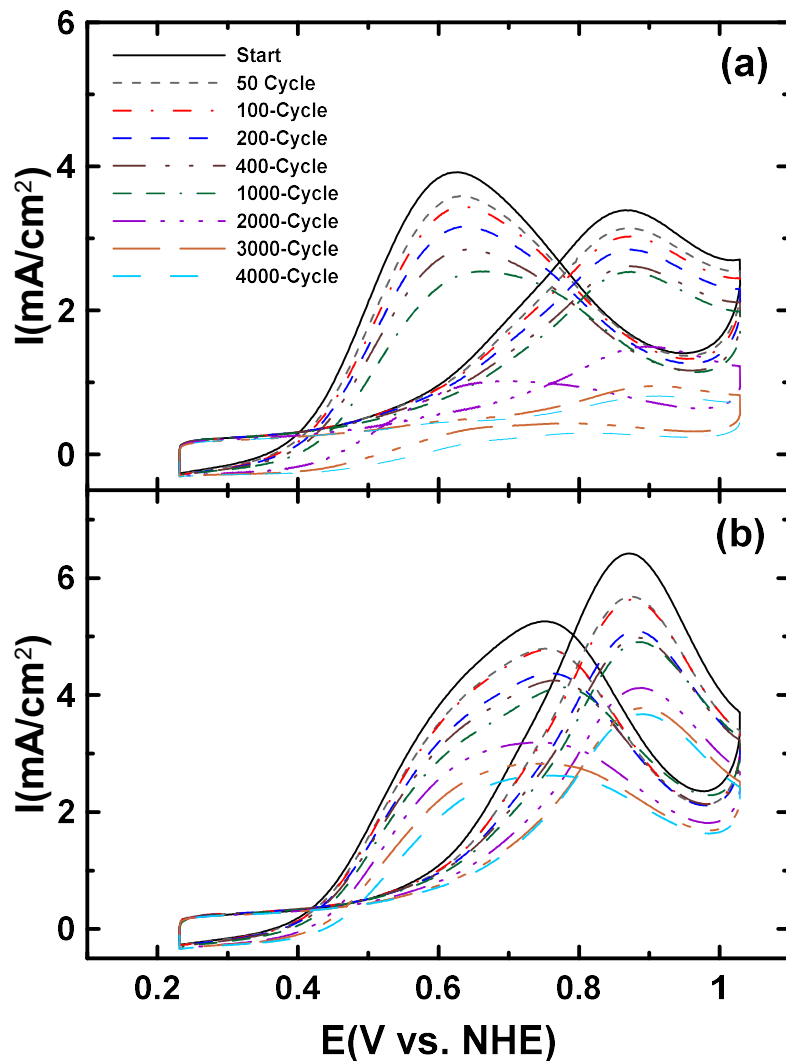


Figure 6.21. CVs obtained for (a) Pt-Mn/C-SC and (b) Pt-Mn/C-SC-700 °C at the specific cycles of AST. Measurements were made in the N₂-purged 0.5 M H₂SO₄ containing 0.1 M ethanol at a scan rate of 20 mV/s.

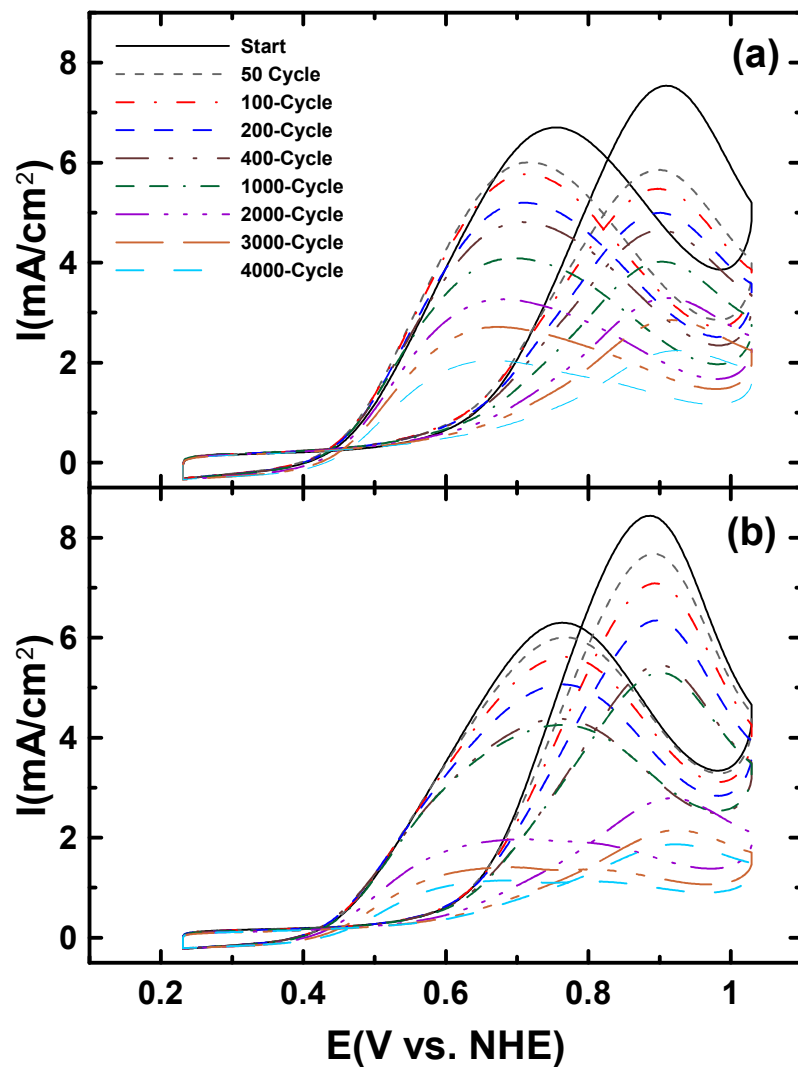


Figure 6.22. CVs obtained for (a) Pt-Cu/C-POL and (b) Pt-Cu/C-POL-700 °C at the specific cycles of AST. Measurements were made in the N_2 -purged 0.5 M H_2SO_4 containing 0.1 M ethanol at a scan rate of 20 mV/s.

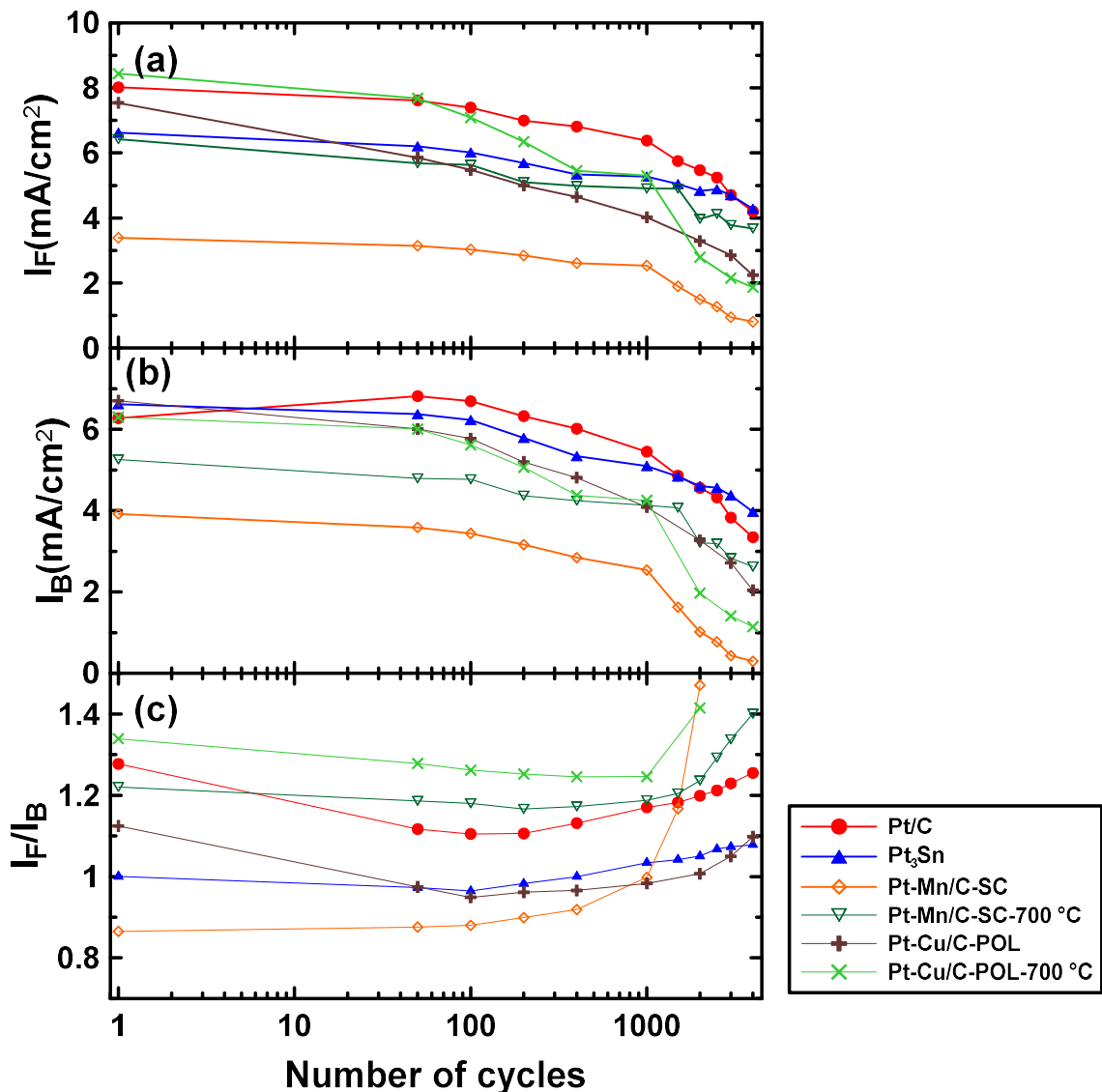


Figure 6.23. The intensity of the peak current measured by (a) the forward scan (I_F), (b) backward scan (I_B) and (c) the ratio of I_F/I_B for different samples which were determined from Figure 6.20, 6.21 and 6.22 at the specific cycles of AST.

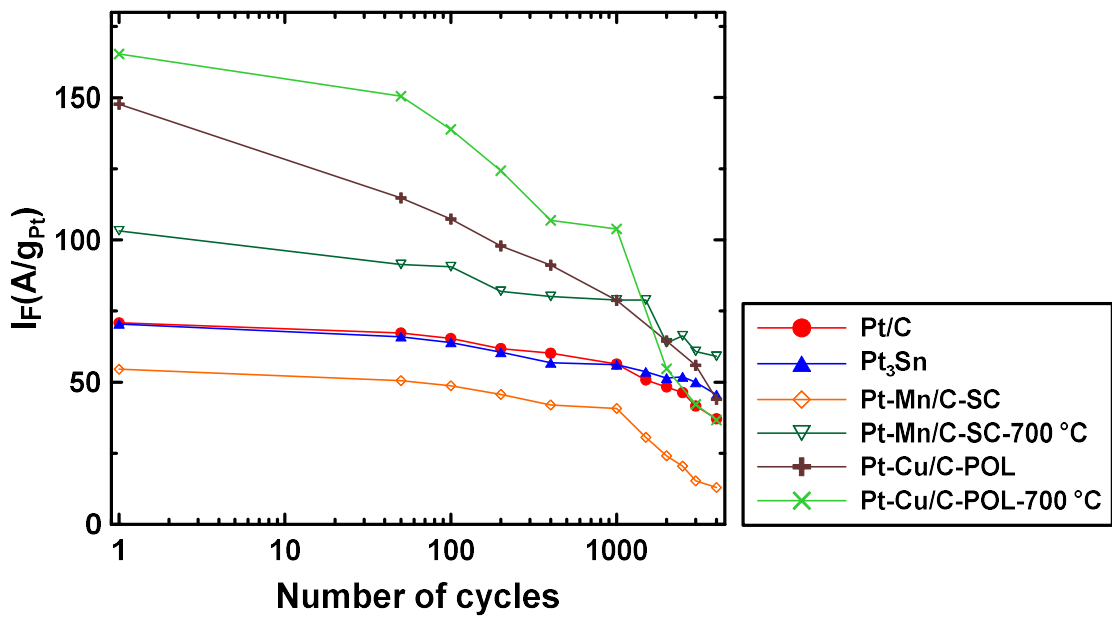


Figure 6.24. The intensity of the peak current measured by the forward scan (I_F) and normalized for Pt loading for different samples which were determined from Figure 6.20, 6.21 and 6.22 at the specific cycles of AST.

The Pt-Cu samples before and after heat treatment showed a great EOR activity (Figure 6.23). Similar to the Pt-Mn samples, the heat treatment enhanced I_F more than I_B of the Pt-Cu samples, as a result the poisoning should also be eliminated for the heat treated Pt-Cu samples. The highest activity was recorded for Pt-Cu/C-POL-700 °C until the first 50 cycles in comparison with the other samples. The EOR activity (I_F) decreased after the first 50 cycles for Pt-Cu/C-POL-700 °C compared to P₁₀₀ but it is still better than the other samples before 1000 cycles. In addition, the highest I_F/I_B ratio was determined for Pt-Cu/C-POL-700 °C which indicates that this sample had the highest resistance to the poisoning among the samples which were tested in this study. The crystalline changes of the Pt-Cu samples on the heat treatment were similar to the heat treated Pt-Mn and promoted the (100) planes on the particle surface. Therefore, the improvement of activity and the

elimination of poisoning should cause by promoted favorable crystalline planes due to the heat treatment. Figure 6.24 shows that the Pt utilization was also improved after the heat treatment. The differences in the activity of Pt-Cu/C-POL and Pt-Cu/C-POL-700 °C was higher at BOL but it was decreased faster during cycling compared to the Pt-Mn samples.

Based on the electrochemical studies, it can be concluded that we were able to produced samples with high durability and high EOR activity from the Pt-Mn and Pt-Cu alloys by using proper surfactants and synthetic methods along with a proper heat treatment procedure. Our studies show that the heat treatment improved the durability and activity of samples. Additionally, we could closely monitor the structural changes of the Pt alloys during AST and our findings show that the ECSA loss and the crystalline modifications were the most important factors which were controlled the EOR activity of the alloyed samples.

6.4 Conclusion

This chapter was mainly dedicated to the stability and durability testing of different samples. The Pt-Mn/C and Pt-Cu/C alloys were produced by the impregnation and microwave assisted polyol methods, respectively. The effect of heat treatment and crystalline structure on the durability of these samples were studied using accelerated stress test (AST) combined with the *ex-situ* ICP, *ex-situ* XRD and EIS analyses. In addition, the durability of the samples produced in-house compared to the durability of the commercially available samples (Pt/C and Pt₃Sn/C). The *ex-situ* ICP and XRD analyses indicate that the dealloying occurred for all the alloyed samples. By increasing the Pt content and applying the heat treatment, the lower amount of the alloying element depleted and the content of

the alloying element at the end of AST was higher. The *ex-situ* XRD analysis also shows that the crystalline structure of the alloyed particles was modified and changed back to the pure Pt structure with cycling. The AST results checks with the results determined by XRD and ICP. Our studies indicate that particles with a Pt-rich shell was formed during running AST on the alloyed sample and there were two stages of degradation, the first stage controlled by the alloying element depletion and second stage controlled by the ECSA loss and the crystalline structure modification. Based on the AST findings, the heat treatment improved the durability and the EOR activity of samples. Our findings show that the ECSA loss and the crystalline modifications were the most important degradation factors which were controlled the EOR activity of the alloyed samples. Finally, our results confirm that AST combined with the EIS analysis was a very powerful electrochemical method to identify and separate different degradation mechanisms even for the Pt-alloy samples.

6.5 References

- [1] Y. Xu, B. Zhang, Chemical Society Reviews, 43 (2014) 2439-2450.
- [2] Y.-W. Lee, S. Cha, K.-W. Park, J.I. Sohn, J.M. Kim, Journal of Nanomaterials, 2015 (2015) 1-20.
- [3] E. Antolini, Materials Chemistry and Physics, 78 (2003) 563-573.
- [4] H. Liu, C. Song, L. Zhang, J. Zhang, H. Wang, D.P. Wilkinson, Journal of Power Sources, 155 (2006) 95-110.
- [5] L. Li, L. Hu, J. Li, Z. Wei, Nano Res., 8 (2015) 418-440.
- [6] W. Vielstich, A. Lamm, H.A. Gasteiger, Handbook of Fuel Cells: Fundamental, Technology, and Applications, Wiley, 2003.
- [7] X. Yu, S. Ye, Journal of Power Sources, 172 (2007) 133-144.
- [8] L. Su, W. Jia, C.-M. Li, Y. Lei, ChemSusChem, 7 (2014) 361-378.

- [9] F. Vigier, S. Rousseau, C. Coutanceau, J.-M. Leger, C. Lamy, *Top Catal.*, 40 (2006) 111-121.
- [10] M.R. Zamanzad Ghavidel, E.B. Easton, *Applied Catalysis B: Environmental*, 176–177 (2015) 150-159.
- [11] X. Zhang, D. Li, D. Dong, H. Wang, P.A. Webley, *Materials Letters*, 64 (2010) 1169-1172.
- [12] X. Zhang, W. Lu, J. Da, H. Wang, D. Zhao, P.A. Webley, *Chemical Communications*, (2009) 195-197.
- [13] T. Page, R. Johnson, J. Hormes, S. Noding, B. Rambabu, *Journal of Electroanalytical Chemistry*, 485 (2000) 34-41.
- [14] C. Sealy, *Materials Today*, 11 (2008) 65-68.
- [15] O.T. Holton, J.W. Stevenson, *Platinum Metals Review*, 57 (2013) 259-271.
- [16] K. Matsutani, K. Hayakawa, T. Tada, *Platinum Metals Review*, 54 (2010) 223-232.
- [17] in, 2014, pp. 1-49.
- [18] M. Ammam, L.E. Prest, A.D. Pauric, E.B. Easton, *Journal of The Electrochemical Society*, 159 (2011) B195-B200.
- [19] M. Ammam, E.B. Easton, *Journal of Power Sources*, 222 (2013) 79-87.
- [20] E. Antolini, F. Colmati, E.R. Gonzalez, *Electrochemistry Communications*, 9 (2007) 398-404.
- [21] T. Ghosh, B.M. Leonard, Q. Zhou, F.J. DiSalvo, *Chemistry of Materials*, 22 (2010) 2190-2202.
- [22] N. Hodnik, C. Jeyabharathi, J.C. Meier, A. Kostka, K.L. Phani, A. Recnik, M. Bele, S. Hocevar, M. Gaberscek, K.J.J. Mayrhofer, *Physical Chemistry Chemical Physics*, 16 (2014) 13610-13615.
- [23] X. Yu, S. Ye, *Journal of Power Sources*, 172 (2007) 145-154.
- [24] R. Lin, T. Zhao, M. Shang, J. Wang, W. Tang, V.E. Guterman, J. Ma, *Journal of Power Sources*, 293 (2015) 274-282.
- [25] F.S. Saleh, E.B. Easton, *Journal of Power Sources*, 246 (2014) 392-401.
- [26] F.S. Saleh, E.B. Easton, *Journal of The Electrochemical Society*, 159 (2012) B546-B553.
- [27] O.R. O'Rian, F.S. Saleh, E.B. Easton, *ECS Transactions*, 61 (2014) 25-32.

- [28] F.S. Saleh, E.B. Easton, *Electrochimica Acta*, 114 (2013) 278-284.
- [29] C. Odetola, L. Trevani, E.B. Easton, *Journal of Power Sources*, 294 (2015) 254-263.
- [30] K. Artyushkova, P. Atanassov, M. Dutta, S. Wessel, V. Colbow, *Journal of Power Sources*, 284 (2015) 631-641.
- [31] C. He, S. Desai, G. Brown, S. Bollepalli, *Interface-Electrochemical Society*, 14 (2005) 41-46.
- [32] A. Mehmood, M.A. Scibioh, J. Prabhuram, M.-G. An, H.Y. Ha, *Journal of Power Sources*, 297 (2015) 224-241.
- [33] Y. Shao, G. Yin, Y. Gao, *Journal of Power Sources*, 171 (2007) 558-566.
- [34] J. Wu, X.Z. Yuan, J.J. Martin, H. Wang, J. Zhang, J. Shen, S. Wu, W. Merida, *Journal of Power Sources*, 184 (2008) 104-119.
- [35] F. Hasché, M. Oezaslan, P. Strasser, *ChemCatChem*, 3 (2011) 1805-1813.
- [36] P. Mani, R. Srivastava, P. Strasser, *The Journal of Physical Chemistry C*, 112 (2008) 2770-2778.
- [37] M. Oezaslan, M. Heggen, P. Strasser, *Journal of the American Chemical Society*, 134 (2012) 514-524.
- [38] C.-J. Tseng, S.-T. Lo, S.-C. Lo, P.P. Chu, *Materials Chemistry and Physics*, 100 (2006) 385-390.
- [39] Y.-X. Wang, H.-J. Zhou, P.-C. Sun, T.-H. Chen, *Journal of Power Sources*, 245 (2014) 663-670.
- [40] L. Xiong, A. Manthiram, *Journal of The Electrochemical Society*, 152 (2005) A697-A703.
- [41] D. Xu, S. Bliznakov, Z. Liu, J. Fang, N. Dimitrov, *Angewandte Chemie*, 122 (2010) 1304-1307.
- [42] T.-H. Yeh, C.-W. Liu, H.-S. Chen, K.-W. Wang, *Electrochemistry Communications*, 31 (2013) 125-128.
- [43] M. Ghavidel, E. Easton, *Catalysts*, 5 (2015) 1016.
- [44] J.E. Harlow, D.A. Stevens, R.J. Sanderson, G.C.-K. Liu, L.B. Lohstroter, G.D. Vernstrom, R.T. Atanasoski, M.K. Debe, J.R. Dahn, *Journal of The Electrochemical Society*, 159 (2012) B670-B676.
- [45] D.A. Stevens, R. Mehrotra, R.J. Sanderson, G.D. Vernstrom, R.T. Atanasoski, M.K. Debe, J.R. Dahn, *Journal of The Electrochemical Society*, 158 (2011) B905-B909.

- [46] M. Huang, L. Guan, International Journal of Hydrogen Energy, 40 (2015) 6546-6551.
- [47] J.I. Eastcott, K.M. Yarrow, A.W. Pedersen, E.B. Easton, Journal of Power Sources, 197 (2012) 102-106.
- [48] I. Dutta, M.K. Carpenter, M.P. Balogh, J.M. Ziegelbauer, T.E. Moylan, M.H. Atwan, N.P. Irish, The Journal of Physical Chemistry C, 114 (2010) 16309-16320.
- [49] E.B. Easton, P.G. Pickup, Electrochimica Acta, 50 (2005) 2469-2474.
- [50] N. Jia, R.B. Martin, Z. Qi, M.C. Lefebvre, P.G. Pickup, Electrochimica acta, 46 (2001) 2863-2869.
- [51] F.G. Will, Journal of The Electrochemical Society, 112 (1965) 451-455.
- [52] T. Frelink, W. Visscher, J. Van Veen, Electrochimica acta, 40 (1995) 545-549.
- [53] J. Zhang, H. Liu, Electrocatalysis of Direct Methanol Fuel Cells: From Fundamentals to Applications, John Wiley & Sons, Germany, 2009.
- [54] X. Xia, H.-D. Liess, T. Iwasita, Journal of Electroanalytical Chemistry, 437 (1997) 233-240.
- [55] M.-C. Morin, C. Lamy, J.-M. Leger, J.-L. Vasquez, A. Aldaz, Journal of electroanalytical chemistry and interfacial electrochemistry, 283 (1990) 287-302.

**Chapter 7: Oxygen
Reduction Properties of Pt-
Mn/C and Pt-Cu/C Alloys
in Comparison with
Commercial Samples**

7.1 Introduction

In last few decades, great number of studies have focused on developing catalysts for improving the oxygen reduction reaction (ORR) in fuel cells [1-6]. It is well known that ORR suffers from large overpotentials and thus limits the overall performance of fuel cells [3]. In addition, in direct alcohol fuel cells (DAFCs) slow kinetics of the alcohol (ethanol or methanol) reduction along with sluggish ORR behaviour could reduce the performance of the DAFC dramatically [6-10]. Therefore, in addition to synthesising very active catalysts for anodic reaction, it is essential to develop new catalysts which are improving ORR activities. Pt is the most commonly used electrocatalyst for both cathodic and anodic reaction in the commercial fuel cells. Pt is an expensive element and the efforts to reduce Pt and other noble metal contents in fuel cells are challenging [11-14]. On the other hand, the new non-noble metal catalysts have shown a low mass activity in fuel cells [3, 15, 16]. As a result, developing alloy catalysts that have lower Pt contents are more appealing due to proven high activity of the Pt-alloy catalysts toward oxygen reduction [17-24]. In addition, it has been shown that the Pt-alloys can be effective to reduce the costs and increase the efficiency of DAFCs [7, 9, 11, 25].

The ORR activity enhancement in the presence of alloying elements could be due to:

- (i) variation in Pt–Pt bond distances (ii) inhibition of OH_{ads} adsorption (iii) formation of the metal particles with rougher surface because of surface oxide or alloying element dissolution (iv) changes in the electronic structure and formation of greater number of Pt d-band vacancies [3, 4]. Therefore, the ORR activity of supported catalysts could be altered by particle size, shape, composition, supporting material and method of preparation [3, 4].

Different Pt-alloys have been examined in order to improve ORR activity [19-22, 24, 26-30]. One study on different PtM alloys (M= Cr, Mn, Co, Ni) on carbon supports has shown

that the ORR limiting current has exhibited Volcano plot versus the electronic (d-band vacancy) and geometric (Pt-Pt distance) factors and the Pt-Cr alloy have reported as the most active sample [31]. Another study on sputtered Pt₃M (M= Ni, Co, Fe, V, Ti) alloys has illustrated that an optimal catalytic activity will be achieved when there is balance between the energy of reactive intermediate adsorption and desorption of blocking species. In this case, Pt₃Co has shown the highest activity compared to other alloyed samples [2]. Studies on Pt-Sn/C, Pt-Ni/C and Pt-Sn-Ni/C also have shown that the ORR activity of samples in the presence of alloying element have improved and the Pt-Sn alloy have resulted in the highest mass activity [19]. In addition, it has been indicated that Sn oxide phases facilitate ORR [28, 29, 32].

Recent studies have revealed that Pt-Cu are also very good candidate for ORR [12, 22-24, 27, 30, 33, 34]. Pt-Cu nanoparticles with Pt rich surface have shown that the presence of Cu modified the electronic properties of Pt atoms on the surface and enhanced the ORR activity [23]. Different Pt-M (M=Au, Pd, or Cu) nanorods have also been studied, with Pt-Cu nanorods displaying the highest ORR activity [24]. Tseng et al.[30] used both the impregnation and polyol methods to produce Pt-Cu alloys and studied the effect of heat treatment on the ORR activity of the Pt-Cu particles. Their findings have illustrated that the polyol method and the heat treatment at 300 °C in a hydrogen atmosphere caused the ORR activity enhancement. In addition, it has been shown that heat treatment and formation of the ordered Pt-Cu alloys could improve the stability and the ORR activity due to better retention of the copper inside the ordered structure [27].

The Pt-Mn and Pt-Cu alloy system has recently been identified by our group as having enhanced activity towards the ethanol oxidation reaction (EOR) [35-38]. Alloy formation was confirmed with X-ray powder diffraction (XRD) analysis, and the most active alloys

contained less than 25 at% Pt, which is beneficial from a cost standpoint. In addition, it have shown that presence of Cu as a ternary alloying element enhanced the activity of the Pt-Mn alloys toward EOR [36]. However, the impregnation method usually results in a mixture of weakly alloyed samples and a high degree of agglomeration which makes it difficult to gain a solid conclusion on the catalytic activity of samples [35-39]. The studies described in Chapters 3 - 5 showed that post-heat treatment had a great impact on the activity of the Pt-Mn and Pt-Cu alloys, and the main reason for enhancing the EOR activity was the formation of the PtMn and PtCu intermetallic phases [40].

While there have been a few studies of ordered heat treated Pt-Cu systems [13, 20, 22, 27, 41], there are very limited studies of the heat treated Pt-Mn systems [13, 42]. The heat treatment and structural ordering process could significantly affect the ORR activity of Pt-Mn and Pt-Cu systems, due to particle size growth and formation of new alloy phases [1, 22, 40, 43]. The particle size growth during heat treatment is an unwanted consequence. Sintering can happen by the migration and coalescence of the catalyst particles or by evaporation and condensation of the atoms from small crystallites [1]. However, the impact of structural ordering along with particle growth on the ORR activity in Pt-Cu and Pt-Mn systems are poorly studied, especially for the Pt-Mn alloys.

In this chapter, the ORR activity of the Pt-Mn and Pt-Cu samples was studied in details. The most active and stable samples in both Pt-Mn and Pt-Cu systems were selected based on the studies reported in chapter 3 to 6 and they tested by rotation ring-disc electrode (RRDE) in oxygenated solution. The ORR activity of these alloys has compared to different commercially available samples (Pt/C and Pt-Sn/C). Finally, the effects of heat treatment and formation of ordered structures in both Pt-Cu and Pt-Mn systems were investigated.

7.2 Experimental

7.2.1 Catalyst synthesis

The carbon supported Pt-Mn and Pt-Cu alloys were prepared as discussed in chapter 4 and 5. Impregnation in the presence of sodium citrate (SC) was used for Pt-Mn/C samples and microwave assisted polyol method used for the Pt-Cu/C samples. In addition, two commercial control samples Pt/C (Premetek Co.) and Pt-Sn/C (Premetek Co.) were studied and compared to the samples made in-house. These samples are hereafter referred to as Pt-Mn/C-SC, Pt-Cu/C-POL, Pt/C and Pt₃Sn/C, respectively. The target composition was of Pt_{0.25}M_{0.75}/C (M=Mn and Cu). This composition was chosen based on our group previous studies [38], primary work on Pt-Cu and Pt-Mn alloys in chapter 3, 4 and 5 and recently published articles [27, 44-46]. Metal precursors were H₂PtCl₆.H₂O (Aldrich), MnCl₂.4H₂O (Aldrich), and CuCl₂.2H₂O (Aldrich). Vulcan XC72R carbon black (Cabot Corp.) was used as the carbon support in all cases. The total metal loading was targeted as ~20 wt% for all samples. The pH of the reaction solution was adjusted using a HCl solution (15 v/v %) and/or a 1M NaOH solution. For the impregnation method with the additive, Trisodium Citrate (SC) (Aldrich) was added in a weight ratio of 2:1 to the metal ratios. NaBH₄ powder was used as a reduction agent. The weight ratio of NaBH₄ to the metal content was 3:1. The pH of the solution was adjusted to 3 for the impregnation method. For the polyol method, the metal precursors and Vulcan carbon were mixed with ethylene glycol (EG) (Aldrich) using a mechanical stirrer. The solution pH was adjusted to pH 9, after which it was sonicated for 45 min to achieve a uniform suspension. The suspension was placed into the household microwave oven (SANYO - 2450 MHz) and heated for 8 min and then left to cool down under continues mechanical stirring. In all the methods, the resulting powder

was filtered and washed with isopropanol alcohol (IPA), acetone, and deionized water, and finally dried in an oven at 80 °C overnight.

The selected samples were heat treated in a nitrogen atmosphere at 700 °C in a Barnstead Thermolyne tube furnace with a quartz tube. The period of heat treatment was kept constant (1 h) for all the samples. The heat treatment time and temperature was also chosen base on previous studies by our group [39]. After the heat treatment, the samples were cooled down under a constant flow of nitrogen gas and were preserved inside the furnace until room temperature was reached.

7.2.2 Electrochemical characterization

In this chapter, the electrochemical activity of samples studied using a rotating ring disk electrode (RRDE) with a 5 mm glassy carbon disk and a platinum ring with a 7.5 mm inner diameter and 8.5 mm outer diameter from Pine research instrumentation. The catalyst inks were produced by mixing 10 mg of the catalyst with 100 µL Nafion solution (5% in alcohols, Dupont) and a 400 µL 50:50 mixture of isopropyl alcohol (IPA) and water. A uniform suspension was achieved after sonicating for 45 minutes. A 5 µL droplet of the well-dispersed catalyst ink was deposited onto the clean and polished glassy carbon disk and dried in the air at room temperature prior to electrochemical tests. The total metal loading of the catalyst layer was ~0.12 mg/cm². The electrodes were used to measure the electrochemical active surface area (ECSA) and to study oxygen reduction reaction (ORR). Cyclic voltammetry (CV) was in a 0.5 M H₂SO₄ solution was used to determine ECSA and clean the samples. Linear sweep voltammograms (LSVs) were obtained without any rotation in N₂-purged solution to determine the background due to the Vulcan carbon

particles. Following the background test, LSVs were recorded to evaluate ORR in a 0.5M H₂SO₄ solution saturated with pure O₂ gas for 15 min. LSV was repeated at five different rotation rates: 200 rpm, 400 rpm, 900 rpm, 1600 rpm, and 2500 rpm, starting from the highest rpm. The determined limiting current and onset potentials (potentials at which the oxygen reduction was occurred) were compared at a rotation rate of 1600 rpm unless otherwise specified. The limiting current is determined from the point at which the measurements plateau (0.332 mV vs NHE) and the onset potential is defined as the potential at 5% of the limiting current. The RRDE collection experiments were utilized to study the hydrogen peroxide production (H₂O₂). The ring potential was held at 1.2 V to oxidize any evolved H₂O₂.

7.3 Result and discussion

In chapter 3, 4 and 5, the composition and structural properties of the Pt-Mn and Pt-Cu alloys were studied in details. In addition, the electrochemical activity of these alloys toward ethanol oxidation examined thoroughly. Finally, in chapter 6 the stability of these alloys were investigated. Based on these studies, the most active and stable samples were chosen for the ORR studies. Therefore, in this chapter the Pt-Mn samples prepared by the impregnation method in the presence of SC and the Pt-Cu samples prepared by the polyol method were compared to the commercial samples and the possibility of decreasing Pt contain in cathode side of the alcohol sensors was investigated. The reduction Pt loading in a membrane electrode assembly (MEA) is commercially favourable.

7.3.1 Materials characterization

The chemical and physical properties of Pt-Cu and Pt-Mn samples have studied in previous chapters. However, thermogravimetric results in Argon atmosphere was not reported for the Pt-Cu samples. Figure 7.1 shows the thermogravimetry (TG) and derivative thermogravimetry (DTG) curves obtained for the Pt-Cu/C-POL samples. The mass loss occurring between 100 °C and 150 °C was attributed to the thermal decomposition of functional groups on carbon and the evaporation of any residual water in the samples [47, 48]. The mass loss detected between 150 and 250 °C was due to removal of the trace of ethylene glycol or other contamination which still remain in the structure of the catalyst powder and was not removed during the washing process. This temperature is very close to the boiling temperature of EG (197.3 °C). The third major mass loss was observed around 300 °C, which was attributed to the oxidation of the carbon support by oxygen or the air trapped within the powdered samples [48]. Comparing the DTG diagrams of Pt-Cu/C-POL and Pt-Cu/C-POL-700 °C shows that after the heat treatment the peaks lower than 250 °C was completely removed (Figure 7.1b). This indicated that the heat treatment reduced the amount of contamination and removed any ethylene glycol was existed in the catalysts structure.

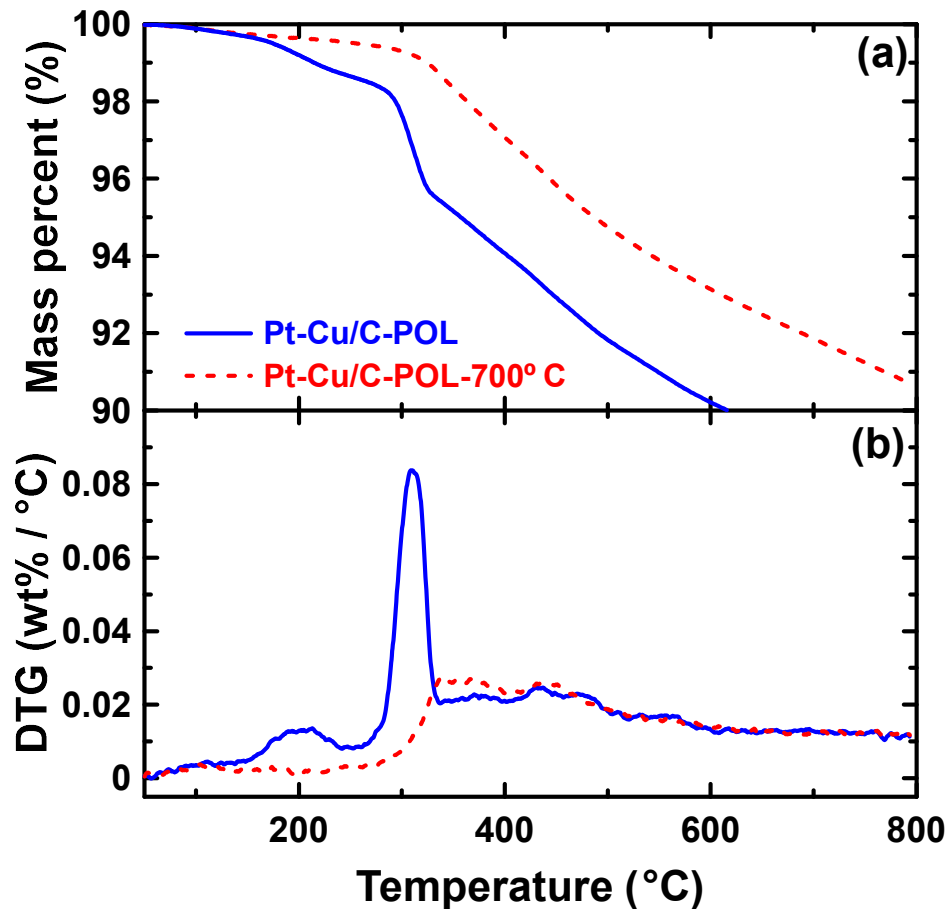


Figure 7.1. (a) The weight loss and (b) derivative weight loss versus temperature for Pt-Cu/C-POL and Pt-Cu/C-POL-700 °C. Measurements were made at a heating rate of 20 °C/min under flowing argon.

7.3.2 Electrochemical characterization

7.3.2.1 ECSA measurements

Electrochemical studies in chapter 4 and 5 showed that the ECSA of the Pt-alloy samples reduced after adding the alloying element (Mn, Cu or Sn). The highest ECSA was recorded for Pt/C and the least one was recorded for the Pt-Cu/C-Pol sample. Besides, the

heat treatment at 700 °C decreased ECSA for the alloy samples although the activity toward ethanol oxidation and stability of the samples was improved greatly.

7.3.2.2 ORR measurements

Figure 7.2, 3 and 4 show LSVs recorded for the Pt, Pt₃Sn, Pt-Mn/C and Pt-Cu/C samples in oxygen saturated solution. LSVs curves displayed the typical activation polarization and diffusion limited current as well as mixed kinetic/diffusion polarization for oxygen reduction. The limiting current density (j_L) was measured at the end of each scan (0.332 mV vs NHE) at different rotating speeds and used to plot the Koutecky–Levich diagram. The limiting current is a combination of diffusion current (j_D) and kinetic current (j_K), but it is controlled mainly by diffusion of O₂. The limiting current measured by a rotating disc experiment is described by the Koutecky–Levich equation [3, 19].

$$\frac{1}{j_L} = \frac{1}{j_K} + \frac{1}{j_D} \quad \text{Equation 7-1}$$

j_D is defined by Levich equation:

$$j_D = 0.62nFD^{2/3}\omega^{1/2}\nu^{-1/6}C = \beta\omega^{1/2} \quad \text{Equation 7-2}$$

In this equation, n is the average number of electrons transferred, F is the Faraday constant (96485 C/mol), D is the diffusion coefficient of oxygen ($1.93 \times 10^{-5} \text{ cm}^2/\text{s}$), ω is the angular velocity (rad/s), ν is the kinematic viscosity of the solution ($0.01 \text{ cm}^2/\text{s}$) and C is the concentration of O₂ dissolved in the electrolyte ($1.10 \times 10^{-6} \text{ mol/cm}^3$) [15, 16]. This equation can be written in short form as shown in Equation 7-2. If j_D in Equation 7-1 is replaced by Equation 7-2, a plot of j_L^{-1} vs $\omega^{-1/2}$ at a fixed potential yields a straight line

with the slope of $1/\beta$, which is called Koutecky–Levich (K-L) plot. The slope can be used to predict the average number of electrons transferred due to the oxygen reduction. The K-L plots are shown in Figure 7.5 for different samples and the slop calculated are presented in Table 7.1.

In Figure 7.2, the ORR activity of two commercial samples are compared. The on-set potential ($V_{\text{on-set}}$) and limiting current for the rotating speed of 1600 rpm are reported in Table 7.1. The on-set potential and j_L for Pt_3Sn were reduced slightly compared to Pt/C. This indicates that adding Sn to the Pt structure marginally reduced the ORR activity. However, by considering the reduction of the Pt loading, it can be concluded that Pt_3Sn is a good candidate to replace the Pt/C catalyst on the cathode side, especially for the sensing application.

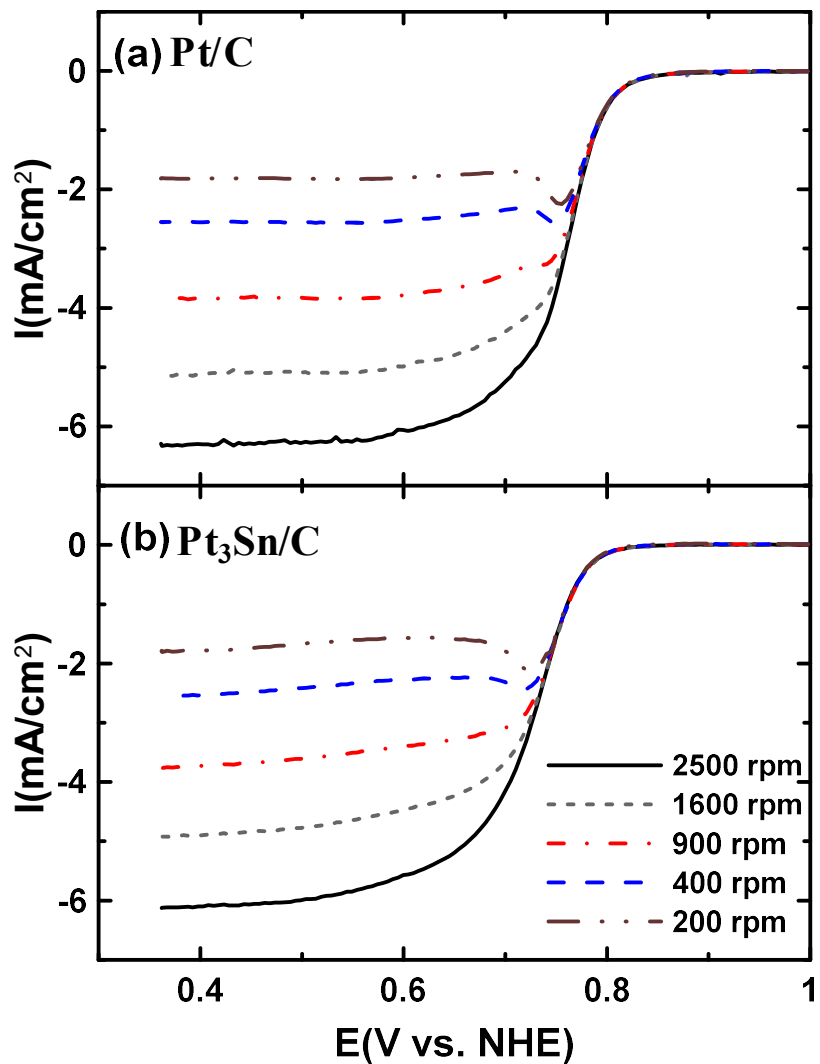


Figure 7.2. RRDE measurements of (a) Pt/C (b) $\text{Pt}_3\text{Sn/C}$ to study the ORR activity of the samples. Measurements were carried out in O_2 -saturated 0.5 M H_2SO_4 using different rotation rates by a scan rate of 10 mV/s.

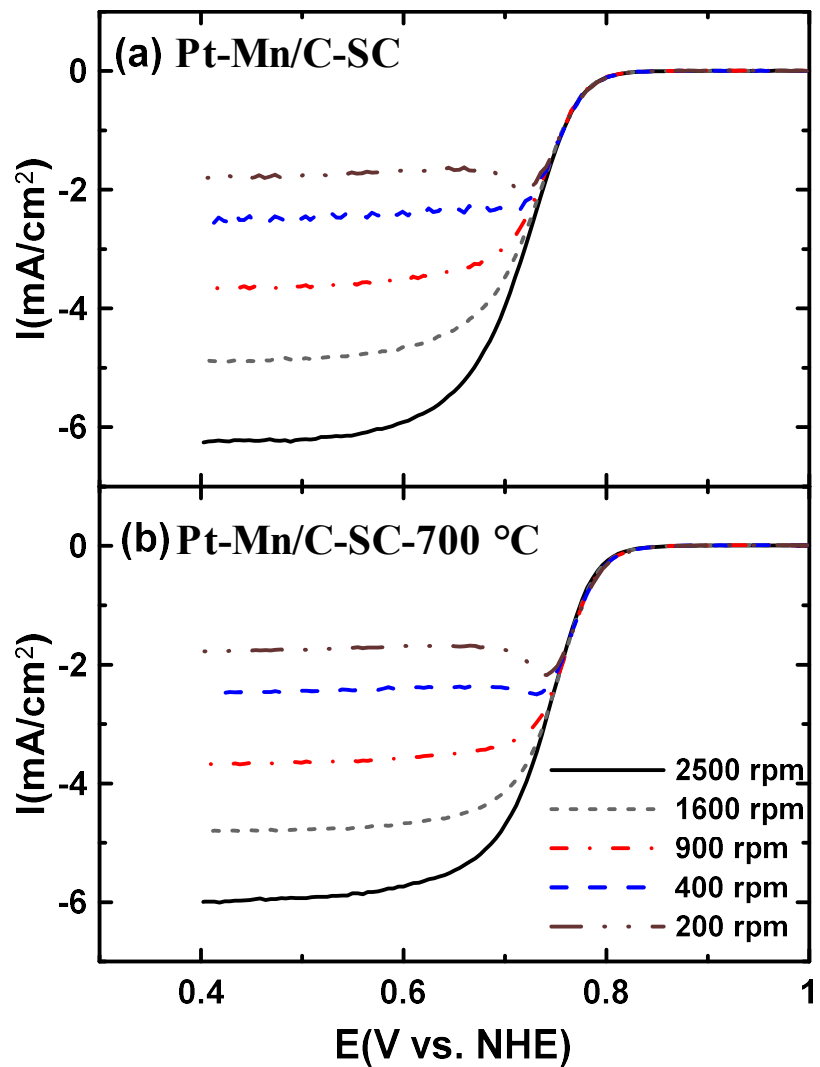


Figure 7.3. RRDE measurements of (a) Pt-Mn/C-SC (b) Pt-Mn/C-SC-700 °C to study the ORR activity of the samples. Measurements were carried out in O₂-saturated 0.5 M H₂SO₄ using different rotation rates by a scan rate of 10 mV/s.

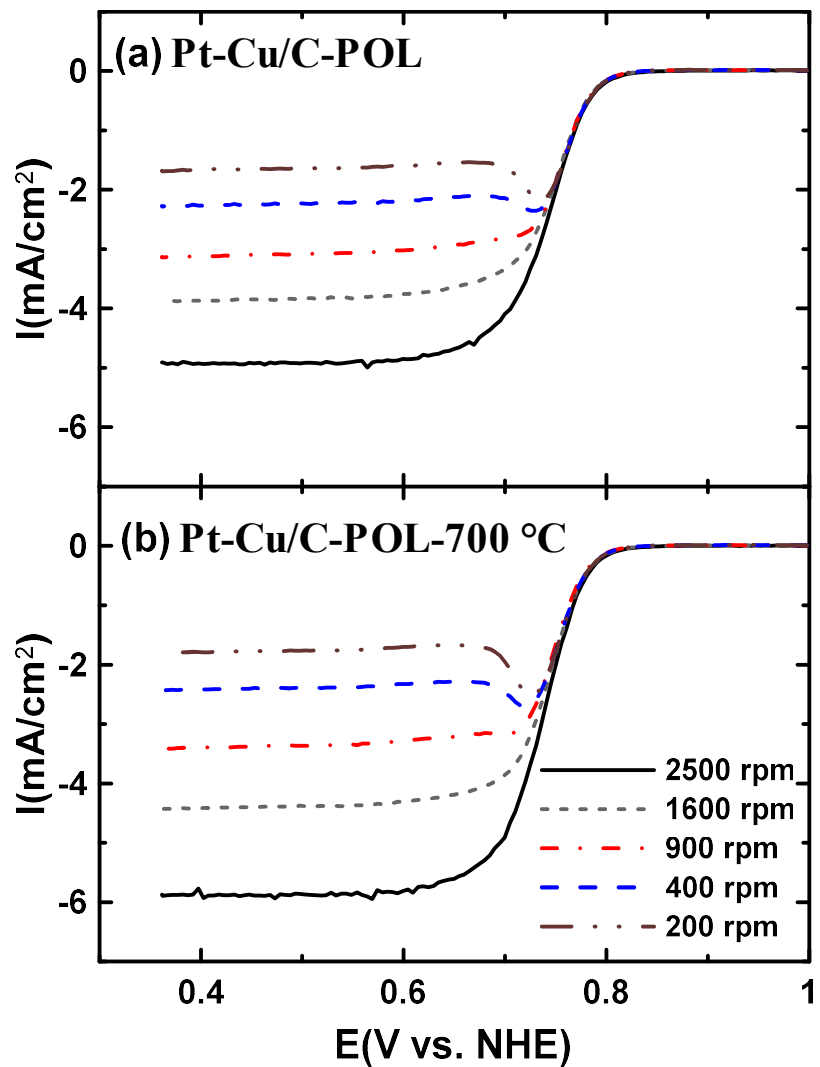


Figure 7.4. RRDE measurements of (a) Pt-Cu/C-POL and (b) Pt-Cu/C-POL-700 °C to study the ORR activity of the samples. Measurements were carried out in O_2 -saturated 0.5 M H_2SO_4 using different rotation rates by a scan rate of 10 mV/s.

Table 7.1. The on-set potential ($V_{\text{on-set}}$) and limiting current density (j_L) calculated from Figure 7.2, 3 and 4 and the slop of Koutecky–Levich plot measured using Figure 7.5.

Samples	$V_{\text{on-set}}$ (mV) at 1600 rpm	j_L (mA/cm ²) at 1600 rpm	β^{-1}
Pt/C	821.0	5.12	2.53
Pt ₃ Sn/C	791.2	4.92	2.56
Pt-Mn/C-SC	786.2	4.89	2.58
Pt-Mn/C-SC-700 °C	801.5	4.81	2.60
Pt-Cu/C-POL	795.9	3.90	2.86
Pt-Mn/C-POL-700 °C	790.9	4.43	2.63

The ORR activity of Pt-Mn/C-SC and Pt-Mn/C-SC-700 °C are compared in Figure 7.3.

The $V_{\text{on-set}}$ and j_L of the samples were measured at 1600 rpm and reported in Table 7.1. These results illustrate that the heat treatment had no effect on j_L , but it shifted $V_{\text{on-set}}$ to higher potential and improved the ORR activity for Pt-Mn/C-SC-700 °C. These results indicate that during the heat treatment although there were particle enlargement and ECSA loss, the ORR activity was slightly improved in the opposite of what was expected.

The slope of the K-L plot for the Pt-Mn/C-SC and Pt-Mn/C-SC-700 °C samples was very close to the 4 electron reaction. This implies that the alloying of Pt with Mn did not changed the mechanism of the oxygen reduction. The slope of the K-L plot was changed slightly after the heat treatment. In the chapter 3 and 4, it has been shown that the heat treatment changed the structure of the Pt-Mn alloys and formed ordered intermetallic PtMn phase. The structural modification is the reason to increase the activity of the Pt-Mn alloys toward the ethanol oxidation. Therefore, it can be concluded that the formation of the intermetallic phases compensated the ECSA loss and moved the mechanism of ORR toward 4 electron reaction process. Besides, it was confirmed in the chapter 6 that the

stability of the Pt-Mn alloys after the heat treatment were improved. As a result, the heat treatment is favourable from different point of views.

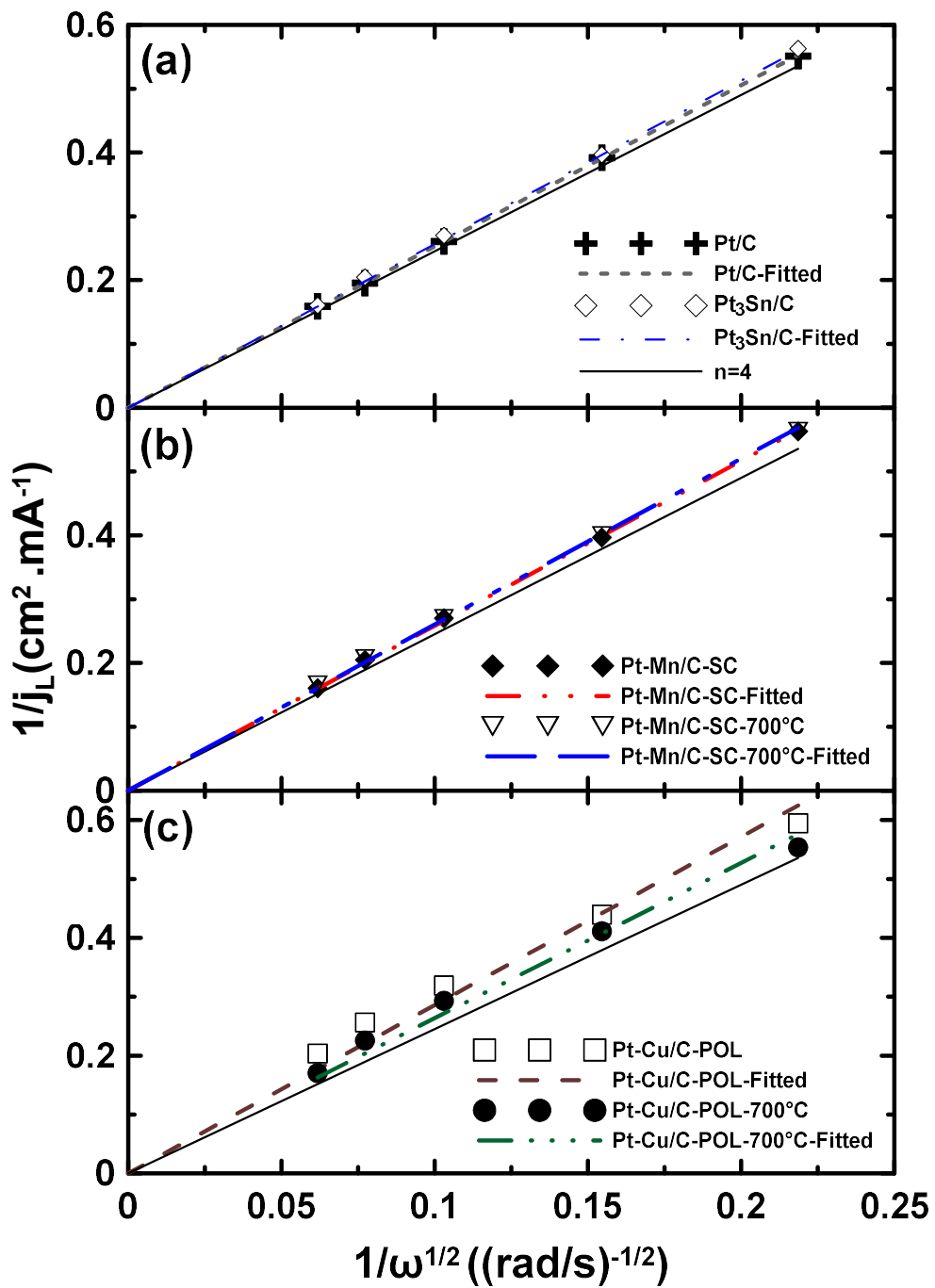


Figure 7.5. Koutecky-Levich plot for different samples (a) Pt/C and Pt₃Sn/C (b) Pt-Mn/C-SC and Pt-Mn/C-SC-700 °C (C) Pt-Cu/C-POL and Pt-Mn/C-POL-700 °C which were determined using Figure 7.2, 7.3 and 7.4.

The ORR activity of the Pt-Mn alloys compared to the commercial samples (Figure 7.7) shows that the V_{on-set} was close to but slightly lower than Pt/C even after the heat treatment. However, the Pt loading has reduced to almost third of the commercial sample (Pt/C) due to alloying Pt with Mn. Therefore, the Pt-Mn alloys can be a good candidate to replace the Pt/C catalyst in the cathode side from cost point of view in the sensor application.

In Figure 7.4, the ORR activity of Pt-Cu/C-POL and Pt-Cu/C-POL-700 °C are compared. The results in Table 1 for these samples indicates that V_{on-set} was not changed during the heat treatment. The heat treatment resulted in larger particles which could have reduced V_{on-set} , but V_{on-set} of the Pt-Cu alloy was not affected. This could be due to the formation of active phases during the heat treatment. It was shown in Chapter 5 that the heat treatment resulted in the ordered phases. It can be concluded that the formation of the ordered phases compensates the ECSA loss. This has been seen for Pt-Mn samples as well. However, j_L was improved a lot by applying the heat treatment. The Pt-Cu samples were produced by the polyol method and the samples were washed very carefully to remove the ethylene glycol after synthesizing. However, a trace of ethylene glycol evaporation was detected by the TGA analysis in argon atmosphere which could be removed by the heat treatment. In Figure 7.6, it is possible to observe the intensity of the cracks which occurred before and after heat treatment on the surface of the deposited electrodes. The number and severity of the cracks after the heat treatment were reduced which could be due to the removal of contamination from the catalyst particles. Formation of the cracks and delamination of the catalyst layer deposited on the GC electrodes affected the smoothness of the deposits. As a result, the limiting current was altered for the samples before and after heat treatment. The improvement of j_L was due to the removing of the residual of ethylene

glycol and improvement of the smoothness of the deposit on the GC electrodes. However, the smoothness of the samples was not as perfect as the Pt/C and Pt-Mn samples. Therefore, j_L was slightly lower than other samples even after the heat treatment. Studies on the slope of K-L plots of Pt-Cu samples show that the heat treatment also improved the slope of the plot and the mechanism of ORR was shifted more toward the 4 electron reaction. The K-L plot also shows that higher roughness on the surface of electrodes caused the plot for Pt-Cu/C-POL shifted parallel to the direction of the current axis and the intersection of plot was changed which was improved after the heat treatment.

The ORR activity of the Pt-Cu alloys are also comparable to commercial samples (Figure 7.7). V_{on-set} and j_L were reduced a little after the alloying of Pt with Cu. Similar results also observed for Pt-Mn and Pt-Sn samples. This shows that the Pt-Cu alloys after the heat treatment can be a good choice for ORR in the sensor application.

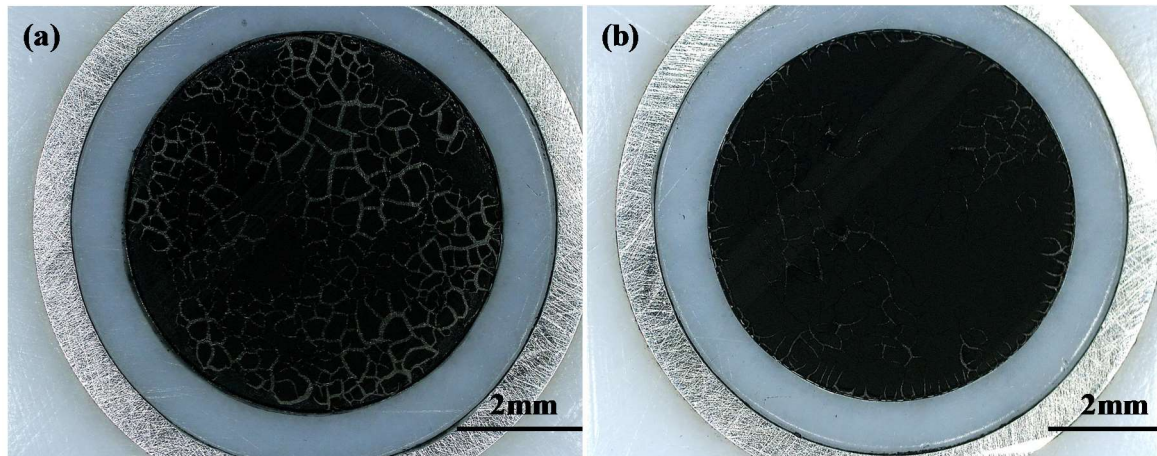


Figure 7.6. The cracks and delamination of the catalyst layer deposited on the GC electrode for Pt-Cu samples (a) before and (b) after heat treatment.

In Figure 7.7, different samples are compared at two different rotating speeds. The results indicate that the behaviour of the samples which was seen at 1600 rpm were reproducible at 900 rpm as well. In this figure it is easier to compare V_{on-set} and j_L . The highest V_{on-set} and j_L were achieved for Pt/C and the heat treatment improved V_{on-set} and j_L for Pt-Mn/C-SC and Pt-Cu/C-POL, respectively. In general, it can be concluded that the alloyed samples after the heat treatment are good candidates to be utilized in the cathode side of MEA to reduce the price of sensors in the cost of losing very small ORR activity. However, the behaviour of these samples should be further studied in a real fuel cell to confirm the half-cell results.

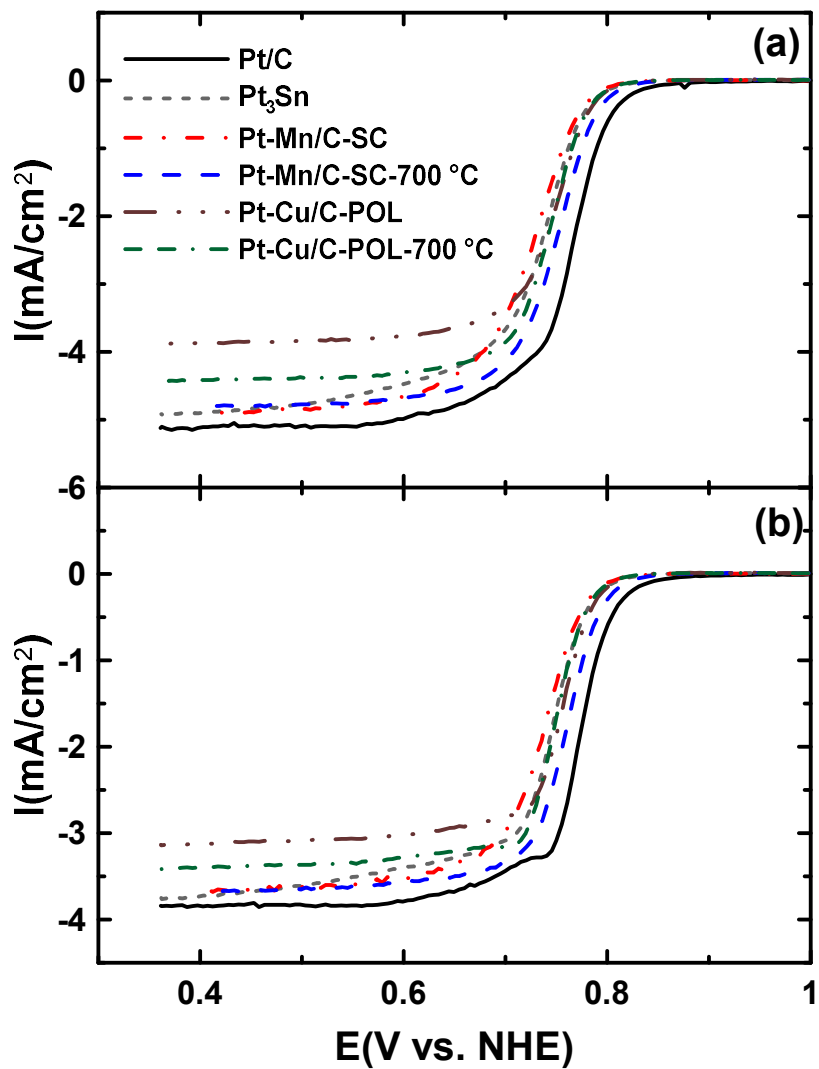


Figure 7.7. Comparison of the ORR activities of different samples. Measurements were carried out in O₂-saturated 0.5 M H₂SO₄ at a scan rate of 10 mV/s using an electrode rotation rate of (a) 1600 RPM and (b) 900 RPM.

7.4 Conclusion

In this chapter, the selected Pt-Mn and Pt-Cu alloys were examined for the ORR activity. The ORR activity of these alloys has also compared to the Pt/C and Pt-Sn/C commercial samples. Finally, the effects of heat treatment and formation of ordered structures on the ORR activity in both Pt-Cu and Pt-Mn systems were investigated. It is

difficult to compare the ORR results achieved by different groups due to diverse sample production methods and catalyst layer deposition process on GC electrodes. As explained in section 7.1, there are limited number of studies on the Pt-Mn systems but comparing the Pt-Cu systems shows that the V_{on-set} reported in this chapter are slightly lower than the ones reported in other articles. One of the reason could be due to different strategies used to report the ORR activity. Some groups used LSVs in which the potential were scanned from lower potentials to higher potentials and some others reported the opposite direction. There could be slight changes in V_{on-set} , depends on which direction was chosen for recording LSV. On the other hand, the carbon black could introduce background to LSV responses. In this chapter, I removed the background assigned to carbon particles by subtracting the respond in the absence of oxygen from the respond in the presence of oxygen. This could also be one of the reasons to determine lower V_{on-set} for the Pt-Cu samples. Finally, the thickness of the catalysts layer on GC could also affect the ORR respond. However, the process was kept same for all the samples reported here and commercial samples (Pt/C and Pt₃Sn/C) was used as controlled samples. The activity of samples made in-house were compared to the commercial samples.

The studies show that the ECSA values were decreased due to the presence of alloying elements and the ESCA loss reduced V_{on-set} . The highest V_{on-set} was recorded for Pt/C. Therefore, adding the alloying elements may slightly reduce the ORR activity but resulted in catalysts with a very low Pt content which is very important from cost stand point. In addition, our findings show that the heat treatment and formation of ordered phases had a great impact on the ORR activity of the alloyed samples. It was expected after the heat treatment due to ECSA loss, V_{on-set} would be reduced but V_{on-set} for the Pt-Mn system was improved and V_{on-set} for the Pt-Cu system did not change after the heat

treatment. As well, the limiting current density for Pt-Mn was unchanged and it was improved for the Pt-Cu system due to removal of the contamination and improving the catalyst layer deposition on the GC electrode. Finally, the limiting current density of commercial samples and Pt-Mn samples were almost same and they were close to theoretical values.

7.5 References

- [1] C.W. Bezerra, L. Zhang, H. Liu, K. Lee, A.L. Marques, E.P. Marques, H. Wang, J. Zhang, *Journal of Power Sources*, 173 (2007) 891-908.
- [2] V.R. Stamenkovic, B.S. Mun, M. Arenz, K.J. Mayrhofer, C.A. Lucas, G. Wang, P.N. Ross, N.M. Markovic, *Nature materials*, 6 (2007) 241-247.
- [3] H.A. Gasteiger, S.S. Kocha, B. Sompalli, F.T. Wagner, *Applied Catalysis B: Environmental*, 56 (2005) 9-35.
- [4] U. Paulus, T. Schmidt, H. Gasteiger, R. Behm, *Journal of Electroanalytical Chemistry*, 495 (2001) 134-145.
- [5] D. Thompsett, Pt alloys as oxygen reduction catalysts, in: *Handbook of Fuel Cells*, John Wiley & Sons, Ltd, 2010.
- [6] N. Markovic, T. Schmidt, V. Stamenkovic, P. Ross, *FUEL CELLS-WEINHEIM-*, 1 (2001) 105-116.
- [7] H. Liu, C. Song, L. Zhang, J. Zhang, H. Wang, D.P. Wilkinson, *Journal of Power Sources*, 155 (2006) 95-110.
- [8] Y. Nie, L. Li, Z. Wei, *Chemical Society Reviews*, 44 (2015) 2168-2201.
- [9] Y. Xu, B. Zhang, *Chemical Society Reviews*, 43 (2014) 2439-2450.
- [10] S. Zhang, X.-Z. Yuan, J.N.C. Hin, H. Wang, K.A. Friedrich, M. Schulze, *Journal of Power Sources*, 194 (2009) 588-600.
- [11] E. Antolini, *Materials Chemistry and Physics*, 78 (2003) 563-573.
- [12] A. Rabis, P. Rodriguez, T.J. Schmidt, *ACS Catalysis*, 2 (2012) 864-890.

- [13] T. Ghosh, B.M. Leonard, Q. Zhou, F.J. DiSalvo, *Chemistry of Materials*, 22 (2010) 2190-2202.
- [14] W. Vielstich, A. Lamm, H.A. Gasteiger, *Handbook of Fuel Cells: Fundamental, Technology, and Applications*, Wiley, 2003.
- [15] S.G. Mavilla, B.J. MacLean, E.B. Easton, *ECS Transactions*, 53 (2013) 31-41.
- [16] A.D. Pauric, A.W. Pedersen, T. Andrusiak, E.B. Easton, *Journal of the Electrochemical Society*, 157 (2010) B370-B375.
- [17] A.B. Anderson, J.m. Roques, S. Mukerjee, V.S. Murthi, N.M. Markovic, V. Stamenkovic, *The Journal of Physical Chemistry B*, 109 (2005) 1198-1203.
- [18] B.C. Beard, P.N. Ross, *Journal of the Electrochemical Society*, 137 (1990) 3368-3374.
- [19] S. Beyhan, N.E. Şahin, S. Pronier, J.-M. Léger, F. Kadırgan, *Electrochimica Acta*, 151 (2015) 565-573.
- [20] P. Mani, R. Srivastava, P. Strasser, *Journal of Power Sources*, 196 (2011) 666-673.
- [21] S. Mukerjee, S. Srinivasan, *Journal of Electroanalytical Chemistry*, 357 (1993) 201-224.
- [22] L. Xiong, A. Manthiram, *Journal of The Electrochemical Society*, 152 (2005) A697-A703.
- [23] Z. Xu, H. Zhang, S. Liu, B. Zhang, H. Zhong, D.S. Su, *International Journal of Hydrogen Energy*, 37 (2012) 17978-17983.
- [24] T.-H. Yeh, C.-W. Liu, H.-S. Chen, K.-W. Wang, *Electrochemistry Communications*, 31 (2013) 125-128.
- [25] Y.-W. Lee, S. Cha, K.-W. Park, J.I. Sohn, J.M. Kim, *Journal of Nanomaterials*, 2015 (2015) 1-20.
- [26] E.B. Easton, R. Yang, A. Bonakdarpour, J. Dahn, *Electrochemical and solid-state letters*, 10 (2007) B6-B10.
- [27] N. Hodnik, C. Jeyabharathi, J.C. Meier, A. Kostka, K.L. Phani, A. Recnik, M. Bele, S. Hocevar, M. Gaberscek, K.J.J. Mayrhofer, *Physical Chemistry Chemical Physics*, 16 (2014) 13610-13615.
- [28] A. Ignaszak, C. Teo, S. Ye, E. Gyenge, *The Journal of Physical Chemistry C*, 114 (2010) 16488-16504.

- [29] G. Samjeské, S.-i. Nagamatsu, S. Takao, K. Nagasawa, Y. Imaizumi, O. Sekizawa, T. Yamamoto, Y. Uemura, T. Uruga, Y. Iwasawa, *Physical Chemistry Chemical Physics*, 15 (2013) 17208-17218.
- [30] C.-J. Tseng, S.-T. Lo, S.-C. Lo, P.P. Chu, *Materials Chemistry and Physics*, 100 (2006) 385-390.
- [31] S. Mukerjee, S. Srinivasan, M.P. Soriaga, J. McBreen, *Journal of The Electrochemical Society*, 142 (1995) 1409-1422.
- [32] B.-J. Su, K.-W. Wang, T.-C. Cheng, C.-J. Tseng, *Materials Chemistry and Physics*, 135 (2012) 395-400.
- [33] J. Sun, J. Shi, J. Xu, X. Chen, Z. Zhang, Z. Peng, *Journal of Power Sources*, 279 (2015) 334-344.
- [34] H. El-Deeb, M. Bron, *Electrochimica Acta*, 164 (2015) 315-322.
- [35] M. Ammam, L.E. Prest, A.D. Pauric, E.B. Easton, *Journal of The Electrochemical Society*, 159 (2011) B195-B200.
- [36] M. Ammam, E.B. Easton, *Journal of The Electrochemical Society*, 159 (2012) B635-B640.
- [37] M. Ammam, E.B. Easton, *Journal of Power Sources*, 215 (2012) 188-198.
- [38] M. Ammam, E.B. Easton, *Journal of Power Sources*, 222 (2013) 79-87.
- [39] M. Ghavidel, E. Easton, *Catalysts*, 5 (2015) 1016.
- [40] M.R. Zamanzad Ghavidel, E.B. Easton, *Applied Catalysis B: Environmental*, 176–177 (2015) 150-159.
- [41] P. Mani, R. Srivastava, P. Strasser, *The Journal of Physical Chemistry C*, 112 (2008) 2770-2778.
- [42] J.E. Harlow, D.A. Stevens, R.J. Sanderson, G.C.-K. Liu, L.B. Lohstroter, G.D. Vernstrom, R.T. Atanasoski, M.K. Debe, J.R. Dahn, *Journal of The Electrochemical Society*, 159 (2012) B670-B676.
- [43] R. Lin, T. Zhao, M. Shang, J. Wang, W. Tang, V.E. Guterman, J. Ma, *Journal of Power Sources*, 293 (2015) 274-282.
- [44] X. Zhang, D. Li, D. Dong, H. Wang, P.A. Webley, *Materials Letters*, 64 (2010) 1169-1172.
- [45] M. Oezaslan, M. Heggen, P. Strasser, *Journal of the American Chemical Society*, 134 (2012) 514-524.

- [46] M. Huang, L. Guan, International Journal of Hydrogen Energy, 40 (2015) 6546-6551.
- [47] K.H. Kangasniemi, D. Condit, T. Jarvi, Journal of The Electrochemical Society, 151 (2004) E125-E132.
- [48] O.A. Baturina, S.R. Aubuchon, K.J. Wynne, Chemistry of Materials, 18 (2006) 1498-1504.

Chapter 8: Sensor Performance of the Pt-Mn and Pt-Cu Samples and Durability of Sensors

8.1 Introduction

One of the great application of fuel cells is in devices that measure breath alcohol concentration (BrAC) [1-6]. It is well proven that there are volatile compounds in human breath which makes it possible to detect chemical compounds present in the body [7]. Breath sampling is a very appealing method because it is non-invasive and it can be done in a very short time. Studies have shown that the breath alcohol concentration is proportional to the alcohol concentration in blood, with the ratio of 1:2100 [8]. Other expensive and complicated methods such as solid-state sensing [3], infrared spectrometry [3, 9], biosensors [3, 10], gas chromatography [3, 11], multi-sensor array (semiconductors and infrared devices) [12] and colorimetry [13] can be also used to measure BrAC. However, implementing the fuel-cell based breath alcohol sensor (BrAS) beside simplicity has other benefits. The BrAS devices which are produced using direct alcohol fuel cells (DAFCs) are both cheap and portable. Therefore, the police enforcement is also interested in using the fuel cell breathalysers for road side detection of impaired drivers. The analysis of blood alcohol concentration (BAC) is required for conviction in a court of law [14]. A legal limit for ethanol concentration in a driver's blood was added to the Criminal Code of Canada (Section 235) in December 1969. Since then it has been illegal in Canada to operate a motor vehicle with a BAC greater than 0.08 g/dL, which is equivalent to 80 mg of ethanol per 100 mL of blood [1].

In commercial sensors, a membrane electrode assembly (MEA) is composed of a porous polyvinyl chloride (PVC) membrane that is filled with H_2SO_4 (aq) [15, 16] and two electrodes that contain large amounts of Pt black catalyst (7- 14 mg/cm²) held together with a Teflon binder. Studies in our group have indicated that the Pt utilization was very low in the commercial sensors [1, 4]. However, innovation in the fuel cell industry has resulted in

manufacturing fuel cells with substantially lower Pt loadings. These developments have not been utilized in the production of commercial sensors, nor has the applicability of these technologies been validated for alcohol sensors. Recent studies have shown that Pt loading can be extremely reduced to $\sim 0.5 \text{ mg cm}^{-2}$ or less with using carbon supported Pt nanoparticle [17-24]. On the other hand, new research has shown that the activity of Pt-based catalysts can be further increased by increasing the accessible surface area of the Pt particles typically, by reducing the particle size and improving the particle dispersion [20, 25-27] by developing Pt-alloy catalysts and producing co-catalysts such as Ru, Sn, Mo, Mn, Cu or Ni [26, 28-33] or, by modifying the structure of the Pt or Pt-alloy particles [20, 25, 33-35].

Studies in chapter 3, 4, 5 and 6 showed that the Pt-Mn and Pt-Cu samples have enhanced activity toward the ethanol oxidation. Investigation on the electrochemical activity and stability of the Pt-Mn and Pt-Cu samples indicated that the Pt-Mn and Pt-Cu alloys could replace the commercial Pt samples. In addition, the activity and durability of these alloys were increased utilizing a proper heat treatment procedure. It was shown the heat treatment developed new crystalline phases and improved the Pt-Mn and Pt-Cu alloy structures.

In this chapter, sensing property of selected Pt-Mn and Pt-Cu samples were compared to the commercial samples. The changes in sensing responses and accuracy of different samples were studied over time by two different methods. Finally, the effect of heat treatment on the sensing properties of the Pt-Mn and Pt-Cu alloys was investigated.

8.2 Experimental

8.2.1 Catalyst synthesis

The carbon supported Pt-Mn and Pt-Cu alloys were prepared as explained in section 4.2.1 and 5.2.1. Impregnation in the presence of an additive was used for Pt-Mn/C samples and microwave assisted polyol method used for the Pt-Cu/C samples. In addition, two carbon support commercial samples with 20 wt% metal loading, Pt/C (Premetek Co.) and Pt-Sn/C (Premetek Co.), were studied and compared to the samples made in-house. These samples are hereafter referred to as Pt-Mn/C-SC, Pt-Cu/C-POL, Pt/C and Pt₃Sn/C, respectively.

8.2.2 Electrodes and MEAs Fabrication

Fuel cell electrodes were prepared from catalyst inks, which were produced by mixing the appropriate amounts of catalyst powder, Nafion solution, water and isopropyl alcohol (IPA). The mixture was thoroughly mixed and then sonicated for 45 min. The ink was mechanically stirred overnight to produce a uniform mixture and the ink was further sonicated for 45 min before spray deposited using an airbrush onto carbon paper (Toray TPGH-090, 10 % wet-proofing) as a gas diffusion layer (GDL). The electrodes were dried for 30 min at room temperature and then at 80 °C overnight. The electrode had a Nafion loading of 30 wt% in all cases. The total metal loading of the catalyst layer was kept almost similar at around 0.4 mg/cm². The ink was made using a 5 wt% Nafion solution (Sigma Aldrich). The volumetric ratio of water/IPA was 50% and the ratio of solution to catalyst powder for producing ink was kept constant for all samples.

Later, MEAs were prepared by hot-pressing (150 kg cm^{-2} 120 s at 130°C) two 4 cm^2 electrodes across a Nafion 115 membrane (Ion Power). The cathode electrode was made using the Pt/C powder with metal loading of 0.43 mg/cm^2 and kept same for all MEAs. The electrode utilized as an anode was prepared by different samples and named after the sample powder which was used for making the ink. The total metal loading of anode electrodes was as follows: (a) Pt-Mn/C-SC with 0.33 mg/cm^2 (b) Pt-Mn/C-SC- 700°C with 0.41 mg/cm^2 (c) Pt-Cu/C-POL with 0.4 mg/cm^2 (d) Pt-Cu/C-POL- 700°C with 0.31 mg/cm^2 and (e) $\text{Pt}_3\text{Sn}/\text{C}$ with 0.33 mg/cm^2 metal loading

8.2.3 Fuel cell and Sensing Measurements

The structure of the cell and breath simulator were explained in detail in chapter 2. A cell with electrode surface area of 4 cm^2 was used for all the measurements. The temperature of the aqueous alcohol solution kept constant at 34°C to simulate typical human expired breath [1, 8]. In order to obtain calibration curves for different samples, the concentration of ethanol was varied between 0 and 0.18 g/dL by adding the proper amount of ethanol solution (95%) to the simulated breath. A DC rotary pump (Parker CTS Diaphragm Pump, Model Number E155-11-050) was used for the alcohol injection to the cell which was connected to the breath simulator. The pump was connected to a 5 V DC power supply to keep the flow rate constant for all readings (145 mL/min). The injections were controlled with electronic timers (Omega TRFP240AC). Nitrogen gas with high purity (99.998%) with the pressure of 10 PSI was used as a carrier gas to eliminate any contribution from oxygen or other contaminations to the sensor readings.

Two different testing protocol was used to investigate sensing properties of the samples, which explained as follows:

8.2.3.1 Calibration curves and 7-day sensing tests

In this set of tests, the pump was triggered to operate for 10 s via the electronic timer to simulate a breath injection and the current transient was recorded. A minimum of four breath injections were made at each concentration (0, 0.03, 0.06, 0.08, 0.12, 0.15 and 0.18 g/dL). The resting time between injections was 10 min. From every set of 4 injections, last three were used to determine the charge under the peaks and to calculate standard deviation. This test was repeated for 7 days and the cell was kept in sealed bag overnight to prevent the MEA drying. A recovery protocol was applied to the cell every day before running the sensing test. Our studies showed that the recovery is necessary to achieve more reproducible sensing results [1]. In this protocol, the cell was exposed to humidified Nitrogen gas in the anode side and humidified hydrogen gas in the cathode side while cyclic voltammetry (CV) was recorded at scan rate of 100 mV/s. This continued until a clean and reproducible CVs (~10 to 20 cycles) were observed. CVs at scan rate of 20 mV/s was also recorded to determine the electrochemical active surface area (ESCA). In addition, immediately after recording the cycles at 20 mV/s, electrochemical impedance spectroscopy (EIS) analysis was conducted at 0.360 V vs. NHE (double layer region in CVs) in order to study the performance of the electrodes and estimate the degradation of samples during the 7-day tests.

8.2.3.2 Sensing tests at constant concentration

In these set of experiments, a protocol similar to the section 8.2.3.1 was used with some modifications. The injection and resting time was kept same but the alcohol concentration was not changed during these tests. A single alcohol concentration of 0.06 g/dL was used for all samples. The testing time was ~8 hours and repeated for 7 days. The alcohol solution was replaced every ~4 hours to prevent alcohol depletion and the first four reading of alcohol sensing for fresh solution was used to study the behaviour of sensors over time in the single concertation. The first four readings at beginning of test referred as the first set and the second four readings after changing the solution was accounted as the second set. This test aimed to study the fluctuation and errors would happen in a signal reading for the sensors over time such as effects of alcohol poisoning, or other parameters such as dryness of MEA. The recovery protocol was used at the beginning of every day.

8.3 Result and discussion

8.3.1 CVs and EIS responses of MEA

Figure 8.1 shows the CVs which were recorded for Pt/C and Pt₃Sn/C before the beginning of sensing test at 7 different days. All recorded CVs showed the common Pt CV shape. The hydrogen desorption peak at low potential was used to calculate ECSA which are reported in Table 8.1. The MEA produced with Pt/C showed higher ECSA compared to Pt₃Sn/C, due to higher Pt loading and the calculated ECSA is in good agreement with the values reported in other articles [36, 37]. This shows that the catalyst layer on carbon paper was fabricated with good quality and the cell was assembled in good working condition. The ECSA for Pt/C increased slightly after the first day test, after which

remained fairly stable for the next 6 days of operation. However, the ECSA recorded for Pt₃Sn/C changed more radically over the course of the experiment. ECSA almost doubled and the Pt oxide reduction peak moved to higher potential. This could be due to the removal of Sn oxide which exposed a greater amount of clean Pt surface. After day 4, ECSA decreased slightly which is an indication of degradation in this sample.

The EIS profile of the MEA made by Pt/C and Pt₃Sn/C are shown in Figure 8.2 and 8.3. The Nyquist diagram in Figure 8.2a and 8.3a indicates that the samples illustrated a 45° Warburg-like region. The intersection of Warburg length with the real impedance (Z') axis is proportional to the total catalyst layer resistance ($R_{\Sigma}/3$), where R_{Σ} corresponds to the sum of ionic (R_{ionic}) and electronic resistance (R_{elect}) in the catalyst layer [38]. The capacitance and normalized capacitance (NC) plots are useful diagrams to visualize the ionic resistivity of catalyst layer [39, 40]. In the capacitance plots, the series capacitance ($-1/\omega Z''$) is plotted against Z' . The slope of the high frequency region of the capacitance plot is proportional to the proton conductivity within the catalyst layer and the limiting capacitance (LC) at lower frequency region represents the active surface area (Platinum + carbon) [37, 40]. In NC plots, the maximum capacitance in each graph was used to normalize the capacitances. Comparing the resistance and capacitance of the anode made by Pt/C on different days shows that R_{Σ} decreased while LC increased after first day and then they were almost same until day 7 although there were some small changes. The decrease in the initial R_{Σ} and increase in LC is due to the hydration of ionomer which enhanced the proton conductivity and exposed more carbon and Pt particles to humidified N₂ gas. This is supported by the observed increase in ECSA after the first day. However, the Pt-Sn sample was shown different behaviour. The R_{Σ} decreased and LC was increased

until the fourth day, but R_{Σ} increased and LC decreased after fourth day. This kind of degradation of the Pt-Sn catalyst layer was also seen in chapter 6 in the half-cell measurements. It seems that ECSA followed the same trend as LC. The highest ECSA was measured at day four and then it declined as LC decreased. Based on the results in chapter 6, this is due to modification of ionomer and formation of higher concentration of the Sn oxide inside the catalyst layer.

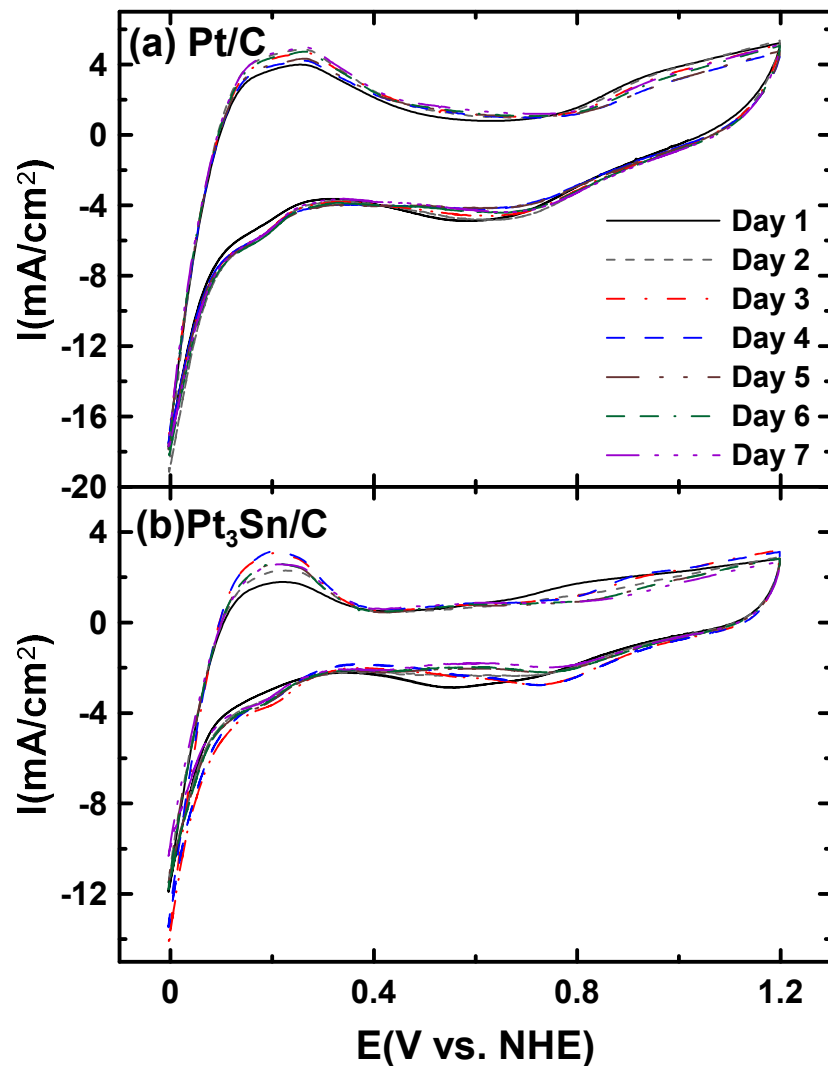


Figure 8.1. CVs obtained for the anode electrodes produced by commercial samples (a) Pt/C and (b) $\text{Pt}_3\text{Sn}/\text{C}$ before the beginning of every day sensing test. Measurements were

made in the full cell configuration at a scan rate of 20 mV/s. In both case the cathode electrode made by Pt/C and humidify-H₂ gas was used at the cathode electrode and the humidify-N₂ gas was used at the anode.

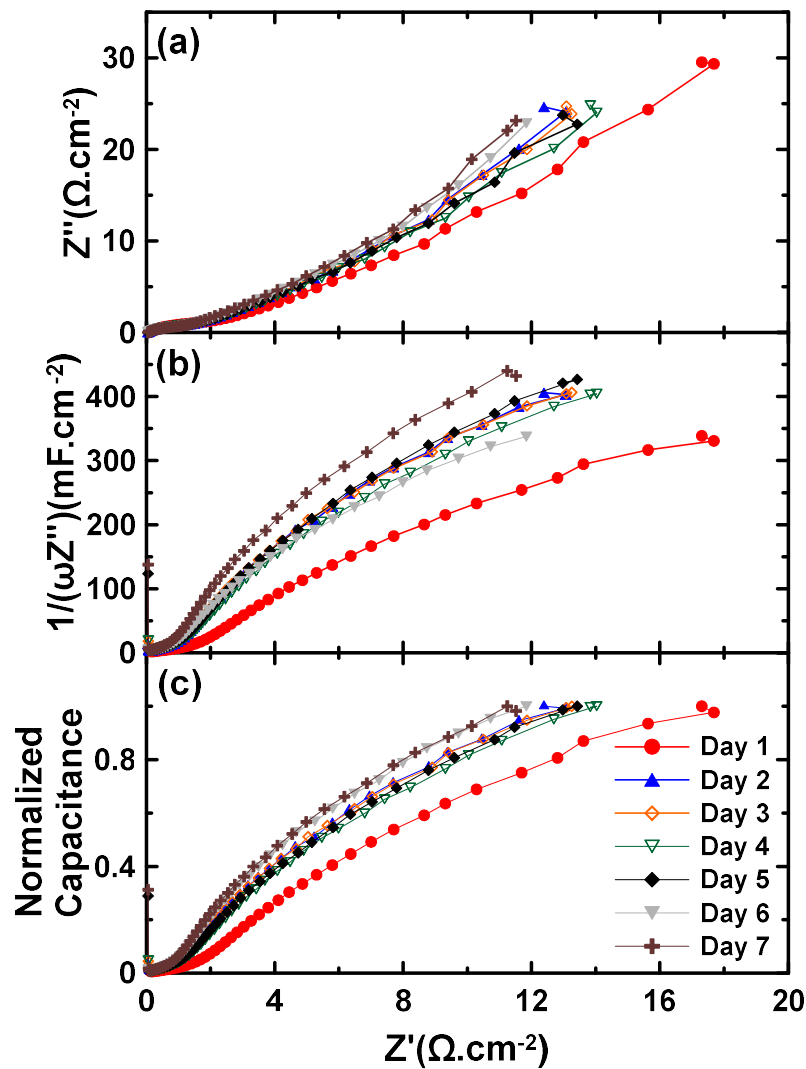


Figure 8.2. (a), (b) and (c) The EIS responses obtained at a DC bias potential of 0.360 V vs. NHE for Pt/C before the beginning of every day sensing test. The cathode electrode made by Pt/C and the humidify-H₂ gas was used at the cathode electrode and the humidify-N₂ gas was used at the anode.

Figure 8.4 shows CVs of the electrodes produced by Pt-Mn/C-SC and Pt-Mn/C-SC-700 °C. The common Pt CV shape with hydrogen adsorption/desorption peaks at lower potentials was also seen for these samples. ECSA was calculated for each day and reported in Table 8.2. The behaviour of CVs was slightly different from what observed for commercial samples. In both samples, the intensity of the Pt oxide reduction peak at ~ 0.8 V vs. NHE was reduced but new peak was appeared at lower potential (~ 0.4 V vs. NHE) after the first day. The peak at lower potential may be due to the quinone formation or may related to Mn oxide reduction. However, it is a little difficult to come to a definite conclusion. The intensities of these peaks were almost unchanged during the next days.

The ECSA calculated for Pt-Mn/C-SC and Pt-Mn/C-SC-700 °C, and was shown to decrease over the course of the 7-day experiment for the both samples. The ECSA loss was more pronounced for the Pt-Mn/C-SC sample. However, the ECSA changes were not as large as the Pt-Sn samples.

The EIS profiles for Pt-Mn/C-SC and Pt-Mn/C-SC-700 °C are shown in Figure 8.5 and 8.6. Figure 8.5a shows that R_{Σ} for Pt-Mn/C-SC increased after the first day, after which it remained relatively stable for the next 6 days. In the opposite, R_{Σ} was decreased for Pt-Mn/C-SC-700 °C when the test extended to higher number of days. There was slightly increase in R_{Σ} at second day which most likely caused by the drying of MEA overnight (which was later rehydrated with further operation). The catalyst layer R_{Σ} for Pt-Mn/C-SC-700 °C was slightly lower than Pt-Mn/C-SC which could be a result of lower Mn oxide content.

LC for Pt-Mn/C-SC was slightly increased but it was fairly stable during throughout sensor testing. However, the LC for Pt-Mn/C-SC-700 °C was almost stayed the same in

whole 7-day test. Pt-Mn/C-SC-700 °C showed higher LC which indicates that the heat treatment helped to expose the higher surface area of the catalyst powder to the humidified gas. It should be mentioned here that the catalyst loading for these two samples was almost similar. These results are a little different from the result that we have seen for the half-cell measurements. I believe that the differences are due to the stability of the Mn oxide in the acidic environment. Previous studies have shown that the Mn oxides dissolves in the presence of acid [41]; therefore, in the half-cell measurements where the electrode are immersed completely in the acid, it is difficult to see the effects of the Mn oxide in the electrochemical responses due to the Mn oxide fast dissolution. However, the presence of metal oxides had stronger effects in the sensor measurements because the dissolution rate is much slower.

In Figure 8.7, the voltammetric response of Pt-Cu/C-POL and Pt-Cu/C-POL-700 °C are displayed. It is possible to observe copper oxidation and dissolution for Pt-Cu/C-POL in Figure 8.7a. Cu_{II} represents the dissolution of Pt-coordinated Cu atoms while Cu_I is a result of losing the Cu atoms coordinated to the other Cu atoms [34, 42]. The Cu_{II} peak was decayed by increasing the number of days. The highest Cu_{II} peak was seen for the first day. On the other hand, the intensity of Cu_I was increased by increasing the number of sensing tests (Figure 8.7a). This shows that the dissolved copper in the catalyst layer was depositing back as the bulk copper. In addition, Table 8.3 illustrates that ECSA was reduced during the 7-day sensing test. It can be concluded that the ECSA loss was caused by dissolution of alloy particles and redepositing of Cu on the surface of catalyst particles which could block the active sites.

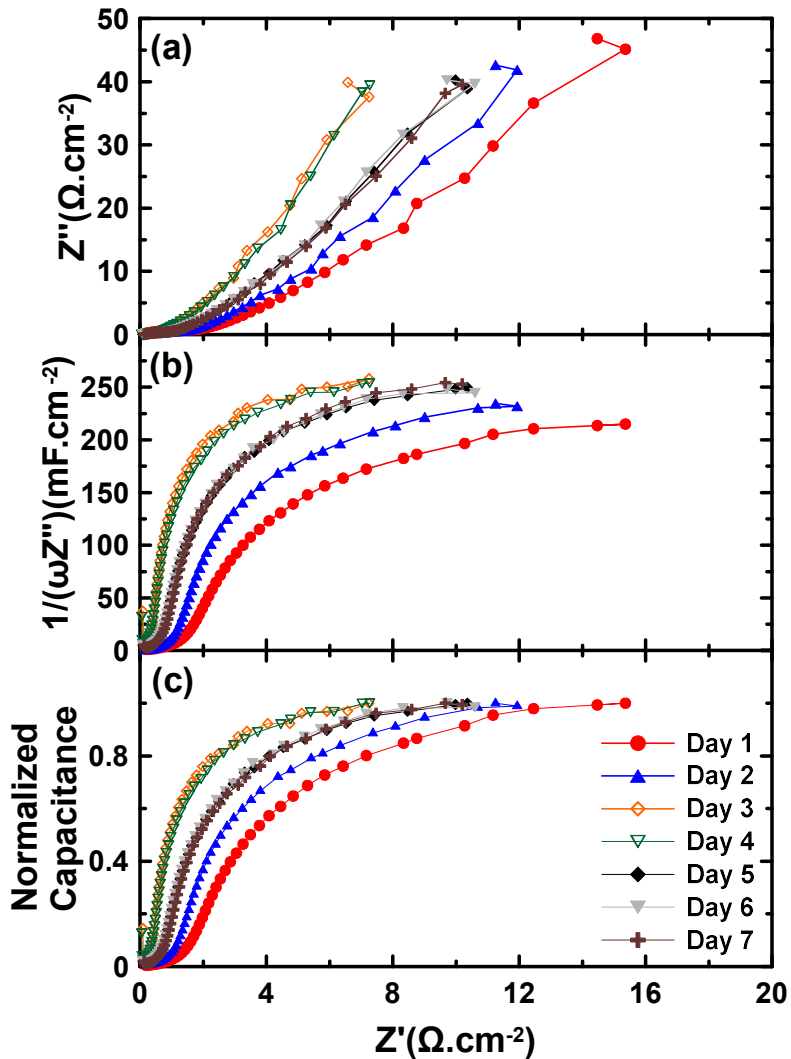


Figure 8.3. (a), (b) and (c) The EIS responses obtained at a DC bias potential of 0.360 V vs. NHE for Pt₃Sn/C before the beginning of every day sensing test. The cathode electrode made by Pt/C and the humidify-H₂ gas was used at the cathode electrode and the humidify-N₂ gas was used at the anode.

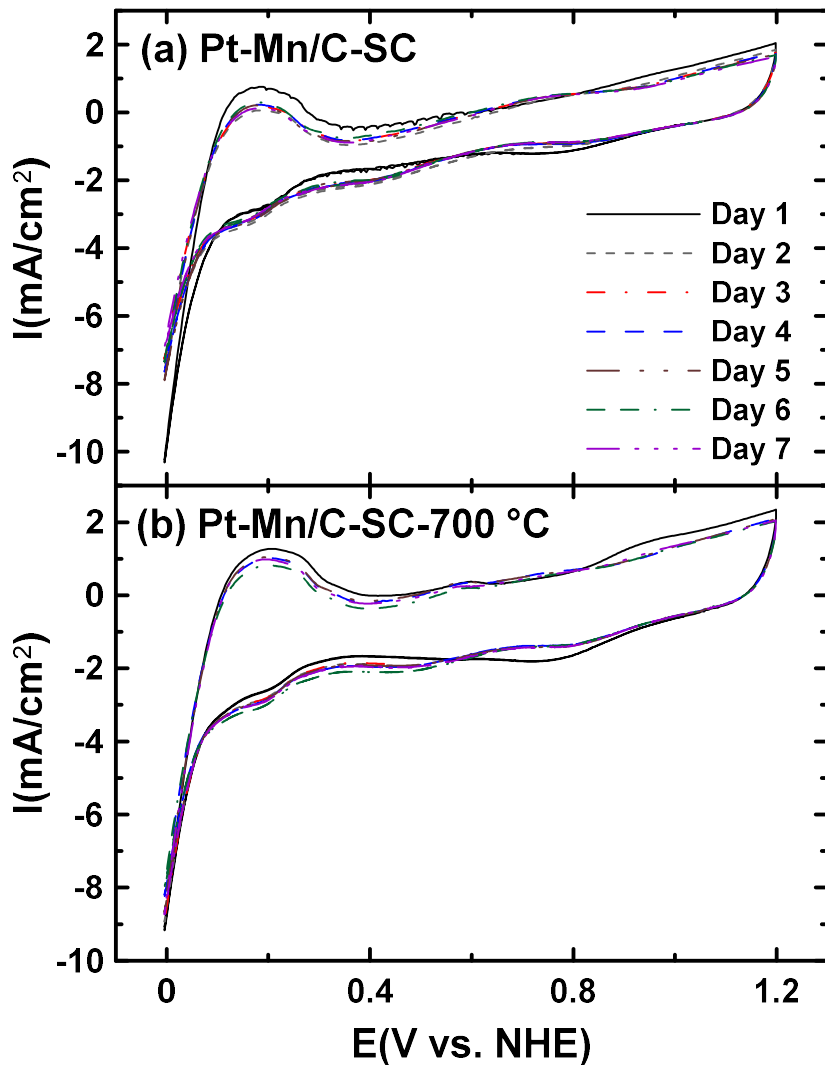


Figure 8.4. CVs obtained for the anode electrodes produced by (a) Pt-Mn/C-SC and (b) Pt-Mn/C-SC-700 °C before the beginning of every day sensing test. Measurements were made in the full cell configuration at a scan rate of 20 mV/s. In both case the cathode electrode made by Pt/C and humidify-H₂ gas was used at the cathode electrode and the humidify-N₂ gas was used at the anode.

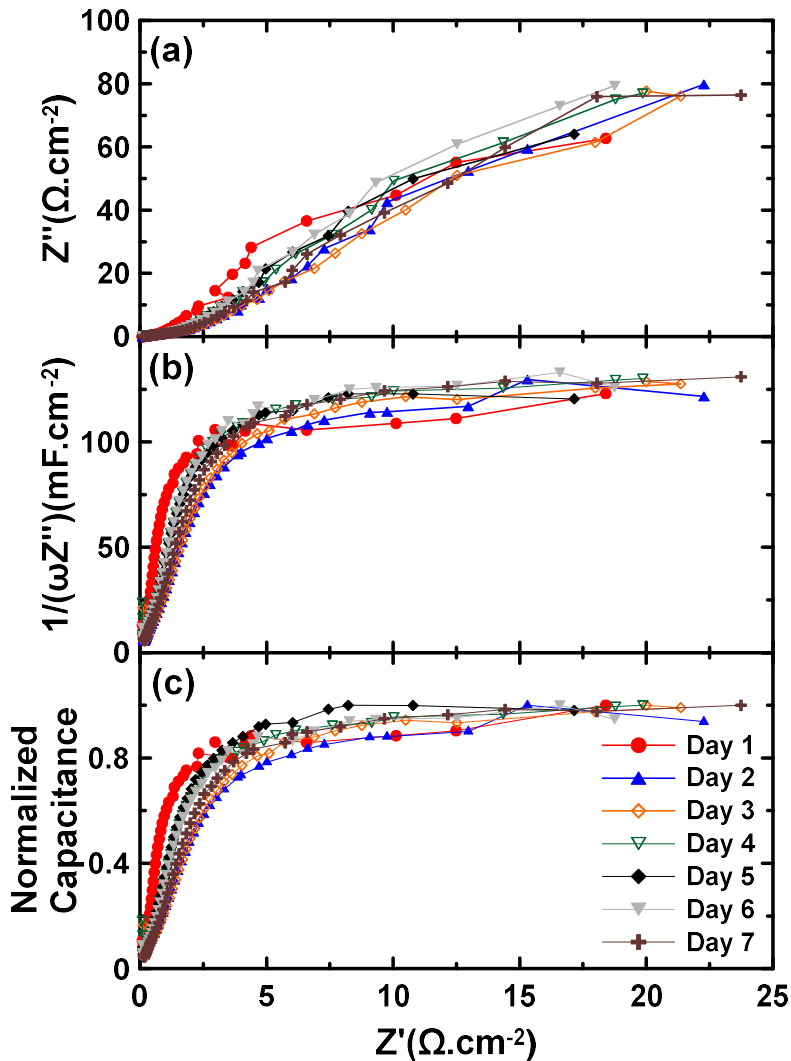


Figure 8.5. (a), (b) and (c) The EIS responses obtained at a DC bias potential of 0.360 V vs. NHE for Pt-Mn/C-SC before the beginning of every day sensing test. The cathode electrode made by Pt/C and the humidify-H₂ gas was used at the cathode electrode and the humidify-N₂ gas was used at the anode.

On the contrary, the Cu_I and Cu_{II} peaks were much less prevalent for Pt-Cu/C-POL-700 °C. It was also shown in chapter 5 that the heat treatment reduced copper dissolution. It is possible to see a trace of the Cu_I peak for Pt-Cu/C-POL-700 °C after 6 days of the sensing tests but it is much smaller than the peak observed for Pt-Cu/C-POL. In addition,

Table 8.3 shows that ECSA was varied in different days for Pt-Cu/C-POL-700 °C but it was mostly higher than the ECSA calculated for Pt-Cu/C-POL. However, the ECSA difference was not huge between these two samples.

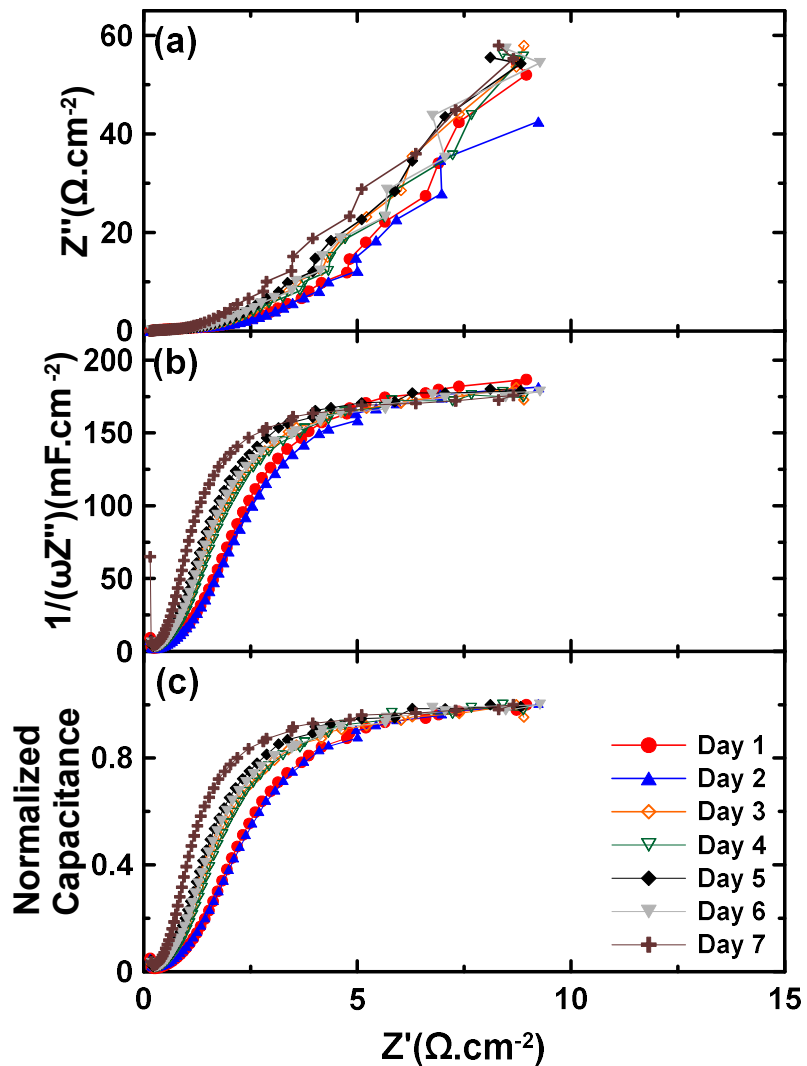


Figure 8.6. (a), (b) and (c) The EIS responses obtained at a DC bias potential of 0.360 V vs. NHE for Pt-Mn/C-SC-700 °C before the beginning of every day sensing test. The cathode electrode made by Pt/C and the humidify-H₂ gas was used at the cathode electrode and the humidify-N₂ gas was used at anode side.

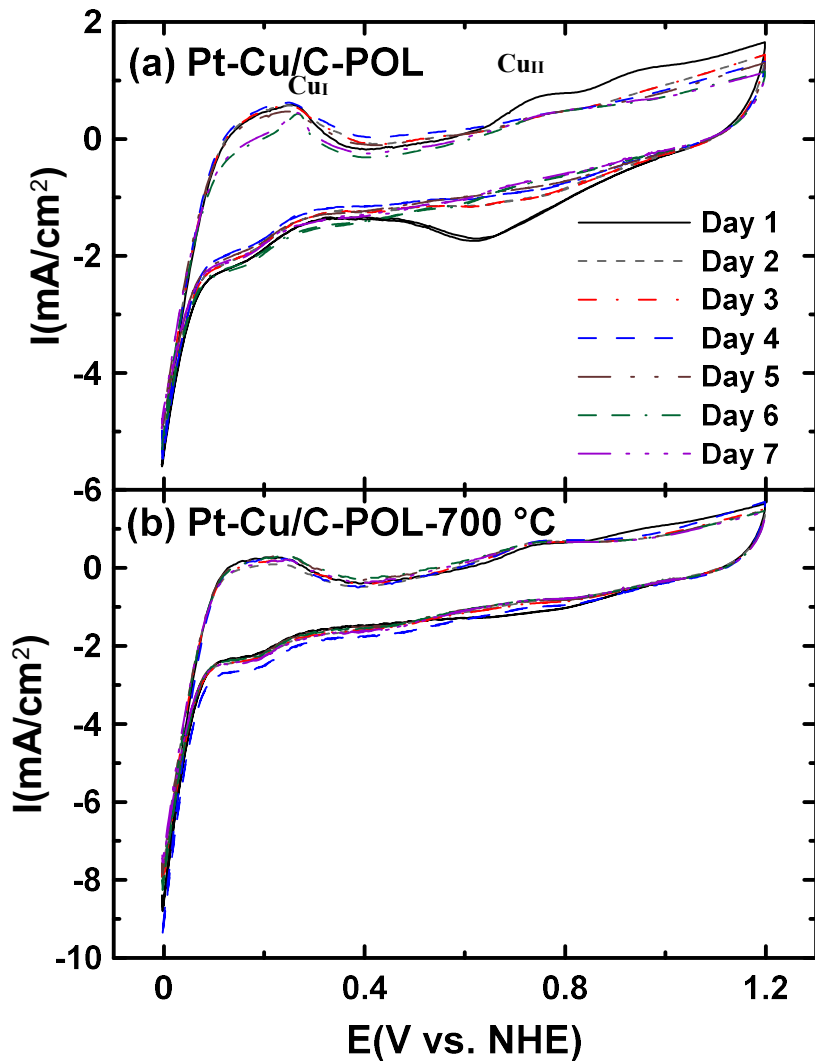


Figure 8.7. CVs obtained for the anode electrodes produced by (a) Pt-Cu/C-POL and (b) Pt-Cu/C-POL-700 °C before the beginning of every day sensing test. Measurements were made in the full cell configuration at a scan rate of 20 mV/s. In both case the cathode electrode made by Pt/C and humidify-H₂ gas was used at the cathode electrode and the humidify-N₂ gas was used at the anode.

The EIS analyses of Pt-Cu/C-POL and Pt-Cu/C-POL-700 °C are shown in Figure 8.10 and 8.11. The EIS profile of Pt-Cu/C-POL was very similar to Pt-Mn/C-SC. The catalyst

layer R_{Σ} was increased and LC was decreased for Pt-Cu/C-POL. This shows that dissolution of Cu and the Cu oxide inside the catalysts layer reflected on the electrochemical response and increased the ionic resistance of catalyst layer. In addition, redeposition of bulk copper on the catalysts reduced the capacitance. However, comparing R_{Σ} of Pt-Cu/C-POL-700 °C and Pt-Cu/C-POL indicates that the heat treatment of the Pt-Cu sample reduced the ionic resistance of the catalysts layer (Figure 8.9). R_{Σ} determined for Pt-Cu/C-POL-700 °C was almost constant over the course of 7-day experiment. LC of Pt-Cu/C-POL-700 °C was slightly increased during the experiment which could be due to the hydration of the catalyst layer.

In this section, it was shown that MEAs with reasonable qualities were produced. Although there are some differences in the electrochemical response of different samples, the overall behaviour of the samples and their stability did not change significantly during the 7-day sensing test. In addition, it was demonstrated that the heat treatment improved the properties of the catalysts layer for the Pt-Mn and Pt-Cu alloyed samples. However, the sensitivity of the samples and sensing response of the fuel cell is related to overall performance of the MEA assembled using these samples.

8.3.2 Sensing properties of the selected samples

MEAs were produced by selected samples showed reasonable response to EIS and CV analyses. However, the main goal of this project was to produce accurate and reliable sensors. Therefore, in this section the sensing properties of different samples was examined and compared in order to identify the best candidates for building a sensitive breath alcohol sensor.

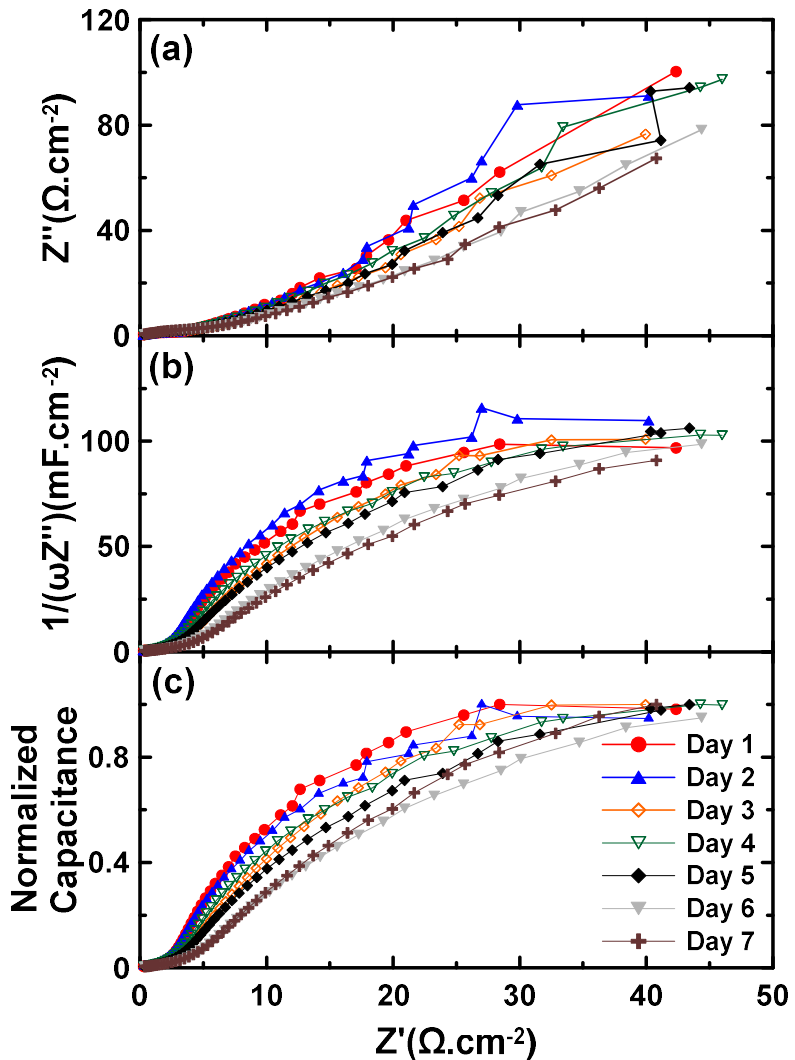


Figure 8.8. (a), (b) and (c) The EIS responses obtained at a DC bias potential of 0.360 V vs. NHE for Pt-Cu/C-POL before the beginning of every day sensing test. The cathode electrode made by Pt/C and the humidify-H₂ gas was used at the cathode electrode and the humidify-N₂ gas was used at the anode.

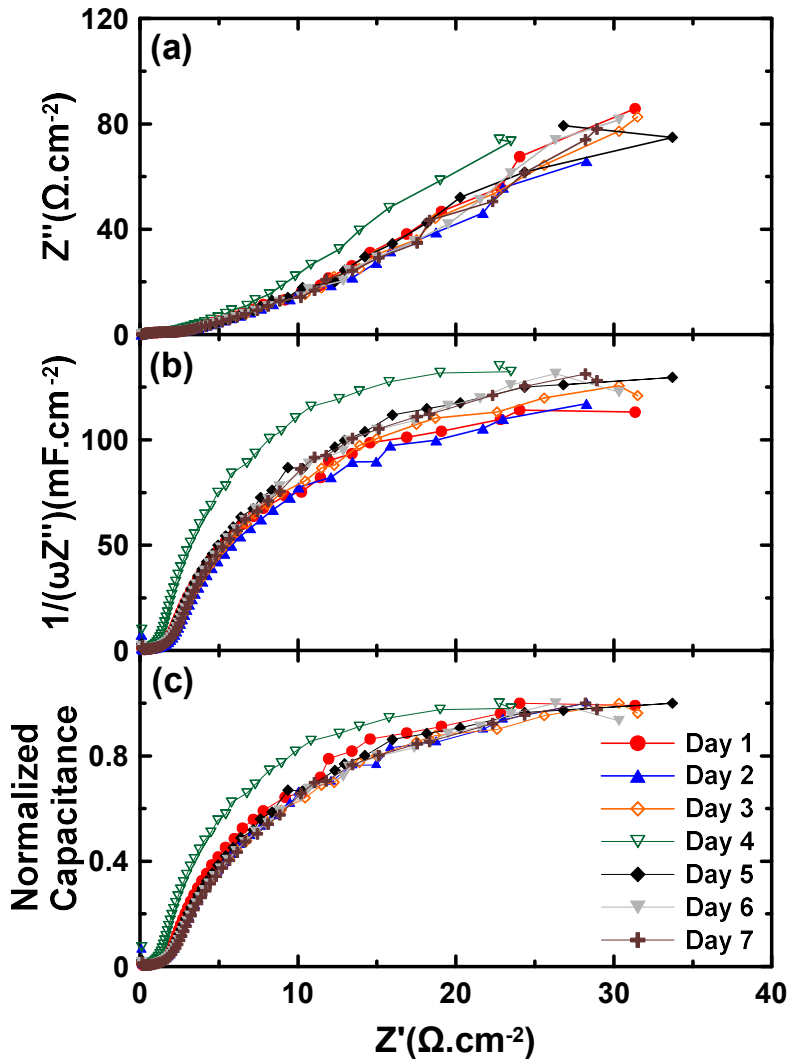


Figure 8.9. (a), (b) and (c) The EIS responses obtained at a DC bias potential of 0.360 V vs. NHE for Pt-Cu/C-POL-700 °C before the beginning of every day sensing test. The cathode electrode made by Pt/C and the humidify-H₂ gas was used at the cathode electrode and the humidify-N₂ gas was used at the anode.

Figure 8.10 shows the calibration curve for the Pt/C and Pt₃Sn/C samples. These samples showed linear responses to an increase in the concentration of alcohol even at very high concentration. The slope of each diagram represents the sensitivity of the sample at specific day. Sensitivity was determined from linear fit to each set of data. The sensitivities

and the R^2 values of the fitting curves are also reported in Table 8.1. The very high R^2 values confirm the linear behaviour of the samples. Comparison between the R^2 values for the commercial samples showed that the linearity of the sensing responses for Pt/C was better. These results and the error bars in Figure 8.10 shows that error in measuring BAC could be slightly higher utilizing the Pt₃Sn/C sample, but the Pt₃Sn/C sample could detect lower amount of alcohol. However, the errors at concentration lower than 0.12 g/dL was negligible which still higher than the legal limit of BAC (0.08 g/dL).

The sensitivity of sample for better visualization and comparison also presented in Figure 8.11. These data show that the sensitivity of the commercial sample was changed slightly in the course of the 7-day sensing tests but still, there is a great reproducibility in the sensitivity. Specially, Pt₃Sn/C showed higher reproducibility during the 7-day tests. Although CVs and the EIS studies showed that there were some changes in the electrochemical behaviour of Pt₃Sn/C during these 7 days, the sensitivity for Pt₃Sn/C was very reproducible. The reproducibility of the sensitivity is directly related to the poisoning of the catalyst layer in the course of sensing process. It has been shown in our lab that the sensitivity of the samples poisoned by the ethanol oxidation can be recovered by cleaning cycles in the absence of ethanol [1] which was utilized in these tests before each test. Therefore, the recovery of the Pt₃Sn/C sensitivity was better than Pt/C. In addition, Figure 8.11 indicates that the sensitivity of Pt₃Sn/C was higher than Pt/C which illustrates that utilization of Pt was better in the Pt₃Sn/C sample.

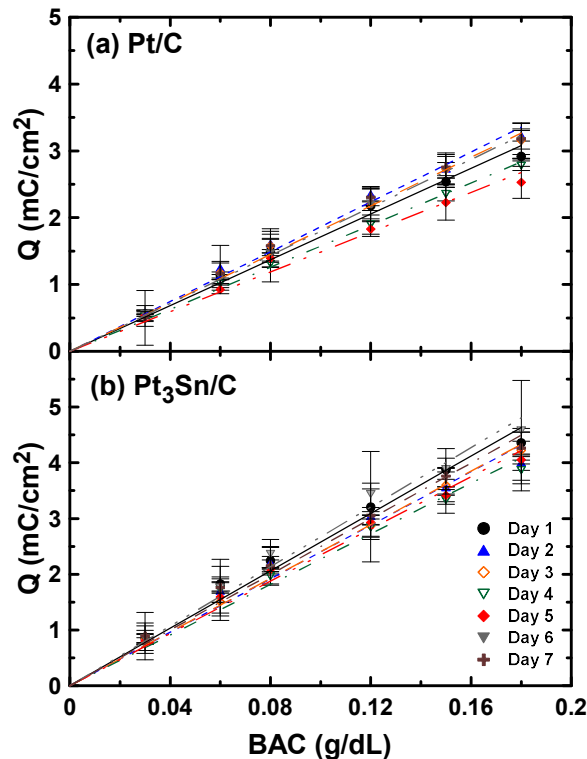


Figure 8.10. Calibration curve obtained at different days for commercial samples (a) Pt/C and (b) $\text{Pt}_3\text{Sn}/\text{C}$ as the anode electrode on the carbon paper. Measurements were made in the full cell. The humidify- N_2 gas was used as the carrier gas at the anode. The cathode electrode was exposed to air.

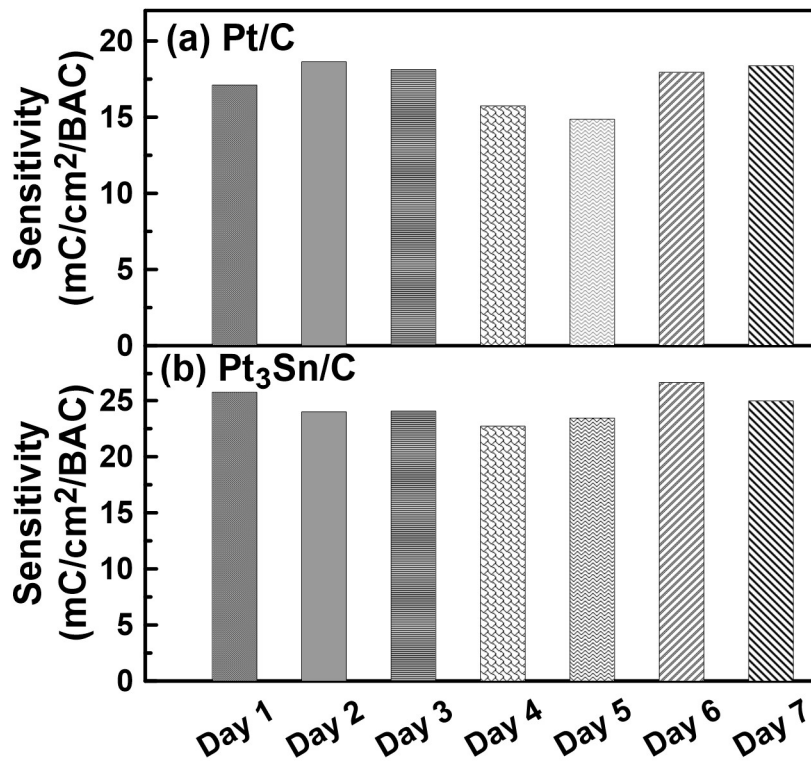


Figure 8.11. Sensitivity of the commercial samples (a) Pt/C and (b) Pt₃Sn/C calculated using Figure 8.10.

Table 8.1. Summary of ECSA and sensitivity data determined for Pt/C and Pt₃Sn/C.

	Sensitivity (mC/cm ² /BAC)	Normalized Sensitivity (C/BAC/g _{Pt})	R ²	ECSA (m ² /g _{Pt})
Pt/C-Day 1	17.11	14.26	0.982	62.83
Pt/C-Day 2	18.64	15.53	0.986	75.49
Pt/C-Day 3	18.14	15.12	0.992	71.57
Pt/C-Day 4	15.74	13.12	0.996	67.24
Pt/C-Day 5	14.86	12.38	0.974	67.33
Pt/C-Day 6	17.95	14.96	0.997	70.10
Pt/C-Day 7	18.38	15.32	0.991	72.67
<hr/>				
Pt ₃ Sn/C-Day 1	25.75	28.61	0.976	23.14
Pt ₃ Sn/C-Day 2	24.00	26.67	0.956	34.12
Pt ₃ Sn/C-Day 3	24.07	26.74	0.990	44.79
Pt ₃ Sn/C-Day 4	22.72	25.24	0.961	46.18
Pt ₃ Sn/C-Day 5	23.44	26.04	0.981	39.26
Pt ₃ Sn/C-Day 6	26.70	29.67	0.980	38.90
Pt ₃ Sn/C-Day 7	24.98	27.76	0.979	34.32

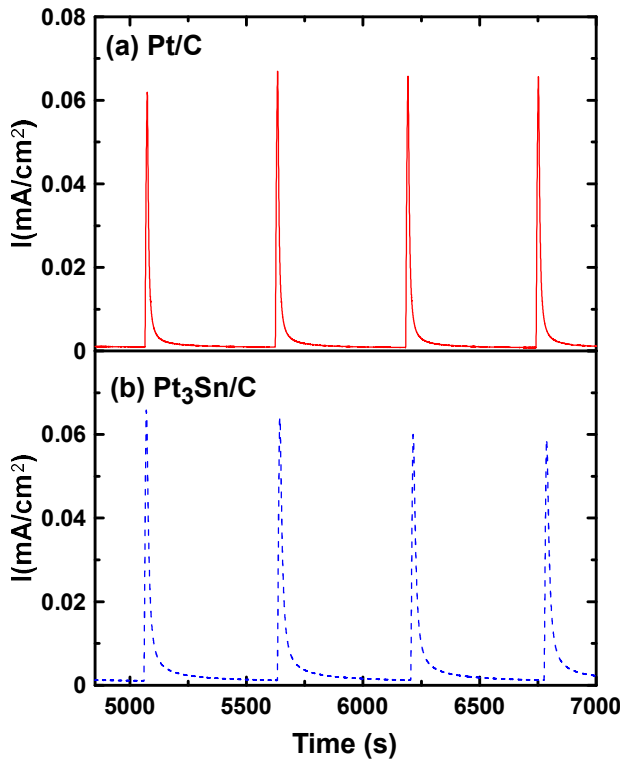


Figure 8.12. Sensing responses for (a) Pt/C and (b) $\text{Pt}_3\text{Sn}/\text{C}$ at 0.06 g/dL for the first day.

The sensing responses for the Pt/C and $\text{Pt}_3\text{Sn}/\text{C}$ samples at 0.06 g/dL for the first day are presented in Figure 8.12. The peaks recorded for these samples were very sharp. The intensity of the peaks recorded for these samples were close but the charge calculated for the peaks was different. Therefore, the higher sensitivity of $\text{Pt}_3\text{Sn}/\text{C}$ could be due to changes in the mechanism of ethanol oxidation and production of more electrons per mole of ethanol, resistivity toward poisoning and/or better recovery after the sensing test.

Figure 8.13 displays the calibration curves for Pt-Mn/C-SC and Pt-Mn/C-SC-700 °C. The sensitivity determined from Figure 8.13 and presented in Table 8.2. The sensitivity of Pt-Mn/C-SC and Pt-Mn/C-SC-700 °C are compared in Figure 8.14. The calibration curve for Pt-Mn/C-SC did not show a linear behaviour for the first two days. However, the

response to the ethanol sensing improved after third day. The first two days may account as break-in time, but the sensitivity of the Pt-Mn/C-SC sample was not quite good and it fluctuated a lot in the process of the 7-day sensing tests. The R^2 values showed that the linearity of the fittings also changed dramatically. The best sensitivity was recorded at the 5th day. On the other hand, the Pt-Mn/C-SC-700 °C MEA showed a very linear behaviour in responses to the ethanol sensing. The R^2 values was close to 1 which shows that the linear plot fitted very well to the sensing data. The sensitivity of Pt-Mn/C-SC-700 °C was higher than Pt-Mn/C-SC and also it was highly reproducible in the course of 7-day. These results show that the recovery of sensitivity was good for Pt-Mn/C-SC-700 °C and recovery protocol was also successful for this sample. The only exception in this sample was the result achieved for the second day. This most likely caused by the drying of MEA overnight (which was later rehydrated with further operation). However, even dryness of MEA did not affect the linearity of sensing response for Pt-Mn/C-SC-700 °C.

The sensing responses of Pt-Mn/C-SC and Pt-Mn/C-SC-700 °C at 0.06 g/dL for the first day are illustrated in Figure 8.15. This figure shows that the intensity and sharpness of the sensing responses were increased dramatically after the heat treatment. These results confirmed the results was reported using the half-cell measurements in chapter 3 and 4. The higher sensitivity of Pt-Mn/C-SC-700 °C could be due to removal of the Mn oxide and formation of more active phases upon heat treatment, which also affected the quality of the MEA preparation using this sample. The delamination of MEA even after very long sensing process was not observed for Pt-Mn/C-SC-700 °C. On the other hand, delamination of MEA was a great problem for Pt-Mn/C-SC, especially during long sensing tests. The lower sensitivity of Pt-Mn/C-SC could also be caused by delamination of MEA.

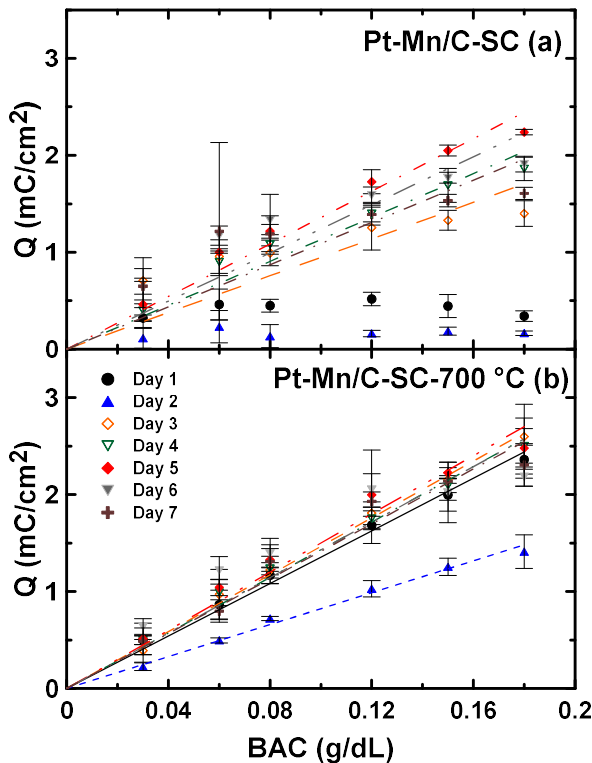


Figure 8.13. Calibration curve obtained at different days for (a) Pt-Mn/C-SC and (b) Pt-Mn/C-SC-700 °C as the anode electrode. Measurements were made in the full cell. The humidify-N2 gas was used as the carrier gas at the anode. The cathode electrode was exposed to air.

The calibration curves of Pt-Cu/C-POL and Pt-Cu/C-POL-700 °C are demonstrated in Figure 8.16. The sensitivity for each test was determined by Figure 8.16 and reported in Table 8.2. The sensitivity of Pt-Cu/C-POL and Pt-Cu/C-POL-700 °C are compared in Figure 8.17. The calibration curves of the Pt-Cu sample before heat treatment was shown linearity just at lower alcohol concentration, usually lower than 0.08 g/dL. The linearity of the calibration curve was altered in the course of the 7-day sensing test but it declined dramatically after the 4th day. The best linearity was seen at the 4th day. As shown in section 8.3.1, the Pt-Cu samples before the heat treatment showed the copper dissolution

and the bulk copper redeposited in the catalyst layer. This could be one the reasons to observe poor sensitivity for this sample. Besides, Pt-Cu/C-POL were more vulnerable to delamination similar to the Pt-Mn samples. It was difficult to produce a MEA which would not delaminate during the sensing tests, while the sensitivity of Pt-Cu/C-POL before delamination was also lower than the heat treated sample. However, the heat treated Pt-Cu sample showed a linear response to the ethanol concentration. The sensitivity of Pt-Cu/C-POL-700 °C was higher than the Pt/C sample but decreased in the course of the 7-day sensing test. This could be due to dissolution of Cu from alloyed particles and deposition of bulk Cu in the catalyst layer which was blocking the available surface area. Although the dissolution of Cu in the heat treated samples was reduced, these results indicates that Pt-Cu samples are vulnerable to decay in the sensitivity during long periods of operation. The R^2 values indicate that the linearity of the calibration curves was not changed during overall experiment.

The sensing responses for Pt-Cu/C-POL and Pt-Cu/C-POL-700 °C at 0.06 g/dL for the first day are compared in Figure 8.1. These results show that the intensity of peaks were improved after the heat treatment. The higher sensitivity of the Pt-Cu samples after the heat treatment was due to removal of oxide phases and other contaminations and also caused by formation of more active phases and reduction of Cu dissolution. Similar to Pt-Mn samples, the heat treatment also improved the quality of MEA which delayed the delamination of catalyst layers. However, the chance of delamination was higher for the heat treated Pt-Cu samples compared to the heat treated Pt-Mn samples. The problem with delamination of MEAs may be solved by optimizing and changing some of the MEA fabricating parameters. However, in this thesis the previously well-studied fabrication protocol was used [1], in order to compare samples in the same conditions.

Table 8.2. Summary of ECSA and sensitivity data determined for Pt-Mn/C-SC and Pt-Mn/C-SC-700 °C.

	Sensitivity (mC/cm ² /BAC)	Normalized Sensitivity- (C/BAC/g _{Pt})	R ²	ECSA (m ² /g _{Pt})
Pt-Mn/C-SC-Day 1	-	-		27.35
Pt-Mn/C-SC-Day 2	-	-		21.82
Pt-Mn/C-SC-Day 3	9.47	14.35	0.410	20.34
Pt-Mn/C-SC-Day 4	11.32	17.15	0.921	19.97
Pt-Mn/C-SC-Day 5	13.58	20.58	0.954	20.60
Pt-Mn/C-SC-Day 6	12.41	18.80	0.549	20.58
Pt-Mn/C-SC-Day 7	10.89	16.50	0.120	20.14
Pt-Mn/C-SC-700 °C -Day 1	13.55	20.53	0.988	30.42
Pt-Mn/C-SC-700 °C -Day 2	8.23	12.47	0.989	30.49
Pt-Mn/C-SC-700 °C -Day 3	14.66	22.21	0.994	28.23
Pt-Mn/C-SC-700 °C -Day 4	14.31	21.68	0.986	27.48
Pt-Mn/C-SC-700 °C -Day 5	15.00	22.73	0.956	27.69
Pt-Mn/C-SC-700 °C -Day 6	14.30	21.67	0.717	26.33
Pt-Mn/C-SC-700 °C -Day 7	14.15	21.44	0.946	26.72

In Figure 8.19, the mean sensitivity and normalized sensitivity of different samples in the course of 7-day measurements are demonstrated. The highest sensitivity was recorded for Pt₃Sn/C and the highest normalized sensitivity was determined for Pt-Cu/C-POL-700 °C. These results indicate that the utilization of Pt was the best for Pt-Cu/C-POL-700 °C and it was the most active samples which was produced in this project toward the ethanol sensing. However, the sensitivity of this sample decreased overtime and further research in order to improve its stability is necessary. In addition, the stativity data for the commercial cell is shown in Figure 8.19 for further comparison which have been measured previously by our group [1]. The raw sensitivity of the alloys developed in-house are close or better than commercial cell. The normalized sensitivity of the in-house samples indicates that the utilization of Pt is extremely better than the commercial cell. These results show that there

are alternative catalysts to replace Pt black in commercial cells, to reduce the Pt content and to improve the sensitivity of the commercial alcohol sensors.

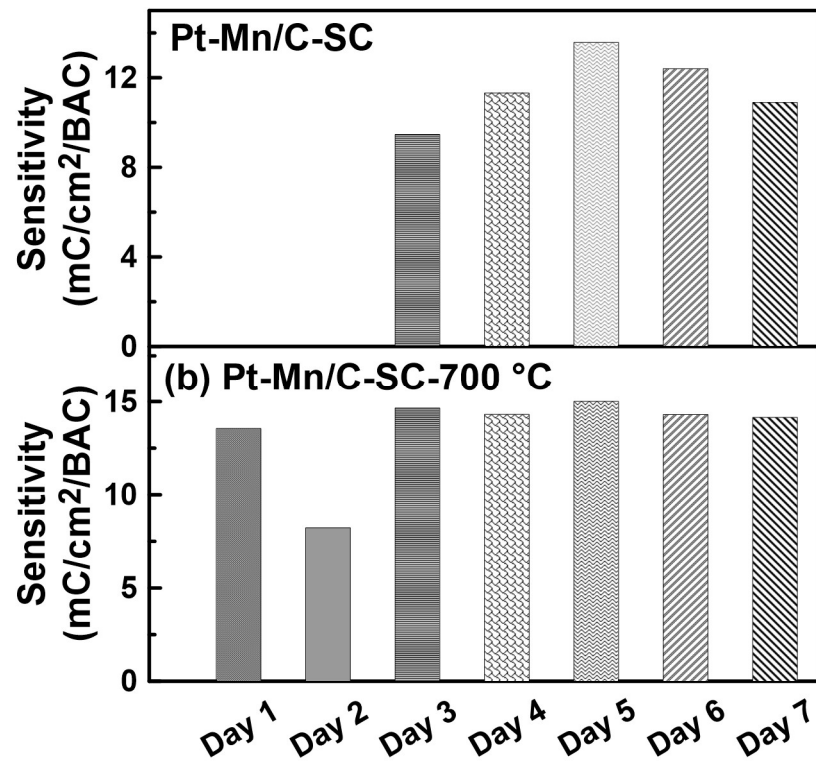


Figure 8.14. Sensitivity of the commercial samples (a) Pt-Mn/C-SC and (b) Pt-Mn/C-SC-700 °C calculated using Figure 8.13.

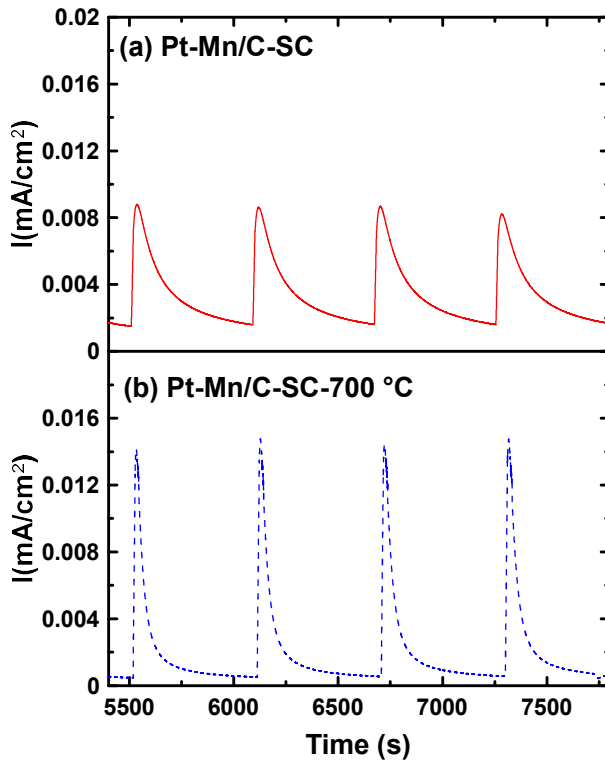


Figure 8.15. Sensing responses for (a) Pt-Mn/C-SC and (b) Pt-Mn/C-SC-700 °C at 0.06 g/dL for the first day.

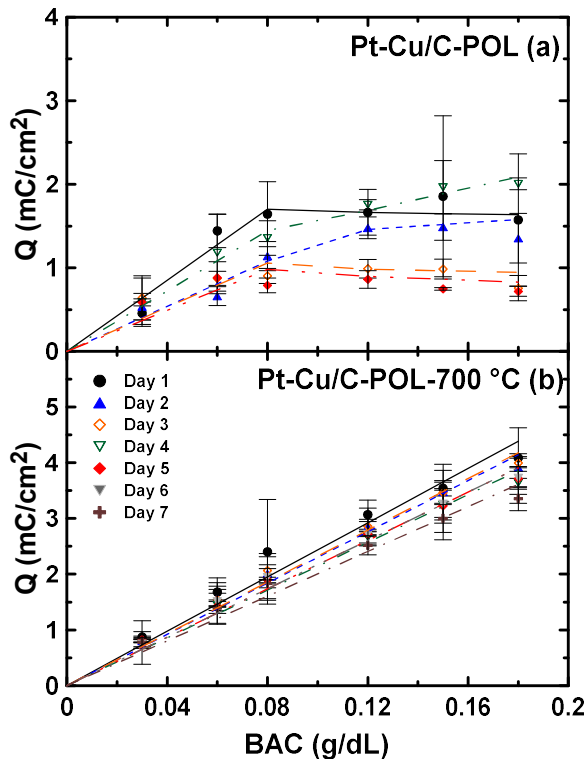


Figure 8.16. Calibration curve obtained at different days for (a) Pt-Cu/C-POL and (b) Pt-Cu/C-POL-700 °C as the anode electrode. Measurements were made in the full cell. The humidify-N₂ gas was used as the carrier gas at the anode. The cathode electrode was and exposed to air.

8.3.3 Sensing behaviour in single concentration

The calibration of alcohol breath sensors in the industry is usually done with single reading at specific concentration. Additionally, it was shown in section 8.3.2 that the measurements in each alcohol concentration involved some errors. However, the road-side BrAC measurement would be done just with single reading. Therefore, it is important to study the behaviour of sensors in single concentration over time. In this section, the same fuel cells examined in section 8.3.2 were exposed to the 0.06 g/dL concentration of alcohol

for ~8 hours every day in the course of 7 days. The first four readings at beginning of test referred as the first set and the second four readings after changing the solution account as the second set. The 0.06 g/dL concentration was chosen based on previous studies in our group [1] and also it was selected because the most of the samples showed linear behaviour with lower errors in this region.

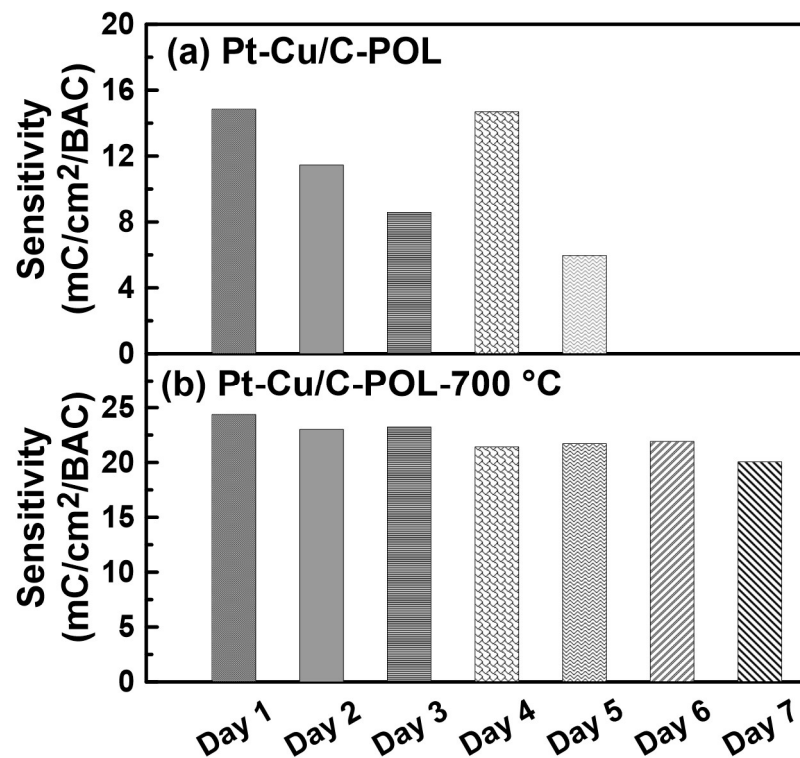


Figure 8.17. Sensitivity of the commercial samples (a) Pt-Cu/C-POL and (b) Pt-Cu/C-POL-700 °C calculated using Figure 8.16.

Table 8.3. Summary of ECSA and sensitivity data determined for (a) Pt-Cu/C-POL and (b) Pt-Cu/C-POL-700 °C.

	Sensitivity (mC/cm ² /BAC)	Normalized Sensitivity- (C/BAC/gPt)	R ²	ECSA (m ² /gPt)
Pt-Cu/C-POL-Day 1	14.84	22.48	0.460	16.63
Pt-Cu/C-POL -Day 2	11.46	17.36	0.811	16.61
Pt-Cu/C-POL -Day 3	8.59	13.02	0.224	15.14
Pt-Cu/C-POL -Day 4	14.69	22.26	0.824	13.60
Pt-Cu/C-POL -Day 5	5.96	9.03	0.511	12.76
Pt-Cu/C-POL -Day 6	-	-	-	11.20
Pt-Cu/C-POL -Day 7	-	-	-	10.76
<hr/>				
Pt-Cu/C-POL-700 °C -Day 1	24.37	36.93	0.946	16.20
Pt-Cu/C-POL-700 °C -Day 2	23.01	34.87	0.981	13.02
Pt-Cu/C-POL-700 °C -Day 3	23.23	35.20	0.984	14.35
Pt-Cu/C-POL-700 °C -Day 4	21.43	32.47	0.982	17.53
Pt-Cu/C-POL-700 °C -Day 5	21.71	32.89	0.980	15.46
Pt-Cu/C-POL-700 °C -Day 6	21.92	33.21	0.977	12.75
Pt-Cu/C-POL-700 °C -Day 7	20.07	30.40	0.961	12.88

The results of the single concentration readings are shown in Figure 8.20 and 8.21. The charge densities, which were measured on different days, were changed and the standard deviation associated to each day were also altered in the course of test. The higher variations in the charge densities were observed for the Pt/C and Pt-Mn/C-SC-700 °C samples. The Pt₃Sn/C and Pt-Cu/C-POL-700 °C samples showed the higher mean charge intensities at this concentration compared to other samples. The fluctuation in the charge readings of the Pt₃Sn/C and Pt-Cu/C-POL-700 °C samples was less than Pt/C. In all the samples, the standard deviation of readings was generally larger in the second set of readings where the recovery cycle was not applied. These results show that without a recovery procedure, the accuracy of single readings could be reduced over time which could be worse for the higher concentration of alcohol. The higher errors could be caused by poisoning of samples by intermediates of the EOR or due to dehydration of MEA.

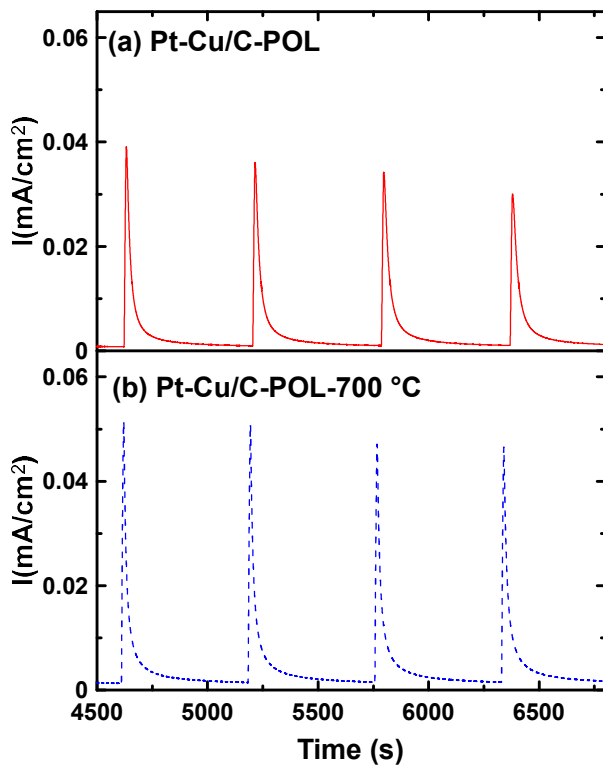


Figure 8.18. Sensing responses for (a) Pt-Cu/C-POL and (b) Pt-Cu/C-POL-700 °C at 0.06 g/dL for the first day.

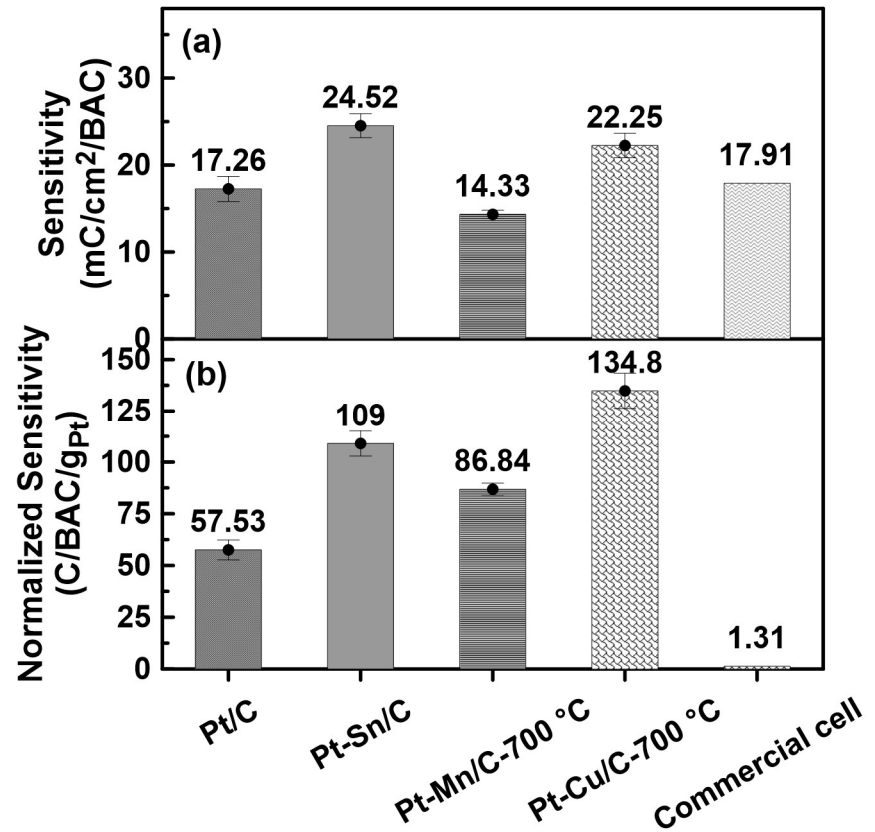


Figure 8.19. The mean sensitivity and normalized sensitivity of different samples in the course of 7-day measurements.

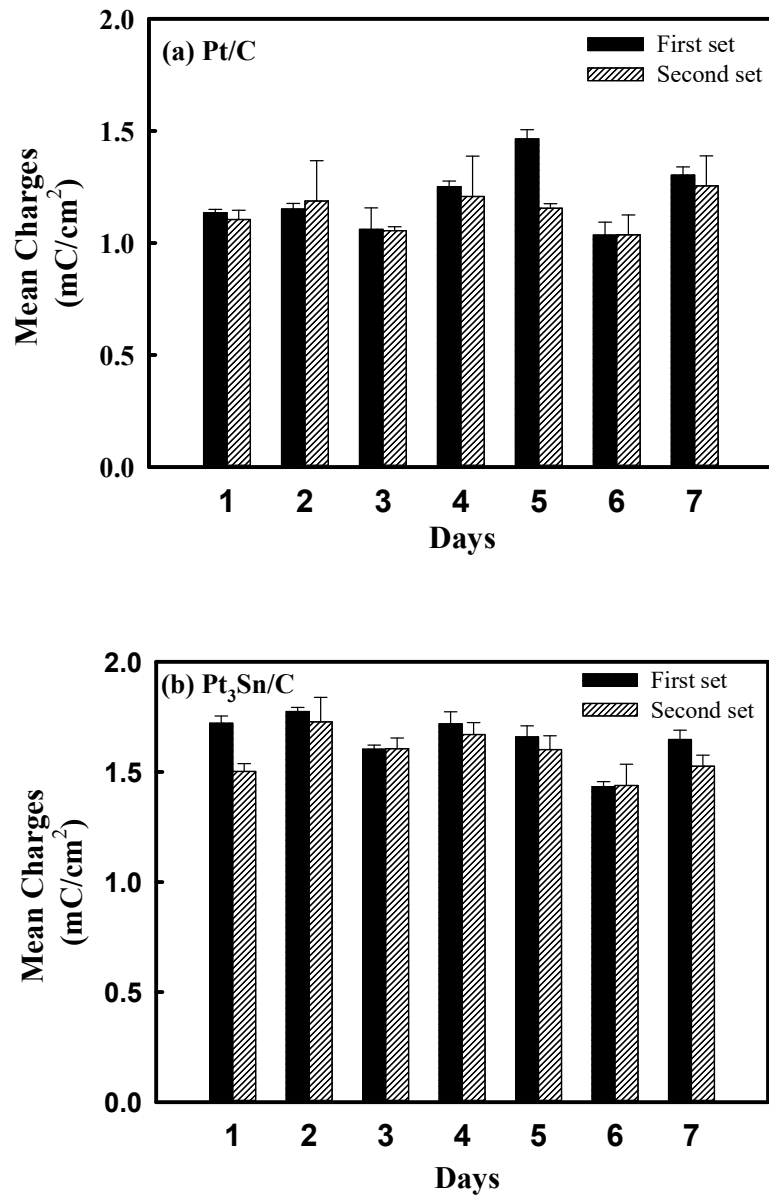


Figure 8.20. The results of readings at the single concentration of 0.06 g/dL for commercial sample (a) Pt/C and (b) Pt₃Sn/C.

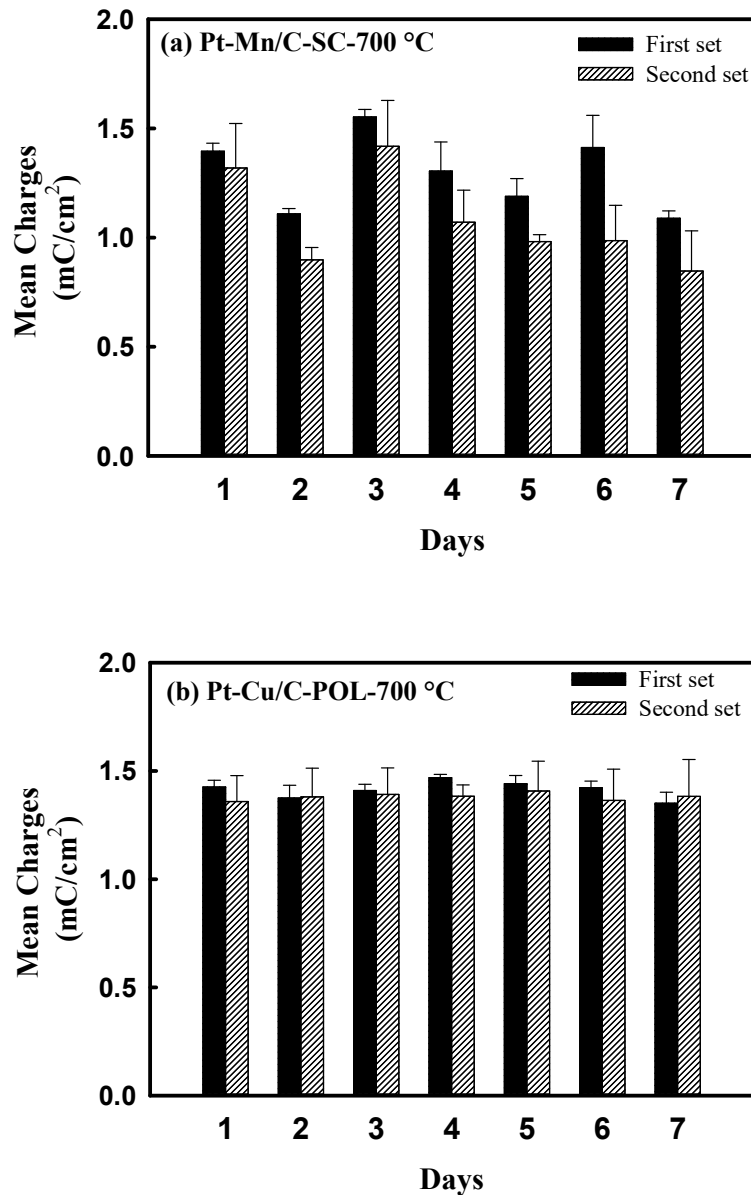


Figure 8.21. The results of readings at the single concentration of 0.06 g/dL for (a) Pt-Mn/C-SC-700 °C and (b) Pt-Cu/C-POL-700 °C.

8.4 Conclusion

In this chapter, the alcohol sensing of Pt/C and Pt₃Sn/C and selected Pt-Mn and Pt-Cu samples were studied and the variation of sensitivity over time was compared for different

samples. In order to study the sensing responses of different samples, two different protocols were used. In addition, the effect of heat treatment on the sensing properties of the Pt-Mn and Pt-Cu alloys was investigated. The voltammetric and EIS studies were shown that catalyst layers and MEAs were prepared with reasonable qualities. There were some changes in the ECSA values, the ionic resistance and the limiting capacitance of the catalyst layers in the course of 7-day sensing test. These changes were less pronounced for Pt/C and the heat treated Pt-Cu and Pt-Mn. Furthermore, it was demonstrated that the heat treatment improved the properties of the catalysts layer and MEA and it was reduced the chance of delamination for the Pt-Mn and Pt-Cu samples. Considering the commercial samples which was tested in this section, Pt₃Sn/C showed the highest sensitivity but with slightly higher standard deviation. Moreover, the heat treatment improved the sensitivity of the Pt-Mn and Pt-Cu samples and the sensitivity of the heat treated Pt-Mn showed higher reproducibility over time compared to the heat treated Pt-Cu. However, the highest normalized sensitivity among all samples was belonged to the Pt-Cu samples produced by polyol method and heat treated at 700 °C. These results dictated that alloying of Pt with Cu or Mn and using a proper production method combined with optimum heat treatment would improve the utilization of Pt. Finally, it can be concluded that the heat treated Pt-Mn and Pt-Cu samples could be used as an alternative to replace Pt black in commercial sensors which would dramatically decrease the Pt loading. This could reduce the price and increase the sensitivity of commercial alcohol sensors.

8.5 References

- [1] M.R. Rahman, J.T.S. Allan, M. Zamanzad Ghavidel, L.E. Prest, F.S. Saleh, E.B. Easton, Sensors and Actuators B: Chemical, 228 (2016) 448-457.
- [2] R.G. Gullberg, Forensic science international, 131 (2003) 30-35.
- [3] M. Mason, K.M. Dubowski, Journal of forensic sciences, 21 (1976) 9-41.
- [4] L. Prest, in, UOIT, UOIT, 2011.
- [5] G.C. Forrester, in, Google Patents, 1995.
- [6] N.C. Jain, R.H. Cravey, Journal of chromatographic science, 12 (1974) 214-218.
- [7] B. Krotoszynski, G. Gabriel, H. O'Neill, M. Claudio, Journal of chromatographic science, 15 (1977) 239-244.
- [8] P. Millet, A. Michas, R. Durand, J Appl Electrochem, 26 (1996) 933-937.
- [9] B. Goldberger, Y. Caplan, Journal of forensic sciences, 31 (1986) 16-19.
- [10] J.-K. Park, H.-J. Yee, K.S. Lee, W.-Y. Lee, M.-C. Shin, T.-H. Kim, S.-R. Kim, Analytica chimica acta, 390 (1999) 83-91.
- [11] T. Kamei, T. Tsuda, Y. Mibu, S. Kitagawa, H. Wada, K. Naitoh, K. Nakashima, Analytica chimica acta, 365 (1998) 259-266.
- [12] N.J. Paulsson, F. Winquist, Forensic science international, 105 (1999) 95-114.
- [13] M.B. Williams, H.D. Reese, Analytical chemistry, 22 (1950) 1556-1561.
- [14] A.W. Jones, L. Andersson, Forensic science international, 132 (2003) 18-25.
- [15] J.T. Allan, L.E. Prest, E.B. Easton, Journal of Membrane Science, 489 (2015) 175-182.
- [16] K. Kamiya, M. Sudoh, ECS Transactions, 58 (2014) 1-10.
- [17] S. Litster, G. McLean, Journal of Power Sources, 130 (2004) 61-76.
- [18] Y. Xu, B. Zhang, Chemical Society Reviews, 43 (2014) 2439-2450.
- [19] M. Watanabe, K. Tsurumi, T. Mizukami, T. Nakamura, P. Stonehart, Journal of The Electrochemical Society, 141 (1994) 2659-2668.
- [20] F. Vigier, S. Rousseau, C. Coutanceau, J.-M. Leger, C. Lamy, Top Catal, 40 (2006) 111-121.

- [21] J. Zhang, H. Liu, *Electrocatalysis of Direct Methanol Fuel Cells: From Fundamentals to Applications*, John Wiley & Sons, Germany, 2009.
- [22] W. Vielstich, A. Lamm, H.A. Gasteiger, *Handbook of Fuel Cells: Fundamental, Technology, and Applications*, Wiley, 2003.
- [23] C. He, S. Desai, G. Brown, S. Bollepalli, *Interface-Electrochemical Society*, 14 (2005) 41-46.
- [24] C. Lamy, S. Rousseau, E. Belgsir, C. Coutanceau, J.-M. Léger, *Electrochimica Acta*, 49 (2004) 3901-3908.
- [25] H. Liu, C. Song, L. Zhang, J. Zhang, H. Wang, D.P. Wilkinson, *Journal of Power Sources*, 155 (2006) 95-110.
- [26] T. Sato, K. Okaya, K. Kunimatsu, H. Yano, M. Watanabe, H. Uchida, *ACS Catalysis*, 2 (2012) 450-455.
- [27] M. Ghavidel, E. Easton, *Catalysts*, 5 (2015) 1016.
- [28] T. Ghosh, B.M. Leonard, Q. Zhou, F.J. DiSalvo, *Chemistry of Materials*, 22 (2010) 2190-2202.
- [29] E. Antolini, J.R.C. Salgado, E.R. Gonzalez, *Applied Catalysis B: Environmental*, 63 (2006) 137-149.
- [30] W. Roh, J. Cho, H. Kim, *J Appl Electrochem*, 26 (1996) 623-630.
- [31] T.J. Schmidt, H.A. Gasteiger, R.J. Behm, *Electrochemistry Communications*, 1 (1999) 1-4.
- [32] M. Ammam, E.B. Easton, *Journal of The Electrochemical Society*, 159 (2012) B635-B640.
- [33] M.R. Zamanzad Ghavidel, E.B. Easton, *Applied Catalysis B: Environmental*, 176–177 (2015) 150-159.
- [34] N. Hodnik, C. Jeyabharathi, J.C. Meier, A. Kostka, K.L. Phani, A. Recnik, M. Bele, S. Hocevar, M. Gaberscek, K.J.J. Mayrhofer, *Physical Chemistry Chemical Physics*, 16 (2014) 13610-13615.
- [35] M. Oezaslan, M. Heggen, P. Strasser, *Journal of the American Chemical Society*, 134 (2012) 514-524.
- [36] F.S. Saleh, E.B. Easton, *Electrochimica Acta*, 114 (2013) 278-284.
- [37] F.S. Saleh, E.B. Easton, *Journal of The Electrochemical Society*, 159 (2012) B546-B553.

- [38] E.B. Easton, P.G. Pickup, *Electrochimica Acta*, 50 (2005) 2469-2474.
- [39] N. Jia, R.B. Martin, Z. Qi, M.C. Lefebvre, P.G. Pickup, *Electrochimica acta*, 46 (2001) 2863-2869.
- [40] F.S. Saleh, E.B. Easton, *Journal of Power Sources*, 246 (2014) 392-401.
- [41] J.E. Harlow, D.A. Stevens, R.J. Sanderson, G.C.-K. Liu, L.B. Lohstroter, G.D. Vernstrom, R.T. Atanasoski, M.K. Debe, J.R. Dahn, *Journal of The Electrochemical Society*, 159 (2012) B670-B676.
- [42] M. Oezaslan, F. Hasché, P. Strasser, *Journal of The Electrochemical Society*, 159 (2012) B444-B454.

Chapter 9: Summary and Future Directions

9.1 Summary

In this thesis, carbon supported Pt-Mn and Pt-Cu electrocatalysts were synthesized with different methods and the effects of heat treatment and structural modification on the ethanol oxidation reaction (EOR) activity, oxygen reduction reaction (ORR) activity and durability of these samples were thoroughly studied. In addition, the Pt-Mn and Pt-Cu samples with the highest EOR activity and durability were selected to build the fuel-cell based breath alcohol sensor (BrAS) and the performance of the samples developed in-house were compared to the commercially available samples such as Pt/C and Pt₃Sn/C (Premetek Co.). The final goal of this thesis is to understand which factors influence catalytic activity of the Pt-Mn and Pt-Cu electrocatalysts and if the alloy catalysts are viable catalysts for a BrAS.

The Pt-Mn/C prepared by the impregnation method was studied with differential scanning calorimetry (DSC), powder X-ray diffraction (XRD) and X-ray photoelectron spectroscopy (XPS). The as-deposited Pt-Mn/C catalyst contained a mixture of weakly alloyed Pt-Mn and inactive oxide phases, which are limiting factors for the catalytic performance of the Pt-Mn alloys. Previous studies have shown that heat treatment could remove undesirable impurities, increase stability and enhance the catalytic activity [1-4]. For this reason, the heat treatment in an inert atmosphere (N₂- gas) was conducted at different temperatures 500, 700, 875 and 950 °C. The XRD analysis indicates that the ordered PtMn intermetallic was formed at 700 °C, and that this phase transition required about 4 hours at that temperature to completely form. The phase evolution at 875 °C was faster and resulted in the formation of a mixture of PtMn and Pt₃Mn intermetallic phases. Particle size growth was observed for all heat treated samples by Transmission Electron Microscopy (TEM). Therefore, loss in the electrochemical active surface area (ECSA) was

detected as well. Further electrochemical studies in an ethanol solution illustrate that the heat treatment higher than 700 °C improved the catalytic activity toward EOR. Comparing the EOR activity for catalysts prepared at different heat treatment temperatures and time indicates that the most active phase of the Pt-Mn alloys toward EOR is the PtMn intermetallic phase. Maximum EOR activity occurred when the samples were heat treated at 700 °C for 4 h, which corresponded to the highest concentration of this PtMn intermetallic phase with a small loss in ECSA compared to the as-produced samples.

The TEM images show that the presence of particle agglomeration in the Pt-Mn samples was one of the main reason for the particle growth. Therefore, the effects of adding SC on particle dispersion and grain sizes of the Pt-Mn particles was investigated. The TEM results indicate that adding SC to the impregnation solution improved the particle dispersion and decreased particle sizes. Additionally, because of the improvement in the particle deposition, the time required for heat treatment at 700 °C was reduced from 4 h to 1 h. Overall, adding SC to the impregnation solution improved the particle dispersion and increased the ECSA even after the heat treatment. Similar crystalline structure evolution was observed for the heat treated Pt-Mn/C-SC and the heat treatment enhanced the EOR activity of the Pt-Mn/C-SC catalysts. Studies on finding optimum concentration of SC illustrate that the weight ratio of SC to metal loading should be kept lower than 2 and at higher weight ratios the metal particle dispersion was hindered. Furthermore, it was shown that SC is sensitive to pH of the impregnation solution and pH should be adjusted to lower than 4 in order to achieve optimum results. Moreover, the heat-treated samples prepared in the presence of SC showed superior the EOR activity compared to the samples made without SC.

In the next part of this thesis, the Pt-Cu/C alloys were produced with similar protocols in order to find the best method and crystalline structure for the Pt-Cu/C catalysts. The effects of three different production methods and heat treatment on the structure and the electrochemical properties of the Pt-Cu catalysts were explored. The coupled plasma optical emission spectroscopy (ICP-OES) and thermogravimetric analysis (TGA) results indicate that using different methods altered the chemical composition and the metal loading of samples. The impregnation method without an additive (Pt-Cu/C-IMP) produced the samples with the highest metal loading and the Cu content. The lowest metal loading was achieved by the polyol method (Pt-Cu/C-POL) and the lowest Cu loading was reached by the impregnation method with SC (Pt-Cu/C-SC). Studies by TEM shows that the particle dispersion was improved by using the polyol method. The XRD analysis indicates that the heat treatment at 700 °C developed ordered crystalline structures similar to the Pt-Mn samples and the PtCu and PtCu₃ ordered phases were observed in this case. The highest EOR activity was measured for the Pt-Cu/C-POL samples that heat treated at 700 °C for 1h which also had the lowest metal loading and low ECSA. Comparing the EOR activity of the Pt-Cu and Pt-Mn samples also demonstrates that the Pt-Cu/C-POL samples, especially after the heat treatment, showed higher EOR activity compared to the heat treated Pt-Mn/C-SC.

In general, it can be concluded that the enhancement of EOR activity for the Pt-Mn and Pt-Cu systems was due to the formation of the ordered crystalline phases, especially regarding the PtMn and PtCu ordered crystalline structures. However, the formation of a superior crystalline structure is the consequence of an optimal heat treatment and effective chemical composition. These results indicate that the benefits of thermally treating alloy

nano particles could outweigh any activity losses that may occur due to the particle size growth and the ECSA loss.

With the intention of understanding the effects of heat treatment and structural modifications on the stability and durability of different samples. The samples with the best particle dispersion and EOR activity was chosen and studied in more details. The Pt-Mn/C-SC and Pt-Cu/C-POL alloys were studied using accelerated stress test (AST) combined with the *ex situ* ICP, *ex situ* XRD and electrochemical impendence spectroscopy (EIS) analyses. For better comparison, the durability of the samples produced in-house compared to the durability of the commercially available samples (Pt/C and Pt₃Sn/C). The *ex situ* ICP and XRD analyses indicate that the dealloying occurred during the electrochemical cycling or AST tests for all the alloyed samples. However, the dealloying was decreased by increasing the Pt content and applying the heat treatment. The *ex situ* XRD analysis also shows the crystalline structure of the alloyed particles was modified and changed back to the pure Pt structure with cycling due to the dealloying.

The studies indicate that particles with a Pt-rich shell were formed during the AST and there were two stages of degradation; the first stage controlled by the alloying element depletion and second stage controlled by the ECSA loss and the crystalline structure modification. The findings show that the ECSA loss and the crystalline modifications were the most important degradation factors which were controlled the EOR activity of the alloyed samples. Based on the AST findings, heat treatment improved the durability and the EOR activity of samples. Moreover, the results confirm that AST combined with the EIS analysis was a very powerful electrochemical method to identify and separate different degradation mechanisms even for the Pt-alloy samples.

These studies showed that the samples prepared in-house are highly equivalent or even better regarding the EOR activity and stability compared to commercial samples. The stability and EOR activity of the Pt-Cu/C-POL was the highest over the course of 2000 cycles.

The oxygen reduction reaction (ORR) is one of the important chain reactions in fuel cells which can be improved by the Pt-base alloys [5-7]. In this study the ORR activity of the selected Pt-Mn and Pt-Cu alloys were also examined and compared to the Pt/C and Pt-Sn/C commercial samples and the effects of heat treatment and formation of ordered structures on the ORR activity in both Pt-Cu and Pt-Mn systems were investigated. The studies show that, before the heat treatment, on-set potential ($V_{\text{on-set}}$) for ORR decreased due to the presence of alloying elements. The highest $V_{\text{on-set}}$ was recorded for Pt/C. Therefore, adding the alloying elements was slightly reduced the ORR activity. However, the economic benefits from using lower Pt loading compensate the small activity loss. In addition, the findings show the ORR activity of the alloyed samples was affected by the heat treatment and formation of ordered phases. After the heat treatment at 700 °C, $V_{\text{on-set}}$ for the Pt-Mn system was improved and $V_{\text{on-set}}$ for the Pt-Cu system did not change but the limiting current density of the Pt-Cu system was improved.

Finally, the alcohol sensing properties of Pt/C and Pt₃Sn/C and Pt-Mn/C-SC and Pt-Cu/C-POL samples were evaluated. The sensing responses of different samples were studied using two different protocols: 7-day sensing and constant concentration protocols. The voltammetric and EIS studies were used to control examine the properties of the catalyst layers and membrane electrode assemblies (MEAs). The electrochemical and sensing responses show that there were some changes in the ECSA values, the ionic resistance and the limiting capacitance of the catalyst layers in the course of 7-day sensing

test. These changes were less pronounced for Pt/C and the heat treated Pt-Cu/C-POL and Pt-Mn/C-SC samples. It was demonstrated that the heat treatment improved the properties of the catalysts layer and MEA and it was reduced the chance of delamination for the Pt-Mn and Pt-Cu samples. Among the commercial samples, Pt-Sn/C showed the highest sensitivity but with slightly higher standard deviation. Further studies on the Pt-Cu/C-POL and Pt-Mn/C-SC samples indicate that the heat treatment improved the sensitivity of these samples and the sensitivity of the heat treated Pt-Mn/C-SC was more reproducible than the heat treated Pt-Cu/C-POL in the course of 7 days. However, the highest normalized sensitivity among all samples was belonged to the Pt-Cu/C-POL sample produced by polyol method and heat treated at 700 °C.

In conclusion, these results indicate that alloying of Pt with Cu or Mn and using proper production method combined with optimum heat treatment would improve the utilization of Pt. Furthermore, it can be concluded that the heat treated Pt-Mn/C-SC and Pt-Cu/C-POL samples could be used as an alternative to replace Pt black in commercial sensors which would dramatically decrease the Pt loading. This could reduce the price and increase the sensitivity of commercial alcohol sensors.

9.2 Future Directions

Future works on the Pt-Mn and Pt-Cu systems could continue with studying the mechanism of the ethanol electrooxidation on these alloys. As discussed in chapter 1, the ethanol oxidation on Pt-base catalysts is a complex process and could result in different by-products. Understanding the complete mechanism of ethanol oxidation on the Pt-Mn and Pt-Cu samples and identifying by-products is very important to build more efficient fuel

cells. Previous studies have shown that *in situ* Fourier-Transform Infrared (*in situ* FTIR) is one of the effective ways to study the products of the ethanol oxidation. FTIR makes it possible to monitor the ethanol oxidation in course of different potentials and compare different samples [8, 9]. There are also other methods to study and predict the ethanol oxidation pass ways such as differential electrochemical mass spectrometry (DEMS) [10], or with combination of conductivity cell, gas chromatography and infrared CO₂ analyzer [11].

Another interesting topic to investigate is the activity of the Pt-Mn and Pt-Cu samples toward the formic acid and methanol oxidation in the half-cell configuration, especially for the Pt-Mn samples which there are very limited number of publications. These tests will be helpful to understand more about the mechanism of the alcohol oxidation on these alloys. These studies also would be more interesting if they will combine with measurements in a direct alcohol fuel cell setup. It will be informative to correlate the half-cell measurements with the full cell measurements and investigate the performance of the heat treated samples in the fuel cell configuration. In addition, it will be valuable to study the surface composition of the alloy catalysts after exposure to the electrochemical processes by XPS. This would enable one to correlate the surface composition to the activity of these catalysts.

It was shown in chapter 7 that the Pt-Mn and Pt-Cu samples after the heat treatment have shown promising ORR activities. Therefore, in the next step of investigating alternative electrocatalysts for the alcohol sensors. It is worth studying the performance of these alloys as a cathode electrode for the fuel-cell based sensors. Using these alloys as both the cathode and anode for the sensors will dramatically reduce the Pt loading.

The other important topic which could extend the understanding of the fuel-cell based sensors and will help to build more sensitive and accurate sensors is to study the effects

other substances in the breath which may interfere with sensor readings. Previous studies have shown that the presence of acetone in the breath could cause some inaccuracy for FTIR measurement [12]. In addition, the sensing responses for Pt and Pt-alloys could be studied in the presence of oxygen in order to evaluate oxygen interferences for each set of samples.

9.3 References

- [1] W. Vielstich, A. Lamm, H.A. Gasteiger, *Handbook of Fuel Cells: Fundamental, Technology, and Applications*, Wiley, 2003.
- [2] C.W. Bezerra, L. Zhang, H. Liu, K. Lee, A.L. Marques, E.P. Marques, H. Wang, J. Zhang, *Journal of Power Sources*, 173 (2007) 891-908.
- [3] T. Ghosh, B.M. Leonard, Q. Zhou, F.J. DiSalvo, *Chemistry of Materials*, 22 (2010) 2190-2202.
- [4] S. Liao, K.-A. Holmes, H. Tsapralis, V.I. Birss, *Journal of the American Chemical Society*, 128 (2006) 3504-3505.
- [5] S. Beyhan, N.E. Şahin, S. Pronier, J.-M. Léger, F. Kadırgan, *Electrochimica Acta*, 151 (2015) 565-573.
- [6] P. Mani, R. Srivastava, P. Strasser, *Journal of Power Sources*, 196 (2011) 666-673.
- [7] L. Xiong, A. Manthiram, *Journal of The Electrochemical Society*, 152 (2005) A697-A703.
- [8] C. Lamy, S. Rousseau, E. Belgsir, C. Coutanceau, J.-M. Léger, *Electrochimica Acta*, 49 (2004) 3901-3908.
- [9] T. Sato, K. Okaya, K. Kunimatsu, H. Yano, M. Watanabe, H. Uchida, *ACS Catalysis*, 2 (2012) 450-455.
- [10] V. Rao, C. Cremers, U. Stimming, L. Cao, S. Sun, S. Yan, G. Sun, Q. Xin, *Journal of The Electrochemical Society*, 154 (2007) B1138-B1147.
- [11] D.D. James, D.V. Bennett, G. Li, A. Ghuman, R.J. Helleur, P.G. Pickup, *Electrochemistry Communications*, 11 (2009) 1877-1880.
- [12] J. Wigmore, R. Langille, *Canadian Society of Forensic Science Journal*, 42 (2009) 276-283.

Chapter 10:Appendices

Appendix A: Copyright Permissions

This is a License Agreement between Mohammadreza Ghavidel ("You") and Springer ("Springer"). The license consists of your order details, the terms and conditions provided by Springer, and the [payment terms and conditions](#).

[Get the printable license.](#)

License Number	3843250648940
License date	Apr 06, 2016
Licensed Content Publisher	Springer
Licensed Content Publication	JOM Journal of the Minerals, Metals and Materials Society
Licensed Content Title	An investigation of phase transformation behavior in sputter-deposited PtMn thin films
Licensed Content Author	C. X. Ji
Licensed Content Date	Jan 1, 2006
Volume number	58
Issue number	6
Type of Use	Thesis/Dissertation
Portion	Figures/tables/illustrations
Number of figures/tables/illustrations	1
Author of this Springer article	No
Original figure numbers	Figure 1.
Title of your thesis / dissertation	Alloy catalysts for fuel cellbased alcohol sensors
Expected completion date	May 2016
Estimated size(pages)	250
Total	0.00 CAD

This is a License Agreement between Mohammadreza Ghavidel ("You") and Springer ("Springer"). The license consists of your order details, the terms and conditions provided by Springer, and the [payment terms and conditions](#).

[Get the printable license.](#)

License Number	3851500708419
License date	Apr 17, 2016
Licensed Content Publisher	Springer
Licensed Content Publication	Journal of Phase Equilibria (and diffusion)
Licensed Content Title	Thermodynamic assessment of the Cu–Pt system
Licensed Content Author	Taichi Abe
Licensed Content Date	Jan 1, 2006
Volume number	27
Issue number	1
Type of Use	Thesis/Dissertation
Portion	Figures/tables/illustrations
Number	of 1
figures/tables/illustrations	
Author of this Springer article	No
Original figure numbers	Figure 1
Title of your thesis / dissertation	Alloy catalysts for fuel cellbased alcohol sensors
Expected completion date	May 2016
Estimated size(pages)	250
Total	0.00 CAD